View metadata, citation and similar papers at core.ac.uk

brought to you by CORE

provided by Nottingham ePrints

Hamer, Matthew James (2013) Analytical models of polymer nucleation. PhD thesis, University of Nottingham.

Access from the University of Nottingham repository:
http://eprints.nottingham.ac.uk/13440/1/thesis.pdf

Copyright and reuse:

The Nottingham ePrints service makes this work by researchers of the University of Nottingham available open access under the following conditions.

- Copyright and all moral rights to the version of the paper presented here belong to the individual author(s) and/or other copyright owners.
- To the extent reasonable and practicable the material made available in Nottingham ePrints has been checked for eligibility before being made available.
- Copies of full items can be used for personal research or study, educational, or not-for-profit purposes without prior permission or charge provided that the authors, title and full bibliographic details are credited, a hyperlink and/or URL is given for the original metadata page and the content is not changed in any way.
- Quotations or similar reproductions must be sufficiently acknowledged.

Please see our full end user licence at:
http://eprints.nottingham.ac.uk/end_user_agreement.pdf

A note on versions:

The version presented here may differ from the published version or from the version of record. If you wish to cite this item you are advised to consult the publisher’s version. Please see the repository url above for details on accessing the published version and note that access may require a subscription.

For more information, please contact eprints@nottingham.ac.uk

Analytical models of polymer nucleation

Matthew James Hamer, MMath

Thesis submitted to the University of Nottingham
for the degree of Doctor of Philosophy

December 2013

Abstract

In this thesis we investigate and develop analytic models for polymer nucleation and other barrier crossing problems. Our most broadly appealing method for certain multi-dimensional barrier crossing problems is a one-dimensional projection which includes a novel technique to extract rate kinetics from simulations [M J Hamer et al., *Soft Matter*, 2012, **8**, 11396-11408]. The scenarios we expect our method to be potentially useful are situations where barrier crossings are rare, and the dominant mechanism is through a series of unlikely incremental steps. The rate kinetics extraction technique is also reliant on the equilibrium energy barrier being relevant to non-equilibrium system, but is not appropriate when strong kinetic contributions dominate the process, and enable crossings over highly unfavouable energetic pathways.

We explore and significantly enhance the Graham-Olmsted (GO) polymer nucleation simulation [R S Graham and P D Olmsted, *Phys. Rev. Lett.*, 2009, **103**, 115702], producing a combinatorial calculation to obtain exact energy landscapes from it's basic stochastic rules of monomer attachment [M J Hamer et al., *J. Non-Newton. Fluid.*, 2010, **165**, 1294-1301]. We apply our rate kinetics extraction technique to the GO model and find that for most flow rates in purely long chain melts, nuclei tend to grow along similar paths over energy landscapes. The technique reveals a clear signature when this pattern is disobeyed, as in the case of blends of long and short chain polymer melts, some of which display highly anisotropic growth. In addition, we design several one-dimensional barrier crossing models with distinct characteristics, predicting the average and the distribution of crossing times with great accuracy. That finally enables us to completely describe the GO simulation's nucleation rates with analytic theory, by presenting a model of polymer nucleation featuring crystal rotation, which vastly impacts nucleation rates when polymer melts are subject to flow.

Acknowledgements

First and foremost, I would like to thank my supervisors Richard Graham and Jonathan Wattis. Without their experience and insightful advice this thesis simply would not have happened. I am particularly indebted to Rich for passing on a considerable amount of knowledge and methodologies in the field of polymer physics, as well as improving my research skills remarkably over the course of the PhD. I acknowledge the prior work of Rich and Peter Olmsted for developing the successful GO polymer nucleation simulation, which is the base of the majority of my analytical work. Furthermore, I am also grateful to Kenny Jolley for producing the brilliant fast barrier crossing algorithm; that technique enabled me to access a much larger area of the nucleation parameter space, and significantly enhanced the scope of my analysis and results.

I would also like to express my gratitude to Keith Hopcraft and Alexei Likhtman for agreeing to act as my assessors. Their detailed efforts reading the initial manuscript and probing questions in the viva voce examination improved this document significantly, in particular regarding the one-dimensional projection method in chapter 3.

I also hugely appreciate the financial support of the EPSRC.

I thoroughly enjoyed my four years in the School of Mathematical Sciences and in the city of Nottingham as a whole. I was privileged to receive so much help and kindness from within the Department and I am thankful that I met so many wonderful people during my studies, making the experience very pleasant indeed. Finally, I am eternally grateful to my family and Ruth for their unwavering support throughout my journey.

Contents

Abstract **i**

Acknowledgements **ii**

1 Introduction **1**

1.1 Overview 1

1.1.1 Outline of introduction 4

1.1.2 Outline of thesis 5

1.2 Representing polymer melts through the tube model 5

1.2.1 The Rouse model 6

1.2.2 Relaxation mechanisms 8

1.2.2.1 Reptation 9

1.2.2.2 Contour length fluctuations 12

1.2.2.3 Constraint release 15

1.3 The GLaMM model 17

1.4 Classical nucleation theory 20

1.4.1 One-dimensional nucleation over a simple energy landscape 20

1.4.2 Kinetic prefactor 22

1.5 Continuous energy barrier crossing 24

1.5.1 General energy well calculation 24

1.5.2 Application to star polymers 26

1.6 Simulation techniques 27

1.6.1 Detailed balance 27

1.6.2 Kinetic Monte Carlo algorithm 28

1.6.3 Graham-Olmsted simulation of flow-induced crystallisation 29

1.6.3.1 Elastic free energy derivation for monomer attachment 33

1.6.3.2 Entropic penalty of nucleus orientation 36

1.6.3.3 Implementation of nucleus rotation 38

1.6.3.4 Fast simulation technique for barrier crossing . 39

1.6.3.5 Summary of results 42

1.6.3.6 Comparison to experiments 43

1.7 Space-filling models for crystallisation 43

1.7.1 Model with unlimited growth 44
1.8 Discussion 45

2 Combinatorial calculation of polymer nucleation 47
2.1 Calculation of free energy nucleation landscapes 47
2.1.1 Quiescent nucleation 48
2.1.2 Two species 48
2.1.3 The general case of n species 50
2.1.4 Concentration of attaching stems 51
2.2 Results 52
2.2.1 Nucleation rates for stretched polymers 52
2.2.2 Bimodal blends 55
2.3 Discussion 58

3 One-dimensional projection for complex barrier crossing problems 60
3.1 One-dimensional barrier crossing model 61
3.1.1 Rate kinetics extraction techniques 62
3.1.1.1 Technique 1: Direct measurement from non-equilibrium systems 63
3.1.1.2 Technique 2: Extraction in relation to equilibrium barrier 63
3.1.1.2.1 Boltzmann region 66
3.1.1.2.2 Approach applicable to the entire landscape 66
3.1.1.3 Simple multi-route barrier crossing example . . 67
3.1.2 Generality and applicability discussion 71
3.2 Application to GO model; Rate kinetics investigation 71
3.2.1 Spherical nuclei growth 72
3.2.2 Initial investigation into the rate kinetics of the GO model 73
3.2.2.1 Boltzmann region 74
3.2.2.1.1 Rate kinetics calculation 74
3.2.2.1.2 Rate kinetics comparison to the direct extraction technique 76
3.2.2.2 Entire landscape 77
3.2.3 Full investigation into the rate kinetics of the GO model 78
3.2.3.1 Rate kinetics over the entire energy landscape 78
3.2.3.2 Rate kinetics at critical nuclei 80
3.2.4 GO model rate kinetics discussion 82
3.3 Discussion 85

4 **One-dimensional models of energy barrier crossing** **87**
4.1 Static barriers 88
4.1.1 Steady state occupancy method for finding average crossing times 88
4.1.1.1 Average crossing time calculation for one-dimensional energy barriers 88
4.1.1.2 Rotation model specific fraction of success and average failure time 90
4.1.2 Continuum approximations 93
4.1.2.1 Analogous continuous system 94
4.1.2.2 Average crossing time simplification for smooth energy landscapes 96
4.1.2.2.1 Average crossing time results 99
4.1.2.3 Fraction of success and average failure time calculations 101
4.1.3 Probability distribution of crossing times 103
4.1.3.1 Three-state system 103
4.1.3.2 The n-state system 105
4.1.3.2.1 Worked example of the four-state calculation 107
4.1.3.3 Average crossing time and variance from probability distribution in Laplace space 109
4.2 Dynamic energy barriers 110
4.2.1 Three state system with a random barrier height and reset capability 111
4.2.2 $n + 1$ state energy barrier with a discrete random path selector 113
4.2.2.1 Early pathway selection (state 1) 114
4.2.2.1.1 Probability distribution of failure times 117
4.2.2.1.2 Example: Two potential pathways . . 118
4.2.2.2 Delayed pathway selection 118
4.2.2.2.1 Example: delayed pathway selection . 122
4.3 Discussion 123

5 **Rotation model of polymer nucleation** **125**
5.1 Analysis of rotation within GO simulation 126
5.2 Model construction 130
5.2.1 Rate kinetics for nuclei highly-aligned with flow direction 130
5.2.2 Discrete angular selection 132
5.2.3 Rotation model calculation 133
5.2.3.1 Reduced angular considerations 135

5.2.3.2 Approximation to the average crossing time for the rotational model 136
5.3 Results 138
5.3.1 Test calculation 138
5.3.2 Calculation of polymer nucleation during a transient flow 142
5.4 Discussion 149

6 Discussion and future work 151
6.1 Summary 151
6.2 Conclusions 153
6.3 Comparison with experiments 154
6.4 Immediate future work 155
6.4.1 Polymers 155
6.4.2 General applications to barrier crossing 156
6.5 Long term future work 157

Bibliography 159

A Concentration of attaching stems free energy argument 166

B Further investigations into full landscape rate kinetics 168

C Three state system with decreasing barrier and reset capability 171

Chapter 1

Introduction

1.1 Overview

Polymers are long chain molecules, formed by covalently bonding together a large number (typically more than 10^3) of repeating units or monomers. A polymer melt is a crowded mixture of numerous long chain molecules. Due to the highly entangled nature of polymer melts, describing their internal dynamics has been a significant scientific challenge for nearly half a century. Individual monomers have a large amount of freedom to thermally diffuse, however whole polymer chains are to a high degree confined by surrounding chains in the melt. This creates a difficult multi-scale problem to investigate. Building upon Rouse's initial picture [1, 2] and work by Edwards [3], De Gennes pioneered the field with his idea of the tube model [4].

Polymer crystallisation is the transformation from a liquid or amorphous state, in which chains are arranged randomly, into a semi-crystalline state containing highly ordered regions called crystallites. The amount and arrangement of this crystalline material, is known as the morphology, and strongly impacts on many physical characteristics of the final plastic, such as the strength, flexibility, and transparency. During the manufacture of plastic materials, polymer melts are subjected to flow, which significantly enhances the formation of crystallites. This effect is called flow-induced crystallisation (FIC) [5, 6, 7, 8]. The widely suggested mechanism for FIC, is that the flow stretches chain configurations, and this lowers the entropic penalty of crystallisation. However, a quantitative model in the molecular regime that describes the underlying physics has yet to be developed. As semi-crystalline polymers make up a significant fraction of the plastics industry's production, the introduction of such a model would be hugely beneficial, since it would enable control over the solid-state characteristics of polymer products by simply tailoring the manufacturing process. The current progress and potential future directions in the field of molecular modelling of polymer crystallisation have been described in a recent review article [9].

In experiments the most dramatic effects of FIC happen at low undercooling, namely temperatures marginally below the melting point. The formation of elongated nuclei-shaped like shish-kebabs being one of the more curious effects. Such crystals contain long chained molecules arranged in cylinders, with folded chains arranged in disk-like lamellae attached to the central cylindrical core. The shish-kebab shaped crystals have a strong effect on the strength of a material [10]. These strange structures have been imaged directly under a microscope [8], as well as by electron microscopy [11, 12]. Additionally, shish-kebabs produce a striking signature in both X-ray [5, 12, 13] and neutron scattering [14].

As with many phase transitions, polymer crystallisation is initiated by a process called nucleation. This is the mechanism by which solid crystals or nuclei are formed. Nucleation is driven by energetically favourable interactions between neighbouring monomers in an ordered crystal. However, these favourable interactions must overcome the entropic loss of existing in a crystal state as opposed to the positional freedom of a liquid state, to create a thermodynamic driving force for crystal formation. There is also a cost due to the liquid-crystal interface. This creates an energy balance between the gain due to the volume of the nucleus and the cost of its surface area [15]. For small nuclei, the surface area penalty dominates, and thus the path to successful nucleation is blocked by a free energy barrier. Once nuclei have diffused over this energy barrier and developed to a sufficient size that the crystal is stable, spontaneous growth occurs. The shape of this energy barrier, particularly the height, has a huge impact on the morphology of the semi-crystalline material. Small energy barriers allow nucleation to occur quickly, and produce many small, evenly sized spherulites. On the other hand, large energy barriers make nucleation events rare, so the internal structure of the material becomes an assortment of irregularly sized crystals.

In general, nucleation is a rare event, which makes the process extremely slow. This implies the employment of stochastic simulations to investigate polymer nucleation is a huge challenge especially at low undercooling. Molecular dynamical (MD) simulations that resolve all activity for each monomer in a given system are too detailed to investigate nucleation due to their immense cost. As the process involves the repeated formation and highly probable breakdown of a large number of small nuclei that have little prospect of developing into a stable crystal. These MD simulations, have however provided important information about the growth stage in polymer crystallisation [16, 17], which is a faster, simpler process. A more suitable approach to the simulation of polymer nucleation is with the kinetic Monte Carlo method [18, 19, 20], applied to highly coarse-grained models. In particular, the Graham-Olmsted (GO) polymer nucleation simulation [21, 22] uses this approach, retaining a minimal description of the nucleus, and employing a variable timestep. Thus large timesteps are taken for small nuclei but greater resolution is introduced for larger nuclei. These techniques enable nucleation events to be investigated; however, they are still restricted by the rarity of the process, and this directly linked to the size of the energy barrier a nucleus must overcome.

Other models have taken an empirical approach for polymer crystallisation, and particularly for FIC, use ordinary differential equations to describe the phase transitions under flow [23, 24, 25, 26]. The Schneider/Kolmogorov rate equations tend to be employed [27, 28], which determine the evolution of crystalline regions. The crystal formation models require both nucleation and growth rates to be known functions of time. Vitally important information about the crystalline morphology is produced, including spherulite density, volume, and shape. Additionally, they are computationally inexpensive and can be implemented in finite element solvers even for complex flow geometries. A significant obstacle in the success of these empirical models, is the inability to accurately determine the evolving nucleation rate as the polymer melt is subjected to flow. The input assumptions for the dependence of the nucleation rate on the flow are too simplistic. Moreover, since the nucleation rate is so crucial to the resultant morphology, any significant inaccuracies mean that the models cannot be predictive.

The GO model agrees with experimental data [21, 22], but requires greater testing and comparisons are expensive. In general stochastic simulation is an instrumental tool in the study of polymer nucleation; however, practical restrictions will always apply. Hence there is a great requirement for analytic theory that not only predict the results of simulations, for example the GO model, but also have the ability to overcome limitations. Analytic models would also be a more efficient method of comparison to experimental data. Additionally, empirical crystal growth models in finite element schemes rely on a deterministic nucleation rate, even though it is a random process. So, dependable analytic predictions are a necessity to advance understanding of FIC in polymers. Therefore the global objective of this thesis is to develop analytic models that describe the nucleation of polymer melts.

In this thesis, we aim to accurately predict the results of the GO polymer nucleation simulation. However we also envisage the majority of our ideas and methodologies will have the potential to be applied to other types of simulation with minimal modification. Initially, we set out to calculate energy landscapes of nucleation by counting the number of arrangements of energetically equivalent nuclei. The key piece of information to obtain from energy landscapes is the height of the barriers, and then we will be able to estimate the nucleation rate through the Boltzmann approximation. Our next goal will be to improve on the Boltzmann approximation with a one-dimensional discrete barrier crossing formulation. The difficultly in this approach will arise in finding the correct rate kinetics between the merged states of our one-dimensional projection. To investigate this problem, we develop a simulation technique to extract the rate kinetics from a multi-dimensional simulation.

Another aspect of polymer nucleation we intend to study is the crystal's orientation with respect to the flow direction during the process. This orientation is hugely influential on the probability of a successful nucleation event, as aligned crystals have greater opportunities to grow since more monomers in the melt are able to attach. The GO simulation stores this orientation and it is a vital component of monomer attachment moves. The simulation also enables the crystal to rotate through random diffusion and a convective drag force from the flow. We aim to investigate the effects of crystal rotation on the nucleation rate, and the main objective of this thesis is to develop an analytical model that will represent the most physically relevant regime.

1.1.1 Outline of introduction

This introductory chapter essentially reviews the literature in the areas related to polymer nucleation. Beginning with the tube model in section 1.2, which is the most established and successful theory that models the dynamics of polymer melts. It builds upon the Rouse model, which represents a polymer chain as a set of beads connected together by springs, the tube model confines these chains to a tube-like region. Several relaxation mechanisms that describe how chains are able to escape these tubes are also presented. In section 1.3, we detail the Graham, Likhtman and Milner, McLeish (GLaMM) model of entangled polymers under fast flows, which is a refinement of the original tube model.

We review classical nucleation theory that considers simple atomic systems in section 1.4. Focusing on a one-dimensional barrier crossing calculation over an energy landscape based on a balance between the energy gain due to the volume and the associated cost of the surface area. In section 1.5, a calculation of a particle escaping a potential well through diffusion is explained. An important component of this thesis is to adapt these calculations of continuous systems on to discrete barrier crossing problems.

All of the barrier crossing simulations in this work are based on the kinetic Monte Carlo algorithm, which is introduced in section 1.6. We also detail the GO simulation of FIC, which uses a highly coarse-grained description of a nucleus, in which monomers attach and detach through stochastic events. The simulation is also able to incorporate the flow modelling of the GLaMM model to analyse FIC. Another key objective of this thesis is to produce an analytic calculation to predict the nucleation rates of the GO model.

In section 1.7, the next stage in the modelling of the crystallisation process is briefly discussed. That is the procedure describing how stable nuclei grow into macroscopic spherulites, and how the initial nucleation rate affects the morphology or internal structure of the resulting solid material. The overall goal for the research area is to produce a complete bottom up, multi-length scale, and multi-time scale model that can be applied in a finite element scheme in an industrial context that can predict FIC in polymers. In this thesis, we develop several techniques that solve important issues relating to this formidable task.

1.1.2 Outline of thesis

This thesis contains four genuine research chapters, and will present innovative ideas, models, solutions to the area of polymer nucleation. We begin in chapter 2 with an analytic calculation of energy landscapes to polymer nucleation. Using ideas from statistical mechanics and combinatorics to count the number of arrangements of similar nuclei, we aim to accurately predict the energy landscapes produced by the GO model to investigate FIC. Moreover, we intend to apply the calculation to polymer melts containing a mixture of short and long chains, referred to as bimodal blends.

A general aim of this thesis is to improve the accuracy of nucleation rates as opposed to relying on the Boltzmann approximation. To this end, in chapter 3 we develop a one-dimensional projection for energy barrier crossing problems. In particular, we present a novel simulation technique to extract rate kinetics from certain multi-dimensional simulations. We successfully apply this projection to analyse rate kinetics of the GO model.

In chapter 4, we aim to create mathematical tools to fully investigate one-dimensional energy barrier crossing problems. We intend to obtain a formulation for the average crossing time as well as developing a method to predict the complete distribution of crossing times. This technique will be based on a probabilistic approach to solving the escape rates from individual states in a convoluted system. It will enable us to model some dynamic energy barriers along with basic static cases.

The main objective of this thesis is to develop an analytic model of polymer nucleation that includes crystal rotation. In chapter 5, we will analyse the GO model and consider the most physically sensible rotational phenomena. To adapt a dynamical one-dimensional model to closely replicate crystal rotation during the nucleation process of polymers, with the ultimate ambition to apply this model to investigate FIC.

1.2 Representing polymer melts through the tube model

The tube model is an extremely successful approach to modelling the dynamics of entangled polymer melts, first introduced by de Gennes [4] building upon work by Edwards [3]. In this section, the main concepts and ideas of the model are presented, as well as the more recent refinements, beginning with the foundations of the approach in section 1.2.1, where the Rouse model is introduced. In section 1.2.2, the three main relaxation mechanisms of the tube model are discussed, which are reptation, contour length fluctuations, and constraint release.

1.2.1 The Rouse model

The Rouse model [1], which is detailed in chapter 4 of [2], represents polymer chains by sets of beads connected together with linear springs. The dynamics of polymer chains are described by the Brownian motion of such beads.

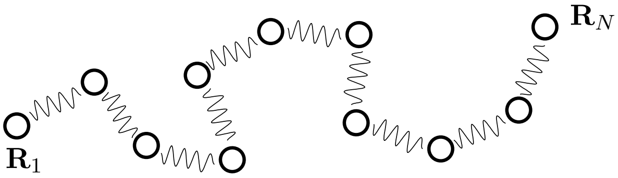

Figure 1.1: Rouse model

Let $(\mathbf{R}_1, \mathbf{R}_2, \ldots, \mathbf{R}_N) = \{\mathbf{R}_N\}$ be the position of the beads, see figure 1.1. The motion of the beads is described by the Smoluchowski equation (or the Langevin equation)

$$\frac{\partial}{\partial t}\mathbf{R}_n(t) = \sum_m \mathbf{H}_{nm} \cdot \left(-\frac{\partial \mathbf{U}}{\partial \mathbf{R}_m} + \mathbf{f}_m(t)\right) + \frac{1}{2}k_B T \sum_m \frac{\partial}{\partial \mathbf{R}_m} \cdot \mathbf{H}_{nm} \ . \qquad (1.2.1)$$

The Rouse model disregards the excluded volume interaction and the hydrodynamic interaction. The mobility tensor, $\mathbf{H}_{nm}$, and the elastic spring potential, $\mathbf{U}$, are written as

$$\mathbf{H}_{nm} = \frac{\mathbf{I}}{\zeta}\delta_{nm} \ ,$$

$$\mathbf{U} = \frac{k}{2}\sum_{n=2}^{N}(\mathbf{R}_n - \mathbf{R}_{n-1})^2 \quad \text{with} \quad k = \frac{3k_B T}{b^2} \ .$$

The Langevin equation (1.2.1) is reduced to a linear equation in this model, for middle beads $(n = 2, 3, \ldots, N-1)$

$$\zeta\frac{\mathrm{d}\mathbf{R}_n}{\mathrm{d}t} = -k\left(2\mathbf{R}_n - \mathbf{R}_{n+1} - \mathbf{R}_{n-1}\right) + \mathbf{f}_n \ , \qquad (1.2.2)$$

and for the end beads $(n = 1, N)$

$$\zeta\frac{\mathrm{d}\mathbf{R}_1}{\mathrm{d}t} = -k\left(\mathbf{R}_1 - \mathbf{R}_2\right) + \mathbf{f}_1 \ , \quad \text{and} \quad \zeta\frac{\mathrm{d}\mathbf{R}_N}{\mathrm{d}t} = -k\left(\mathbf{R}_N - \mathbf{R}_{N-1}\right) + \mathbf{f}_N \ .$$

The distribution of the random force $\mathbf{f}_n$ is Gaussian, characterised by the moments

$$\langle \mathbf{f}_n(t)\rangle = 0 \quad \text{and} \quad \left\langle f_{n\alpha}(t) f_{m\beta}(t')\right\rangle = 2\zeta k_B T \delta_{nm}\delta_{\alpha\beta}\delta(t - t') \ . \qquad (1.2.3)$$

The discrete variable n is transformed to be continuous, and hence equation (1.2.2) becomes

$$\zeta\frac{\partial \mathbf{R}_n}{\partial t} = k\frac{\partial^2 \mathbf{R}_n}{\partial^2 n} + \mathbf{f}_n \ . \tag{1.2.4}$$

Imaginary beads $\mathbf{R}_0 = \mathbf{R}_1$ and $\mathbf{R}_{N+1} = \mathbf{R}_N$ are chosen, so that the end points obey equation (1.2.2), and in the continuous limit the boundary conditions are

$$\left.\frac{\partial \mathbf{R}_n}{\partial n}\right|_{n=0,N} = 0 \ . \tag{1.2.5}$$

The continuous stochastic differential equation (1.2.4) is transformed using normal coordinates $\mathbf{X}_p$ defined by

$$\mathbf{X}_p \equiv \frac{1}{N}\int_0^N \cos\left(\frac{p\pi n}{N}\right)\mathbf{R}_n(t)\mathrm{d}n \text{ with } p = 0, 1, 2, \dots \ , \tag{1.2.6}$$

therefore

$$\zeta_p\frac{\partial}{\partial t}\mathbf{X}_p = -k_p\mathbf{X}_p + \mathbf{f}_p \ , \tag{1.2.7}$$

where $\zeta_0 = N\zeta$ and $\zeta_p = 2N\zeta$ for $p = 1, 2, \dots$, and
$k_p = 2\pi^2 kp^2/N = (6\pi^2 k_B T/Nb^2)p^2$ for $p = 0, 1, 2, \dots$, and the random forces $\mathbf{f}_p$ must satisfy (note $\mathbf{f}_p = (f_{px}, f_{py}, f_{pz})$)

$$\langle f_{p\alpha}\rangle = 0 \text{ and } \left\langle f_{p\alpha}(t) f_{q\beta}(t')\right\rangle = 2\delta_{pq}\zeta_p k_B T\delta_{\alpha\beta}\delta(t-t') \ , \tag{1.2.8}$$

with the angled brackets representing an averaging calculation, where
$\alpha, \beta = x, y, z$. All of these results are described in Appendix 4.II of [2]. Since each random force $\mathbf{f}_p$ is independent of the others, the motions of the $\mathbf{X}_p$ are also independent of each other. Thus the motion of the polymer chain is broken down into independent modes. The inverse transformation of equation (1.2.6) is

$$\mathbf{R}_n = \mathbf{X}_0 + 2\sum_{p=1}^{\infty}\mathbf{X}_p\cos\left(\frac{p\pi n}{N}\right) \ , \tag{1.2.9}$$

with the coordinate $\mathbf{X}_0$ representing the position of the centre of mass

$$\mathbf{R}_G \equiv \frac{1}{N}\int_0^N \mathbf{R}_n \mathrm{d}n = \mathbf{X}_0 \ . \tag{1.2.10}$$

The self diffusion constant, D_G, of the centre of mass, $\mathbf{R}_G$, is defined as

$$D_G = \lim_{t\to\infty}\frac{1}{6t}\left\langle \left(\mathbf{R}_G(t) - \mathbf{R}_G(0)\right)^2\right\rangle \ . \tag{1.2.11}$$

This is solved with equation (1.2.7) to obtain

$$D_G = \frac{k_B T}{N\zeta} \ , \tag{1.2.12}$$

and so it is of order N^{-1}.

Another physical parameter of interest is the end-to-end vector

$$\mathbf{P}(t) = \mathbf{R}_N(t) - \mathbf{R}_0(t) \ ,$$

which can be expressed in terms of normal coordinates using the inverse relation (1.2.9) as

$$\mathbf{P}(t) = -4 \sum_{p\text{: odd}} \mathbf{X}_p(t) \ .$$

The time correlation function of the end-to-end vector is defined as $\langle \mathbf{P}(t) \cdot \mathbf{P}(0) \rangle$, hence $\langle X_{p\alpha}(t) X_{q\beta}(0) \rangle$ is required for $p, q > 0$. Using the fact that $\langle f_{p\alpha}(t) X_{q\beta}(0) \rangle$ is uncorrelated and hence equal to zero from (1.2.8), a simple differential equation is obtained from (1.2.7)

$$\frac{\partial}{\partial t} \langle X_{p\alpha}(t) X_{q\beta}(0) \rangle = -\frac{1}{\tau_p} \langle X_{p\alpha}(t) X_{q\beta}(0) \rangle \quad \text{with } \tau_p = \frac{\zeta_p}{k_p} \ .$$

An important element to complete the calculation, the Dirac-delta function in the second average moment (1.2.8), must be slightly modified, to a tall thin Gaussian

$$\delta(t - t') \approx \lim_{B \to \infty} \sqrt{\frac{B}{\pi}} \exp\left(-B(t - t')^2 \right) \ .$$

The resulting correlation function

$$\langle \mathbf{P}(t) \cdot \mathbf{P}(0) \rangle = 16 \sum_{p\text{: odd}} \langle \mathbf{X}_p(t) \cdot \mathbf{X}_p(0) \rangle = N b^2 \sum_{p\text{: odd}} \frac{8}{p^2 \pi^2} \exp\left(-\frac{t p^2}{\tau_1} \right) , \tag{1.2.13}$$

which is dominated by the first mode $\mathbf{X}_1$. The longest relaxation time of the correlation function of the end-to-end vector is called the Rouse time

$$\tau_R = \tau_1 = \frac{\zeta N^2 b^2}{3 \pi^2 k_B T} \ . \tag{1.2.14}$$

Since N is proportional to the molecular weight, M, then $\tau_R \propto M^2$, and the diffusion constant, $D_G \propto M^{-1}$. The Rouse model works well for short, unentangled polymers in melts, unfortunately these predictions are inconsistent with experimental results of unentangled polymers in solutions. This failure is due to the Rouse model disregarding hydrodynamic interactions, which are included in the Zimm model, detailed in chapter 4.2 of [2]. This thesis is focused on highly entangled polymer melts, so hydrodynamic interactions are not of concern.

1.2.2 Relaxation mechanisms

Polymer melts are highly complicated systems containing extremely long chain molecules. The tube model represents this by focusing on a single chain and assumes that neighbouring chains are effectively fixed in position for short timescales, creating a network of obstructions, see figure 1.2(a). The freedom of motion is restricted, as a chain cannot cross a neighbouring chain. Hence the chain is almost confined to a tube-like region shown in figure 1.2(b) because most conformations that go outside will cross a neighbouring chain and break the constraint. In this section, the three main relaxation mechanisms within the tube model are described, these are reptation, in section 1.2.2.1, contour length fluctuations, in section 1.2.2.2, and finally constraint release, in section 1.2.2.3, based on the ideas collected in chapter 6 of [2].

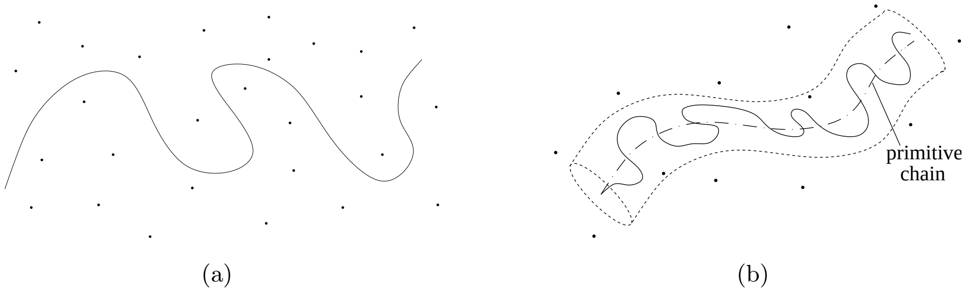

Figure 1.2: (a) A polymer chain in a fixed network of obstacles, dots represent neighbouring chains confining the chain to a tube-like region. (b) A polymer chain contained within an imaginary tube made up of neighbouring chains which restricts our chains movement considerably, the primitive chain is the dashed/dotted line in the centre of the tube.

1.2.2.1 Reptation

In this section, the first relaxation mechanism within the tube model is introduced. The meandering chain will be much longer than its enclosing tube, so the slack is free to explore inside of the tube and even outside circular extremities of the tube. The end points of the chain are not fixed, they are free to move outside of the existing tube, creating new tube in the process. On the other hand, a chain end can also move inside the tube, destroying that section of tube. This process of creating and destroying sections of tube is called reptation.

The polymer chain is represented by the Rouse model containing N segments with bond length, b, and the drag constant, ζ. The neighbouring chains are assumed to be thin lines that have no effect on the static properties but a huge effect on the dynamic properties by confining the chain to a tube-like region. At a fixed time, the shortest path connecting the end points of the chain with the same topology as the tube confining the chain is defined as the primitive path. On small timescales the polymer wriggles around the primitive path, on longer timescales the primitive path moves as the tube reptates. On these longer timescales, the small variations around the primitive path are ignored as movement of the path itself is of more importance and referred to as the primitive chain shown in figure 1.2(b).

Position on the primitive chain is defined by contour length, s, measured from one end of the primitive chain. The vector $\mathbf{R}(s,t)$ represents the position of segment s at time, t, the vector tangent to the primitive chain at segment,

s, is

$$\mathbf{u}(s,t) = \frac{\partial}{\partial s}\mathbf{R}(s,t) \ . \tag{1.2.15}$$

The primitive chain is defined by the following assumptions.

(i) The primitive chain has a constant length, L.

(ii) The primitive chain can only move along its own axis with a diffusion constant, D_c.

(iii) The correlation of the tangent vectors $\mathbf{u}(s,t)$ and $\mathbf{u}(s',t)$ decreases quickly with the contour distance $|s-s'|$.

Assumption (i) neglects contour length fluctuations, reviewed in section 1.2.2.2, (ii) states the primitive chain can only move through reptation. Assumption (iii) ensures that the primitive chain becomes a random walk at large enough length scales. This ensures that the movement of the primitive chain is Gaussian. The mean square distance on a Gaussian chain is proportional to $|s-s'|$, giving

$$\left\langle \left(\mathbf{R}(s,t) - \mathbf{R}(s',t)\right)^2 \right\rangle = a\left|s-s'\right| \quad \text{for} \quad \left|s-s'\right| \gg a \ , \tag{1.2.16}$$

where the length, a, is called the step length of the primitive chain. The diffusion constant, D_c in this model must be the same as the diffusion coefficient from the Rouse model in equation (1.2.12), therefore

$$D_c = \frac{k_B T}{N\zeta} \ . \tag{1.2.17}$$

Finally the mean square distance of the end-to-end vector is La and from the Rouse model of the chain it is also known to be Nb^2, thus

$$L = \frac{Nb^2}{a} \ . \tag{1.2.18}$$

The step length, a, is the only parameter left not fully defined, and this depends on the nature of the entanglement network.

Calculating the time correlation of the end-to-end vector

$$\mathbf{P}(t) = \mathbf{R}(L,t) - \mathbf{R}(0,t) \ , \tag{1.2.19}$$

to find information about the timescales involved in the reptation process. Figure 1.3 shows an example of a primitive chain reptating out of its original tube. To calculate $\langle \mathbf{P}(t)\cdot\mathbf{P}(0)\rangle$, $\mathbf{P}(t)$ and $\mathbf{P}(0)$ are expressed using figure 1.3(d) as

$$\mathbf{P}(0) = \overrightarrow{A_0C} + \overrightarrow{CD} + \overrightarrow{DB_0} \quad \text{and} \quad \mathbf{P}(t) = \overrightarrow{AC} + \overrightarrow{CD} + \overrightarrow{DB} \ . \tag{1.2.20}$$

Since tube sections $\overrightarrow{AC}$ and $\overrightarrow{DB}$ are independent of the original tube section

$$\langle \mathbf{P}(t)\cdot\mathbf{P}(0)\rangle = \left\langle \overrightarrow{CD}^2 \right\rangle = a\,\langle\sigma(t)\rangle \ , \tag{1.2.21}$$

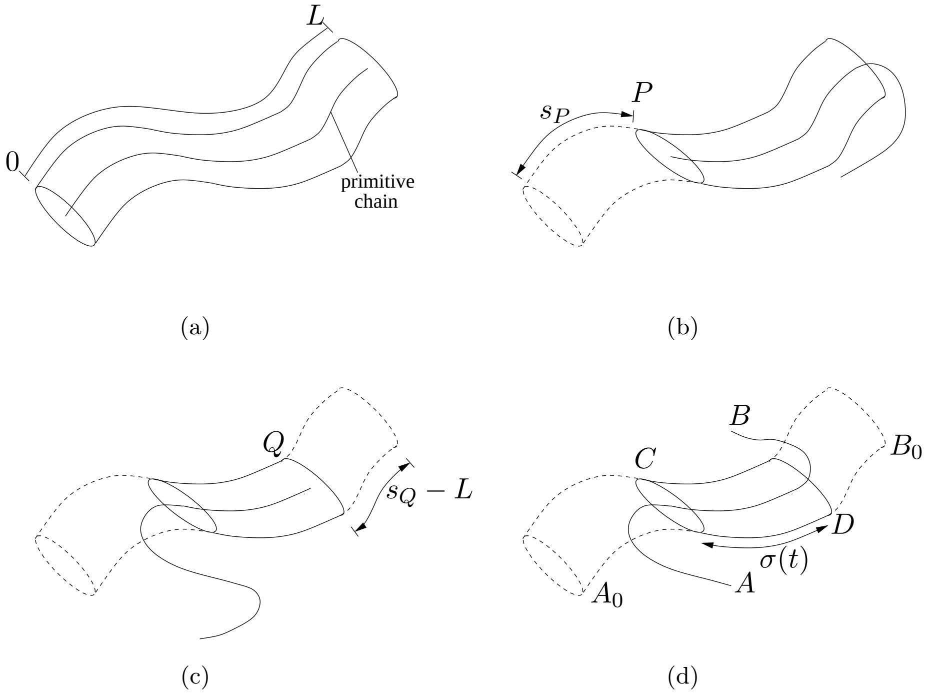

(a) (b)

(c) (d)

Figure 1.3: (a) At time, $t = 0$, the primitive chain is confined to a tube of contour length L. (b) After a period of time, t_1, the primitive chain has reptated along the contour length a displacement of, s_P, destroying a section of tube. (c) At a later time, t_2, the primitive chain has reptated in the opposite direction a displacement of, $s_Q - L$, destroying another section of tube. (d) At time, t, after reptating back and forth the primitive chain has lost most of the original tube, leaving only a small section CD.

where $\sigma(t)$ is the contour length of CD or in general the contour length of the original tube still remaining. The method focuses on a particular tube segment, s, which will disappear when it is passed by either end of the primitive chain. The probability that the tube segment remains at time, t, is $\psi(s,t)$, therefore

$$\langle\sigma(t)\rangle = \int_0^L \psi(s,t)\mathrm{d}s \ . \tag{1.2.22}$$

The probability that the primitive chain has moved a displacement, ξ, while the tube segment s still remains at time, t is given by $\Psi(\xi,t;s)$. This probability must satisfy the one-dimensional diffusion equation

$$\frac{\partial\Psi}{\partial t} = D_c\frac{\partial^2\Psi}{\partial\xi^2} \ , \tag{1.2.23}$$

with the initial condition that $\Psi(\xi,0;s) = \delta(\xi)$ since at time, $t = 0$, the primitive chain has not moved, and $\Psi(\xi,0;s)$ must be contained at the origin. The boundary conditions are $\Psi(\xi,t;s) = 0$ when $\xi = s$ and $\xi = s - L$ because once the ends of the primitive chain has reached segment, s, the tube segment is destroyed immediately. A separable solution is sought, and together with the standard Fourier series method to solve the diffusion equation, the solution of equation (1.2.23) with the given conditions is

$$\Psi(\xi, t; s) = \sum_{p=1}^{\infty} \frac{2}{L} \sin\left(\frac{p\pi s}{L}\right) \sin\left(\frac{p\pi(s-\xi)}{L}\right) \exp\left(-\frac{p^2 t}{\tau_d}\right) , \tag{1.2.24}$$

where $\tau_d = L^2/D_c\pi^2$. Thus for the segment to remain, ξ, must be in between $s-L$ and s, so the probability, $\psi(s,t)$ must obey

$$\psi(s,t) = \int_{s-L}^{s} \Psi(\xi, t; s)\mathrm{d}\xi = \sum_{p\text{: odd}} \frac{4}{p\pi} \sin\left(\frac{p\pi s}{L}\right) \exp\left(-\frac{p^2 t}{\tau_d}\right) . \tag{1.2.25}$$

Equations (1.2.21), (1.2.22) and (1.2.25) lead to the result

$$\begin{aligned} \langle \mathbf{P}(t) \cdot \mathbf{P}(0) \rangle &= a \langle \sigma(t) \rangle = La\psi(t) = Nb^2\psi(t) \ , \\ \text{where } \psi(t) &= \frac{1}{L}\int_0^{\infty} \psi(s,t)\mathrm{d}s = \sum_{p\text{: odd}} \frac{8}{p^2\pi^2} \exp\left(-\frac{p^2 t}{\tau_d}\right) . \end{aligned} \tag{1.2.26}$$

The longest relaxation time of $\langle \mathbf{P}(t) \cdot \mathbf{P}(0) \rangle$ is given by τ_d which is called the reptation time and can be rewritten using (1.2.17) and (1.2.18) as

$$\tau_d = \frac{1}{\pi^2} \frac{\zeta N^3 b^4}{k_B T a^2} . \tag{1.2.27}$$

This reptation time, τ_d, is the timescale a tube segment in the middle of the tube ($s \approx L/2$) is expected to last, obviously the nearer to the end points a segment is, the shorter its expected lifetime will be, and at the end points the tube is likely to disappear almost immediately. Comparing the reptation time with the Rouse time from equation (1.2.14), $\tau_d \propto N^3$ whereas $\tau_R \propto N^2$. Defining the number of entanglements, Z, in a chain to be

$$Z = \frac{L}{a} = \frac{Nb^2}{a^2} . \tag{1.2.28}$$

The reptation time, τ_d, can be expressed in terms of Z and τ_R as

$$\tau_d = 3Z\tau_R , \tag{1.2.29}$$

thus reptation is a process that acts on a significantly longer timescale than the relaxation of the chain due to the Rouse model.

1.2.2.2 Contour length fluctuations

In section 1.2.2.1, the primitive chain length, L, is fixed, a more realistic model however allows the contour length to fluctuate with time. The statistical distribution of contour lengths made of Rouse chains confined to a tube is considered. The number density of conformations that are represented by a certain primitive chain is defined as ω. This quantity is calculated in appendix 6.I of [2] by confining a Rouse chain within a tube of length, L, with a square cross-sectional a_0^2, the result is

$$\omega(L) = \omega_0 \exp\left(-\frac{3L^2}{2Nb^2} - \alpha_0 \frac{Nb^2}{a_0^2}\right) , \tag{1.2.30}$$

where ω_0 is the number of configurations in free space and α_0 is a numerical factor which depends on the shape of the cross-section of tube. The number of primitive paths of length, L, is defined as, $\Omega(L)$, and the probability that a primitive chain has a contour length, L, is therefore

$$\Psi(L) \propto \omega(L)\Omega(L) \ . \tag{1.2.31}$$

The quantity $\Omega(L)$ is approximated as the number of random walks with step-size, L/a_0, therefore

$$\Omega(L) \approx \exp\left(\alpha_1 \frac{L}{a_0}\right) , \tag{1.2.32}$$

where α_1 is a numerical value dependent on the structure of the entanglement network. Hence

$$\Psi(L) \propto \exp\left(-\frac{3L^2}{2Nb^2} + \alpha_1 \frac{L}{a_0}\right) \propto \exp\left(-\frac{3}{2Nb^2}\left(L - \widehat{L}\right)^2\right) , \tag{1.2.33}$$

with $\widehat{L} = \alpha_1 Nb^2/3a_0$, and together with equation (1.2.18), this implies that $a = 3a_0/\alpha_1$, hence the step length of the primitive chain, a, is of the same order as the tube diameter, a_0.

The average fluctuation is calculated using $\widehat{\Psi}$ which is the normalised form Ψ in equation (1.2.33)

$$\left\langle \Delta L^2 \right\rangle^{1/2} = \left[\int_0^\infty \widehat{\Psi}(L)\left(L - \widehat{L}\right)^2 \mathrm{d}L\right]^{1/2} = \left(\frac{Nb^2}{3}\right)^{1/2} \quad \text{for } \widehat{L} \gg \left(Nb^2\right)^{1/2} \ . \tag{1.2.34}$$

The dynamics of the contour length fluctuations are of particular interest, and are described by the continuous form of the Langevin equation (1.2.4)

$$\zeta \frac{\partial}{\partial t} s_n(t) = \frac{3k_BT}{b^2} \frac{\partial^2}{\partial n^2} s_n(t) + f_n(t) \tag{1.2.35}$$

$$\text{with } \ \langle f_n(t) \rangle = 0 \ \text{ and } \ \left\langle f_n(t) f_m(t') \right\rangle = 2\zeta k_B T \delta(n-m)\delta(t-t') \ ,$$

where $s_n(t)$ is the curvilinear coordinate of the n-th Rouse segment. The contour length of the primitive chain is defined by $L(t) = s_N(t) - s_0(t)$. The analysis is similar to the Rouse model with the important difference that in equilibrium, the average contour length $\langle s_N - s_0 \rangle = \widehat{L}$, whereas in the Rouse model the corresponding quantity $\langle \mathbf{R}_N - \mathbf{R}_0 \rangle = 0$. To obtain the correct equilibrium average length, the boundary conditions must be altered. Equation (1.2.35) is averaged and since at equilibrium $\partial/\partial t \equiv 0$ and $\langle f_n(t) \rangle = 0$ gives

$$\frac{\partial^2}{\partial n^2} \langle s_n \rangle = 0 \ , \ \text{ therefore } \ \frac{\partial}{\partial n} \langle s_n \rangle = B \ ,$$

hence the average contour length, $\widehat{L} = \langle s_N(t) - s_0(t) \rangle = BN$. This leads to the boundary conditions

$$\frac{\partial}{\partial n} s_n \bigg|_{n=0,N} = \frac{\widehat{L}}{N} \ ,$$

which is equivalent to a tensile force $F_{\text{eq}} = 3k_BT\widehat{L}/Nb^2 = 3k_BT/a$ acting on the chain ends. This force can be understood intuitively by considering the dynamical process at the chain end. The chain has more options to increase its length than options to move back into the tube, decreasing the length of the tube. This imbalance tends to increase the contour length, causing the effective tensile force.

To satisfy the boundary condition, the following normal modes are employed

$$\begin{aligned} Y_0 &= \frac{1}{N}\int_0^N s_n \mathrm{d}n \ , \\ Y_p &= \frac{1}{N}\int_0^N \cos\left(\frac{p\pi n}{N}\right)\left(s_n - \frac{n\widehat{L}}{N}\right)\mathrm{d}n \ \text{ for } \ p = 1, 2, \ldots \ , \end{aligned} \tag{1.2.36}$$

$$\text{or} \ \ s_n = Y_0 + \frac{n\widehat{L}}{N} + 2\sum_{p=1}^{\infty} Y_p \cos\left(\frac{p\pi n}{N}\right) \ . \tag{1.2.37}$$

The coordinate Y_0 represents the centre of mass

$$s_G(t) = (1/N)\int_0^N s_n \mathrm{d}n = Y_0(t) \ ,$$

while the other coordinates Y_p for $p > 0$ describe the fluctuations along the tube. This leads to the result

$$\left\langle (Y_0(t) - Y_0(0))^2 \right\rangle = \frac{2k_BT}{N\zeta} t \ , \tag{1.2.38}$$

which is the same diffusion constant result as in the Rouse model. The second time correlation function

$$\langle Y_p(t)Y_p(0) \rangle = \frac{Nb^2}{6\pi^2 p^2} \exp\left(-\frac{p^2 t}{\tau_R}\right) \ , \tag{1.2.39}$$

for $p > 0$, is a useful object in the analysis of the correlation of the contour length, $L(t)$. Where τ_R is the Rouse time given by (1.2.14). The contour length of the primitive chain from equation (1.2.37) can be written as

$$L(t) = \widehat{L} - 4\sum_{p \text{ odd}}^{\infty} Y_p(t) \ , \tag{1.2.40}$$

and the time correlation function for $L(t)$ is

$$\langle L(t)L(0) \rangle = \widehat{L} + \frac{8Nb^2}{3\pi^2}\sum_{p \text{ odd}}^{\infty} \frac{1}{p^2} \exp\left(-\frac{p^2 t}{\tau_R}\right) \ . \tag{1.2.41}$$

In particular, when $t = 0$, $\left\langle \Delta L^2 \right\rangle = \left\langle L^2 \right\rangle - \widehat{L} = Nb^2/3$ which corroborates equation (1.2.34). Finally, a typical length scale of the fluctuations compared to the length of the primitive chain, is

$$\frac{\Delta L}{\widehat{L}} = \frac{(Nb^2/3)^{1/2}}{L} = \left(\frac{a}{3L}\right)^{1/2} \approx \left(\frac{1}{Z}\right)^{1/2} , \tag{1.2.42}$$

and hence contour length fluctuations can only be ignored for very large number of entanglement segments, Z.

1.2.2.3 Constraint release

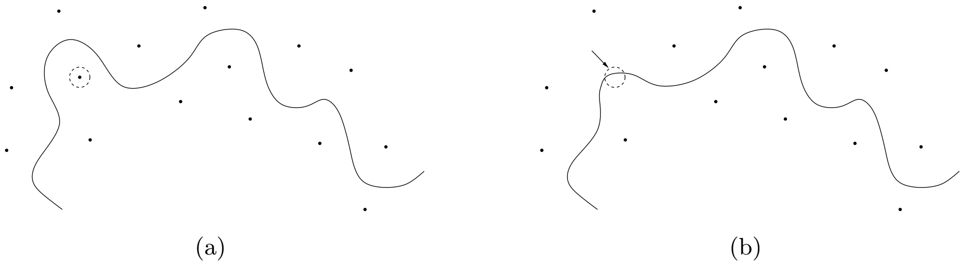
(a) (b)

Figure 1.4: (a) Configuration of a primitive chain before a constraint release event. (b) After the constraint is removed the polymer chain is able to relax into a state with a lower energy cost.

In this section, another relaxation mechanism is discussed, referred to as constraint release. In physical terms this is the process of one chain reptating towards or away from another chain, which adds or removes a constraint from the second chain, and alters the topology of the confining tube, as shown in figure 1.4. The difficultly in this problem arises from the wide distribution of relaxation rates [29], arising because the expected time of a constraint release event is heavily dependent on the distance to the nearest chain end.

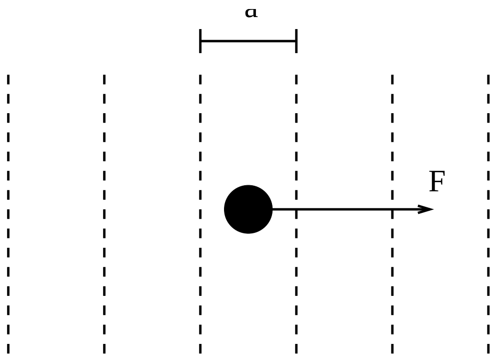

Figure 1.5: Brownian motion of a particle in a one dimensional strip with disappearing and reappearing walls with frequency, ν and separation, a.

If the assumption is made that constraint release events occur at the same rate, which is a huge simplification, these events can be modelled from the

Brownian motion of a particle in a one-dimensional strip with evenly separated walls which disappear and reappear with frequency, ν, see figure 1.5. The probability that a particle moves with or against the force, F, can be found by using Smoluchowski's diffusion equation

$$\frac{\partial \Psi}{\partial t} = \frac{\partial}{\partial x}\frac{1}{\zeta}\left(k_B T \frac{\partial \Psi}{\partial x} + \frac{\partial U}{\partial x}\Psi\right) ,$$

with zero flux and $F = -\partial U/\partial x$ to obtain

$$k_B T \frac{\partial \Psi}{\partial x} - F\Psi = 0 \ , \ \text{ hence } \ \Psi(x) = A \exp{(\alpha x)} \ , \ \ \alpha = \frac{F}{k_B T} \ .$$

For a right hop, $\Psi(x)$ is normalised in the region $[0, 2a]$ with probability of success

$$P_+(a) = \int_a^{2a} \Psi(x) \mathrm{d}x \ .$$

Similarly, for a left hop, but the region is $[-a, a]$ with

$$P_-(a) = \int_{-a}^{0} \Psi(x) \mathrm{d}x \ .$$

These probabilities are used to calculate the average first moment

$$\langle x(t) \rangle = \nu t a \left[P_+(a) - P_-(a)\right] = \nu t a \left[\frac{e^{\alpha a} - 1}{e^{\alpha a} + 1}\right]$$

and the second moment is approximated as $\left\langle x^2(t) \right\rangle = \nu t a^2$, as long as $\alpha a \ll 1$. In comparison with the one-dimensional Langevin equation

$$\frac{\mathrm{d}x}{\mathrm{d}t} = \frac{1}{\zeta_{\text{eff}}} F_{\text{eff}} + g(t) \ \text{ with } \ \left\langle g(t) g(t') \right\rangle = \frac{2 k_B T}{\zeta_{\text{eff}}} \delta(t - t') \ .$$

The effective force F_{eff} is taken directly from the Rouse model (1.2.4) but the variables need to be rescaled from $n \in [0, N]$ with step length b to $s \in [0, Z = Nb/a]$ with step length a, hence $\mathrm{d}s = (b/a)\mathrm{d}n$. Therefore,

$$F_{\text{eff}} = \frac{3 k_B T}{a} \frac{\partial^2 R_x(s)}{\partial s^2} \ \text{ and } \ \zeta_{\text{eff}} = 2 k_B T / \nu a^2 \ ,$$

from matching the second moment. Hence in three space dimensions the full expression is

$$\frac{\partial \mathbf{R}(s,t)}{\partial t} = \frac{3\nu}{2} \frac{\partial^2 \mathbf{R}(s,t)}{\partial s^2} + \mathbf{g}(s,t) \ , \tag{1.2.43}$$

with $\langle \mathbf{g}(s,t) \mathbf{g}(s',t') \rangle = \nu a \mathbf{I} \delta(t - t') \delta(s - s')$ where $\mathbf{g}(s,t)$ describes the random constraint release events, see appendix 2.III of [30] for more details.

In conclusion, this section described elements of the tube model, its concepts, and reviewed its results. Initially the Rouse model was introduced, which represented the evolution of the polymer chain as the Brownian motion of a set of beads connected together by linear springs. The main result from the Rouse model is the longest relaxation time of a chain, the Rouse time, τ_R, given by equation (1.2.14). The tube model restricts polymer chains to a tube-like region, the physical methods to escape these tubes or relaxation mechanisms have been discussed in detail. The process of a chain leaving a tube section is reptation, and the crucial result is the expected lifetime of an original tube, which is the reptation time, τ_d, given by (1.2.27), and is significantly longer than the Rouse time. The realisation that polymer chains are not fixed in length is added to the model through contour length fluctuations. The length scales of these fluctuations relative to the chain length, from equation (1.2.42), in terms of the number of entanglement segments is $Z^{-1/2}$, and therefore is certainly significant for all but the most entangled systems. Constraint release is a rare event, consisting of a chain reptating away from another chain, removing a physical constraint in the second chain's tube network. The main result is the stochastic differential equation (1.2.43) that describes random constraint release events in all cases. However, the model is unsatisfactory, and too simple to be fully effective in general, due to the single constraint release rate.

1.3 The GLaMM model

In this section, the Graham, Likhtman and Milner, McLeish (GLaMM) model of entangled polymers under fast flows is presented [31], which is based upon the tube model, see section 1.2. The model originates from considering Rouse motion within a tube and includes the effects of reptation, constraint release, chain stretch, and even contour length fluctuations are approximated. It models the chain configuration under flow, down to the length scale of the tube diameter and has been extensively tested against experimental data for flow of amorphous polymers. It accurately predicts both stresses [31, 32, 33] and neutron scattering [34, 35, 36] of polymers under strong flow.

The model considers all chains to have the same molecular weight, i.e. a monodisperse distribution. A chain is divided into Z entanglement segments, each containing N_e Kuhn steps or monomers (in this thesis $N_e = 100$ is used throughout). Chain configurations are described by a continuous time-dependent space curve $\mathbf{R}(s;t)$, where $\mathbf{R}$ denotes the monomer spatial position and $s \in (0, Z)$ is the monomer label, normalised by N_e, at time t, as shown in figure 1.6.

The first term included in the model is due to retraction or Rouse motion within a tube, see section 1.2.2.1. Each tube entanglement segment has N_e monomers and is considered to be a linear spring. Hence equation (1.2.4) is modified to give

$$N_e \zeta_0 \frac{\partial \mathbf{R}(s,t)}{\partial t} = \frac{3k_B T}{N_e b^2} \mathbf{R}''(s,t) \ ,$$

with the primes denoting derivatives with respect to s. However, since the motion must remain in the tube, the force must be projected along a tangent,

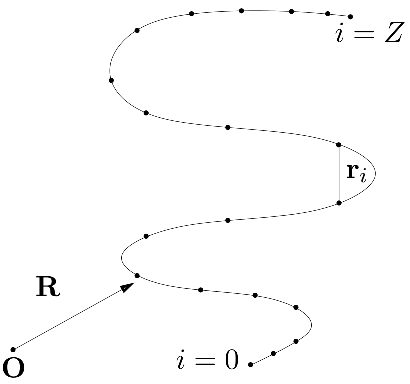

Figure 1.6: Diagram of space curve $\mathbf{R}(s;t)$ which describes the movement of a polymer chain; an entanglement segment is shown by $\mathbf{r}_i$.

unit vector $\mathbf{R}'(s,t)/\left|\mathbf{R}'(s,t)\right|$ to produce

$$\frac{\partial \mathbf{R}(s,t)}{\partial t} = \frac{1}{\pi^2 \tau_e} \frac{(\mathbf{R}''(s,t) \cdot \mathbf{R}'(s,t))}{\left|\mathbf{R}'(s,t)\right|^2} \mathbf{R}'(s,t) \ ,$$

thus

$$\frac{\partial \mathbf{R}(s,t)}{\partial t} = \frac{1}{2\pi^2 \tau_e} \mathbf{R}'(s,t) \left(\frac{\partial}{\partial s} \ln \left[\mathbf{R}'(s,t) \cdot \mathbf{R}'(s,t) \right] \right) \ , \tag{1.3.1}$$

with $\tau_e = \zeta_0 b^2 N_e^2 / 3\pi^2 k_B T$ being the Rouse time of a single entanglement segment.

A key component of this model is the inclusion of chain stretch which affects both reptation and constraint release. Chain stretch refers to the contour length being stretched beyond its equilibrium length by the flow. Basic reptation with the chain length constant is modelled by moving a monomer at position, s, at time, t, to a new position that was occupied by another monomer at position, $s + \Delta\xi$, at time, t, in a time interval Δt. Hence

$$\mathbf{R}(s, t + \Delta t) = \mathbf{R}\left(s + \Delta\xi(t), t\right) \ ,$$

with $\Delta\xi(t)$ describing Brownian motion along the tube. Although if the chain is stretched that term is incorrect since the chain diffuses through real space not monomer space. Thus, the factor $Z/Z^*(t)$ must be introduced, where $Z^*(t)$ is the effective number of entanglements the chain is confined by, compared to Z which is the number of entanglements an unstretched chain has. The new reptation term is

$$\mathbf{R}(s, t + \Delta t) = \mathbf{R}\left(s + \frac{Z}{Z^*(t)} \Delta\xi(t), t\right) \ . \tag{1.3.2}$$

Constraint release is greatly affected by both chain retraction and stretch, the release rate grows with the convection rate, hence the process is known as convective constraint release (CCR). Without stretch included CCR is modelled by Rouse motion of tube segments that jump a tube diameter, a, with frequency, ν. CCR gives the following term in the model, see section 1.2.2.3

$$\frac{\partial \mathbf{R}(s,t)}{\partial t} = \frac{3\nu}{2} \frac{\partial^2 \mathbf{R}(s,t)}{\partial s^2} + \mathbf{g}(s,t) \ ,$$

with $\mathbf{g}(s,t)$ describing the motion of the random constraint release events. If stretch is included, constraint release events will have less effect, this term is reduced proportional to the local stretch ratio $\left|\mathbf{R}'(s,t)\right|/a$. All the terms are collected together into one stochastic differential equation

$$\begin{aligned} \mathbf{R}(s,t+\Delta t) = \mathbf{R}(s,t) &+ \Delta\xi(t)\frac{Z}{Z^*(t)}\mathbf{R}'(s,t) + \frac{\Delta\xi(t)^2}{2}\frac{Z^2}{Z^*(t)^2}\mathbf{R}''(s,t) \\ &+ \Delta t\Bigg[\underline{\underline{\kappa}} \cdot \mathbf{R}(s,t) + \mathbf{g}(s,t) + \frac{3\nu}{2}\frac{a}{\left|\mathbf{R}'(s,t)\right|}\mathbf{R}''(s,t) \\ &+ \frac{1}{2\pi^2\tau_e}\mathbf{R}'(s,t)\left(\frac{\partial}{\partial s}\ln\left[\mathbf{R}'(s,t)\cdot\mathbf{R}'(s,t)\right]\right)\Bigg] \end{aligned} \qquad (1.3.3)$$

with the reptation term expanded up to order $\Delta\xi^2$, the applied deformation produces affine motion, and is described by the velocity gradient tensor $\underline{\underline{\kappa}} = \nabla \mathbf{v}$ and relaxation of the chain is relative to that motion.

Note that $\partial\mathbf{R}(s;t)/\partial s$ is a tangent to the polymer chain at position, s, and leads to the following continuous tube tangent correlation function

$$\mathbf{f}(s,s';t) = \left\langle \frac{\partial \mathbf{R}(s;t)}{\partial s}\frac{\partial \mathbf{R}(s';t)}{\partial s'} \right\rangle \ . \qquad (1.3.4)$$

This quantity is extremely important for calculating average end-to-end vectors of entanglement segments, and also gives the mechanical stress. Moreover, $\mathbf{f}$ is also used in the GO model of polymer nucleation [21, 22], see section 1.6.3, and is also of interest because it can be verified by small angle neutron scattering (SANS). In order to calculate the correlation the following closure approximation is required

$$\begin{aligned} &\left\langle R'_\alpha(s)R_\beta(s')\frac{\partial}{\partial s}\ln\left[\mathbf{R}'(s)\cdot\mathbf{R}'(s)\right]\right\rangle \\ &\approx \mathcal{R}_s\left\langle R'_\alpha(s)R_\beta(s')\right\rangle\frac{\partial}{\partial s}\ln\left[\left\langle\mathbf{R}'(s)\cdot\mathbf{R}'(s)\right\rangle\right] \ , \end{aligned}$$

with $\mathcal{R}_s$ initially approximated as unity. However, using $\mathcal{R}_s = 1$ produces significant differences when the output is compared to experimental data, see figure 10 in [31]. To correct this error, $\mathcal{R}_s$ is fitted against one set of data and that value is tested against the other sets, shown by figure 11 in [31] with $\mathcal{R}_s = 2.0$. Accepting the universal value of $\mathcal{R}_s$ in the model compares well to experimental data especially in calculating the overshoot in shear. The model; however, has a few weaknesses, for example neglecting finite extensibility of polymer chains, as allowing chains to be potentially infinite in length is clearly unphysical. The GLaMM model approximates industrial polymer melts by studying bimodal blends of short and long chained molecules, it is unable to include a truly polydisperse distribution of chain lengths. Another weakness is the single constraint release rate, briefly discussed in section 1.2.2.3.

1.4 Classical nucleation theory

Nucleation is the process which initiates most phase transitions. In this thesis our interest is solely in the case of liquid to solid transitions. The process of changing a liquid into a solid begins with the formation of small clusters of atoms called crystals or nuclei. At temperatures just below the melting point of a substance, the energy per particle in a solid state is lower than in a liquid one. However, the solid-liquid interface contains an energy cost. The free energy of a nucleus is a balance between the energy gained by the bulk volume and the cost due to the interface. For small nuclei, with a high surface area to volume ratio, increasing their size is energetically unfavourable. However, if enough unlikely events occur in sequence, a stable crystal is eventually formed, so that adding atoms to it becomes favourable and spontaneous growth occurs. Nucleation can be a slow process, especially if the height of the energy barrier is large.

In section 1.4.1, a simple one-dimensional system is introduced, based on a continuous energy landscape. In section 1.4.2, the kinetic prefactor to nucleation is discussed, and a simulation technique to determine its value directly is described.

1.4.1 One-dimensional nucleation over a simple energy landscape

In classical nucleation theory, the free energy of a solid nucleus is a balance between the reduction due to the bulk volume and the surface area cost. By assuming nuclei grow spherically, one of the parameters to describe the evolving nucleus in one-dimension is the volume or in dimensionless terms the number of particles, i, and the free energy landscape is of the form

$$\frac{\Delta F_i}{k_B T} = A i^{2/3} - B i \ . \tag{1.4.1}$$

The classical nucleation paper by Turnbull and Fisher [15] sets out to find the steady state rate of nucleation, N_R, over an energy barrier. Figure 1.7 shows the free energy between two states i and $i+1$, it is assumed that the intermediate configurations in between the two local minima correspond to free energies greater than that of either ΔF_i or ΔF_{i+1}, this is known as an activation complex, Δf^*. If n_i represents the steady state concentration of nuclei of size i in the whole system then the forward rate from state i to state

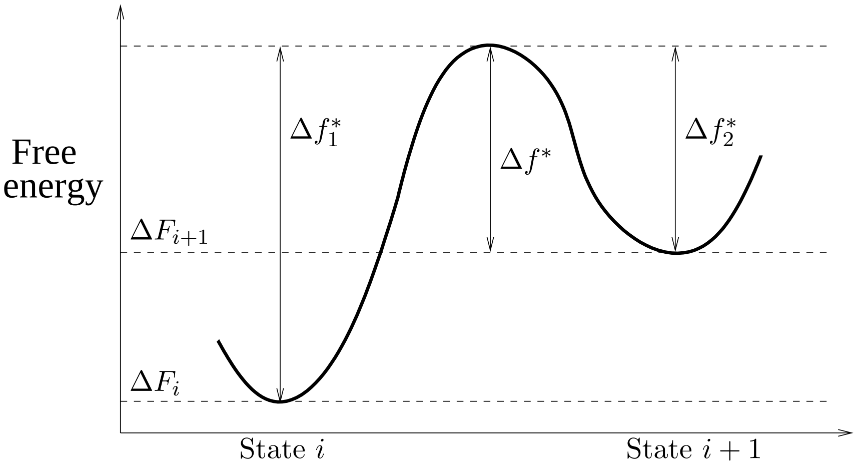

Figure 1.7: Free energy landscape with activation complex in between state i and state $i+1$.

$i+1$ is given by

$$r_i^+ = n_i a_i^+ i^{2/3} \left(\frac{1}{\tau}\right) \exp\left[(-\Delta f_1^*)/k_B T\right] \ , \tag{1.4.2}$$

where $a_i^+ i^{2/3}$ is the number of particles externally adjacent to the surface of a nucleus of size i and τ is a typical timescale for describing the movement of a single particle, and $(\exp\left[(-\Delta f_1^*)/k_B T\right]/\tau)$ is the reaction rate for ascending over a barrier of height Δf_1^*. The rate of the reverse reaction is

$$r_{i+1}^- = n_{i+1} a_{i+1}^- i^{2/3} \left(\frac{1}{\tau}\right) \exp\left[(-\Delta f_2^*)/k_B T\right] \ , \tag{1.4.3}$$

where $a_{i+1}^- i^{2/3}$ is the number of particles on the surface of a nucleus of size $i+1$, and $(\exp\left[(-\Delta f_2^*)/k_B T\right]/\tau)$ is the reaction rate for ascending over a barrier of height Δf_2^*. The whole system is assumed to be in steady state, hence the net rate of reaction N_R must be the same as the net flux between state i to state $i+1$ for any i

$$N_R = r_i^+ - r_i^- \ . \tag{1.4.4}$$

The authors make several continuum approximations which are valid for large nuclei. The difference between available particle numbers for opposite forward and reverse reactions is considered to be negligible and the raw values have a consistent prefactor, hence $a_i^+ \approx a_{i+1}^- \approx a$. The quantities n_i and ΔF_i, are assumed to be smooth functions of i, so incremental changes can be approximated by their differentials $(\mathrm{d}\Delta n_i/\mathrm{d}i)\Delta i = \mathrm{d}\Delta n_i/\mathrm{d}i$ and $\mathrm{d}(\Delta F_i)/\mathrm{d}i$, hence

$$\Delta f_1 * \approx \frac{\mathrm{d}(\Delta F_i)}{\mathrm{d}i} + \Delta f^* \ \text{ and } \ \Delta f_2 * = \Delta f^* \ .$$

Also the values $(1/n_i)\mathrm{d}n_i/\mathrm{d}i$ and $(1/k_B T)\mathrm{d}(\Delta F_i)/\mathrm{d}i$ are presumed to be much less than unity, the former is justified by the expectation that concentration of nuclei of similar sizes will be also similar, especially for large i. The latter implies $B \ll 1$ in equation (1.4.1) which corresponds to the requirement for large critical nuclei. All of these assumptions lead to an expression for the overall nucleation rate

$$N_R = \left(\frac{-a}{\tau}\right) \exp\left[\frac{-\Delta f^*}{k_B T}\right] \left[n_i \left(\frac{2}{3} A i^{-1/3} - B\right) + \frac{\mathrm{d}n_i}{\mathrm{d}i}\right] i^{2/3} \ . \tag{1.4.5}$$

Defining $C_r = (N_R \tau / a) \exp[\Delta f^* / k_B T]$ simplifies the differential equation and it has the following solution

$$n_i = \exp[(-\Delta F_i)/k_B T] \left[- C_r \int_{i_0}^{i} \exp[\Delta F_{i'}/k_B T] i'^{-2/3} \mathrm{d}i' + N \right] \ , \tag{1.4.6}$$

where N is the total number of un-nucleated particles. In the limit $i \to \infty$, n_i must tend to zero, which infers

$$C_r = \frac{N}{\int\limits_{i_0}^{\infty} \exp[\Delta F_i / k_B T] i^{-2/3} \mathrm{d}i} \ . \tag{1.4.7}$$

The authors expand around the global maximum of the nucleation landscape, this is the critical nucleus size, n^*, and its associated free energy, ΔF_{n^*}. The integral becomes a Gaussian, and the nucleation rate is found to be

$$N_R = \Gamma \exp[-(\Delta F_{n^*} + \Delta f^*)/k_B T] \ . \tag{1.4.8}$$

This maximum height ΔF_{n^*} of the nucleation landscape dominates the nucleation rate, and $\Gamma = (1/\tau)\, S(n^*)(A/9\pi)^{1/2} N$, where $S(n^*)$ is the number of particles at the surface of the critical nucleus. This vital prefactor is discussed in section 1.4.2. For more complicated energy landscapes the integral may have to be evaluated numerically instead of using a similar analytic technique.

1.4.2 Kinetic prefactor

Classical nucleation theory states that the nucleation rate is dominated by the Boltzmann factor of the height of the barrier, see equation (1.4.8). However, the evaluation of the kinetic prefactor, Γ, requires further investigation. Auer and Frenkel reviewed numerical simulations of nucleation in colloids [37]. This paper contains a section looking at this kinetic prefactor and also presents a method of simulation to find its value. Beginning with a similar expression to (1.4.1), the Gibbs free energy landscape uses the radius, R, of the growing spherical nuclei as its reaction coordinate, and is again a balance between the bulk gain and the cost due to the solid/liquid interface

$$\Delta G(R) = \frac{4\pi}{3} R^3 \rho_s \Delta\mu + 4\pi R^2 \gamma \ , \tag{1.4.9}$$

where ρ_s is the number density of the solid bulk, $\Delta\mu$ is the difference in potential energy between solid and liquid states per unit mass, and γ is the free energy cost due to the solid/liquid interface per unit of surface area. The maximum of the free energy landscape at

$$R^* = \frac{2\gamma}{\rho_s \left|\Delta\mu\right|} \ ,$$

is the radius of the critical nucleus, n^*, and the height of the nucleation barrier is given by

$$\Delta G^* = \frac{16\pi}{3} \frac{\gamma^3}{\left(\rho_s \left|\Delta\mu\right|\right)^2} \ . \qquad (1.4.10)$$

Classical nucleation theory states that the nucleation rate is

$$N_R \approx \Gamma \exp\left(-\frac{\Delta G^*}{k_B T}\right) \ , \qquad (1.4.11)$$

where the prefactor $\Gamma = Z_f \rho_l k^+_{n^*}$. Here $Z_f = \sqrt{\left(\left|\Delta\mu\right| / 6\pi k_B T n^*\right)}$ is the Zeldovich factor, ρ_l is the number density of the liquid state, and $k^+_{n^*}$ is the rate at which atoms attach to the critical nucleus [38]. The Zeldovich factor is due to re-crossing events, since some critical nuclei do not result in successful nucleation, a fraction will return to the base of the energy landscape. However, it is the rate $k^+_{n^*}$ that is difficult to quantify. One suggestion is that the attachment rate is related to the number of atoms available at the surface, which is proportional to $n^{*2/3}$. Together with a typical transition rate for new atoms to join the nucleus, which is proportional to D_s/λ^2, where D_s is a self diffusion constant and λ is a typical distance over which the atoms must travel.

A commonly used expression for analysing nucleation experiments is

$$k^+_{n^*} = \frac{24 D_s n^{*2/3}}{\lambda^2} \ , \qquad (1.4.12)$$

the problem is that λ is difficult to measure accurately. A simulation technique is described in [37], that computes the attachment rate directly through an investigation of the diffusion of critical nuclei. The effective diffusion constant for change in nucleus size at the critical nuclei is

$$D^{\text{att}}_{n^*} = \frac{1}{2} \frac{\left\langle \Delta n^{*2}(t) \right\rangle}{t} \ ,$$

where $\Delta n^{*2}(t) = \left[n^*(t) - n^*(0)\right]^2$ is the mean square change in the size of a nucleus that begins as a critical nuclei at time $t = 0$. The simulation is run multiple times on short timescales, the initial slope of $\left\langle \Delta n^{*2}(t) \right\rangle$ is connected to the attachment and detachment rates $k^+_{n^*}$ and $k^-_{n^*}$ by

$$\frac{\left\langle \Delta n^{*2}(t) \right\rangle}{t} = \frac{k^+_{n^*} + k^-_{n^*}}{2} \ .$$

Moreover, since at the top of the barrier, the forward and backward rates are similar ($k^+_{n^*} \approx k^-_{n^*}$), the attachment rate is found through the equation

$$k^+_{n^*} = \frac{\left\langle \Delta n^{*2}(t) \right\rangle}{t} \ . \qquad (1.4.13)$$

This method is applied to molecular dynamics simulations to obtain the important kinetic prefactor, to approximate nucleation rates with the expression (1.4.11).

1.5 Continuous energy barrier crossing

This thesis is predominantly concerned with developing discrete energy barrier crossing models. However, to compliment these, continuous barrier crossing systems are also investigated. In this section, a diffusive barrier crossing calculation of a continuous one-dimensional system is reviewed. At first a general calculation of particles escaping from a potential well is presented in section 1.5.1. The original application of this calculation was to determine the relaxation of star arms in branched polymers, and is detailed in section 1.5.2.

1.5.1 General energy well calculation

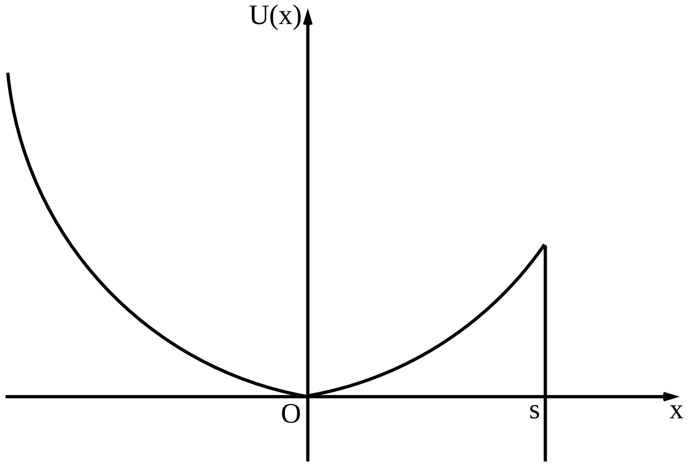

Figure 1.8: Illustration of the potential energy well, $U(x)$, in which a particle diffuses, exiting the system only at $x = s$, which is represented by $U(s) = -\infty$.

In this section, a problem of a particle escaping a one-dimensional potential well is reviewed, from McLeish's chapter in [39]. A particle is placed in a potential well, $U(x)$, see figure 1.8, with a single minimum at the origin and is said to have escaped the well if it reaches some point s, where $s > 0$. The most important piece of information to find is the average escape time of diffusing particles. To solve the problem, particles are not allowed to drop back below s once they have passed it, which is equivalent to imposing a potential that drops sharply to $-\infty$ at $x = s$. A steady current of particles $j\delta(x)$ is introduced at the origin and the steady-state number density of particles is defined as $n(x)$, the average survival time, $\tau(s)$, is given by

$$\tau(s) = \frac{1}{j} \int_{-\infty}^{s} n(x) \mathrm{d}x \ . \tag{1.5.1}$$

The diffusivity, D, is assumed to be constant and all energies are expressed in units of k_BT, then with time included the number density of particles $n(x,t)$ must satisfy equation (51) in chapter 3 of Doi and Edwards [2], namely

$$\frac{\partial n}{\partial t} = -\frac{\partial}{\partial x} D\bigg(-\frac{\partial n}{\partial x} - n\frac{\partial U}{\partial x}\bigg) + j\delta(x) \ , \tag{1.5.2}$$

which originates from Fick's law with an additional force from the potential $U(x)$, and the continuity equation.

At steady-state $\partial n/\partial t = 0$, in the region $x > 0$, equation (1.5.2) is integrated directly with the conditions

$$\frac{\partial n}{\partial x}\bigg|_{x=-\infty} = n(x)|_{x=-\infty} = 0 \ \text{ to obtain } \ \frac{\partial n}{\partial x} + n\frac{\partial U}{\partial x} = -\frac{j}{D} \ .$$

An integrating factor $\exp\left(U(x)\right)$ is used with the boundary condition $n(s) = 0$ to acquire

$$n(x) = \frac{j}{D}\exp\left(-U(x)\right)\int_x^s \exp\big(U(x')\big)\mathrm{d}x' \ , \ \ (x > 0) \ . \tag{1.5.3}$$

For $x < 0$ there is no net current so the steady-state density must be the equilibrium (Boltzmann) distribution with a prefactor to match the solution for $x > 0$ in equation (1.5.3), hence

$$n(x) = \frac{j}{D}\exp\left(-U(x)\right)\int_0^s \exp\big(U(x')\big)\mathrm{d}x' \ , \ \ (x < 0) \ . \tag{1.5.4}$$

The average survival time is found by substituting this density $n(x)$ into equation (1.5.1), and the order of integration is reversed, to attain

$$\tau(s) = \frac{1}{D}\int_0^s \exp\big(U(x')\big)\int_{-\infty}^{x'} \exp\left(-U(x)\right)\mathrm{d}x\mathrm{d}x' \ . \tag{1.5.5}$$

This is a general result for an arbitrary $U(x)$.

Now we formulate an approximation by expanding the integrals around regions of their dominant contributions. For the inner integral, an expansion around $x = 0$ is required, where $U(0) = 0$ and $U'(0) = 0$, and the region $-\infty$ to x' is approximated by the whole x axis to obtain a complete Gaussian integral, thus

$$\tau(s) \approx \frac{1}{D}\int_0^s \exp\big(U(x')\big)\sqrt{\frac{2\pi}{U''(0)}}\mathrm{d}x' \ .$$

For the outer integral, the integrand is expanded around the dominant point $x' = s$ and, with the assumption $sU'(s) \gg 0$, this gives the average first passage time, with the Boltzmann factors k_BT restored, as

$$\tau(s) \approx \frac{k_BT}{DU'(s)}\sqrt{\frac{2\pi k_BT}{U''(0)}}\exp\left[\frac{U(s)}{k_BT}\right] \ . \tag{1.5.6}$$

This expression is dominated by the Boltzmann factor of the height of the barrier at position s, but also includes information about the slope at s and the curvature of the minimum at the origin.

1.5.2 Application to star polymers

In this section, the energy well escape calculation of section 1.5.1 is applied to the problem of relaxing star arms in the tube model. In entangled star polymers, a branch is contained by a tube due to the fixed network of surrounding chains. The branch can only escape the tube through path length fluctuations, in which the free end must travel all the way back to the branch point, and is free to leave along a new tube [40, 41, 42]. To travel back to the branch point the chain must work against the energy potential. McLeish models the potential as

$$U(z) = \frac{3k_BT}{2Nb^2}z^2 - \frac{3k_BT}{a}z \ , \tag{1.5.7}$$

which includes a quadratic entropic spring force and a linear end-tension term, with tube diameter, a, bond length, b, and N being the number of monomers in the branch [39]. Therefore $L = Nb^2/a$ is the equilibrium length, because $z = L$ is the minimum of the potential (1.5.7). The potential is translated so that the minimum is at the origin, to apply the energy well calculation. Since the end of the star arm is required to travel the whole length, the escape point is set to $s = L$. All of the relevant derivatives of the translated potential are substituted into equation (1.5.6) to find that the average survival time in the potential well is

$$\tau(L) = \frac{a}{3D}\sqrt{\frac{2\pi Nb^2}{3}}\exp\left[\frac{3Nb^2}{2a^2}\right] \ . \tag{1.5.8}$$

The number of monomers N refers to the arm, so it is relabelled N_a, the number of monomers between entanglements on the main chain is defined as N_e. The tube diameter is considered to obey the relation $a^2 = (4/5)N_eb^2$, and the diffusion constant is $D = (2k_BT/N_a\zeta_0)$ with ζ_0 being the drag per monomer, see section 1.2.1. The Rouse time of an entanglement segment is $\tau_e = (\zeta_0 N_e^2 b^2/3\pi^2 k_BT)$ and equation (1.5.8) gives

$$\tau(L) = \tau_e\left(\frac{N_a}{N_e}\right)^{3/2}\sqrt{\frac{2\pi^5}{15}}\exp\left[\frac{15N_a}{8N_e}\right] \ , \tag{1.5.9}$$

which is the time star arms are expected to spend confined to a tube.

Unfortunately this theory fails when compared to experimental data of star arms [39, 43, 44]. The problems arise in the requirement to include constraint release, which for star polymers is important. Constraint release controls the dynamics of the entanglement segments. Due to the exponential separation of relaxation timescales along a star arm, tube segments near the end relax quickly whereas segments close to the branch point relax very slowly and effectively do not entangle with the faster relaxing segments. This dilution argument widens the tube near branch points due to the reduction in entanglements. The solution is to introduce an effective number of monomers between entanglement points $N_e(x) = N_{e0}/(1-x)$ to replace the old N_e with $x = s/L$ being the fraction of arm length retracted. The differential equation

$$\frac{\partial U}{\partial x}(x, N_e(x)) = \frac{\mathrm{d}U_{\text{eff}}}{\mathrm{d}x}(x) \ , \tag{1.5.10}$$

is employed, and the effective energy potential $U_{\text{eff}}(x)$ is calculated to be

$$U_{\text{eff}}(x) = \frac{15}{8}\frac{N}{N_e}\left(x^2 - \frac{2}{3}x^3\right) \ , \tag{1.5.11}$$

to which the diffusive barrier crossing method of section 1.5.1 can be applied.

To conclude this section, a general method for calculating average escape times from a continuous one-dimensional energy well has been reviewed, resulting in equation (1.5.6). Also this calculation was applied to the relaxation of star arms obtaining (1.5.9), and has the capability to be adapted to many other barrier crossing problems including nucleation. Provided the energy well is deep, particles will tend to revisit the origin (or minimum) on many occasions before successfully escaping. Hence this process is similar to a first-order process, and the distribution of escape times can be accurately described by a exponential distribution based on the average escape time. However, if the energy well has a gentler slope, then the process is more diffusional, which produces more complex distributions.

1.6 Simulation techniques

In this section, the simulation techniques used within this thesis are explained, beginning with the fundamental property of detailed balance in section 1.6.1. All of the simulation techniques are based on the kinetic Monte Carlo algorithm summarised by Voter [45], the basics of which are introduced in section 1.6.2. The Graham and Olmsted polymer simulation of flow-induced crystallisation is thoroughly detailed in section 1.6.3, which contains a simple outline of the simulation for quiescent melts, and also additional features of chains being subjected to flow via the GLaMM model as well as nucleus rotation. In section 1.6.3.4, fast, efficient methods by Jolley are presented [46], to aid the simulation of extremely high barriers.

1.6.1 Detailed balance

To obey detailed balance a system must have the following property at equilibrium; for every pair of connected states i and j the number moves per unit time on average from i to j must be equal to the moves from j to i. When states i and j are in a Boltzmann distribution, at equilibrium the fraction of time spent in state i, the occupancy, χ_i, is proportional to $\exp\left(-F(i)/k_BT\right)$ with $F(i)/k_BT$ being the free energy of state i relative to some base level. The rate of moves from state i to state j, per unit time, is denoted as k_{ij}, and similarly for k_{ji}. In equilibrium detailed balance gives

$$\chi_i k_{ij} = \chi_j k_{ji} \ , \ \text{ therefore } \frac{k_{ij}}{k_{ji}} = \exp\Big(-\big(F(j) - F(i)\big)/k_B T\Big) \ . \tag{1.6.1}$$

Away from equilibrium, the reaction rates remain constant but the occupancies may not.

1.6.2 Kinetic Monte Carlo algorithm

The kinetic Monte Carlo algorithm relies on an important property that the system must obey. This property is that the transition probabilities between different states are independent of the history of the system, which is the key feature of a Markov chain. These probabilities are fixed in time, therefore during a period of time, the probability of escape is the same as it had been in the previous period or will be in the next period. This is a first-order process with exponential decay statistics, the probability that the system remains in state i is given by

$$p_{\mathrm{survival}}(t) = \exp\left(-k_{\mathrm{tot}} t\right) \ , \ \text{ where } k_{\mathrm{tot}} = \sum_j k_{ij} \ , \tag{1.6.2}$$

and k_{tot} is the total escape rate to all adjacent states, j. Here, since events are independent, the sum of Poisson processes is also a Poisson process, and the overall rate is a sum of all the contributing rates. The probability distribution $p(t)$ for the time of first escape of a particle from a particular state, is a critical component of the algorithm. The integral of $p(t)$ from $t = 0$ to a dummy time $t = t'$, gives the probability that the particle has escaped by time t' which is equal to $1 - p_{\mathrm{survival}}(t')$. The derivative of $p_{\mathrm{survival}}(t)$ gives the required probability distribution

$$p(t) = k_{\mathrm{tot}} \exp\left(-k_{\mathrm{tot}} t\right) \ , \tag{1.6.3}$$

and from this the average escape time can be obtained

$$\tau = \int_0^\infty t p(t) \mathrm{d}t = \frac{1}{k_{\mathrm{tot}}} \ . \tag{1.6.4}$$

The procedure taken by the algorithm to move between states is as follows. First, the path to take is randomly selected, with probabilities proportional to the rate constant for each path. It then decides the time taken to escape the current state, which is independent of the selected path and depends only on the total escape rate k_{tot} using the distribution (1.6.3). It is clear the algorithm needs to be able to manufacture exponentially distributed random numbers. To do this, assuming that the ability to draw a random number r uniformly on the interval $(0, 1)$ is known, then the time taken by the move out of state i is selected to be

$$t_{\mathrm{draw}} = -(1/k_{\mathrm{tot}}) \ln\left(r\right) \ . \tag{1.6.5}$$

The algorithm continues to the next state while recording the amount of time spent in previous state.

In this work we take advantage of two types of simulation to investigate nucleation: single barrier crossing and energy landscape sampling. In single barrier crossing, a particle begins at the base of the energy barrier and freely diffuses around the energy landscape until it reaches some fixed size, usually significantly larger than the critical nucleus, and the total time taken is recorded. After many such trials, a distribution of first passage times is produced. For energy landscape sampling, the nucleus is not allowed to grow beyond a certain size, N, hence the nucleus moves from state to state between 1 and N. Once the simulation has run for a significant period of time, an energy landscape can be obtained from the equilibrium occupancies, χ_i, of each state, which is the fraction of total simulation time that is spent in state i.

In summary, the kinetic Monte Carlo algorithm has become a popular simulation technique in many areas of physics and chemistry [47, 48]. The algorithm is a much faster method than standard molecular dynamical simulations which resolves interactions between every atom or molecule using the most basic physical laws. It is also very practical, as it is simple to apply and requires little operational memory. However, in kinetic Monte Carlo, the rates between all adjacent states in a given system must be known, which is not always practical.

1.6.3 Graham-Olmsted simulation of flow-induced crystallisation

This section describes in detail how the kinetic Monte Carlo algorithm is applied to polymer nucleation by Graham and Olmsted, see [21, 22]. Stochastic simulation of nucleation is difficult because it is intrinsically a rare event, to ease this, the Graham and Olmsted (GO) simulation uses a variable step method. This method suits nucleation, particularly with high barriers, since large timesteps are taken when nuclei are small, but for the rare occasions when nuclei are larger, a more refined time resolution is employed. Nevertheless these simulations are still expensive when the free energy barrier to nucleation is especially high.

Here, an outline of the simulation algorithm is presented. Each nucleus is described as a list of N_S stems each containing a number of monomers, with the total number of monomers being N_T. Nuclei are composed of monomers represented by Kuhn steps of size $b_l \times b_w \times b_w$. The model is highly coarse-grained to practically enable large simulations, the internal structure of each nuclei is not resolved, it is assumed that N_T and N_S describe a spheroid independent of the arrangement of monomers on the stems. The spheroid's cross sectional area is related to N_S

$$\text{Area} = \pi W^2 = b_w^2 N_S \ , \tag{1.6.6}$$

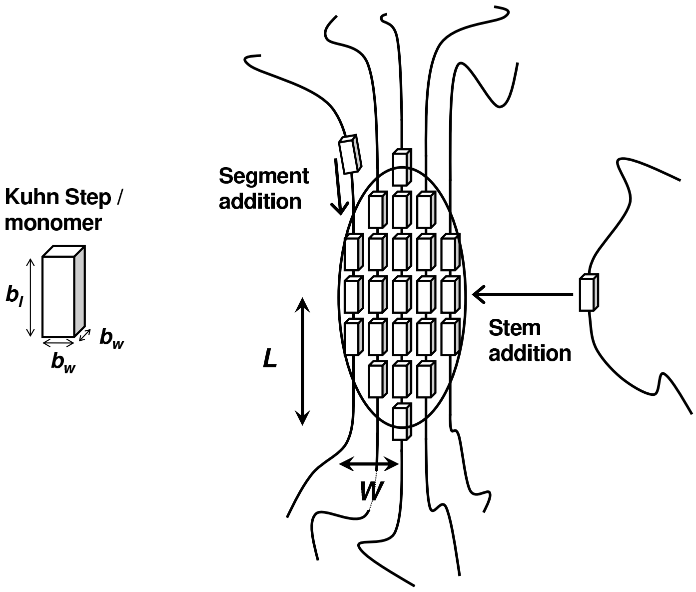

Figure 1.9: Highly coarse-grained description of nucleus within the GO model, comprising of monomers represented by Kuhn steps. Also showing two different moves, stem addition and stem lengthening or segment addition.

and the volume is connected to N_T

$$\text{Volume} = \frac{4\pi}{3} L W^2 = b_w^2 b_l N_T, \tag{1.6.7}$$

see figure 1.9. The free energy of each individual crystal, $\mathcal{F}^*(N_T, N_S)$, with N_T total monomers on N_S stems, is a balance between the bulk energy reduction and the surface area cost, defined by

$$\mathcal{F}^*(N_T, N_S) = -E_0^* N_T + \mu_\mathrm{S}^* S(N_T, N_S) \ , \tag{1.6.8}$$

where E_0^* is the dimensional bulk energy reduction of adding one monomer, μ_S^* is the dimensional surface energy cost per unit area, and S is the surface area of the spheroid. The parameters are non-dimensionalised by $\mathcal{F} = \mathcal{F}^*/k_BT$, $E_0 = b_l b_w^2 E_0^*/k_BT$, $\mu_\mathrm{S} = b_w^2 \mu_\mathrm{S}^*/k_BT$ and $S = b_w^2 \widetilde{S}$. For a prolate spheroid we have

$$\widetilde{S}(N_T, N_S) = 2N_S + 2a_r \frac{N_T}{\epsilon_p \sqrt{N_S}} \arcsin \epsilon_p \ , \quad \epsilon_p = \sqrt{1 - \frac{N_S^3}{a_r^2 N_T^2}}. \tag{1.6.9a}$$

For an oblate spheroid we have

$$\widetilde{S}(N_T, N_S) = 2N_S + a_r^2 \frac{N_T^2}{\epsilon_o N_S^2} \ln\left(\frac{1+\epsilon_o}{1-\epsilon_o}\right) \ , \ \epsilon_o = \sqrt{1 - \frac{a_r^2 N_T^2}{N_S^3}}, \tag{1.6.9b}$$

where $a_r = 3\sqrt{\pi} b_l / 4 b_w$ is a dimensionless prefactor. From hereon in this thesis, all free energies will be expressed in units of k_BT and $b_l = b_w$ is taken throughout.

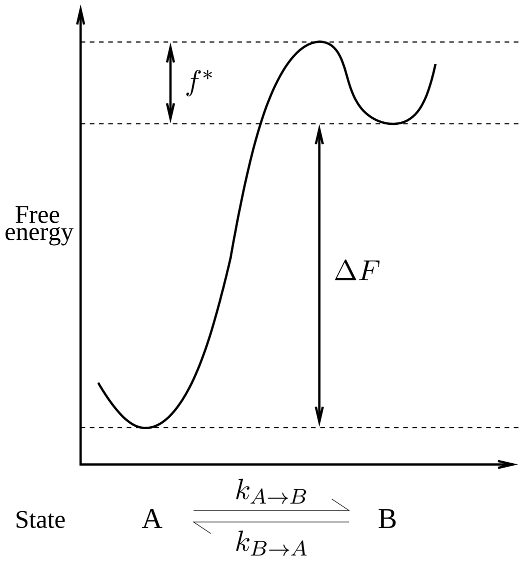

Figure 1.10: Rates of simple system from state A to state B, ΔF is the difference in free energy and f^* is the minimum height for all moves.

The GO simulation makes changes to the solid nucleus by following the kinetic algorithm of Gillespie [49]. Move rates are dependent on the free energy difference between each state. Energetically unfavourable moves are dependent on the free energy increase of the system. However, the model assumes that all energetically favourable moves occur at the same universal base rate $1/\tau_0$. Figure 1.10 shows the move rates between two states A and B, with A being favourable, these rates are defined by

$$k_{A\to B} = \frac{1}{\tau_0}\exp\left(-\Delta F\right) \ , \tag{1.6.10a}$$

$$k_{B\to A} = \frac{1}{\tau_0} \ . \tag{1.6.10b}$$

Where τ_0 is the timescale of the fastest move in the system, and is related to f^* the minimum barrier height between two adjacent states.

The solid nucleus evolves through the addition or removal of single monomers, no amalgamation or fragmentation of several monomer clusters occurs. The simulation has two basic moves, see figure 1.9, these are stem addition and stem lengthening, both of which are reversible in accordance with detailed balance. Stem addition involves binding one monomer from a completely new stem to the side of the crystal and its rate is also scaled with the amount of available surface area. Which is modelled as a thin band around the nuclei's equator, denoted as $f_{\mathrm{add}}(N_S)$ which is a function of the total number of stems, N_S,

$$f_{\mathrm{add}}(N_S) = 2\sqrt{\pi}\sqrt{N_S} \ .$$

Stem lengthening moves involve adding a monomer to the nucleus from a chain that is already included within the nucleus. Furthermore the new monomer must be the next monomer along the chain, from either the top or the bottom of the nucleus. Chains are modelled as containing a huge, but still finite number of monomers, on the extremely rare occasion the end monomer is selected to be in a nucleus, then no stem lengthening moves can occur in that direction.

The algorithm has thus far only been described for quiescent nucleation. In other words, a polymer melt that is not subjected to flow, so all monomers are assumed to have the same attachment value, E_0. However, the GO model is capable of incorporating an assortment of monomers with different attachment values. The GLaMM model of polymer flow (section 1.3), outputs an average end-to-end vector for each entanglement segment. In section 1.6.3.1, a statistical mechanical derivation of the elastic free energy, ΔF^{el}, for monomer attachment is presented. It is assumed chain dynamics under flow is not affected by the nucleus. The GLaMM model shows that entanglement segments in the middle of polymer chains are significantly more affected by flow, than those close to the chain's end points. Under flow, each entanglement segment has a different elastic free energy, ΔF_i^{el}. This also greatly influences the free energy of attachment, hence monomers from different entanglement segments (N_e monomers in each) produce different attachment values, given by

$$E_i = E_0 + \frac{1}{N_e} \Delta F_i^{\mathrm{el}} \; . \tag{1.6.11}$$

The different competing monomer types are referred to as different species. This assortment of species competing to attach, affects the stem addition moves. A concentration scaling, ϕ_i, is now required as a prefactor to the stem addition rate, reflecting the proportion of each species within the melt. Hence rare species have slow stem addition rates. Stem lengthening involves adding a monomer to the nucleus from one of the stems already connected to the crystal, and is still considered to be at 100% concentration. This makes physical sense as, when a monomer is added to an existing stem it simply 'zips-up' the chain. The next monomer will usually be within the same entanglement segment, although occasionally it will be the next species along the chain or the chain end. However, such events are rare because the number of monomers in each chain segment, $N_e = 100$, is large.

The tube model predicts that the relaxation times of chains significantly increase at length scales greater than the tube diameter. Thus the smallest length scale required in the GLaMM model is the tube diameter or primitive path segment. All length scales below this are considered to be in equilibrium (with respect to the constraint imposed by deformation on longer length scales). However, nucleation occurs on the Kuhn step or monomer level. Nevertheless the monomer statistics can be calculated from the GLaMM model by assuming that monomers are in equilibrium with respect to the slow Rouse time of an entanglement segment, τ_e, and from hereon all deformation rates will be expressed in terms of τ_e. The attachment base timescale τ_0 is of the order of the monomer diffusion time, thus $\tau_0 \ll \tau_e < 1/\dot{\gamma}$, where $\dot{\gamma}$ is the flow rate.

The GO simulation has the additional feature of including the rotation of the nucleus, through the processes of random rotational diffusion and convection with the flow, see [21] for details, and the effects on nucleation times are throughly investigated in chapter 5. The model allows only monomers closely aligned to the nucleus to attach. In section 1.6.3.2, a statistical mechanics derivation of the entropic cost of nucleus orientation to monomer attachment is explained. This results in an extra concentration term, Θ_i, for all addition moves for each species i. In section 1.6.3.3, the processes in which the nucleus is able to rotate relative to the flow direction in the GO model are described.

The computer algorithm has an underlying set of dynamical master equations defined by the rules that determine all possible transitions out of a given nuclear microstate, and their rates. The correct equilibrium behaviour of this set of master equations is ensured by detailed balance. However, this set of equations is cumbersome to write down as one ordinary differential equation is required for each possible nucleus state. The number of nucleus states grows rapidly with size. Furthermore, many of these states make a negligible contribution to the rate of nucleation because they are visited extremely infrequently. This illustrates the great strength of the kinetic Monte Carlo method as move rates are calculated ‘on the fly’ and the simulation preferentially samples the most important paths to nucleation.

1.6.3.1 Elastic free energy derivation for monomer attachment

In this section the elastic free energy of polymer chains is derived, which is the key link between the flow modelling of the GLaMM model, in section 1.3, and the GO simulation of FIC within polymer melts. Deformation induced by flow modifies the free energy of a segment which affects nucleation. This is because polymer chains are deformed and stretched under flow, which reduces the entropic penalty for the attachment of a monomer onto a crystal. A free energy is used to derive the dynamics of the model, based on the statistics of random walks. Gradients in this free energy also drive chain retraction and influence constraint release. Based on the same statistics, the elastic free energy change on stretching, ΔF_i^{el}, is derived for each entanglement segment subject to a constraint on its average bond vector. To begin the derivation, the partition function, Z_p, is introduced, which is the sum over all energy states in a system and includes the number of conformations, $w(i)$, of each state, i,

$$Z_p = \int w(i) \exp\left(-E(i)\right) \mathrm{d}i \ .$$

Polymer chains take independently selected random walks, and hence the energy of each state is the same. Thus the only contribution to the partition function is from the number of permutations of each state. For that reason, the number of conformations of a particular set of chains is equal to the reciprocal of the probability that one of the set is chosen at random. For example, the partition function for sets with the same end-to-end vector is

$$Z_p(\mathbf{r}) = \int P_0(\mathbf{r})\delta\left(\mathbf{r} - \sum_{\{i\}} \mathbf{R}_i\right) \mathrm{d}\left\{\mathbf{R}_i\right\} \ .$$

The derivation aims is to express the partition function in terms of the GLaMM model output which is the averaged tube tangent correlation function of the ensemble

$$\mathbf{f}_{ij}(t) = \left\langle \left.\frac{\partial \mathbf{R}(s;t)}{\partial s}\right|_{s=i} \left.\frac{\partial \mathbf{R}(s';t)}{\partial s'}\right|_{s'=j} \right\rangle \approx \left\langle \frac{\Delta\mathbf{R}(i;t)}{\Delta i}\frac{\Delta\mathbf{R}(j;t)}{\Delta j} \right\rangle \ ,$$

which is a discrete version of equation (1.3.4). For a single entanglement segment $i = j$, $\Delta i = 1$, and $\Delta\mathbf{R} = \mathbf{r}$ is the end-to-end vector. To this end and for reasons that will become clear, an artificial scalar energy field $\mathbf{r}\,\underline{\underline{\tau}}\,\mathbf{r}$ is introduced. The partition function in terms of the tensor $\underline{\underline{\tau}}$ is

$$Z_p[\underline{\underline{\tau}}] = \int_{-\infty}^{\infty} P_0(\mathbf{r}) \exp\left(-\mathbf{r}\,\underline{\underline{\tau}}\,\mathbf{r}\right)\mathrm{d}\mathbf{r} \ . \tag{1.6.12}$$

The chains are assumed to have a Gaussian distribution with mean length Nb^2 in each of the three dimensions, which gives the probability distribution

$$P_0(\mathbf{r}) = \left(\frac{3}{2\pi N b^2}\right)^{\frac{3}{2}} \exp\left(-\frac{3\mathbf{r}^2}{2Nb^2}\right) \ . \tag{1.6.13}$$

This is non-dimensionalised by rescaling with $\mathbf{r}' = (\mathbf{r}/Nb^2)$ and $\underline{\underline{\tau}}' = Nb^2\underline{\underline{\tau}}$, then the primes are dropped to obtain

$$Z_p[\underline{\underline{\tau}}] = \left(\frac{3}{2\pi}\right)^{\frac{3}{2}} \int_{-\infty}^{\infty} \exp\left(-\mathbf{r}\,\underline{\underline{\tau}}\,\mathbf{r} - \frac{3}{2}\mathbf{r}^2\right)\mathrm{d}\mathbf{r} \ . \tag{1.6.14}$$

The elastic free energy for a set of chains is defined as

$$F[\underline{\underline{\tau}}] = -\ln Z_p[\underline{\underline{\tau}}] \ , \tag{1.6.15}$$

and differentiating this with respect to $\underline{\underline{\tau}}$ gives

$$\frac{\partial F[\underline{\underline{\tau}}]}{\partial \underline{\underline{\tau}}} = -\frac{1}{Z_p[\underline{\underline{\tau}}]}\frac{\partial Z_p[\underline{\underline{\tau}}]}{\partial \underline{\underline{\tau}}} = \frac{1}{Z_p[\underline{\underline{\tau}}]} \int \mathbf{r}^2 P_0(\mathbf{r}) \exp\left(-\mathbf{r}\,\underline{\underline{\tau}}\,\mathbf{r}\right)\mathrm{d}\mathbf{r} = \left\langle \mathbf{r}^2 \right\rangle = \underline{\underline{\mathbf{P}}} \ . \tag{1.6.16}$$

The relationship between $F[\underline{\underline{\tau}}]$ and $\left\langle \mathbf{r}^2 \right\rangle$ enables the Legendre transform to be taken advantage of, and that was the reason the artificial field was introduced.

The tensor $\underline{\underline{\tau}}$ is assumed to be symmetric, and then $\underline{\underline{\mathbf{A}}} = 2\underline{\underline{\tau}} + 3\underline{\underline{\mathbf{I}}}$ is also symmetric, and equation (1.6.14) becomes

$$Z_p[\underline{\underline{\tau}}] = \left(\frac{3}{2\pi}\right)^{\frac{3}{2}} \int_{-\infty}^{\infty} \exp\left(-\frac{1}{2}\mathbf{r}\,\underline{\underline{\mathbf{A}}}\,\mathbf{r}\right)\mathrm{d}\mathbf{r} \ . \tag{1.6.17}$$

Since $\underline{\underline{\mathbf{A}}}$ is symmetric, it can be diagonalised through $\underline{\underline{\mathbf{X}}}^{-1}\,\underline{\underline{\mathbf{A}}}\,\underline{\underline{\mathbf{X}}} = \underline{\underline{\mathbf{D}}}$, with $\underline{\underline{\mathbf{A}}}$ and $\underline{\underline{\mathbf{D}}}$ similar matrices hence $\det\left(\underline{\underline{\mathbf{A}}}\right) = \det\left(\underline{\underline{\mathbf{D}}}\right)$. As the transformation to $\widehat{\mathbf{r}}$ is a pure rotation with unit Jacobian, the partition function becomes

$$Z_p[\underline{\underline{\tau}}] = \left(\frac{3}{2\pi}\right)^{\frac{3}{2}} \int_{-\infty}^{\infty} \exp\left(-\frac{1}{2}\widehat{\mathbf{r}}\,\underline{\underline{\mathbf{D}}}\,\widehat{\mathbf{r}}\right) \mathrm{d}\widehat{\mathbf{r}} = \left(\frac{27}{\det\left(\underline{\underline{\mathbf{D}}}\right)}\right)^{\frac{1}{2}} = \left(\frac{27}{\det\left(\underline{\underline{\mathbf{A}}}\right)}\right)^{\frac{1}{2}} ,$$

$$\text{therefore } F[\underline{\underline{\tau}}] = \frac{1}{2}\ln\det\left(\underline{\underline{\mathbf{A}}}\right) - \frac{1}{2}\ln 27 . \tag{1.6.18}$$

The tensorial Legendre transform is then implemented

$$f^*[\underline{\underline{\mathbf{P}}}] = F[\underline{\underline{\tau}}] - \underline{\underline{\mathbf{P}}} : \underline{\underline{\tau}}, \text{ with } \underline{\underline{\mathbf{P}}} = \frac{\partial F[\underline{\underline{\tau}}]}{\partial \underline{\underline{\tau}}} .$$

$\underline{\underline{\mathbf{P}}} : \underline{\underline{\tau}} = \mathrm{Tr}\left(\underline{\underline{\mathbf{P}}}\,\underline{\underline{\tau}}^T\right)$ is a Frobenius inner product and is invariant under rotation. To find $\underline{\underline{\mathbf{P}}}$, equation (1.6.18) is differentiated with respect to $\underline{\underline{\tau}}$

$$\begin{aligned} \underline{\underline{\mathbf{P}}} &= \frac{\partial F[\underline{\underline{\tau}}]}{\partial \underline{\underline{\tau}}} = \frac{1}{2\det\left(\underline{\underline{\mathbf{A}}}\right)} \frac{\partial \det\left(\underline{\underline{\mathbf{A}}}\right)}{\partial \underline{\underline{\tau}}} = \frac{1}{2\det\left(\underline{\underline{\mathbf{A}}}\right)} \frac{\partial \det\left(\underline{\underline{\mathbf{A}}}\right)}{\partial \underline{\underline{\mathbf{A}}}} \frac{\partial \underline{\underline{\mathbf{A}}}}{\partial \underline{\underline{\tau}}} \\ &= \frac{1}{\det\left(\underline{\underline{\mathbf{A}}}\right)} \frac{\partial \det\left(\underline{\underline{\mathbf{A}}}\right)}{\partial \underline{\underline{\mathbf{A}}}} , \end{aligned}$$

and since $\left(\partial\det\left(\underline{\underline{\mathbf{A}}}\right)/\partial\underline{\underline{\mathbf{A}}}\right) = \mathrm{adj}\left(\underline{\underline{\mathbf{A}}}\right) = \det\left(\underline{\underline{\mathbf{A}}}\right)\underline{\underline{\mathbf{A}}}^{-T}$, using [50], $\underline{\underline{\mathbf{P}}} = \underline{\underline{\mathbf{A}}}^{-1}$ because $\underline{\underline{\mathbf{A}}}$ is symmetric. Consequently the elastic free energy in terms of $\left\langle \mathbf{r}^2 \right\rangle$ is

$$\begin{aligned} f^*\left[\left\langle \mathbf{r}^2 \right\rangle\right] &= \frac{1}{2}\ln\left(\det\left(\underline{\underline{\mathbf{A}}}\right)\right) - \frac{1}{2}\ln 27 - \frac{1}{2}\underline{\underline{\mathbf{A}}}^{-1} : \left(\underline{\underline{\mathbf{A}}} - 3\underline{\underline{\mathbf{I}}}\right) , \\ f^*\left[\left\langle \mathbf{r}^2 \right\rangle\right] &= \frac{1}{2}\ln\left(\det\left(\underline{\underline{\mathbf{A}}}\right)\right) - \frac{1}{2}\ln 27 - \frac{1}{2}\mathrm{Tr}\left(\underline{\underline{\mathbf{I}}}\right) + \frac{3}{2}\mathrm{Tr}\left(\underline{\underline{\mathbf{P}}}\right) , \end{aligned}$$

The relation $\det\left(\exp\left(\underline{\underline{\mathbf{B}}}\right)\right) = \exp\left(\mathrm{Tr}\left(\underline{\underline{\mathbf{B}}}\right)\right)$, with $\underline{\underline{\mathbf{B}}} = \ln\left(\underline{\underline{\mathbf{A}}}\right)$ is used to obtain $\ln\left(\det\left(\underline{\underline{\mathbf{A}}}\right)\right) = \mathrm{Tr}\left(\ln\left(\underline{\underline{\mathbf{A}}}\right)\right)$. Thus, by modelling polymer chains with Gaussian statistics, the elastic free energy in terms of the constraint on the ensemble average is

$$f^*\left[\left\langle \mathbf{r}^2 \right\rangle\right] = \frac{3}{2}\mathrm{Tr}\left(\left\langle \mathbf{r}^2 \right\rangle\right) - \frac{1}{2}\mathrm{Tr}\left(\ln\left(\left\langle \mathbf{r}^2 \right\rangle\right)\right) - \Gamma , \tag{1.6.19}$$

with Γ being a constant, which can be set to normalise the base energy level. However, Gaussian chains, have the disadvantage of being infinitely extensible, which of course polymer chains are not. The free energy derivation can be amended numerically with a more realistic model which does not contain infinite extension. This is achieved by replacing $P_0(\mathbf{r})$ with a finitely extensible probability distribution, and a simpler method that approximates the ensemble average constraint $\left\langle \mathbf{r}^2 \right\rangle$ with $|\mathbf{r}|$ for highly stretched chains, in other words, ignoring small fluctuations when the chains are taut. That replaces

$$\frac{3}{2}\mathrm{Tr}\left(\left\langle \mathbf{r}^2 \right\rangle\right) \text{ with } \frac{1}{2}\mathrm{Tr}\left(\left\langle \mathbf{r}^2 \right\rangle\right) - N_e \ln\left(1 - \frac{1}{N_e}\mathrm{Tr}\left(\left\langle \mathbf{r}^2 \right\rangle\right)\right) ,$$

in equation (1.6.19), N_e is the number of monomers in an entanglement segment. This approximation has been shown to accurately reproduce the numerical Legendre transform results. Finally, the payoff is that this produces an equation which calculates the elastic free energy for a constraint on the ensemble average $\mathbf{f} = \left\langle \mathbf{r}^2 \right\rangle$

$$\Delta F^{\mathrm{el}} = \frac{1}{2}\mathrm{Tr}\left(\mathbf{f}\right) - \frac{1}{2}\mathrm{Tr}\left(\ln\left(\mathbf{f}\right)\right) - N_e \ln\left(1 - \frac{1}{N_e}\mathrm{Tr}\left(\langle \mathbf{f} \rangle\right)\right) - \Gamma \ . \qquad (1.6.20)$$

The length of a particular segment, i, is $\sqrt{\left\langle \mathbf{r}_i^2 \right\rangle} = \sqrt{\mathrm{Tr}\,\mathbf{f}_i}$. This provides the dominant contribution to ΔF_i^{el} through the first and third terms in equation (1.6.37), but the off-diagonal elements of $\mathbf{f}$ also contribute in the second term. If entanglement segments have different elastic free energy values, ΔF_i^{el}, then they are considered to be different species, in terms of attaching to a nucleus.

1.6.3.2 Entropic penalty of nucleus orientation

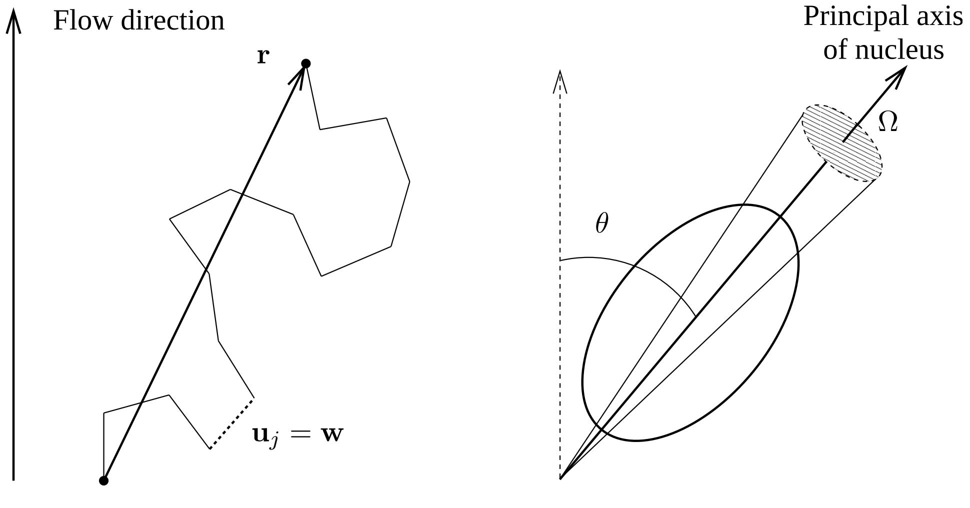

Figure 1.11: A polymer chain configuration for $\mathbf{r}$ with $\mathbf{u}_j = \mathbf{w}$ together with the principal axis of a nucleus, which has an angle of θ with the flow direction, also showing solid tolerance angle Ω.

In this section, the effect of nucleus alignment on the entropic cost of attachment, and how it is implemented in the GO polymer simulation [21, 22] is outlined. A similar idea to that presented by Jarecki [51] is used, that is, an attaching monomer must be oriented within a small solid tolerance angle, Ω, of the principal axis of the nucleus. In a quiescent melt (no flow applied) or even one with a weak flow, the chains are unstretched, and the monomer orientation is isotropic, hence the nucleus orientation is unimportant. However, there is expected to be a noticeable effect for significant flows, producing strongly aligned polymer chains.

To perform the entropy calculation in general, a similar approach to section 1.6.3.1 is applied, but with the constraint that the monomer j must have the same vector as the principal axis of the nucleus $\mathbf{u}_j = \mathbf{w}$ (with $|\mathbf{w}| = 1$), see figure 1.11. Hence the partition function with an artificial field $\mathbf{r}\underline{\underline{\mathbf{\Pi}}}\mathbf{r}$ is

$$\mathcal{Z}[\underline{\underline{\mathbf{\Pi}}}, \mathbf{w}] = \int\int \delta(\mathbf{u}_j - \mathbf{w}) W_0(\mathbf{u}_j) P(\mathbf{r} - \mathbf{w}, N_e - 1) \exp\left(\mathbf{r}\underline{\underline{\mathbf{\Pi}}}\mathbf{r}\right) \mathrm{d}\mathbf{r}\mathrm{d}\mathbf{u}_j \ ,$$

where $W_0(\mathbf{u}) = \delta(|\mathbf{u}|-1)/(4\pi)$ is the distribution of a freely rotating unit vector and $P(\mathbf{r} - \mathbf{w}, N_e - 1)$ is the probability the remaining $N_e - 1$ monomers on the chain sum up to $\mathbf{r}$ along with $\mathbf{u}_j = \mathbf{w}$. The opposite vector $\mathbf{u}_j = -\mathbf{w}$ should also be considered, but as the melt is symmetric along and around the flow direction, the result of including this would be a factor of two which is nullified by normalisation. Since the polymer chains are taut under strong flows, instead of taking the constraint to be an ensemble average, $\langle \mathbf{r}^2 \rangle$, the small fluctuations are again ignored, and a fixed vector $\mathbf{r}$ is imposed. A statistical mechanics result in [51], can be modified so that the cost is related to

$$w(\mathbf{f}, \theta) = \frac{\mathcal{L}^{-1}\left(\sqrt{\mathrm{Tr}\mathbf{f}}/N_e\right)}{4\pi \sinh\left(\sqrt{\mathrm{Tr}\mathbf{f}}/N_e\right)} \cosh\left(\mathcal{L}^{-1}\left(\frac{\sqrt{\mathrm{Tr}\mathbf{f}}}{N_e}\right)\cos\theta\right) \ . \qquad (1.6.21)$$

Here the length $|\mathbf{r}|$ is approximated by $\sqrt{\mathrm{Tr}\mathbf{f}}$, θ is the angle between flow direction and the major axis of the nucleus, and $\mathcal{L}^{-1}$ is the inverse Langevin function which is approximated by Cohen [52] as

$$\mathcal{L}^{-1}(x) \approx x\frac{3 - x^2}{1 - x^2} \ .$$

The solid tolerance angle, Ω is small, then the fraction of monomers aligned to attach is $w(\mathbf{f}, \theta)\Omega$. The additional concentration term due to alignment is

$$\Theta_i = 4\pi w(\mathbf{f}_i, \theta_i) \ , \qquad (1.6.22)$$

for monomers in differently stretched entanglement segments or species i, since it is required to agree with the quiescent limit, and $\ln(\Omega/4\pi)$ is absorbed into the attachment parameter E_0.

A numerical calculation has been completed in appendix A.2 of [21] with the correct ensemble average constraint and the agreement with this approximate fixed length constraint is satisfactory. Asymptotic analysis of equation (1.6.21) supports the expected behaviour of nucleus alignment. For weak flows that produce a small value of $(\sqrt{\mathrm{Tr}\mathbf{f}}/N_e)$, the orientational effect from $\cos\theta$ is minimal. However, for stronger flows, $(\sqrt{\mathrm{Tr}\mathbf{f}}/N_e)$ increases, and the inverse Langevin function enhances the effect, so that the angle θ rapidly becomes significant.

1.6.3.3 Implementation of nucleus rotation

The GO polymer nucleation simulation models nucleus rotation through two processes, both using the theory of solid bodies in a Newtonian fluid. One process is a convection term solely due to the fluid flow and the other is diffusion through Brownian motion. The convection term applies a result given by Leal and Hinch [53], who use Jeffery's work on the motion of ellipsoidal particles in a viscous fluid [54]. The principal axis of the spheroid is represented by the unit vector $\widehat{\mathbf{v}}$ and evolves with the equation

$$\frac{\mathrm{d}\widehat{\mathbf{v}}}{\mathrm{d}t} = \boldsymbol{\Omega} \cdot \widehat{\mathbf{v}} + G(\rho) \left[\mathbf{E} \cdot \widehat{\mathbf{v}} - \widehat{\mathbf{v}} \left(\widehat{\mathbf{v}} \cdot \mathbf{E} \cdot \widehat{\mathbf{v}} \right) \right] \ , \tag{1.6.23}$$

where $\mathbf{E}$ and $\boldsymbol{\Omega}$ are the symmetric and antisymmetric parts of the volume-conserving velocity gradient tensor $\kappa = \mathbf{E} + \boldsymbol{\Omega}$, $\mathbf{E}^T = \mathbf{E}$, $\boldsymbol{\Omega}^T = -\boldsymbol{\Omega}$ and

$$G(\rho) = \frac{\rho^2 - 1}{\rho^2 + 1} \ ,$$

where ρ is the aspect ratio. Hence the principal axis of the spheroid changes according to

$$\widehat{\mathbf{v}}(t + \Delta t) = \widehat{\mathbf{v}} + \Delta t \frac{\mathrm{d}\widehat{\mathbf{v}}}{\mathrm{d}t} \ ,$$

for a timestep Δt, with $(\mathrm{d}\widehat{\mathbf{v}}/\mathrm{d}t)$ given by equation (1.6.23).

The Brownian diffusion step involves selecting a random unit vector $\widehat{\mathbf{u}}$ and a random angle ϕ from a Gaussian distribution with moments

$$\langle \phi \rangle = 0 \ , \qquad \left\langle \phi^2 \right\rangle = \frac{6 \Delta t}{\tau_{\mathrm{rot}}} \ , \tag{1.6.24}$$

to ensure the correct decorrelation statistics. The principal axis is then rotated around $\widehat{\mathbf{u}}$ by ϕ using the rotation formula

$$\widehat{\mathbf{v}}(t + \Delta t) = \widehat{\mathbf{v}} \cos \phi + \widehat{\mathbf{u}} \left(\widehat{\mathbf{u}} \cdot \widehat{\mathbf{v}} \right) (1 - \cos \phi) + \left(\widehat{\mathbf{v}} \times \widehat{\mathbf{u}} \right) \sin \phi \ . \tag{1.6.25}$$

The rotational relaxation time, τ_{rot}, is related to the rotational diffusion constant by $D_{\mathrm{rot}} = (1/\tau_{\mathrm{rot}})$, which is given in Leal and Hinch [53] as

$$D_{\mathrm{rot}} = \frac{k_B T}{4 \eta_s V H(\rho)} \ , \tag{1.6.26}$$

where η_s is the viscosity of the fluid, V is the volume of the body and

$$H(\rho) = \frac{\rho^2 + 1}{\rho^3 \int\limits_0^\infty \left(\rho^2 + \lambda \right)^{-3/2} (1 + \lambda)^{-1} \, \mathrm{d}\lambda + \rho \int\limits_0^\infty \left(\rho^2 + \lambda \right)^{-1/2} (1 + \lambda)^{-2} \, \mathrm{d}\lambda} \ , \tag{1.6.27}$$

is a drag function connected to the shape of the body [55]. Diffusion slows with increasing volume and eccentricity of the spheroid. Hence the rotational relaxation time becomes

$$\tau_{\mathrm{rot}} = \frac{4 \eta_s V H(\rho)}{k_B T} \ , \tag{1.6.28}$$

however, this highlights a clear weakness of the model, namely there is a vast difference between the rotational freedom of a spheroid immersed in a Newtonian fluid and a solid nucleus within a polymer melt. The model acknowledges the uncertainty with an unknown parameter, α, in the rotational relaxation time

$$\tau_{\text{rot}} = \alpha \tau_0 N_T H(\rho) \ , \tag{1.6.29}$$

with N_T now representing the nucleus volume and α set such that when $N_T = 1$ we have $\tau_{\text{rot}} \approx \tau_0$. A major flaw in the model is still included though, the relaxation time is only linear in N_T which is a large underestimate considering the highly connected and restrictive nature of polymer melts.

1.6.3.4 Fast simulation technique for barrier crossing

In this section, a method by Jolley [46], for simulating extremely high energy barriers is introduced. Simulating crossing times for nucleation events tends to be difficult, since the energy barriers are potentially large as nucleation is intrinsically a rare event. A particle in a typical simulation would spend a huge proportion of its time spent at the base of a landscape, which is well-known to obey Boltzmann statistics. The Boltzmann region in a non-equilibrium system is roughly defined as the range of nuclei sizes, where the relative occupancy probability, P_i, of each state is not significantly affected by the occasional crossing event, and is approximately equal to the energy level, $F(i)$, of that state through

$$P_i \approx \frac{1}{Z_{\text{eff}}} \exp\left(-F(i)\right) \ ,$$

where $Z_{\text{eff}} = \exp\left(-F(1)\right) + \exp\left(-F(2)\right) + \exp\left(-F(3)\right) + \dots$ is the effective partition function, which is a sum of all the Boltzmann factors of all states. The aim of this simulation technique is to spend more resources on the region where the Boltzmann assumption is not true, referred to as the non-Boltzmann region and nuclei are close enough to the peak of the barrier to have their occupancy diminished by nuclei leaving the system.

Initially the energy landscape, $F(i)$, must be determined, where i is the number of monomers in a nucleus and is used as a reaction coordinate. The simple method of obtaining this energy landscape is to employ a sampling simulation, which has reflecting boundary conditions that do not allow the nucleus to leave a confined region. Recording the amount of time spent in each state, T_i, as well as the total time, T_{total}, the energy landscape can be determined with

$$\frac{T_i}{T_{\text{total}}} = A \exp\left(-F(i)\right) \ , \tag{1.6.30}$$

where A is set such that $F(1) = 0$. This method is satisfactory for smaller barriers, however, when applied to larger ones, it is difficult to obtain an acceptable amount of information around the peak as it is explored so rarely.

An alternative method, suggested by Jolley, is to do a series of constrained simulations, in each of which a nucleus only explores the relationship between two adjacent states. Beginning at the base of the landscape at $N_T = 1$, placing a reflecting boundary condition at $N_T = 2$. The simulation oscillates between the microstates of theses two states until sufficient statistics are attained and the relative energy of state 2, $F(2)$ is discerned from equation (1.6.30). This constrained simulation can be shifted to explore states 2 and 3 to find $F(3)$ and so on. Hence we obtain the whole energy landscape $F(i)$ efficiently, and provided enough statistics are gained at each stage, the accumulated error is negligible.

The aim of Jolley's simulation technique is to start nuclei within the Boltzmann region, but close enough to the peak or critical nuclei, n^*, of the landscape for enough crossing events to occur. Using the simulated energy landscape, a state N_{min} is selected as a starting point such that $F(N_{\text{min}}) \ll F(n^*)$. The idea in simulating this reduced region is that if the nucleus ever falls below state N_{min} into state $N_{\text{min}} - 1$, then it is said to have failed and a new nucleus tries again starting at state N_{min}. This technique produces many crossing attempts quickly, the majority of which fail in their first few moves. The results of this reduced simulation must then be transformed to represent faithfully a full simulation of particles starting at the base of the landscape. The number of nuclei entering the system, or the input flux, J^r_{in}, per unit time of the reduced simulation, and the number of nuclei that successfully cross the landscape or the output flux, J^r_{nuc}, per unit time of the reduced simulation should have the same ratio as in the full simulation. Also this should be the same ratio as the occupancy probability for state N_{min} for reduced and full simulations

$$C = \frac{J^f_{\text{nuc}}}{J^r_{\text{nuc}}} = \frac{J^f_{\text{in}}}{J^r_{\text{in}}} = \frac{P^r_{N_{\text{min}}}}{P^f_{N_{\text{min}}}} \ . \tag{1.6.31}$$

The desired quantity is the output flux of the full simulation, J^f_{nuc}, which is the inverse of the average crossing time, $\langle\tau\rangle$, and can be written

$$\langle\tau\rangle = \frac{1}{J^f_{\text{nuc}}} = \frac{P^r_{N_{\text{min}}}}{P^f_{N_{\text{min}}} J^r_{\text{nuc}}} \ . \tag{1.6.32}$$

The reduced simulation is able to record the number of successful crossing events, R_{nuc}, and together with the total simulation time, T_{sim}, giving the output flux of the reduced simulation as

$$J^r_{\text{nuc}} = \frac{R_{\text{nuc}}}{T_{\text{sim}}} \ . \tag{1.6.33}$$

The occupancy probability of state N_{min}, $P^r_{N_{\text{min}}}$ in the reduced simulation is found by recording the time spent in that state, $T_{N_{\text{min}}}$, together with the total simulation time, $T_{\rm sim}$, hence

$$P^r_{N_{\rm min}} = \frac{T_{N_{\rm min}}}{T_{\rm sim}} \ . \tag{1.6.34}$$

The only remaining unknown, is the occupancy probability of state $N_{\rm min}$ in the full simulation, $P^f_{N_{\rm min}}$, which is found using the Boltzmann assumption and hence obeys

$$P^f_{N_{\rm min}} \approx \frac{1}{Z_{\rm eff}} \exp\left(-F(N_{\rm min})\right) \ . \tag{1.6.35}$$

A good approximation to the average nucleation time is obtained from the expression

$$\langle\tau\rangle \approx \frac{T_{N_{\rm min}}}{Z_{\rm eff} R_{\rm nuc}} \exp\left(-F(N_{\rm min})\right) \ . \tag{1.6.36}$$

One key element of the reduced simulation, is how a microstate within state $N_{\rm min}$, is selected as a starting point. To produce an accurate representation, the distribution of starting microstates must be equivalent to the visitation frequency of these microstates in the full simulation. In theory, a pre-simulation must be used to find the correct distribution of starting arrangements, by logging the number of visits to each microstate in a confined spanning simulation. Then, upon starting a new nucleation attempt, the initial arrangement would be selected from this distribution. However, in practice, the simulation uses a different method, beginning in a particular microstate, and the next occasion state $N_{\rm min}$ is visited the arrangement is stored, and this microstate will be starting point of the next attempt. Over time the whole of the collection of microstates within state $N_{\rm min}$ is explored with the correct relative frequencies. As state $N_{\rm min}$ is assumed to be within the Boltzmann region, the distribution of starting microstates is also Boltzmann. Also since there will be a huge number of attempts, as nuclei fail or succeed quickly, the initial choice of arrangement is unimportant.

The Jolley simulation technique is an extremely useful method for simulating average crossing times over arbitrarily high barriers, as the height of the energy barrier is no longer a limitation, since the starting state can be chosen to be set distance below the peak. However, it is still difficult to simulate barriers with a long flat plateau at the peak which is more of a diffusional process, not obeying Boltzmann statistics. This technique has been successful at improving the scope the GO model, it would also be a good option for other high barrier crossing simulations. There are alternate approaches to investigate the occupation probabilities of more general systems, such as transition path sampling [56], milestoning [57], Markov models [58] and forward flux sampling [59, 60].

We began this review section on simulation techniques with detailed balance, which showed that the ratio of reaction rates between two adjacent states is proportional to the exponential of the difference in energy level, by equation (1.6.1). The basic kinetic Monte Carlo algorithm was introduced, in which the system moves between states based on random selections. The GO simulation method was outlined, which uses two basic moves, stem addition and stem lengthening, to grow nuclei from a single monomer. The simulation's efficiency is improved by retaining very little information, only the total volume and the number of stems, to describe the current nucleus, the internal structure is unresolved. The simulation is used to model FIC of polymers by applying the GLaMM model of entangled polymers. Under flow, the entanglement segments relax at different rates which, in terms of monomer attachment, produces different monomer types or species. The GO model is designed to allow these different species to compete based on their attachment value, through equation (1.6.11) with the aid of equation (1.6.20), and their concentration within the melt. Another feature of the model, is the inclusion of nucleus rotation, and only allowing monomers to attach if they are sufficiently aligned with the nucleus, this results in an extra concentration term for all addition moves, given by equation (1.6.22). The processes which the GO model uses to alter the orientation of a nucleus with the principal flow direction were also detailed. These are through random diffusion and also convection with flow. Finally, two fast simulation techniques by Jolley were explained. The first was a method to simulate the energy landscape by using a series of constrained simulations. The second and most useful, is a procedure to simulate the crossing rates from energy barriers of arbitrary height, by reducing the simulated region to just below the peak, and adapting the output data with equation (1.6.36) to find accurate average crossing times for the complete system.

1.6.3.5 Summary of results

The GO polymer simulation has produced many interesting results, a select few are summarised here. The first is referred to as the quasi-static result, and is displayed in figure 2(a) of [22]. It shows the evolution of the nucleation rate in a transient flow in comparison to data sets where chain configurations are frozen at set times, and simulation are completed over fixed barriers. The figure also shows that enabling nucleus rotation significantly increases nucleation rates, to be investigated thoroughly in chapter 5. The agreement between data sets is excellent, and the conclusion is that the rate of nucleation is solely determined by the instantaneous configuration of the polymer chains. This is due to the huge separation of timescales between monomer attachment and detachment rates and significant changes to the chain configurations due to the flow ($\tau_0 \ll \tau_e$). This quasi-static result is vitally important in developing analytic models of flow-induced nucleation in polymers.

Another key result from the GO polymer simulation is the master curve shown in figure 2(b) of [22]. This master curve shows that the nucleation rate depends only on the stretch of the chains in the melt. Total stretch for a chain under flow relative to its equilibrium length is given by

$$\lambda = \frac{1}{Z} \sum_{i=1}^{Z} \sqrt{\langle \mathbf{r}_i^2 \rangle} \ , \tag{1.6.37}$$

which is a sum over the length of all entanglement segments. This master curve result holds for different flow geometries and different flow rates, and could be a useful tool to predict flow-induced nucleation.

1.6.3.6 Comparison to experiments

The GO simulation compares well to experimental data, shown in figure 2(c) of [22]. Steady state nucleation rate measurements for an industrial polydisperse isotactic polypropylene melt [6] at $140°C$ for varying shear rates, are compared to simulation results with the polydisperse melt approximated as a bimodal blend using the GLaMM model. In other experiments [5, 10, 11, 12, 13], shish nuclei are especially prevalent in polymer melts containing mostly short chains blended with a sparse amount of long chains at low undercooling. The GO simulation does observe anisotropic nuclei growth when investigating these melts especially at high flow rates, as shown by figure 3 of [22]. Thus providing an initial theoretical framework to explain this crucial phenomena.

1.7 Space-filling models for crystallisation

One of the major motivations for studying polymer nucleation, is that the nucleation rate of a system has a huge effect on the physical properties of the resulting solid crystal. For the plastics industry it would be very appealing to have the potential to tailor the strength, flexibility, transparency, and other physical properties, of their final product by modifying the processing conditions. In vague terms, fast nucleation rates produce a material with an ordered macrostructure containing spherulites of a similar size. For slow nucleation rates, stable nuclei are so rare, that they can grow very large without being blocked by other nuclei. This produces an irregular macrostructure of vastly different sizes of spherulites.

This section reviews several space-filling models, essentially the process of how a volume of liquid is transformed into the solid state. There are two contributing factors, the nucleation rate, which is the rate of formation of stable nuclei and the growth rate of these stable crystals. A model which includes unlimited growth is described in section 1.7.1, providing a primary view of the evolution of the system. As well as two proposals which include basic impingement, by Avrami and Tobin are reviewed, both using the unlimited growth model as a basis. These works have been summarised by Schneider, Koppl and Berger in [27].

1.7.1 Model with unlimited growth

The first attempt at modelling this transformative phase change neglects impingement or adjacent crystals being obstructed from further growth in a particular direction, thus allowing nuclei to grow boundlessly. There are two stages to this process, the first is the spontaneous formation of stable crystals which initially have a negligibly small volume. Once a stable crystal is formed, it then grows linearly with time, transforming the surrounding volume.

The nucleation rate, $n(t)$, defined to be the probability of a stable crystal forming per germ nuclei per unit time, in principle depends on temperature. However, we only consider changes due to advancing time, in the particular case of polymer crystallisation in a shear flow with the nucleation rate increasing due to polymer chain stretch for example. Time, t, is transformed using the relation

$$\mathrm{d}\tau = n(t)\mathrm{d}t \ , \ \ \tau = \int_0^t n(t')\mathrm{d}t' \ , \tag{1.7.1}$$

hence the transformed time, τ, is now non-dimensional, and describes the expected number of stable crystals formed at a given time. The number of germ nuclei or, as yet untransformed nuclei per unit volume is defined as $N(\tau)$. The small consumption of germ nuclei by the initial stage is ignored, and the rate of change of $N(\tau)$ is

$$\frac{\mathrm{d}N(t)}{\mathrm{d}t} = -nN \ \text{ or } \ \frac{\mathrm{d}N(\tau)}{\mathrm{d}\tau} = -N \ \text{ therefore } \ N(\tau) = N_0 e^{-\tau} \ , \tag{1.7.2}$$

where N_0 is the initial number of untransformed germ nuclei. To take into account the reduced volume of germ nuclei available and since polymers tend not to fully crystallise, as suggested by Mandelkern on page 230 in [61], equation (1.7.2) is modified to

$$N(\tau) = N_0 e^{-\tau}(1 - \xi(\tau)) \ \text{ with } \ \xi(\tau) = \frac{V(\tau)}{V_\infty} \ , \tag{1.7.3}$$

where, $V(\tau)$, is the transformed volume and V_∞ is the maximum transformed volume. The expected number of stable crystals per unit volume is

$$N_D(\tau) = N_0 \int_0^\tau e^{-\tau'}(1 - \xi(\tau'))\mathrm{d}\tau' \ .$$

Once a stable crystal is formed it will then grow linearly with time with rate $G(\tau)$. In terms of the transformed time variable, if a crystal begins to grow at time z, then at a later time, τ, it will have grown to a volume

$$\nu(\tau, z) = \sigma \left[\int_z^\tau \frac{G(\tau')}{n(\tau')} \mathrm{d}\tau' \right]^m \ , \tag{1.7.4}$$

with m referring to the dimension and $\sigma = 1$ for one-dimensional rods, $\sigma = 2\pi$ for two-dimensional circles and $\sigma = 4\pi/3$ for three-dimensional spheres. If the ratio $\alpha(\tau) = G(\tau)/n(\tau)$ is approximated by a constant, then

$$\nu(\tau, z) = \sigma\alpha^m(\tau - z)^m \ . \tag{1.7.5}$$

If $\alpha(\tau)$ cannot be approximated by a constant, the integral (1.7.4) must be calculated numerically.

A first attempt at the transformed volume which includes both nucleation and growth stages, called the extended volume, is

$$V_e = \int_0^\tau \nu(\tau, z) N(z) \mathrm{d}z \ , \tag{1.7.6}$$

this is a large overestimate because it does not include impingement.

In the case of unlimited growth, crystals can grow unimpeded until almost all source nuclei are used up. This is quite unrealistic, as the event of growing crystals being blocked either by a wall or another crystal is highly likely. However, attempting to model the impingement of advancing crystals is an incredibly formidable task. However, a few makeshift models have been proposed. The first by Avrami [62, 63, 64] assumes that the rate of change in the actual volume, V, is the same as the rate of change in the extended volume, V_e, scaled by the amount of untransformed volume remaining with Mandelkern's correction as defined in (1.7.3).

Alternatively, Tobin [65, 66] suggested that the actual transformed volume, V, is itself equal to the extended volume scaled by the untransformed volume, hence $V(\tau) = (1-\xi(\tau))V_e(\tau)$, and here the absorption of germ nuclei is included through the use of equation (1.7.3). Both Avrami's and Tobin's initial models of impingement are fairly basic, more complicated models involve tracking multiple over-lapping spheres. The basic models, however, are sufficient as impingement does not concern the work in this thesis.

1.8 Discussion

In this introductory chapter and literature review, we have provided essential background material to develop analytic models of polymer nucleation. We began by studying general entangled polymer theory, with the Rouse model representing polymer chains as the Brownian motion of a series of particles connected by springs. We followed this by describing the tube model, which confines those polymer chains to a tube-like region, with the relaxation mechanisms of reptation, contour length fluctuations, and constraint release. We also outlined the GLaMM model, which is based on the concept of the tube, and models chain configurations under flow down to the length scale of the tube diameter. The various relaxation mechanisms are collected together into a single stochastic differential equation (1.3.3), that describes the movement of a chain within an entangled polymer melt.

We reviewed classical nucleation theory of simple molecules. The transition from a liquid state to a solid state is determined by the free energy landscape of the solid nucleus. This is a balance between the energetically favourable solid state related to the bulk volume and the cost of the surface area. Therefore nucleation is an energy barrier crossing problem, and the rate of nucleation can be estimated by the Boltzmann approximation (1.4.8) as the dominating factor is the barrier height. An improvement to this approximation is suggested after equation (1.4.11) with a kinetic prefactor. Additionally, we presented a continuous barrier crossing calculation, with particles diffusively escaping an energy well, obtaining average escape times through equation (1.5.6). This thesis will investigate both continuous and discrete techniques to enhance the accuracy of nucleation rates.

A significant element of this thesis, will be developing analytic tools that both predict simulations, and investigate regions outside of their practical reach. Primarily the GO simulation of FIC of polymers was discussed in detail. The model is based on the kinetic Monte Carlo algorithm and tracks a nucleus on the molecular level. The nucleus is able to grow and shrink by adding or removing monomers from the surrounding polymer melt. The melt's chain configuration data is obtained from the GLaMM model and includes the effects of flow via stretched chains. The simulation also features the relative orientation of the nucleus with respect to the flow direction which has a massive impact on attachment moves. Moreover, the simulation allows the nucleus to rotate with the flow through a convective or drag force as well as by random diffusion. This introduced several different timescales and together with the disparity in length scales in the complete picture, creates a significantly challenging environment for analytic techniques.

We also briefly described the space-filling models for crystallisation. These models produce information about the morphology based on the nucleation and crystal growth rates. They can also be applied in finite element solvers to study flow-induced crystallisation in complex geometries. Although a satisfactory solution to the problem of impingement has yet to be produced, this thesis is focused on nucleation.

Chapter 2

Combinatorial calculation of polymer nucleation

In this chapter we present an analytic calculation that determines free energy landscapes involved in nucleation. This work and analysis has also been published [67]. We consider monodisperse melts and aim to derive analytically the energy landscape of a forming crystal, since the nucleation rate over this landscape is dominated by the barrier height. We have a polymer melt of n species, each with a different attachment energy, E_i, predicted by the GLaMM model. What we refer to as “species” are actually segments of the chain with varying stretch, see section 1.3. Since the monomers have different stretches they have distinct attachment energies, E_i given by

$$E_i = E_0 + \frac{1}{N_e}\Delta F_i^{\mathrm{el}} \ , \tag{2.0.1}$$

where E_0 is the bulk free energy gain without deformation and ΔF_i^{el} is the free energy of stretching per monomer given by equation (1.6.37). We assume that all monomers on a single stem are of the same species, this is occasionally not so in the simulation, as discussed briefly in section 1.6.3, but we neglect this in the analytic calculation. This gives the constraint that we have only one type of monomer in each stem. We detail our in-depth calculation of the multiplicity or number of arrangements of each equivalent nucleus in section 2.1. In section 2.2, we present and analyse the energy landscapes and implied nucleation rates from the calculation, as well as comparing them to the results of the GO simulation.

2.1 Calculation of free energy nucleation landscapes

As this forthcoming combinatorial calculation is highly detailed, we present our ideas in several stages. In section 2.1.1, we consider the arrangements for quiescent nucleation, and this is built upon in section 2.1.2 which includes two species. We present our full combinatorial calculation for n species in section 2.1.3, and finally include the effect of the concentration of species in the polymer melt in section 2.1.4.

2.1.1 Quiescent nucleation

Before attempting the problem for n species, we simplify matters by analysing quiescent nucleation. Here, all chains are unstretched, therefore we have effectively one species with 100% concentration. The free energy $\mathcal{F}$ is only affected by the total number of monomers, N_T, and the number of stems, N_S, so all we need to calculate is the number of combinations $w(N_T, N_S)$ of each like state. The quantities $w(N_T, N_S)$ and the free energy, $\mathcal{F}(N_T, N_S)$, are combined in the nucleus partition function

$$Z(N_T, N_S) = w(N_T, N_S) \exp\left[-\mathcal{F}(N_T, N_S)\right]. \tag{2.1.1}$$

All quantities are known except for the number of combinations, $w(N_T, N_S)$, which we calculate through combinatorial arguments. We need to find how many combinations of N_T identical monomers are arranged on exactly N_S different stems. Since we need at least one monomer on each stem, we first place one monomer onto each stem, leaving $N_T - N_S$ monomers to be placed onto N_S stems with no conditions. The total number of arrangements is

$$w(N_T, N_S) = \frac{(N_T-1)!}{(N_T-N_S)!(N_S-1)!} \quad \text{for} \;\; N_T \geq N_S > 0 \;, \tag{2.1.2}$$

which is a standard combinatorial formula.

2.1.2 Two species

We now generalise this approach to two species as a way to illustrate the method for n species. We have two different species of monomer that can crystallize, with the condition that only one species of monomer can be present on each stem. The species have different attachment energies E_i and we label these species as type 1 and type 2. Hence the free energy $\mathcal{F}$ will be dependent on the amount of each species of monomer in that particular arrangement. Consequently we need to calculate the total number of arrangements of a given total number of monomers, N_T, number of stems, N_S, and number of type 1 monomers, m_1, and hence $N_T - m_1$ number of type 2 monomers. It is useful to clarify the definition of $w(N_T, N_S)$ from section 2.1.1 as the number of arrangements of N_T identical monomers onto exactly N_S different stems

$$w(N_T, N_S) = \begin{cases} 1, & (N_T = N_S = 0)\,, \\ \dfrac{(N_T-1)!}{(N_T-N_S)!(N_S-1)!}, & (N_T \geq N_S > 0)\,, \\ 0, & \text{otherwise.} \end{cases} \tag{2.1.3}$$

Let $\bar{w}(m_1, N_T, N_S)$ be the number of arrangements of N_T total monomers, split between m_1 type 1 monomers and $N_T - m_1$ type 2 monomers, onto exactly N_S stems. Say we place the m_1 type 1 monomers onto s_1 stems of which there are $w(m_1, s_1)$ arrangements using equation (2.1.3). Then we need to place $N_T - m_1$ type 2 monomers onto $N_S - s_1$ stems of which there are $w(N_T - m_1, N_S - s_1)$ arrangements. Multiplying these two terms together produces the number of ways of ordering two independent sets separately. However, there are many more arrangements than this, by shuffling the ordered sets between each other. So the total number of arrangements is multiplied by

$$C^{N_S}_{s_1} = C(N_S, s_1) = \frac{N_S!}{(N_S - s_1)!s_1!}. \tag{2.1.4}$$

So for a specific number of stems s_1 of type 1 monomers, the number of arrangements is

$$C(N_S, s_1) w(m_1, s_1) w(N_T - m_1, N_S - s_1).$$

To find the total number of arrangements $\bar{w}(m_1, N_T, N_S)$ we sum over s_1 from 0 to whichever is the smaller of N_S and m_1, since we cannot have more stems of type 1 monomer s_1 than we have total number of type 1 monomers, m_1, that is $s_1 \leq m_1$,

$$\bar{w}(m_1, N_T, N_S) = \sum_{s_1=0}^{\min(m_1, N_S)} C(N_S, s_1) w(m_1, s_1) w(N_T - m_1, N_S - s_1). \tag{2.1.5}$$

For two species, the free energy $\mathcal{F}$ of the crystal nucleus is still a balance between the reduction in bulk free energy and the increase in the surface energy, and is given by

$$\mathcal{F}(m_1, N_T, N_S) = -E_1 m_1 - E_2 (N_T - m_1) + \mu_{\mathrm{S}} \widetilde{S}(N_T, N_S). \tag{2.1.6}$$

Now similarly to equation (2.1.1) we define the nucleus partition function $\bar{Z}(m_1, N_T, N_S)$ by

$$\bar{Z}(m_1, N_T, N_S) = \bar{w}(m_1, N_T, N_S) \exp\left[-\mathcal{F}(m_1, N_T, N_S)\right], \tag{2.1.7}$$

and we remove the m_1 dependence of Z by summing over all possible values of m_1 to obtain

$$Z(N_T, N_S) = \sum_{m_1=0}^{N_T} \bar{Z}(m_1, N_T, N_S).$$

This section described two important features of our calculation, the clarification of the number of arrangements (2.1.3) is crucial to the inclusion of multiple species, and introduced the idea of shuffling the independent sets with equation (2.1.4) ensures the calculation is correct.

2.1.3 The general case of n species

To determine the free energy landscape for n species, as before, we need to find the total number of arrangements of alike energy states. In this case we have n different species so let us describe the system by

$$\{m_i\} = \{m_1, m_2, \dots m_{n-1}\} \text{ and } \{s_i\} = \{s_1, s_2, \dots s_{n-1}\} ,$$

where m_i and s_i are the number of monomers and stems, of species i. The number of monomers of the final species is determined by $m_n = N_T - \sum_{i=1}^{n-1} m_i$ and similarly $s_n = N_S - \sum_{i=1}^{n-1} s_i$. We aim to find $\bar{w}(\{m_i\}, N_T, N_S)$ which is the total number of arrangements of placing $\{m_i\}$ and m_n monomers onto N_S stems. So we need to place m_1 species 1 monomers onto s_1 stems and m_2 species 2 monomers onto s_2 stems, etc., until we are left with m_n species n monomers onto s_n stems. We apply equation (2.1.3) to obtain the number of ways of arrange the n sets separately

$$w(m_1, s_1)w(m_2, s_2) \cdots w(m_{n-1}, s_{n-1}) w\left(N_T - \sum_{i=1}^{n-1} m_i, N_S - \sum_{i=1}^{n-1} s_i\right) .$$

Now to find the total number of arrangements we shuffle these sets amongst one another. Firstly shuffle sets 1 and 2 giving us a multiplying factor $C(s_1 + s_2, s_2)$, then we shuffle the combined set of species 1 and 2 with set 3 which gives $C(s_1 + s_2 + s_3, s_3)$. We carry on this process until all n sets have been taken into account, with the last multiplying factor being $C(N_S, s_n)$. Let $P_a(\{m_i\}, \{s_i\}, N_T, N_S)$ be the number of arrangements for specific values of $\{s_i\}$,

$$\begin{aligned} P_a(\{m_i\}, \{s_i\}, N_T, N_S) = C\left(N_S, N_S - \sum_{i=1}^{n-1} s_i\right) w\left(N_T - \sum_{i=1}^{n-1} m_i, N_S - \sum_{i=1}^{n-1} s_i\right) \\ \times \prod_{j=1}^{n-1} C\left(\sum_{j'=1}^{j} s_{j'}, s_j\right) \prod_{i=1}^{n-1} w(m_i, s_i) . \qquad (2.1.8) \end{aligned}$$

Summing over all relevant values of $\{s_i\}$ we obtain

$$\begin{aligned} \bar{w}(\{m_i\}, N_T, N_S) = \sum_{s_1=0}^{\min(m_1, N_S)} \sum_{s_2=0}^{\min(m_2, N_S - s_1)} \cdots \\ \sum_{s_{n-1}=0}^{\min(m_{n-1}, N_S - s_1 - \dots - s_{n-2})} P_a(\{m_i\}, \{s_i\}, N_S, N_T). \end{aligned}$$

Since all states with the same $\{m_i\}$, N_T and N_S will have the same free energy

$$\mathcal{F}(\{m_i\}, N_T, N_S) = -\sum_{i=1}^{n-1} E_i m_i - E_n \left(N_T - \sum_{i=1}^{n-1} m_i\right) + \mu_S \widetilde{S}(N_T, N_S) , \quad (2.1.9)$$

defining $\bar{Z}(\{m_i\}, N_S, N_T)$ in a similar way to equation (2.1.7) eventually leads to

$$Z(N_T, N_S) = \sum_{m_1=0}^{N_T} \sum_{m_2=0}^{N_T-m_1} \cdots \sum_{m_{n-1}=0}^{N_T-m_1-\ldots-m_{n-2}} \bar{Z}(\{m_i\}, N_T, N_S) \ . \tag{2.1.10}$$

Finally we define $F(N_T, N_S)$ as the two-dimensional free energy landscape taking into account all the different combinations

$$F(N_T, N_S) = -\ln\left[Z(N_T, N_S)\right] + \ln\left[Z(1,1)\right] \ , \tag{2.1.11}$$

with $\ln\left[Z(1,1)\right]$ acting as a normalisation term, which ensures that $F(1,1) = 0$. We project the two-dimensional landscape $F(N_T, N_S)$ to a one-dimensional landscape $F(N_T)$, by summing $Z(N_T, N_S)$ over the stems, N_S, which implies that the free energy is dominated by the most favourable states, thus

$$Z(N_T) = \sum_{N_S=1}^{N_T} Z(N_T, N_S) \ , \text{ hence } F(N_T) = -\ln\left[Z(N_T)\right] + \ln\left[Z(1)\right] \ . \tag{2.1.12}$$

2.1.4 Concentration of attaching stems

We need to investigate the effect of the concentration of each species in the polymer melt, on the free energy $\mathcal{F}$ of a particular arrangement. The impact of concentration is only felt when an additional stem is added to the nucleus. If we lengthen an existing stem, the concentration is taken to be 100%. As we are effectively zipping-up the chain connected to the segment already attached to the crystal. Appendix A sets out an argument of the effect on the free energy of adding a stem in a simple system, showing the cost of adding a stem of concentration ϕ_i is $-\ln\phi_i$. We generalise that argument to n species of monomer with different concentrations and obtain a new formula for the free energy of an individual state to replace equation (2.1.9)

$$\begin{aligned} \mathcal{F}(\{m_i\}, \{s_i\}, \{\phi_i\}, N_T, N_S) = & -\sum_{i=1}^{n-1} E_i m_i - E_n \left(N_T - \sum_{i=1}^{n-1} m_i\right) \\ & + \mu_{\mathrm{S}} \widetilde{S}(N_T, N_S) - \sum_{i=1}^{N-1} s_i \log\phi_i \\ & - \left(N_S - \sum_{i=1}^{n-1} s_i\right) \log\phi_n \ , \end{aligned} \tag{2.1.13}$$

which now must include the specific number of stems for each species $\{s_i\}$ and where $\{\phi_i\}$ is set of concentrations for species $1 \leq i \leq n$ in the melt. The first two terms in equation (2.1.13) are bulk volume reductions, the third is a cost due to the surface area and the final two are the costs due to concentrations of attaching species through stem addition.

To summarise, we have presented a detailed combinatorial calculation to determine free energy landscapes to nucleation. We simplified a complicated problem by dividing the different species and counted the number of arrangements of each separately. To combine the independent sets, we used a shuffling term (2.1.4). Finally, we projected this multi-dimensional system onto a one-dimensional energy landscape in equation (2.1.12) with the sole parameter being the nucleus size. Due to the nested sums throughout, it is expensive to calculate energy landscapes for large nuclei size, N_T, especially for a large number of species, n. However unlike the simulation [21], the cost of the analytic calculation does not increase with the height of the nucleation barrier.

2.2 Results

Our first result confirms that the calculation predicts the simulated free energy landscape [21]. We use the GO simulation algorithm to sample the free energy landscape for a single nucleus. We do this through a single long run in which we prevent growth beyond some maximum N_T. The simulation produces a landscape by logging the fraction of time spent with each number of total monomers, N_T. The fraction of time spent with N_T monomers t_{N_T}/t_{total} is proportional to the Boltzmann factor of ΔF_{sim},

$$\frac{t_{N_T}}{t_{\text{total}}} = A \exp\big(-\Delta F_{\text{sim}}(N_T)\big) \ ,$$

with A being a normalisation constant, which we set so that $\Delta F_{\text{sim}}(1) = 0$ and rearrange the equation to recover ΔF_{sim}, which corresponds to $F(N_T)$ in the analytic calculation. Figure 2.1 shows the one-dimensional free energy landscape for both simulation data and our analytic calculation for two species with test parameters $E_1 = 1.9$, $E_2 = 1.6$, and $\mu_{\text{S}} = 1.8$, both species having the same concentration, $\phi_1 = \phi_2 = 0.5$ chosen so such that both simulation and calculation are practical. The clear agreement indicates that the simulation algorithm and calculation are consistent, providing confirmation that both are correct. After validating our calculation in this test case, we apply it to investigate the effect of stretching polymer chains on nucleation rates. Beginning by focusing on monodisperse melts in section 2.2.1, and in section 2.2.2 we explore bimodal blends.

2.2.1 Nucleation rates for stretched polymers

We now compare our analytic calculations with energy landscapes and nucleation rates from direct simulations of the GO simulation algorithm for stretched polymers. These are direct simulation results for the first passage time over a quasi-static barrier, which has been shown to be equivalent to full transient data [22].

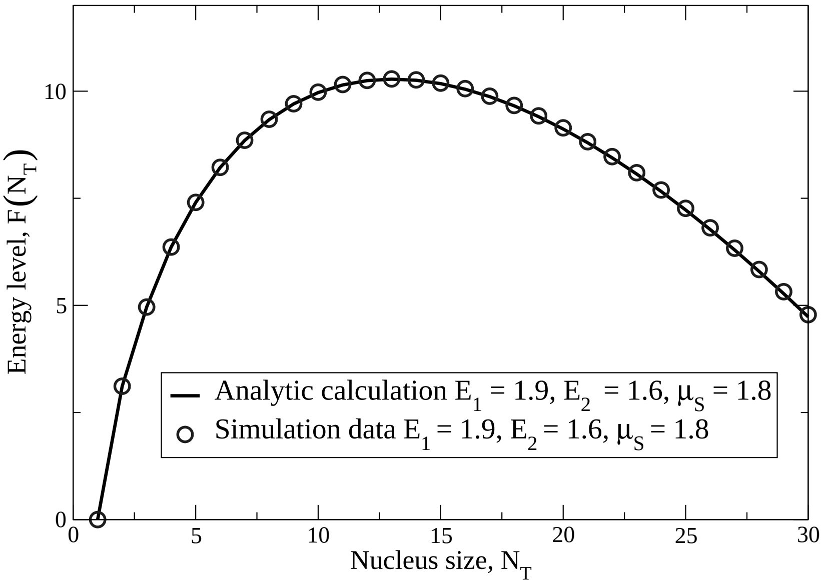

Figure 2.1: Free energy landscape with two species, calculated and simulated data shown.

We use the GLaMM model to produce the tangent vector correlation functions $\mathbf{f}_i$, at first setting the model to a uniaxial extension rate, $\dot{\epsilon} = 0.1/\tau_e$. We choose this extension rate because it produces a wide range of stretch values during a transient flow. Each chain has $Z = 25$ entanglement points, giving 26 entanglement segments. However, we take advantage of the inbuilt head to tail symmetry of all the chains to halve the number of species. Thus we have a total of $n = 13$ different species. The concentration of each species is equal because we have a monodisperse melt hence $\phi_i = 2/(Z+1)$. For every entanglement segment or species the GLaMM model computes $\mathbf{f}_i$, from which we can obtain the elastic free energy ΔF_i^{el} from equation (1.6.37). Therefore the free energy change due to the attachment of a monomer of species i is given by equation (2.0.1). These are put into equation (2.1.13), which eventually provides the energy landscape $F(N_T)$. Figure 2.2 shows simulated and calculated nucleation free energy landscapes at different stretch values, λ, defined by equation (1.6.37). Here we take $E_0 = 1.9$ and $\mu_S = 1.9$ and generate simulated landscapes in the same way as for the quiescent case. This plot shows the agreement between the analytic and simulated results and that the nucleation barrier decreases as the total stretch increases.

Using our calculated free energy landscape, we estimate the average nucleation time by assuming it to be dominated by the height of the barrier. We expect this to hold for barriers with a relatively small critical nucleus size, N_T^*, and a sufficiently high maximum, $F(N_T^*)$, since in this situation the shape of the barrier has little effect on the nucleation time. Nucleation over a fixed barrier, is exponentially distributed, i.e. the probability of crossing is fixed in

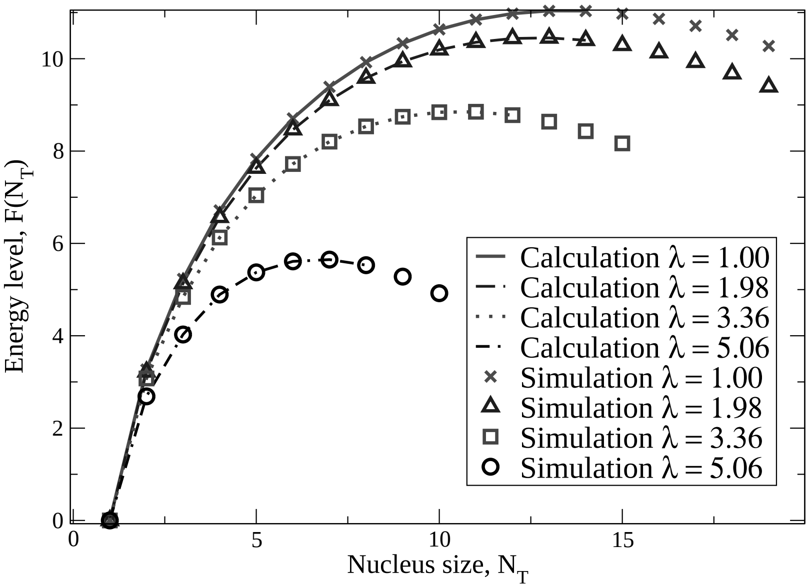

Figure 2.2: Nucleation landscapes for different values of stretch, λ, both analytic and simulation data are shown.

time, so we can take the nucleation rate, N_R, to be the inverse of the average nucleation time, or

$$N_R \approx \frac{1}{\tau_0} \exp\Big\{ - F(N_T^*)\Big\} \ . \tag{2.2.1}$$

Our calculation produces an energy landscape and uses equation (2.2.1) to find the nucleation rate.

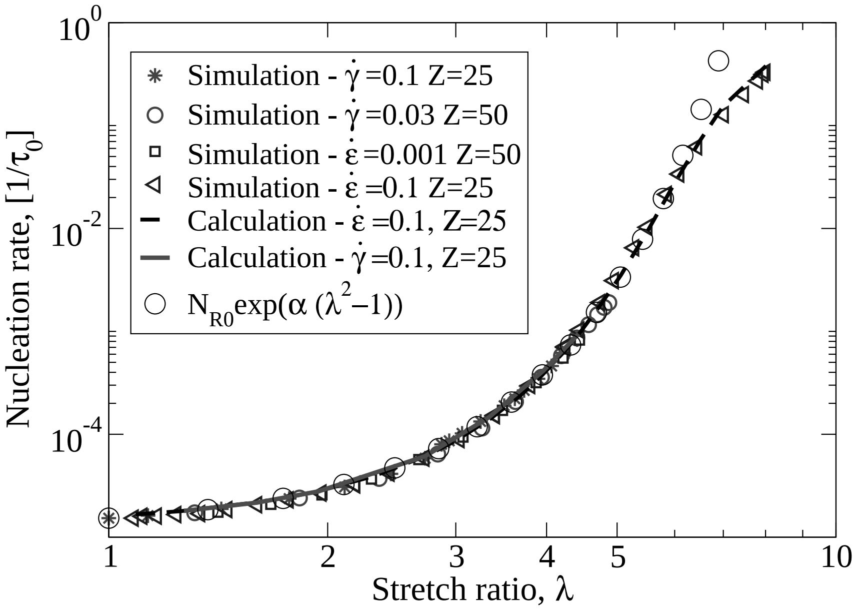

Figure 2.3: Master Curve: the nucleation rate in units of $1/\tau_0$ is plotted against stretch ratio, λ, for various flow geometries with rates in units of $1/\tau_e$, and entanglement segments, Z.

Figure 2.3 is a plot of the nucleation rate against total stretch, λ. At a shear rate of $\dot{\gamma} = 0.1/\tau_e$ the GLaMM model achieves a maximum stretch of $\lambda = 4.4$. For extension, on the other hand, the stretch keeps increasing with time, getting close to the maximum value of $\sqrt{N_e}$ (as the chains have finite length) hence we obtain nearly a full selection of stretch values to calculate nucleation rates. We use both shear and extension to confirm the universality of the master curve. This plot confirms that our analytic approach successfully predicts the master curve behaviour. The different calculated lines sit on top of one another independent of flow history and chain length Z, thus stretch determines the nucleation rate independent of particular flow geometries or chain lengths. This plot shows that nucleation rate has a strong dependence on total stretch, λ. Also included is the empirical fitting function

$$N_R = N_{R0} \exp\left(\alpha(\lambda^2 - 1)\right) , \tag{2.2.2}$$

where N_{R0} is the quiescent nucleation rate. This formula is helpful in summarising the result and in developing simple ODE models of FIC [68]. Both simulated and analytic data deviate slightly from the empirical formula at high stretches. This deviation is most likely due to the stretch approaching the GLaMM model's inbuilt limit of $\sqrt{N_e}$ at which the elastic free energy diverges so the nucleation barrier becomes small. Our analytic result reproduces the master curve to a high degree of precision for both shear and extensional flows.

2.2.2 Bimodal blends

In this section, we present results of bimodal blends. Recent experiments have measured crystallization of polymer blends [5, 13]. Understanding nucleation in bimodal blends is a key stepping stone to polydisperse systems, which can be used to model industrial melts [22]. We take a bimodal blend comprising of short and long linear chains. We assume the short chains remain undeformed under flow, and that long-chain stretching is not strongly affected by the presence of short chains, so we use the GLaMM data for a pure melt of long chains. This assumption is justified as the high stretch suppresses convective constraint release in the long chains. This allows us to focus on the effect of the concentration of long chain molecules in a system with self similar polymer dynamics. An alternative approach would be to use a generalisation of the GLaMM model to bimodal blends as in [69], however, we do not consider this here.

Let $0 \leq \phi \leq 1$ be the volume fraction of long chain molecules in the melt. Under flow, the GLaMM model shows that long chain molecules become stretched particularly in the middle of a chain. However, the end subchain remains unstretched, hence the monomers are effectively of the same species as those in short chain molecules. Therefore the introduction of short chain molecules does not add any additional species into our calculation. The GLaMM model breaks the long chains into $Z+1$ subchains, so the concentration of all species except for the unstretched end species will be $2\phi/\left(Z+1\right)$, due to the natural symmetry. Therefore the concentration of the unstretched species is $1-\phi+2\phi/\left(Z+1\right)$.

To produce figure 2.4, we used the GLaMM model with parameters $E_0 = 1.8$, $\mu_{\mathrm{S}} = 1.9$ and shear rate of $\dot{\gamma} = 0.1/\tau_e$. We have selected a range of concentrations, ϕ, of the long chains within the polymer melt and for each ϕ we have three distinct sets of data. The continuous lines represent the full transient simulations containing a time-dependent nucleation barrier with the nucleation rate calculated as described in [21, 22]. The filled symbols are the quasi-static simulation data produced by freezing the chain configurations at those particular times and simulating nucleation over this fixed barrier. The unfilled symbols are the nucleation times calculated analytically using the same frozen chain configurations.

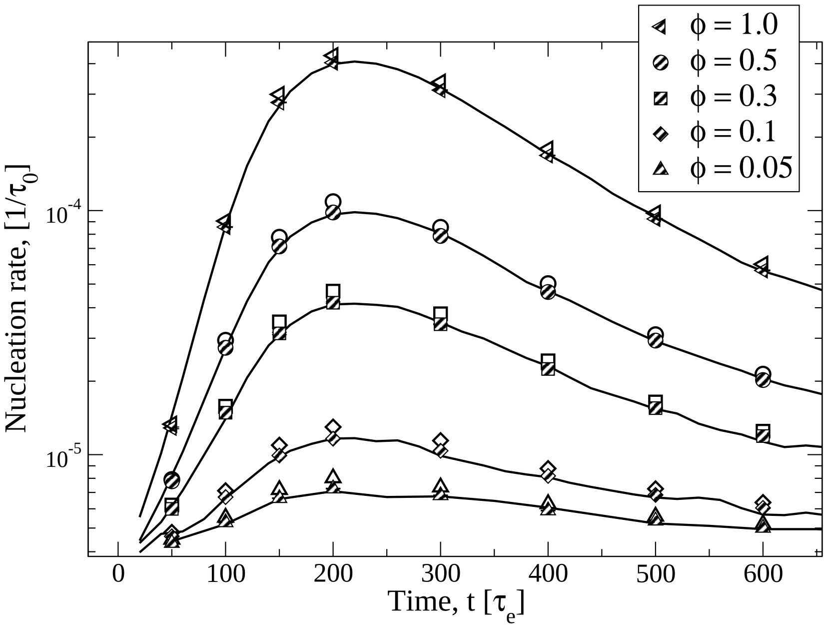

Figure 2.4: Nucleation rate against time for selection of high-molecular-weight concentrations, ϕ. Continuous lines are full transient simulation data, filled symbols are quasi-static simulation data and unfilled symbols are analytic calculations.

The quasi-static result from [22] holds for bimodal blends. The analytic calculation is also close to both the full transient simulation and quasi-static simulations. It is worth noting that the slight discrepancy between the quasi-static simulation and analytic calculations is not due to a difference in the free energy landscapes, in fact they are almost identical, rather, the discrepancy is due to an error in the barrier height approximation (2.2.1) used in the calculation, whereas the simulations provide the first passage time directly. It appears that in a bimodal blend, the route over the nucleation energy landscape is complicated by the many degrees of freedom in which the system can diffuse. This is especially true for a small concentration of long chains. Additionally, figure 2.4 demonstrates a significant rise in the nucleation rate within the first $200\tau_e$ due to the time the chains take to reach full stretch. Experimentally this early time behaviour would be seen as an nucleation induction time [70].

The success of our analytic calculation in matching the full transient simulation gives us confidence to pursue a model for FIC in bimodal blends. We have calculated various nucleation rates and plotted them against stretch for different concentrations, ϕ, of long chain molecules, in this case, we use an extensional flow with a rate of $\dot{\epsilon} = 0.1/\tau_e$ and $E_0 = 1.8$, $\mu_{\mathrm{S}} = 1.9$, as shown in figure 2.5. To check the universality of the master curve for blends, we have overlaid the calculation data from figure 2.4 which uses shear to deform the chains at a rate of $\dot{\gamma} = 0.1/\tau_e$ and both sets indeed lie on the same curve for each concentration. The line $\phi = 0$ refers to a melt of only short chain molecules, which remain unaffected by the application of flow, therefore the quiescent nucleation rate is constant ($N_{R0} \approx 4 \times 10^{-6}/\tau_0$).

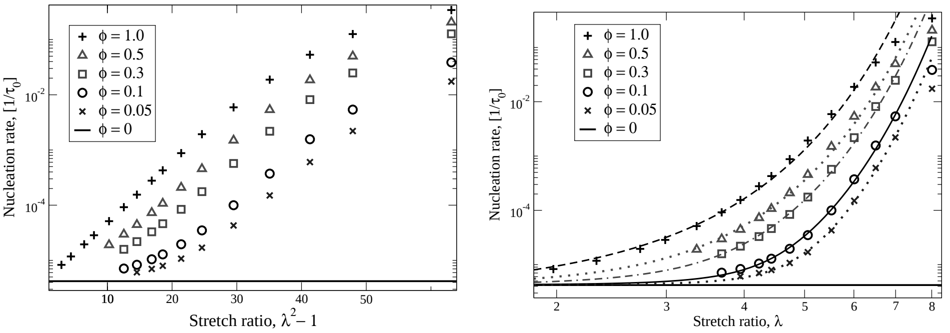

(a) (b)

Figure 2.5: (a) Nucleation rate plotted against scaled high-molecular-weight chain stretch ratio, λ, with a range of concentrations, ϕ; stretch ratio axis is transformed from λ to $\lambda^2 - 1$. (b) Nucleation rate plotted against stretch ratio, λ, data is plotted on a log-log scale, and in addition we have included lines using the formula (2.2.3), empirically fitted for each concentration.

We have already demonstrated that under appropriate conditions, the nucleation rate depends on stretch as in equation (2.2.2); this master curve shown in figure 2.3. Hence we first present our results with the λ-axis transformed to $\lambda^2 - 1$, and nucleation rate logarithmically scaled, as shown in figure 2.5(a). The different concentration curves are parallel at moderately large values of λ, provided that nucleation rate is slow enough such that the barrier height approximation holds, that is, $N_{R0} < N_R \ll 1$. This parallel property indicates we can fit our data with $\exp\big(\alpha(\lambda^2-1)\big)$. Reverting our calculated data back to nucleation rate against stretch ratio, λ, shown in figure 2.5(b). The exponential curves appear to spring out of the quiescent rate, N_{R0}, but we must also ensure that $N_R = N_{R0}$ when $\lambda = 1$. Hence we empirically fit the curves of the different concentrations, ϕ, in figure 2.5(b) with a simple formula that contains the correct asymptotics, namely

$$N_R = N_{R0} - \beta\Big(1 - \exp\big(\alpha(\lambda^2-1)\big)\Big)\ , \tag{2.2.3}$$

where α relates to the shape and β controls the λ-value where the curve begins to deviate from the base rate, and the quiescent nucleation rate is N_{R0}. For dominating concentrations of long chains $\phi \approx 1$, then $\beta \approx N_{R0}$ and the equation reverts back to (2.2.2). The results of applying the fitting formula (2.2.3) to figure 2.5(b) are of particular interest. The parameter, α, remains constant which is why all curves have similar shapes ($\alpha \approx 0.22$ in this case). On the other hand for lower concentrations, the parameter β shows a clear power law dependence on ϕ, and in this particular case can be represented by $\beta(\phi) = 4.82 \times 10^{-6}\phi^{1.45}/\tau_0$.

2.3 Discussion

We present an analytic calculation that supports the GO kinetic Monte Carlo simulation [21, 22]. Through the use of combinatorics we have successfully calculated the number of arrangements of a particular crystal. Our main result is that the analytic calculations accurately predict simulated nucleation times and are especially useful for high energy barriers that are difficult to simulate. We have also confirmed the universal master curve presented in figure 2.3, this shows that the nucleation rate has a clear dependence on the stretch of the attaching polymer chains. The empirical model (2.2.2) which is independent of molecular weight and flow geometry will be useful in developing a simple model of FIC. Although our calculation determines exact energy landscapes, due to the nested summations its scope is severely limited. To calculate energy landcspes for a large number of species only the base is practically attainable. For this reason, in the remainder of the thesis, we use the GO model to simulate the energy barriers as required. However, the analytic calculation is a useful tool for adapting and testing the main simulation algorithm. It has proven to be extremely helpful to ensure the algorithm is correct, particularly when executing alterations. One specific element was the procedure the algorithm employs for stem removal moves, here the comparison was essential to guarantee detailed balance is correctly obeyed.

We also analysed bimodal blends containing long and short linear chains. Investigating the effect of the concentration of the long chains within the polymer melt. We added an extra parameter, β, to our empirical description of the master curve to produce equation (2.2.3). We have shown that β depends on concentration through a power law relationship, this result might be experimentally testable. In this chapter we approximated the nucleation rate using solely the dominating barrier height (2.2.1). However, in chapter 4 a more accurate calculation involving a prefactor that considers the shape of the landscape as well is developed. Additionally, the calculation is computationally expensive for large nuclei, so finding an approximation would be beneficial. We note that the output from the GLaMM model is averaged over many chains, and rare occurrences of significantly stretched chains may potentially have a strong influence on nucleation. However, the nucleation algorithm and our analytic results could readily incorporate data from a more detailed flow model that resolves these rare stretching events.

Chapter 3

One-dimensional projection for complex barrier crossing problems

In this chapter we derive a technique to project complex multi-dimensional barrier crossing problems onto solvable one-dimensional systems. This technique comprises of obtaining important kinetic information from non-equilibrium simulations. We also require the associated equilibrium energy landscapes, which together with the kinetic information, enables us to suggest one-dimensional systems with equivalent crossing properties to the full multi-dimensional simulations.

We anticipate that our method will be useful to a broad range of barrier crossing problems, examples include nucleation [37], entangled polymer dynamics [71], and protein folding [72]. As we will discuss, our technique does require certain conditions, the equilibrium energy barrier must be the dominant influence on the crossing process, which must occur through a series of unlikely incremental steps. Therefore the method may not be suited to problems with strong kinetic influences or processes that take large jumps, bypassing certain stages. There are several examples of techniques to investigate both non-equilibrium and equilibrium simulations for molecular systems in general; these include transition path sampling [56], which uses importance sampling to sample the space of trajectories that cross the barrier, trajectory parallelisation and tilting [73], milestoning [57], Markov models [58], and forward flux sampling [60]. Clearly a suitable one-dimensional order parameter must be selected, and it is essential that it appropriately describes progress over the barrier. For new problems, this will require a certain insight and intuition into that particular area. However, there are numerous examples where suitable order parameters have been found [57, 58, 60, 74].

In section 3.1, we present our one-dimensional barrier crossing model and projection technique. The method includes extracting crucial kinetic information, which we describe as effective rate kinetics because they help produce an equivalent one-dimensional system together with the equilibrium energy barrier. We initially describe a simple way of finding the rate kinetics directly from non-equilibrium systems. However we believe it is useful and sometimes advantageous to be able to produce rate kinetics that relate to the equilibrium energy barrier. We outline two approaches with the equilibrium information to obtain these rate kinetics from simulations, the first is a simple method for within the Boltzmann region of an energy landscape. In addition, we present our main algorithm which is applicable throughout an entire barrier. These rate kinetics could give a new perspective to complex simulations, revealing hidden patterns of the dominant pathways used to traverse non-equilibrium barriers. In section 3.2, we apply these rate kinetics extraction techniques to the GO polymer nucleation simulation [21, 22], see section 1.6.3 for full details. Our one-dimensional projection technique and thorough analysis of the rate kinetics produced by the GO model has been published [75].

3.1 One-dimensional barrier crossing model

The aim of this section is to find a systematic method to project complex multi-dimensional barrier crossing problems onto suitable one-dimensional systems. We assume the problem contains a convenient order parameter that describes progress over the energy barrier. The selection of such a parameter will require particular knowledge and insight into the specific problem of interest. We also assume this order parameter takes discrete values, however our method can be applied to continuous order parameters by dividing the range into appropriate discrete bins. Additionally, we presuppose the system only allows moves to adjacent states on the one-dimensional projection. Figure 3.1 displays the one-dimensional projection in terms of nucleation from the GO model, all microstates with the same volume are merged into new combined states, as shown by the dashed boxes in the diagram. Once a valid projection is performed, the resulting one-dimensional system can be solved analytically (see chapter 4).

Barrier crossing problems by definition must be outside of equilibrium, as there has to be a non-zero net flux, J, across the system. Given a suitable one-dimensional order parameter, most non-equilibrium or driven simulations will be easily able to measure the following quantities for each state i. These are the rate of forward and backward moves, k_i^+ and k_i^- respectively, as well as the occupancy, χ_i, which are related through this discrete flux equation

$$J = k_i^+ \chi_i - k_{i+1}^- \chi_{i+1} \ . \tag{3.1.1}$$

The flux and the occupancies should be simple to record, the respective rates can be obtained by counting the number of moves, m_i^+ and m_i^-, in both direc-

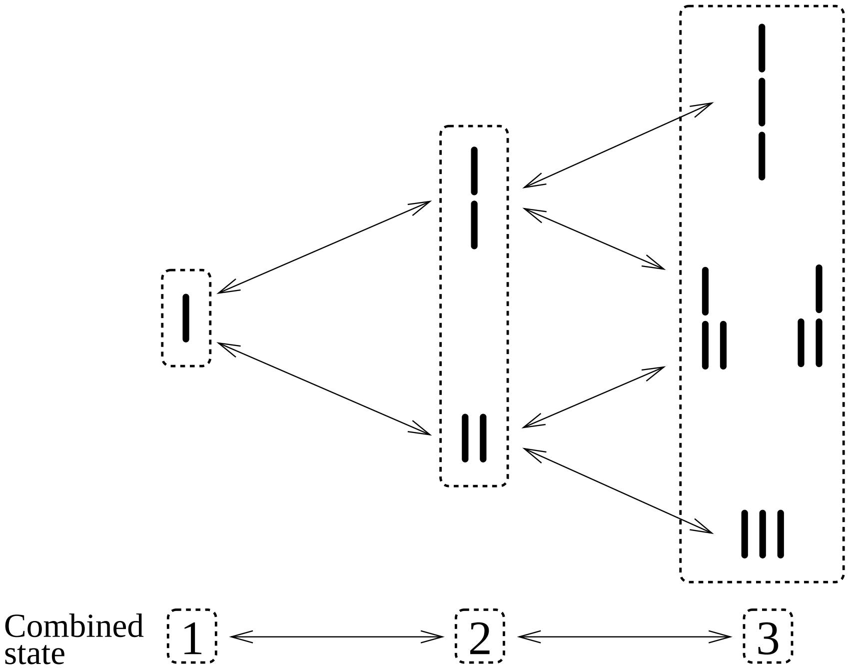

Figure 3.1: This diagram shows a suitable one-dimensional projection for nucleation using the GO model. The microstates are grouped by nucleus size (dashed boxes), and the arrows correspond to specific attachment and detachment moves between microstates.

tions from state i. The rates can then be calculated with

$$k_i^+ = \frac{m_i^+}{\chi_i T_{\text{sim}}} \text{ and } k_i^- = \frac{m_i^-}{\chi_i T_{\text{sim}}} , \tag{3.1.2}$$

where the amount of time that the system spends in each state which is $\chi_i T_{\text{sim}}$ and T_{sim} is the total simulation time.

In section 3.1.1 we introduce two rival rate kinetics extraction schemes for non-equilibrium barrier crossing problems. We discuss the overall generality of our one-dimensional projection and rate kinetics extraction techniques in section 3.1.2, and also produce a set of clear guidelines to which types of barrier crossing problems the method should be applicable.

3.1.1 Rate kinetics extraction techniques

In this section we compare and contrast two rival rate kinetics extraction techniques, the first directly measures the rate kinetics from non-equilibrium systems in section 3.1.1.1. We also present two different techniques that relate the important equilibrium barrier to particular non-equilibrium problems in section 3.1.1.2. We thoroughly evaluate these two techniques in a simple multi-route example in section 3.1.1.3.

In our extraction techniques we seek to chose the one-dimensional quantities A_i and F_i, which are related to the one-dimensiomal rates via

$$k_i^+ = A_i \min\left(1, \exp(-(F_{i+1} - F_i))\right) \ , \tag{3.1.3a}$$

$$k_{i+1}^- = A_i \min\left(1, \exp(F_i - F_{i+1})\right) \ , \tag{3.1.3b}$$

where $k_i^{+/-}$ is for the forward or backward move out of state i. The choice of A_i and F_i should give the correct crossing rate from the high-dimensional non-equilibrium simulation and match as closely as possible the other properties of this simulation. The overall aim is for patterns to emerge in A_i and F_i, as the model parameters for the high-dimensional simulation are varied, which will enable prediction of the simulation crossing rate as a function of the model parameters.

3.1.1.1 Technique 1: Direct measurement from non-equilibrium systems

First we measure the one-dimensional forward and backward rates across the boundary between two adjacent states using a high-dimensional non-equilibrium simulation. This defines the one-dimensional rates k_i^+ and k_i^- for each state, via equations (3.1.2). We then seek the one-dimensional model parameters A_i and F_i. From equation (3.1.3) we can see that the favourable (downhill) move from the pair k_i^+ and k_i^- has rate A_i. Thus

$$A_i^{\mathrm{M}} = \max\left(k_i^+, k_{i+1}^-\right) \ . \tag{3.1.4}$$

We can now obtain the barrier F_i from detailed balance, since

$$F_{i+1}^{\mathrm{M}} - F_i^{\mathrm{M}} = \ln\left(\frac{k_{i+1}^-}{k_i^+}\right) \ . \tag{3.1.5}$$

We note that this new barrier may well be different to the equilibrium barrier due to non-Boltzmann occupancy of the microstates in the multi-dimensional non-equilibrium simulation. These one-dimensional quantities are labelled with superscript M to clarify these have been found through direct measurement from a multi-dimensional system. However these rate kinetics are deeply connected to the non-equilibrium occupancies, and are difficult to analyse and find patterns in relation to other systems. Furthermore, the non-equilibrium energy landscape might be challenging to calculate or predict as the model parameters are modified. We apply this technique to a simple multi-route example in section 3.1.1.3 and discuss the resulting rate kinetics.

3.1.1.2 Technique 2: Extraction in relation to equilibrium barrier

In many systems the equilibrium energy barrier where no net flux is enforced, is of great importance and usually dominates the crossing time for the non-equilibrium problems, and it is also independent in regard to rate kinetics. This equilibrium energy landscape, F_i, has an associated equilibrium occupancy, Q_i, for each state defined by

$$Q_i = \frac{1}{Z_p} \exp\left(-F_i\right) \ , \tag{3.1.6}$$

where $Z_p = \sum_i \exp\left(-F_i\right)$ is the normalising partition function. To include extra information from the equilibrium system, it is necessary to neglect information from the complete non-equilibrium problem in equation (3.1.1). We decide to ignore the forward and backward rates, and hold onto the overall crossing rate, J, as well as the occupancies, χ_i. Creating new effective forward and backward rates that are now based on the equilibrium system, with one vital assumption to complete the solution, that our new set of rates obey detailed balance in respect to the equilibrium occupancies, hence

$$Q_i k_i^+ = Q_{i+1} k_{i+1}^- \ . \tag{3.1.7}$$

Fundamentally, this assumption implies that whilst in non-equilibrium, the distribution of occupancies across the microstate within a single state on the one-dimensional projection, must be close to the equilibrium case. This requires the equilibrium energy barrier to have a strong influence on the non-equilibrium system. We stress that the rates k_i are still from the non-equilibrium system.

This assumption enables us to create a one-dimensional system with energy landscape, F_i, and some effective rate kinetics, A_i^{E}. This formulation by construction produces the correct non-equilibrium occupancies and overall crossing rate of the original multi-dimensional system, we use the superscript E to clarify the use of the one-dimensional extraction technique. Note that these rate kinetics for opposite moves must be same, since we require the one-dimensional projection to obey detailed balance. In our new system the rate of forwards and backwards moves are approximated by

$$k_i^+ \approx A_i^{\mathrm{E}} \min\left(1, \frac{Q_{i+1}}{Q_i}\right) = A_i^{\mathrm{E}} \min\Big[1, \exp\Big(-\big(F_{i+1} - F_i\big)\Big)\Big] \ , \tag{3.1.8a}$$

and

$$k_{i+1}^- \approx A_i^{\mathrm{E}} \min\left(1, \frac{Q_i}{Q_{i+1}}\right) = A_i^{\mathrm{E}} \min\Big[1, \exp\Big(F_{i+1} - F_i\Big)\Big] \ . \tag{3.1.8b}$$

Also note that given the constraint that the system obeys detailed balance and only allows moves between adjacent states, then these Metropolis rates fulfill the most general case.

This projection is only one of numerous choices that can be made, any set of rates k_i^+ and k_i^- that obey equation (3.1.1) for all states are strictly valid. We believe the guidance of the equilibrium landscape, enables fair comparison between different parameter sets, at least in some cases. Especially since the equilibrium landscape is independent of rate kinetics. In section 3.1.1.3, we discuss an example problem comparing our method with the direct rate measurements from section 3.1.1.1. In particular, we will show later in this thesis that this one-dimensional projection method, based on the equilibrium barrier, is extremely effective for projecting the GO model on to a one-dimensional problem. This projection reveals a simple pattern in the kinetics A_i in the GO model as the landscape parameters are varied. This pattern enables us to describe the dominant nucleation pathway in this model and, ultimately, produce an analytic model that removes the need to simulate this model in all but the most extreme flow conditions.

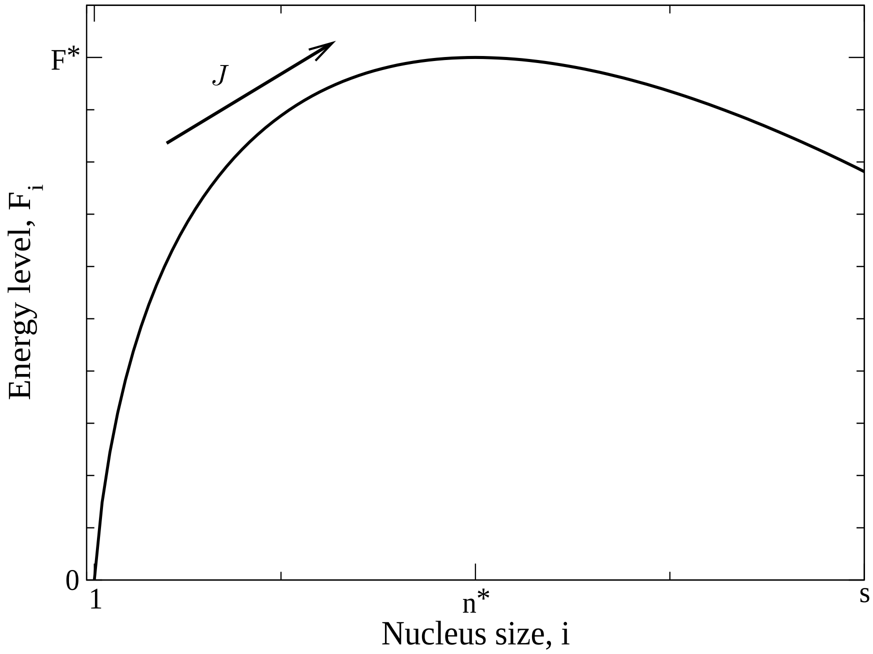

Figure 3.2: This plot shows a typical one-dimensional projected energy landscape, F_i, in terms of nucleation, the order parameter is nucleus size, i, with critical nuclei, n^*, and barrier height F^*. Particles begin at state 1 and nucleate when reaching state s, and hence the system has a net flux J.

As an example, in figure 3.2 we display our one-dimensional projection in terms of nucleation from the GO model, with the order parameter in this case being the nucleus size. Our system begins with a particle in state 1 and it must diffuse over an energy barrier with peak at the critical nucleus, n^*, with barrier height, F^*, to some nucleus size, s, significantly beyond the peak. Crucially, only forwards and backwards moves to the states immediately adjacent are allowed to occur. Once it has reached s, we consider it to have nucleated and another particle is inserted at the base state 1, hence the system has a net flux over the barrier, J.

In this section we present two simple techniques for extracting rate kinetics from a general energy barrier crossing problem. The first method set out in section 3.1.1.2.1 applies only to within the Boltzmann region of an energy landscape. In section 3.1.1.2.2 we introduce an original technique that is applicable throughout the entire landscape, but it is specifically important outside of the Boltzmann region.

3.1.1.2.1 Boltzmann region Within the Boltzmann region, the occupancies of the non-equilibrium system can be considered to be close to the equilibrium occupancies, our one-dimensional projection set-up has forward rates given by

$$k_i^+ \approx A_i^{\mathrm{E}} \min\left(1, \frac{Q_{i+1}}{Q_i}\right) \ ,$$

which can be assumed to be an excellent approximation. We can also obtain the forward rates from equation (3.1.2). With this information we can rearrange the one-dimensional forward rate in equation (3.1.8a), to give the effective rate kinetics as

$$A_i^{\mathrm{E}} \approx \frac{m_i^+}{\chi_i T_{\mathrm{sim}}} \max\left(1, \exp\left(F_{i+1} - F_i\right)\right) \ , \tag{3.1.9}$$

for each state i.

3.1.1.2.2 Approach applicable to the entire landscape Outside of the Boltzmann region, we cannot employ the Boltzmann approximation as the non-equilibrium occupancies are now far away from equilibrium. To find effective rate kinetics we apply the steady state flux equation (3.1.1), together with our detailed balance assertion (3.1.7) and the set of one-dimensional rates given in equations (3.1.8). Combining this information gives us the set of positive moves

$$k_i^+ \approx \frac{J \exp\left(F_i\right)}{\chi_i \exp\left(F_i\right) - \chi_{i+1} \exp\left(F_{i+1}\right)} \ , \tag{3.1.10}$$

and the set of effective rate kinetics

$$A_i^{\mathrm{E}} \approx \frac{J \max\left[\exp\left(F_i\right), \exp\left(F_{i+1}\right)\right]}{\chi_i \exp\left(F_i\right) - \chi_{i+1} \exp\left(F_{i+1}\right)} \ . \tag{3.1.11}$$

By construction the rates in set of equations (3.1.8) along with our effective kinetics produce the correct overall crossing rate. However due to our detailed balance assumption, the effective rate kinetics are only reasonable if the system itself is strongly dominated by the equilibrium barrier. This extraction method is not suited to problems with strong rate kinetics or that contain significant differences between several crossing routes that greatly bias the non-equilibrium occupancies of particular microstates away from the equilibrium energy landscape. This technique is simple to implement, and could potentially reveal important patterns within complex systems. In section 3.1.1.3 we throughly discuss a simple multi-route barrier crossing problem that relates to these recommendations. Since we are primarily interested in barrier crossing problems involving high energy landscapes that vastly dominate crossing times, the method could be extremely useful for these are the type of problems.

3.1.1.3 Simple multi-route barrier crossing example

In this section we investigate the simplest connected system that offers multiple routes over an energy landscape, see figure 3.3. We define the reaction rates between the microstates in terms of their equilibrium occupancies and arbitrarily assign rate kinetics, we ensure they obey detailed balance

$$\begin{aligned}
k_{1,2a} &= A_{1a} \exp\left(-(F_{2a} - F_1)\right) \ , \quad k_{2a,1} = A_{1a} \ , \\
k_{1,2b} &= A_{1b} \exp\left(-(F_{2b} - F_1))\right) \ , \quad k_{2b,1} = A_{1b} \ , \\
k_{2a,3a} &= A_{2a} \exp\left(-(F_{3a} - F_{2a})\right) \ , \\
k_{2a,3b} &= A_{2b} \exp\left(-(F_{3b} - F_{2b})\right) \ . \qquad (3.1.12)
\end{aligned}$$

Note that the system has two separate sinks, states $3a$ and $3b$ with distinct energy levels, so once a particle enters one of the sinks, we re-insert it back into state 1 to form a driven system with net flux, J. This set-up can be easily resolved as we will show, without the need for a one-dimensional projection, however it does demonstrate as well as test our extraction technique.

The analytic steady state solution can be calculated by considering the flux equation for each microstate

$$\begin{aligned}
\dot{\chi_1} &= J - \left(k_{1,2a} + k_{1,2b}\right)\chi_1 + k_{2a,1}\chi_{2a} + k_{2b,1}\chi_{2b} = 0 \ , \\
\dot{\chi_{2a}} &= -\left(k_{2a,1} + k_{2a,3a}\right)\chi_{2a} + k_{1,2a}\chi_1 = 0 \ , \\
\dot{\chi_{2b}} &= -\left(k_{2b,1} + k_{2b,3b}\right)\chi_{2b} + k_{1,2b}\chi_1 = 0 \ ,
\end{aligned}$$

together with the total occupancy of the system being normalised with $\chi_1 + \chi_{2a} + \chi_{2b} = 1$. This gives the following steady state occupancies

$$\begin{aligned}
\chi_1 &= \frac{J}{k_{1,2a} + k_{1,2b} - \frac{k_{1,2a}k_{2a,1}}{k_{2a,1}+k_{2a,3a}} - \frac{k_{1,2b}k_{2b,1}}{k_{2b,1}+k_{2b,3b}}} \ , \\
\chi_{2a} &= \chi_1 \frac{k_{1,2a}}{k_{2a,1} + k_{2a,3a}} \ , \ \chi_{2b} = \chi_1 \frac{k_{1,2b}}{k_{2b,1} + k_{2b,3b}} \ ,
\end{aligned}$$

which produces the overall net flux

$$J = \frac{k_{1,2a} + k_{1,2b} - \frac{k_{1,2a}k_{2a,1}}{k_{2a,1}+k_{2a,3a}} - \frac{k_{1,2b}k_{2b,1}}{k_{2b,1}+k_{2b,3b}}}{1 + \frac{k_{1,2a}}{k_{2a,1}+k_{2a,3a}} + \frac{k_{1,2b}}{k_{2b,1}+k_{2b,3b}}} \ . \qquad (3.1.13)$$

We perform the projection to a one-dimensional parameter by merging states into $A = \{1\}$, $B = \{2a, 2b\}$, and $C = \{3a, 3b\}$ as shown by figure 3.3 with occupancies $\chi_A = \chi_1$ and $\chi_B = \chi_{2a} + \chi_{2b}$. We can calculate the move rates between the new merged states by considering the relative occupancies of the microstates, hence

$$k^{\mathrm{M}}_{A,B} = k_{1,2a} + k_{1,2b} \ , \qquad (3.1.14a)$$

$$k^{\mathrm{M}}_{B,A} = k_{2a,1}\frac{\chi_{2a}}{\chi_{2a} + \chi_{2b}} + k_{2b,1}\frac{\chi_{2b}}{\chi_{2a} + \chi_{2b}} \ , \qquad (3.1.14b)$$

$$k^{\mathrm{M}}_{B,C} = k_{2a,3a}\frac{\chi_{2a}}{\chi_{2a} + \chi_{2b}} + k_{2b,3b}\frac{\chi_{2b}}{\chi_{2a} + \chi_{2b}} \ . \qquad (3.1.14c)$$

We study this example system by fixing the equilibrium landscape with arbitrarily chosen values

$$F_1 = 0 \ , \ \ F_{2a} = 1 \ , \ \ F_{2b} = 2 \ , \ \ F_{3a} = 2 \ , \ \ F_{3b} = 4 \ ,$$

we can then explore alterations in the four rate kinetics A_i to manipulate the set-up. This system has two pathways to escape, in terms of the landscape the favourable route is from $1 \to 2a \to 3a$, labelled route a, as opposed to $1 \to 2b \to 3b$, labelled route b.

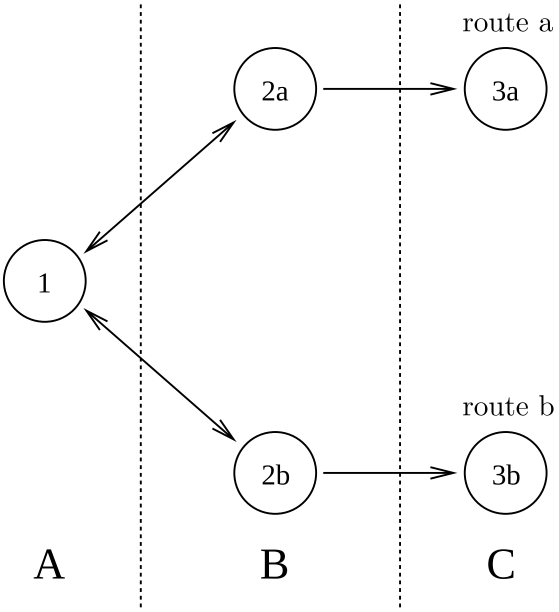

Figure 3.3: This simple diagram shows the layout of our simple multi-route example, displaying the available moves from each microstate. Particles enter system at state 1 and through two different pathways labelled route a and route b can leave the system at one of two sinks in states $3a$ and $3b$.

We investigate eight different sets of microstate rate kinetics to find how they affect the non-equilibrium simulation, and present our results in table 3.1. The overall average crossing time, $\langle\tau\rangle$ or $(1/J)$, and the merged rates of the one-dimensional projection $k^{\mathrm{M}}_{A,B}$, $k^{\mathrm{M}}_{B,A}$ were calculated from equations (3.1.14), and the rate kinetics A^{M}_{A} were then taken from equation (3.1.4), these values could have easily been taken directly from a multi-dimensional simulation.

On the other hand, we use the one-dimensional extraction technique holding just the occupancies for the merged states χ_A and χ_B, together with the flux J and information pertaining to the known equilibrium barrier. To find the rates $k^{\mathrm{E}}_{A,B}$ and $k^{\mathrm{E}}_{B,A}$, which are calculated from equation (3.1.10) along with our imposed detailed balance restriction from equation (3.1.7). For the rate kinetics, we use equation (3.1.11) to find an effective A^{E}_{A} and A^{E}_{B}, although for the latter we must slightly alter the approach since it is connected to the sink

Row	Rate kinetics				$\langle\tau\rangle$	Non-equilibrium measured			One-dimensional extraction			
	A_{1a}	A_{1b}	A_{2a}	A_{2b}	$(1/J)$	$k^{\mathrm{M}}_{A,B}$	$k^{\mathrm{M}}_{B,A}$	A^{M}_{A}	$k^{\mathrm{E}}_{A,B}$	$k^{\mathrm{E}}_{B,A}$	A^{E}_{A}	A^{E}_{B}
1	1	1	1	1	12.1	0.503	1	1	0.503	1	1	0.971
2	1	1	2	2	7.14	0.503	1	1	0.503	1	1	1.90
3	2	1	2	1	6.48	0.871	1.69	1.69	0.936	1.86	1.86	1.81
4	1	2	1	2	10.6	0.639	1.31	1.31	0.574	1.14	1.14	1.11
5	1	1	1	0	14.2	0.503	1	1	0.503	1	1	0.801
6	1	1	0	1	92.2	0.503	1	1	0.503	1	1	0.108
7	1	100	1	0	14.2	13.9	34.1	34.1	0.503	1	1	0.801
8	100	1	0	1	92.2	36.9	75.8	75.8	0.503	1	1	0.108

Table 3.1: Results from the example system, we display eight different sets of microstate kinetics that produce a net flux, J, with the rates $k^{\mathrm{M}}_{A,B}$, $k^{\mathrm{M}}_{B,A}$ and rate kinetics A^{M}_{A} calculated directly from the complete system with equations (3.1.14) and (3.1.4). As well as showing the rates $k^{\mathrm{E}}_{A,B}$, $k^{\mathrm{E}}_{B,A}$ and kinetics A^{E}_{A}, A^{E}_{B} using the one-dimensional projection and extraction technique with equations (3.1.10) and (3.1.11).

state C and there is no occupancy χ_C, hence directly from equation (3.1.1) we have $k^{\mathrm{E}}_{B,C} = J/\chi_B$. This also means there is no equivalent quantity available to be measured in the full system.

From table 3.1 we were are able to make a qualitative assessment of the success of the two rival techniques for different multi-dimensional systems. This provides examples of the general circumstances where one choice is preferable to the other. The manually chosen individual kinetic values for each move in the multi-dimensional system are displayed the “Rate kinetics” block. In the non-equilibrium measured approach A^{M}_{A} relates to A_{1a} and A_{1b}. In the extraction technique, A^{E}_{A} relates to A_{1a} and A_{1b}, and A^{E}_{B} relates to A_{2a} and A_{2b}. There are some clear instances where one or other of the methods is superior, as we describe below.

Prior to analysing the one-dimensional projection and rate kinetics extraction technique, we describe key observations from the complete system. The first, is that this example system has been designed to be small, so an analytic solution is practically available. In fact, the particle can escape in as few as two moves, which produces fast average crossing times and the system is subject to a large flux, J. The one-dimensional extraction technique is aimed at larger, complex systems with high energy barriers that produce rare crossing events, hence slow average crossing times and extremely small fluxes, so this example problem is far from ideal. However, the results are fascinating, and display scenarios which favour direct measurements over our extraction technique and vice versa.

The sets in rows 1 and 2 provide perfectly equal kinetics along the two routes, this ensures the non-equilibrium balance between microstate occupancies within state B is the same as the equilibrium version. This results in the one-dimensional extraction finding $k^{\mathrm{E}}_{A,B}$ and $k^{\mathrm{E}}_{B,A}$ exactly, and hence A^{E}_{A} is the same as A^{M}_{A}. However in finding A^{E}_{B}, multi-dimensional information has been lost in the projection using the equilibrium energy barrier for end state C, the rate kinetics are consequentially altered to produce the correct crossing rate, and although the values are close to expectation, there is a slight error.

The sets in rows 3 and 4, contain a disparity in kinetics between the pathways, row 3 provides faster kinetics for route a, whereas row 4 favours route b. The effective rate kinetics are unknown as we discussed earlier but they are certain to be in the range $1 < A < 2$ and the values are expected to be closer to the kinetics of the energetically dominating route a. Both the direct measurement and one-dimensional extraction approaches fit this criteria and are certainly plausible. However the disparity in rate kinetics between the different routes is large, and this has a significant effect on crossing times for the two sets. Hence the kinetics may be reducing the influence of the equilibrium barrier, which suggests the extraction technique may contain errors. Even so the value of A^{E}_{A} is a reasonable estimate in comparison with A^{M}_{A} for such an extreme system.

For the final four sets shown in table 3.1, we introduce particularly artificial rate kinetics, by placing a block on one of the available routes. In row 5 we block route b by having $A_{2b} = 0$, and in row 6 we block route a by including $A_{2a} = 0$. If the system had uniform kinetics the more influential barrier to the system would be via route a, so the kinetics in row 5 does change the dynamics but the equilibrium barrier is still a reasonable description. The extracted value of A^{E}_{B} is a reasonable estimate given the artificial change in rate kinetics. However, for row 6 the block is placed on the dominating route, then the equilibrium barrier no longer even closely resembles this system, hence the extraction technique produces a nonsensical value for A^{E}_{B}.

For the final two sets in rows 7 and 8, we manipulate the kinetics further by giving the blocked route extremely fast kinetics to and from state 1. These fast kinetics have no impact on the crossing rate, since the only available routes remains the same as previous sets. They do however have a huge influence on the measured rates $k^{\mathrm{M}}_{A,B}$ and $k^{\mathrm{M}}_{B,A}$ for the non-equilibrium system. On the other hand, the one-dimensional extraction technique which only considers the occupancy of the merged states, is unaware of these fast kinetics since they do not affect the crossing time. This is one scenario where our extraction technique is superior in describing the relevant system, as opposed to the measured forward and backwards rates at each state.

3.1.2 Generality and applicability discussion

Our one-dimensional rate kinetics extraction technique is a worthwhile tool and applicable to a large scope of barrier crossing problems. It requires a well chosen order parameter that appropriately describes progress along such barriers. As well as a suitable discretisation into distinct states, with incremental steps between adjacent states being the dominating mechanism to succeed. The equilibrium energy barrier must also be relevant to the crossing problem, as the technique is not appropriate when kinetic contributions dominate the barrier crossing process through energetically unfavourable routes. These cases can be observed as they will have a clear signature of failure, as the kinetics will depend strongly on the barrier characteristics. However, since kinetic terms are logarithmically weak in comparison to energetic effects, this one-dimensional extraction technique could be useful to many systems. Promising candidates that obey these constraints are nucleation problems at low undercooling and spatial diffusion problems, for example the relaxation of star arms in branched polymers [39, 71]. However, we realise that the technique is not suited towards problems which include significant large jumps, bypassing several states at once. Possible examples include nucleation processes containing the merger of large aggregates, and chemical reactions involving complex intermediate phases.

To summarise the section we have presented a systematic method to project complex multi-dimensional barrier crossing problems onto a one-dimensional system. We relate these non-equilibrium situations to their associated equilibrium energy barriers, which naturally must be relevant to the problem and dominate the crossing rate. We detailed two techniques to find effective rate kinetics, which may give the user insight into the favoured routes of the particular problem. The first method applies equation (3.1.9), and is only valid in the Boltzmann region of an energy landscape. The main tool we developed is equation (3.1.11), which is a novel approach that is applicable throughout the entire landscape.

3.2 Application to GO model; Rate kinetics investigation

In this section, we apply our rate kinetics extraction techniques that relate to the equilibrium energy barrier from section 3.1.1.2 to the GO model of polymer nucleation [21, 22], see section 1.6.3 for full details. The system is a highly complicated multi-dimensional problem and even a two-dimensional representation is severe coarse-graining. To perform our one-dimensional analysis, a clear and sensible choice of order parameter is the nucleus size. In the GO model the rate kinetics are the available attachment surface area, known for each addition move. However for the combined states in the projection, this effective attachment area or effective rate kinetics is indeed a complex function, and is dependent on surface area of each move and is weighted by the popularity of that path over the non-equilibrium energy barrier. The optimal path has many contributors including the relative energy levels of the individual states, how many permutations of those states there are, and most unpredictably, the underlying rate kinetics.

We begin by simply estimating this effective attachment area based on the assumption that nuclei grow close to spherically to minimize surface area cost in section 3.2.1, as well as generalising this argument to self similar nuclei growth. These are key tools to understanding the physical relevance of our effective rate kinetics analysis for the model. In section 3.2.2 we perform a proof of concept initial investigation on a single set of GO model barrier parameters. We describe the energy landscape with the critical nuclei, n^*, otherwise known as the peak and with the maximum barrier height, $F(n^*)$, shortened to F^*. Applying both the Boltzmann technique and our main approach that is suitable for extracting rate kinetics outside of the Boltzmann region. Finally, we complete a full investigation into the effective rate kinetics of the GO model in section 3.2.3. At first finding the rate kinetics over the whole energy landscape, then focusing on rate kinetics patterns at the critical nuclei of various types of GO simulations. To examine patterns in the rate kinetics or effective attachment area for nucleation events in quiescent melts (no external force applied), stretched chains within pure long chain melts, and bimodal blends of long and short chains.

3.2.1 Spherical nuclei growth

In this section we derive an estimate for the effective attachment area, A_{N_T}, for our one-dimensional projection by assuming the nuclei grow spherically. To begin with we consider a growing nucleus in a quiescent polymer melt, on a two-dimensional energy landscape with the number of monomers, N_T, and the number of stems, N_S, being the coordinate axes, then our energy barrier is a saddle. We would expect the particles to grow by using numerous paths over this saddle, but we seek the optimal or average path as a function of N_S. Focusing on one particular state and considering the two positive addition moves, which are stem lengthening and stem addition, the attachment areas are solely dependent on N_S

$$A_{\text{add}}(N_S) = f_{\text{add}}(N_S) = 2\sqrt{\pi}\sqrt{N_S}\ , \tag{3.2.1a}$$

$$A_{\text{len}}(N_S) = 2N_S\ . \tag{3.2.1b}$$

We can write down the effective attachment area as a weighted probability of these two moves

$$\begin{aligned} A_{N_T} = {} & A_{\text{add}}(N_S)P(\text{stem addition}|\text{forward move}) \\ & + A_{\text{len}}(N_S)P(\text{stem lengthening}|\text{forward move}) \ . \end{aligned}$$

Now assuming the particle's average path minimizes surface area cost, we have self-similar spherical nuclei growth then $N_S = (9\pi/16)^{1/3}N_T^{2/3} = (a_r N_T)^{2/3}$. Also since we have self-similar growth, to maintain a fixed aspect ratio, the proportion of stem addition moves given that a forward move is chosen, must be the gradient of N_S with respect to N_T

$$\begin{aligned} P(\text{stem addition}|\text{forward move}) &= \frac{\mathrm{d}N_S}{\mathrm{d}N_T} = \frac{2}{3}a_r^{2/3}N_T^{-1/3} \ , \\ \text{and } \ P(\text{stem lengthening}|\text{forward move}) &= 1 - \frac{\mathrm{d}N_S}{\mathrm{d}N_T} = 1 - \frac{2}{3}a_r^{2/3}N_T^{-1/3} \ . \end{aligned}$$

Hence our one dimensional effective attachment area becomes

$$\begin{aligned} A_{N_T} &= A_{\text{add}}(N_S)\frac{\mathrm{d}N_S}{\mathrm{d}N_T} + A_{\text{len}}(N_S)\left(1 - \frac{\mathrm{d}N_S}{\mathrm{d}N_T}\right) \ , \\ &= 2\pi^{1/2}a_r^{1/3}N_T^{1/3} \cdot \frac{2}{3}a_r^{2/3}N_T^{-1/3} + 2a_r^{2/3}N_T^{2/3} \cdot \left(1 - \frac{2}{3}a_r^{2/3}N_T^{-1/3}\right) \ , \\ &= 2(a_r N_T)^{2/3} - \frac{4}{3}a_r^{4/3}N_T^{1/3} + \pi \ . \end{aligned} \tag{3.2.2}$$

This expression has a leading order term with exponent 2/3 that assumes all moves are stem lengthening, with a weaker correction term with exponent 1/3 due to an over-count of stem lengthening moves and a constant term that is associated with stem addition moves.

We can generalise this approach by enabling the average path to be not necessarily spherical, letting $N_S = \beta N_T^{\gamma}$ (with $0 < \gamma < 1$). Maintaining the self-similar growth property, allows us to repeat the argument that the proportion of forward moves which are stem addition is $\mathrm{d}N_S/\mathrm{d}N_T = \beta\gamma N_T^{\gamma-1}$. Hence the effective attachment area in general form is

$$A_{N_T} = 2\beta N_T^{\gamma} - 2\beta^2\gamma N_T^{2\gamma-1} + 2\gamma\left(\pi\beta^3\right)^{1/2}N_T^{3\gamma/2-1} \ . \tag{3.2.3}$$

This general self similar growth formula has the potential to be extremely useful, because, due to the many other contributing factors within our system, we do not expect perfectly spherical growth. Hence this tool gives us the opportunity to investigate the shape of the nuclei as they grow in more detail.

3.2.2 Initial investigation into the rate kinetics of the GO model

In this section, we apply our rate kinetics extraction techniques to a single set of GO model parameters which produce a quiescent energy barrier of height $F^* = 7$ at critical nuclei, $n^* = 98$. At first concentrating on the Boltzmann region in section 3.2.2.1, where we compare an exact calculation specific to the GO model to extracted rate kinetics. In section 3.2.2.2 we perform our main effective rate kinetics extraction technique which is valid for the whole of our landscape.

3.2.2.1 Boltzmann region

We present a rate kinetics calculation specific to the GO model and is only applicable within the Boltzmann region in section 3.2.2.1.1. This is in comparison to section 3.2.2.1.2 which shows the results of our rate kinetics extraction technique for the Boltzmann region.

3.2.2.1.1 Rate kinetics calculation In this section we detail a calculation for the effective attachment area or rate kinetics of the GO model to be implemented within the Boltzmann region of energy landscapes. Building upon the work completed on energy landscapes in chapter 2, for every arrangement we consider all possible moves that increase the nucleus size. Using the one-dimensional projection, see figure 3.1, we define the average rate from state i to state $i+1$ to be

$$\langle k_i^+ \rangle = \sum_{j \in \{S_i\}} k_{i,j}^+ P(j|i) \ . \tag{3.2.4}$$

An individual microstate j is a nucleus arrangement described using the notation from section 2.1.3 with $\{m_k\}$, $\{s_k\}$ being the number of monomers, and the number of stems of species k from a total n species, where $N_S = \sum_{k=1}^{n} s_k$ is the total number of stems. The set of microstates $\{S_i\}$ represents the collection, state i. The quantity $k_{i,j}^+$ is the sum of all positive moves from a particular state j, and $P(j|i)$ is the probability of a nucleus being in microstate j given it is in state i. Now we must determine $k_{i,j}^+$ which can be separated into two types of positive move, stem addition and stem lengthening,

$$k_{i,j}^+ = \left(k_{\text{add}}^+\right)_{i,j} + \left(k_{\text{len}}^+\right)_{i,j} \ . \tag{3.2.5}$$

Stem addition involves attaching a new monomer of any species to the side of the nucleus, the GO model assumes the available area is a band around the spheroid's equator, denoted as $f_{\text{add}}(N_S)$ which is a function of the total number of stems, N_S,

$$f_{\text{add}}(N_S) = 2\sqrt{\pi}\sqrt{N_S} \ .$$

Hence the contribution from all of the stem addition moves is a sum over all species and is of the form

$$\left(k_{\text{add}}^+\right)_{i,j} = f_{\text{add}}(N_S) \sum_{k=1}^{n} \phi_k \Theta_k \min\left[1, \exp\left(-\Delta F_{\text{add}}^{k+}\right)\right] \ , \tag{3.2.6a}$$

$$\text{where } \Delta F_{\text{add}}^{k+} = \mathcal{F}(i+1, j_{\text{add}}^{k+}) - \mathcal{F}(i,j) + \ln\phi_k + \ln\Theta_k \ ,$$

where $\mathcal{F}$ is an energy balance term, defined by equation (2.1.13) and does not include the number of arrangements. The microstate j^{k+}_{add} contains the following sets of monomers and stems of each species $\{m_1, \dots, m_k+1, \dots, m_n\}$ and $\{s_1, \dots, s_k+1, \dots, s_n\}$, and is manufactured by adding a stem with one monomer of species k to arrangement j, hence it is an element of the set $\{S_{i+1}\}$. Also note that as the concentration terms, ϕ_k and Θ_k (see sections 2.1.4 and 1.6.3.2 for full details), are within $\mathcal{F}$ but are outside the minimum function, so whilst making a move, they must be taken away from $\mathcal{F}$ and reapplied outside of the minimum function in order to be consistent.

Stem lengthening involves attaching a new monomer to either end of an existing stem within the nucleus and must be of the same species as the rest of the stem. Thus the contribution due to stem lengthening moves is also a sum over all species and includes the number of stems of each species

$$\left(k^+_{\text{len}}\right)_{i,j} = \sum_{k=1}^{n} 2 s_k \Theta_k \min\left[1, \exp\left(-\Delta F^{k+}_{\text{len}}\right)\right] \ , \tag{3.2.6b}$$

where $\Delta F^{k+}_{\text{len}} = \mathcal{F}(i+1, j^{k+}_{\text{len}}) - \mathcal{F}(i,j) + \ln\Theta_k$.

Similarly to the stem addition move, microstate j^{k+}_{len} has the following sets of monomers and stems of each species $\{m_1, \dots, m_k+1, \dots, m_n\}$ and $\{s_k\}$, manufactured by adding one monomer of species k to an existing stem on arrangement j, and is also an element of the set $\{S_{i+1}\}$.

To expand the conditional probability within equation (3.2.4), we use the Boltzmann approximation which assumes the occupancy or the probability the system is in a particular state at any time depends on the energy level of the microstate, hence

$$\begin{aligned}\sum_{j\in\{S_i\}} k^+_{i,j} P(j|i) &\approx \frac{\sum\limits_{j\in\{S_i\}} k^+_{i,j} P_a(i,j)\exp\left(-\mathcal{F}(i,j)\right)}{\sum\limits_{j\in\{S_i\}} \exp\left(-\mathcal{F}(i,j)\right)} \\ &\approx \frac{\sum\limits_{j\in\{S_i\}} k^+_{i,j} P_a(i,j)\exp\left(-\mathcal{F}(i,j)\right)}{Z(1)\exp\left(-F(i)\right)} \ ,\end{aligned}$$

where $P_a(i,j)$ is the number of arrangements that contain the same numbers of monomers and stems of each species as microstate j, defined by equation (2.1.8). Also $Z(1)$ is a normalisation term to ensure our base state satisfies $F(1) = 0$ as defined in section 2.1. Finally the average rate from state i to state $i+1$ is also defined by equation (3.1.8a) and this allows us to write the effective attachment area as

$$A(i) \approx \frac{\sum\limits_{j\in\{S_i\}} k^+_{i,j} P_a(i,j)\exp\left(-\mathcal{F}(i,j)\right)}{Z(1)\min\Big[\exp\Big(-F(i)\Big), \exp\Big(-F(i+1)\Big)\Big]} \ . \tag{3.2.7}$$

This calculation is only valid within the Boltzmann region. For multiple species melts the scope is extremely limited due to the many nested sums in $F(i)$ and in the kinetics sum (3.2.7), as discussed in chapter 2.

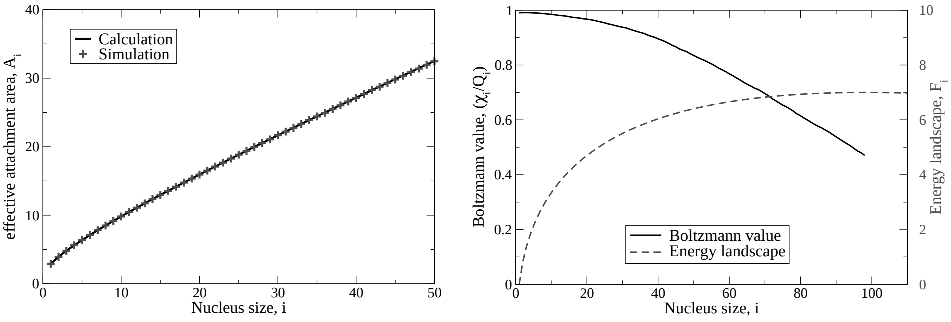

(a)

(b)

Figure 3.4: (a) Comparison of effective attachment area with nucleus size, calculated using equation (3.2.7) and simulated data with equation (3.1.9). (b) Displays Boltzmann value, (χ_i/Q_i), with nucleus size on the left axis (solid line) obtained during simulation as well as showing the energy landscape on the right axis (dashed line).

3.2.2.1.2 Rate kinetics comparison to the direct extraction technique In this section we compare the rate kinetics calculation for our GO model landscape with the direct simulation extraction technique from section 3.1.1.2.1. Figure 3.4(a) displays the rate kinetics comparison for our energy barrier with height $F^* = 7$ and critical nucleus, $n^* = 98$, between the analytic calculation of section 3.2.2.1.1 using equation (3.2.7) and the simulation technique through equation (3.1.9). As expected, the two data sets show complete agreement and this is due to both methods applying the same assumption, the Boltzmann approximation. In figure 3.4(b) we investigate in more detail the validity of this Boltzmann approximation that $\chi_i \approx Q_i$. We define a quantity called the Boltzmann value, (χ_i/Q_i), for a particular state i, which for the Boltzmann approximation to hold, should be close to unity. By recording the occupancies in the simulation we have plotted this Boltzmann value against nucleus size as well as showing the energy landscape. The Boltzmann region is the range of states where the Boltzmann approximation can be applied with confidence; the edge of this region is difficult to define. For this particular energy landscape with a relatively small barrier height of $7k_BT$, only the first half dozen states can be confidently described as the Boltzmann region with the approximation quickly weakening for larger states. For higher and wider barriers the Boltzmann region will also be wider.

This simulation technique is useful for determining rate kinetics at the base of energy landscapes. Moreover it is significantly cheaper than the calculation in section 3.2.2.1.1 with equation (3.2.7) since the number of species able to attach which highly complicates the calculation have no affect on the simulation's cost.

3.2.2.2 Entire landscape

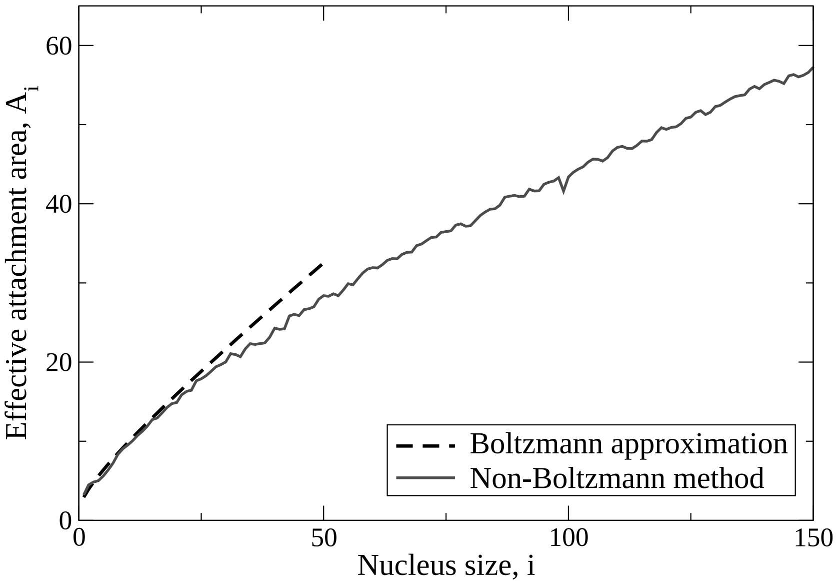

Figure 3.5: Comparison of the effective attachment area with nucleus size between the Boltzmann approximation calculation using equation (3.2.7) and the simulation technique valid throughout the whole landscape with equation (3.1.11) (Non-Boltzmann method).

In this section we execute the effective rate kinetics extraction technique from section 3.1.1.2.2 on our chosen GO model energy barrier. Figure 3.5 displays the effective attachment area against nucleus size and compares two different methods. We have the analytic calculation (3.1.9) described in section 3.2.2.1.1 which relies on the Boltzmann approximation. We also present the extraction technique (Non-Boltzmann method), applying equation (3.1.11) with outputted data from the simulation. The Boltzmann approximation is only valid within the Boltzmann region which, as figure 3.4(b) shows, is only a small set of states at the base, with the accuracy of the calculation decreasing for larger nuclei. Although the non-Boltzmann data is noisy, the general pattern is a deviation away from the Boltzmann approximation results. However it shows good agreement within the Boltzmann region. Even though the difference between Boltzmann values of adjacent states is minimal, the simulation is able to provide good statistics since the majority of its time is spent in these states. For larger barriers with wider Boltzmann regions this method would not be suitable because the differences in Boltzmann values would be too small. The technique has been designed to operate around the critical nuclei in the non-Boltzmann region, which is an area of more interest, where the calculation and simulation from section 3.2.2.1 that rely on the Boltzmann approximation to find rate kinetics are invalid.

This initial investigation into one set of GO model parameters has demonstrated the two different rate kinetics extraction techniques. The Boltzmann assumption reliant method results were displayed in figure 3.4(a) and verified against our nested sum calculation. We also further explained the scope of the Boltzmann region with a key indicator of the Boltzmann value in figure 3.4(b). Finally we implemented our main technique that is valid across the entire energy landscape. In section 3.2.3 this will be our technique to analyse further energy barriers and find patterns in rate kinetics that can indicate which routes to nucleation are dominating these complex multi-dimensional problems of the GO formulation.

3.2.3 Full investigation into the rate kinetics of the GO model

This section presents an extensive investigation into the rate kinetics of the GO polymer nucleation simulation. Applying the rate kinetics extraction technique from section 3.1.1.2.2 with equation (3.1.11), which is valid for the entire landscape. We begin by considering the entire energy landscape in section 3.2.3.1 and investigate the rate kinetics for differently shaped barriers. In section 3.2.3.2, we focus on the rate kinetics at the crucially important critical nuclei, which contribute to the crossing time as chapter 4 will show. We implement the GO simulation in two ways depending on the height of the barrier. For small barriers ($F^* \leq 10$) particles are inserted at the base as normal, but for larger barriers this is impractical as visits to the barrier peak are too rare. For these we take advantage of the fast simulation algorithm which begins each attempt closer to the peak of the energy landscape, in fact we choose a state i that is at least $8K_BT$ below F^*, for details see section 1.6.3.4 and [46]. The error involved in using this approximate technique is minimal for starting states far away from the energy peak. The publication discussed in detail the consistency of crossing times from simulation beginning further than $8K_BT$ below F^*. This enabled us to produce a huge number of crossing events cheaply to achieve highly accurate data.

3.2.3.1 Rate kinetics over the entire energy landscape

In this section, we present the rate kinetics or effective attachment area results from the GO model for the full nucleation landscape. We display a select group of rate kinetics results for different energy landscapes. Initially observing a single fixed critical nucleus, n^*, and varying the height of the barrier, F^*. In appendix B we include more data sets at different critical nuclei. Figure 3.6 displays three sets of effective attachment area extractions for a fixed $n^* = 50$

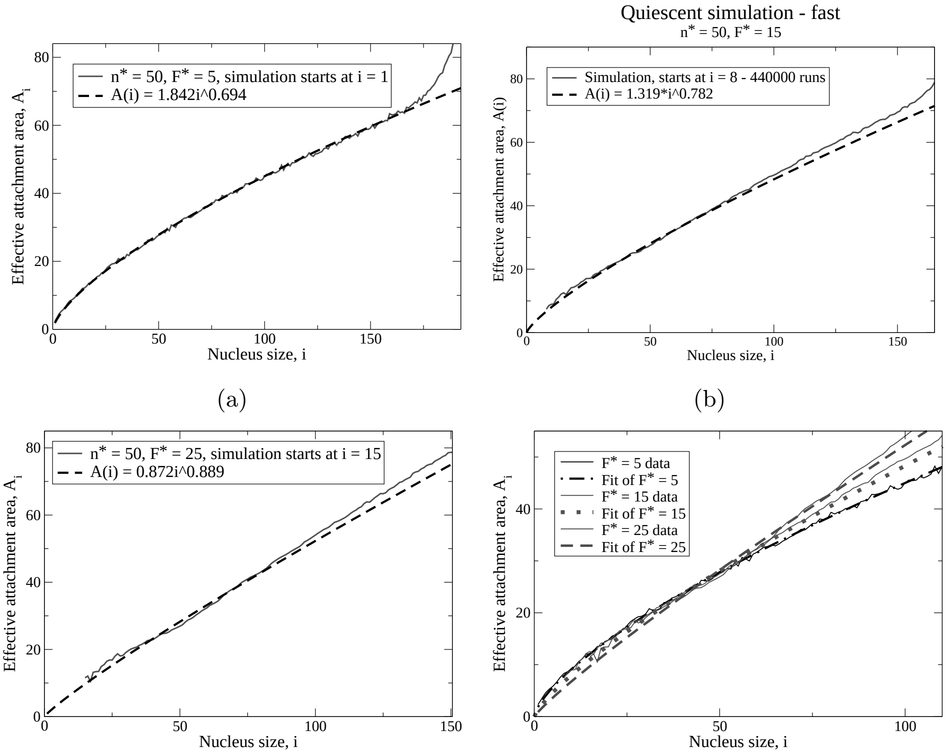

(a) (b)

(c) (d)

Figure 3.6: Effective attachment area data extracted from simulation for energy landscapes with a fixed $n^* = 50$ and a wide range of varying barrier heights (a) $F^* = 5$, (b) $F^* = 15$, (c) $F^* = 25$, as well as a power law fitting formula. (d) Comparison between fitting formula for (a), (b) and (c).

and $F^* = 5$, 15 and 25 respectively. In figure 3.6(a) we used the standard polymer simulation, but for figures 3.6(b) and 3.6(c) we employed the fast simulation algorithm which begins every run with a nucleus that is closer to the top of the landscape, in these cases it resets to a nucleus size of $i = 15$. For each case we apply a power law fit to the data and in figure 3.6(d) we show a comparison. If we focus on the effective attachment area around the critical nuclei, the three data sets are particularly close, in fact the fitting curves almost intersect at $i = 50$. Further investigation shows that, certainly for F^* inside this range and up to realistically crossable barriers, the values of the effective attachment area at the top of the landscape, A_{n^*} are extremely close. Similar investigations in appendix B for different fixed values of n^* produce the same closely related behaviour at n^*. A small note of caution occurs in figure 3.6(c) where the simulation data has a slight but noticeable dip around $i = 50$, this effect becomes more pronounced for energy landscapes with a relatively small critical nuclei and large barrier heights. The effect is even more noticeable in figure B.2(d) and we believe it is caused by the discreteness of the initial system for small n^* and large F^*. However we are more interested in the large critical nuclei limit.

In conclusion, we have an interesting and potentially incredibly useful result. That at the critical nuclei for particular quiescent polymer melts the rate kinetics are, if not independent, certainly only weakly dependent on the maximum height of the barrier. The exact reasons for this occurrence is still unclear. It could be connected to these landscapes having similarly shaped saddles, so that their relative size is unimportant for optimal paths. In section 3.2.3.2, we focus the investigation to reviewing the effective attachment area at this critical nuclei of each energy barrier.

3.2.3.2 Rate kinetics at critical nuclei

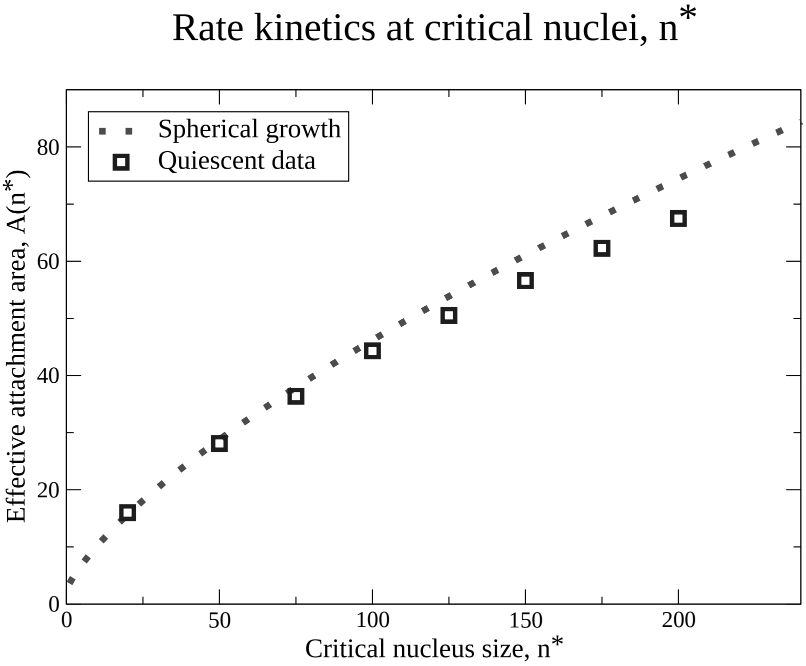

Figure 3.7: The effective attachment area at critical nuclei, n^*, for quiescent melts each with a height of $F^* = 10$, compared to our spherical growth formula (3.2.2).

This section follows on from the result in section 3.2.3.1 showing an intersection of the rate kinetics at the critical nuclei for quiescent melts. We focus on the particular values of the effective attachment area at the critical nuclei, A_{n^*} and review patterns therein. To obtain greater accuracy and negate the noise of the simulation we used a power law fitting around the critical nuclei to find A_{n^*}. In figure 3.7, we present effective attachment area data at the critical nuclei for quiescent melts each with an energy barrier of height $F^* = 10$. As well as showing the spherical growth formula (3.2.2) to compare, and although for smaller critical nuclei the comparison is good, there is a systematic deviation to lower value attachment areas for increasing critical nucleus size.

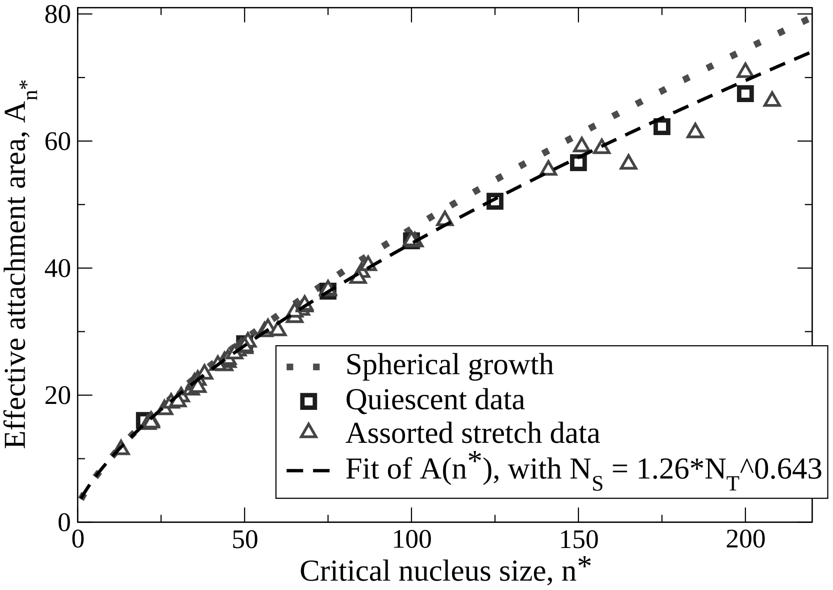

Figure 3.8: An assortment of pure stretched chain data has been added to figure 3.7, and we have also fitted the ensemble with a general growth formula (3.2.3).

In figure 3.8, we have added an assortment of data from from pure monodisperse melts of long stretched chains. These include both shear and extensional flow geometries and for varying degrees of stretch up to $\lambda = 5$, see sections 1.3 and 2.2.1. Examining this set of stretch data with the quiescent data, leads us to the conclusion that they are following a similar pattern, and are growing with comparable average paths over the energy landscape. There are three outliers which correspond to highly stretched melts, so it is possible these follow a marginally different pattern only noticeable for large critical nuclei. To summarise these data sets, we have applied the general growth formula (3.2.3) to fit the ensemble without the outliers. This fit results in a pattern that describes the average nucleus taking the path $N_S = 1.26 N_T^{0.643}$ over the energy landscape. The prefactor of this general growth formula is marginally higher than spherical growth, but the exponent is below the spherical value of 2/3, giving us a lower effective area for larger nuclei.

In figure 3.9, we have added the effective attachment area at critical nuclei for polymer bimodal blends data with 20%, 5%, and 2% long chains respectively, see section 2.2.2. The data sets begin with quiescent or unstretched melts and range up to a melt where the long chains have been stretched to $\lambda = 5$, the short-chain component is always taken to be unstretched. For clarity we have labelled the particular value of stretch $\lambda = 3.45$ for each data set, as the figure displays the 20% long chain melt produces the strongest critical

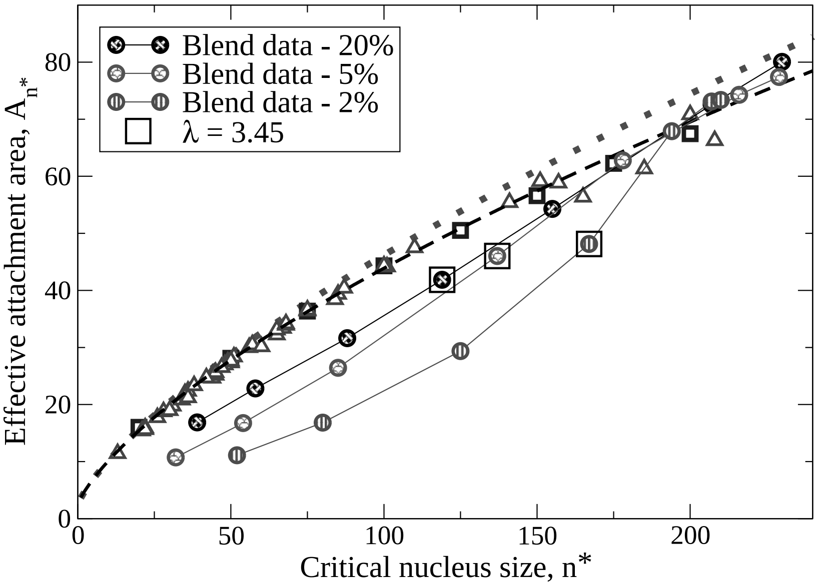

Figure 3.9: In addition to figures 3.7 and 3.8, we have added a series of polymer bimodal blends data with 20%, 5%, and 2% long chains, each have quiescent landscapes described by critical nuclei of $n^* = 230$, 229 and 210, and barrier height $F^* = 50$, 25 and 40 respectively. A stretch of up to $\lambda = 5$ has been applied, we have labelled the particular value of $\lambda = 3.45$ on each data set.

nuclei reduction. Since stretching has the effect of reducing the energy landscape and decreasing the critical nuclei, the larger values of critical nuclei for each set correspond to quiescent or weakly stretched melts.

In comparison to our original quiescent and pure stretched data, clearly the new quiescent values obey the previous pattern. Moreover, for the bimodal blends containing weakly stretched long chains, there is only a small reduction to the energy landscape and so there is no noticeable change to the effective attachment area pattern. However, as stretching begins to have a significant effect on the energy landscape, there is also a significant deviation from the previous curve. Also the fewer long chains within a melt produces more extreme deviation. We have found that the GO model predicts that highly stretched long chains sparsely distributed amongst short chains in a polymer melt, nucleate via significantly different average paths over the energy landscapes than quiescent and modestly stretched purely long chain melts.

3.2.4 GO model rate kinetics discussion

To summarise the section, we applied the one-dimensional projection and rate kinetics extraction technique to analyse the GO polymer nucleation simulation. Our order parameter of nucleus size was a simple choice, due to it being the most convenient to collect microstates together and extract data from various simulations. However, other reaction coordinates could have been chosen such as surface area, nucleus radius or the number of stems. For all of these variables, the particle would still need to cross an energy barrier. The techniques presented in this chapter certainly have the potential to be adapted to investigate rate kinetics for these coordinate systems.

Before performing our rate kinetics investigation, we produced an argument to estimate the rate kinetics of the GO model in section 3.2.1. This was based solely on an assumption that nuclei grow spherically to minimise surface area cost, resulting in equation (3.2.2). Additionally we generalised this approach by allowing non-spherical growth giving us a general formula (3.2.3), which was a useful tool to analyse simulation data.

Initially we tested the two extraction techniques, Boltzmann and full landscape, on a single parameter set, figure 3.5 validated the agreement within the Boltzmann region as expected. This enabled us to examine the rate kinetics for entire landscapes using our main full landscape technique. Immediately a clear order emerged in figure 3.6, that barrier height has zero or only a negligible affect on the rate kinetics at the critical nuclei. We then focused on the rate kinetics at a range of critical nuclei using many types of GO model scenarios. As figure 3.8 shows we found a distinct pattern for quiescent and modestly-stretched pure long chain melts, which clearly deviate from the estimated spherical growth curve. This pattern allows us to approximate the kinetics for any reasonable F^* at a particular n^*. Given that we have a good estimate for $\widetilde{A}(n^*)$, the effective attachment area could be expressed in the form

$$A(i) = \widetilde{A}(n^*) \left(\frac{i}{n^*} \right)^{\alpha} \ , \tag{3.2.8}$$

with a sensible choice of α which we expect to be close to 2/3, this would be a good representation around the top of the barrier.

In addition to quiescent and stretched pure-long chain melts, we have also investigated blends, as shown in figure 3.9, which displayed that blends with a small percentage of long chains in amongst short chains seem to have extremely different rate kinetics. The values of the effective attachment area are considerably lower, implying that nuclei grow in far more elongated shapes on fewer stems than expected. We can explain this observation, by suggesting that within these melts the route to nucleation is through the monomers on stretched chains which are sparsely distributed but vastly more energetically favourable to attach to a nucleus. So on the rare occasion they do attach, stem lengthening moves are far more convenient than finding another stretched chain to do a stem addition move.

In figure 3.10 we have presented a cross section of the energy landscape saddle at the critical nuclei, $n^* = 200$, for an overall barrier height $F^* = 50$. We have displayed the energy level against the number of stems within a nucleus.

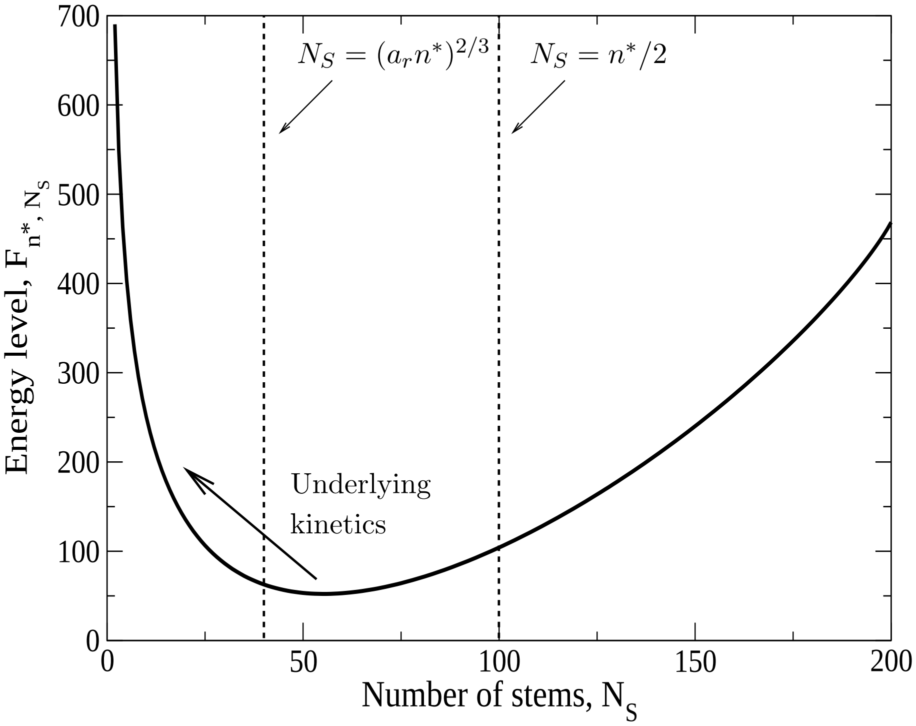

Figure 3.10: On this diagram we show a cross section of the energy landscape at the critical nuclei, $n^* = 200$, and overall barrier height $F^* = 50$. As well as marking optimisations for minimising surface area, $N_S = (a_r n^*)^{2/3}$, and maximising number of arrangements, $N_S = n^*/2$.

From chapter 2 we know the energy landscape has two contributing factors; the local energy level of the particular state and the number of arrangements there are of that state. On the diagram we have marked $N_S = a_r(n^*)^{2/3}$ which minimises surface area cost and $N_S = n^*/2$ which maximises the number of arrangements. Moreover the diagram shows that the combined energy minimum is between these two values. In fact if the attachment areas for all moves were equal, the average path to nucleation would be through a weighted average of this cross section. However the rate kinetics are not equal, see equations (3.2.1a) and (3.2.1b), stem addition moves scale with a square root of N_S, where as the stem lengthening moves scale linearly with N_S. Hence with increasing number of stems the disparity between the two types of move increases. This implies a particle could be more likely to make an energetically unfavourable stem lengthening move due to there being a larger area available to attach. The effect of these underlying rate kinetics is to push the average nucleation paths to the left of our energy landscape saddle or onto nuclei with fewer stems. The problem with these underlying rate kinetics is that it is difficult to predict how strong an effect they have on the average path. It is clear from figure 3.8, in particular for large critical nuclei, the simulation is observing these underlying kinetics. Furthermore the increasing disparity in the two addition moves, begins to explain the systematic deviation from spherical growth.

3.3 Discussion

In this discussion, we primarily review and expand the general one-dimensional projection model presented in section 3.1, and only briefly revisit the analysis of the GO model which has been extensively concluded in section 3.2.4. Our general method projects complex multi-dimensional barrier crossing problems onto one-dimensional systems, that have complete solutions. An integral component of this method were our two rate kinetics extraction techniques, the first given by (3.1.9), is only valid in the Boltzmann region. On the other hand, our main technique derived equation (3.1.11), and is applicable to the whole energy landscape. In order to achieve this we took advantage of an assumption, that the non-equilibrium rate kinetics obey detailed balance when applied to the equilibrium energy barrier. This requires the equilibrium energy barrier to have a strong influence on the non-equilibrium system.

In section 3.1.2 we discussed clear guidelines as to which types of general barrier crossing problems our technique may be suitable to analyse. In summary, the projection is dependent on a problem containing a sensible one-dimensional order parameter that appropriately describes crossing events. As stated we also require the equilibrium energy barrier to be relevant to the crossing rate, and the main crossing process must occur through a series of incremental steps. Promising candidates include nucleation problems containing large energy barriers and spacial diffusion events in deep energy wells. Our rate kinetics extraction technique may not be suitable for problems with strongly varying kinetics in different pathways, negating the influence of the equilibrium energy landscape. Along with scenarios which include large jumps, bypassing several stages in one move.

As we explained in section 3.1, our one-dimensional model is not the only choice of projection. In section 3.1.1.3, we completed a detailed comparison between our technique and direct measurements of rate kinetics on a simple multi-route barrier crossing example. In order to understand the effects on our one-dimensional projection, we artificially varied the rate kinetics along the individual pathways. Our extraction technique performed well considering the extreme regime employed, it produced physically sensible rate kinetics in scenarios where the equilibrium energy landscape was relevant. We also found a set of situations when a fast kinetic pathway is blocked or is too difficult to traverse. In these cases our technique is superior to direct measurements, as it only considers the occupancies not the number of moves that occur, and so dismisses these false routes.

In summary, the one-dimensional projection and in particular our novel rate kinetics extraction technique is potentially of great use to many barrier crossing problems. It is simple to code, and apply to new simulation outputs without significant modification. The strength of the technique is that it enables comparisons between different parameter sets with the equilibrium barrier as a control. A difference in rate kinetics might imply a different pathway may be in use. This could have been obscured from the original simulations, and could also be a signature of a fundamental shift within the physical process. Eventually this technique may enable sufficient coarse graining of stochastic simulations to find deterministic solutions suitable for integrated modelling of industrial problems.

On the whole the analysis of the rate kinetics from the GO polymer nucleation simulation was fascinating. We were able to identify clear patterns, that the height of the energy barrier had little impact on which routes over the saddle were preferred. Also we found a predictable result concerning the critical nuclei kinetics that most quiescent and stretched pure melts obeyed. On the other hand, the technique discovered with physical justification that bimodal blends of long and short chains, used a different average pathway over their energy landscapes.

In terms of usability the inclusion of the equilibrium barrier gives the user an easy method to compare different parameter sets in a fair environment, for example barrier height and critical nuclei. Overall, in the analysis of the GO model the one-dimensional projection and extraction techniques presented in this chapter, have proved to be extremely useful tools. This gives us belief that they may also be able to benefit other barrier crossing simulations in the future.

Chapter 4

One-dimensional models of energy barrier crossing

A key objective of this thesis is to develop an analytical polymer nucleation model that includes crystal rotation. It would be a significant improvement on our combinatorial model of chapter 2 as the relative angle between the principal flow direction and the chains within a growing crystal has a huge effect on its chance of successful nucleation. In the Graham-Olmsted (GO) polymer simulation [21, 22], the nucleus can modify this angle through convection and diffusion, and rotational diffusion is faster for smaller nuclei. We argue that the angular relaxation time of a crystal is much longer than the timescales of a single successful crossing event, this is supported by the quasi-static result from [67]. Hence the crystal's angle remains effectively fixed for each barrier crossing attempt and can only effectively adjust its orientation if it re-visits the base of the energy landscape. These ideas are throughly analysed in chapter 5. We intend to create an analytic nucleation model in which this angle is selected and fixed at an early stage in the crystal's growth but if the attempt is unsuccessful, the angle is re-selected and fixed once more for another attempt. This process continues until a successful fixed angle barrier crossing is completed.

We build upon the work in chapter 3 on projecting multi-dimensional systems onto a one-dimensional energy landscape through approximate kinetics. This chapter details the mathematical machinery that will form the base of our model, these methods apply to any one-dimensional barrier crossing problem or one that can be represented as such. In section 4.1 we investigate static barriers, focusing on average crossing times as well as examining the probability distributions of crossing times. Using static barrier techniques, we present and explore a system with a choice of potential pathways and a reset condition in section 4.2, which are the foundations of our model of polymer nucleation that includes crystal rotation.

4.1 Static barriers

In this section we fully investigate static one-dimensional energy barriers. Our first and most important aim is to calculate the average crossing time for a given system. This objective is achieved in section 4.1.1, where a steady state occupancy method is outlined, within this section we also display a vital calculation that predicts the fraction of particles that successfully nucleate. In section 4.1.2, we investigate several continuum approximations to our discrete model. As well as finding the average crossing times, the ability to compute a full probability distribution of crossing times would be extremely useful; to this end in section 4.1.3 a method based on Laplace transforms is introduced.

4.1.1 Steady state occupancy method for finding average crossing times

This section contains a method for finding average crossing times for particular one-dimensional systems. At first in section 4.1.1.1 we investigate a simple static barrier with only one exit from the system. We then modify these ideas and consider a different system in section 4.1.1.2 where nuclei can leave either by crossing the barrier or by returning to the base state, this set-up has a useful application with a view to including rotation in our model. Our methodology is essentially a discrete version of Kramers' barrier crossing method [76].

4.1.1.1 Average crossing time calculation for one-dimensional energy barriers

Given that we know the relative energy level of each state in our system as well as the effective attachment areas, $A(i)$, for all states, our one-dimensional system is fully defined by all the rates between adjacent states, k_i^+ and k_i^-, known from equation (3.1.8). Say we have s states labelled $\{1, \ldots, s\}$ and once the particle has left state s to go to an imaginary state $s+1$, we consider nucleation to have occurred and a new particle is injected into state 1. At steady state, the current of particles leaving the system, J, is the same as the current of particles entering the system in state 1. Following the example of equation (3.1.1), we investigate the net flux of occupancies of each state, $\dot{\chi}_i$, obtaining the set of differential equations

$$\dot{\chi}_1 = J - k_1^+ \chi_1 + k_2^- \chi_2 \ , \tag{4.1.1a}$$

$$\dot{\chi}_2 = k_1^+ \chi_1 - (k_2^- + k_2^+) \chi_2 + k_3^- \chi_3 \ , \tag{4.1.1b}$$

$$\vdots$$

$$\dot{\chi}_{s-1} = k_{s-2}^+ \chi_{s-2} - (k_{s-1}^- + k_{s-1}^+) \chi_{s-1} + k_s^- \chi_s \ , \tag{4.1.1c}$$

$$\dot{\chi}_s = k_{s-1}^+ \chi_{s-1} - (k_s^- + k_s^+) \chi_s \ . \tag{4.1.1d}$$

Furthermore at steady state, $\dot{\chi}_i = 0$, we have a solvable set of linear equations in the form $A_{i,j}\chi_j = b_i$

$$\begin{pmatrix} -k_1^+ & k_2^- & 0 & \cdots & & & 0 \\ k_1^+ & -(k_2^- + k_2^+) & k_3^- & 0 & \cdots & & 0 \\ 0 & \ddots & \ddots & \ddots & & & \vdots \\ \vdots & & & & k_{s-2}^+ & -(k_{s-1}^- + k_{s-1}^-) & k_s^- \\ 0 & \cdots & & & 0 & k_{s-1}^+ & -(k_s^- + k_s^+) \end{pmatrix}$$

$$\times \begin{pmatrix} \chi_1 \\ \chi_2 \\ \vdots \\ \chi_{s-1} \\ \chi_s \end{pmatrix} = \begin{pmatrix} -J \\ 0 \\ \vdots \\ \\ 0 \end{pmatrix} , \tag{4.1.2}$$

and since the matrix is tridiagonal, it is a simple numerical task to invert and find the occupancies of each state χ_i. However, we can also accomplish this and gain further insight by finding an analytic expression using a systematic approach. The net current J can be obtained through normalising the occupancies, ensuring that $\sum_{i=1}^{s} \chi_i = 1$, from which we have the average crossing time $\langle \tau \rangle = J^{-1}$. Whilst investigating the early solutions to this system for $s = 1, 2, 3, \ldots$, an obvious pattern begins to emerge. We propose that for a general system with s states, the set of steady state occupancies χ_i have the following formula

$$\chi_i = \frac{J}{k_i^+} \left(1 + \sum_{m=i+1}^{s} \prod_{l=i+1}^{m} \frac{k_l^-}{k_l^+} \right) , \tag{4.1.3}$$

and we prove this directly by substituting into equation (4.1.2). The first component of the resultant vector, $\mathbf{b}$, on the right hand side of equation (4.1.2) is

$$\begin{aligned} b_1 &= A_{1,1}\chi_1 + A_{1,2}\chi_2 \\ &= -k_1^+ \frac{J}{k_1^+} \left(1 + \sum_{m=2}^{s} \prod_{l=2}^{m} \frac{k_l^-}{k_l^+} \right) + k_2^- \frac{J}{k_2^+} \left(1 + \sum_{m=3}^{s} \prod_{l=3}^{m} \frac{k_l^-}{k_l^+} \right) , \\ &= -J - J \sum_{m=2}^{s} \prod_{l=2}^{m} \frac{k_l^-}{k_l^+} + J \sum_{m=2}^{s} \prod_{l=2}^{m} \frac{k_l^-}{k_l^+} = -J \quad \text{as required.} \end{aligned}$$

The components of b_i in the range $2 \leq i \leq s-1$ will be

$$
\begin{aligned}
b_i = A_{i,i-1}\chi_{i-1} + A_{i,i}\chi_i + A_{i,i+1}\chi_{i+1} = k_{i-1}^{+}\frac{J}{k_{i-1}^{+}}\left(1+\sum_{m=i}^{s}\prod_{l=i}^{m}\frac{k_l^-}{k_l^+}\right) \\
- \left(k_i^- + k_i^-\right)\frac{J}{k_i^+}\left(1+\sum_{m=i+1}^{s}\prod_{l=i+1}^{m}\frac{k_l^-}{k_l^+}\right) + k_{i+1}^{-}\frac{J}{k_{i+1}^{+}}\left(1+\sum_{m=i+2}^{s}\prod_{l=i+2}^{m}\frac{k_l^-}{k_l^+}\right) ,\\
b_i = J\left(1+\sum_{m=i}^{s}\prod_{l=i}^{m}\frac{k_l^-}{k_l^+}\right) - J\sum_{m=i}^{s}\prod_{l=i}^{m}\frac{k_l^-}{k_l^+} - J\left(1+\sum_{m=i+1}^{s}\prod_{l=i+1}^{m}\frac{k_l^-}{k_l^+}\right) \\
+ J\sum_{m=i+1}^{s}\prod_{l=i+1}^{m}\frac{k_l^-}{k_l^+} = 0 \ ,
\end{aligned}
$$

as predicted and for the last component, b_s, we have

$$
\begin{aligned}
b_s = A_{s,s-1}\chi_{s-1} + A_{s,s}\chi_s = k_{s-1}^{+}\frac{J}{k_{s-1}^{+}}\left(1+\sum_{m=s}^{s}\prod_{l=s}^{m}\frac{k_l^-}{k_l^+}\right) - \left(k_s^- + k_s^+\right)\frac{J}{k_s^+} \ ,\\
b_s = J\left(1+\frac{k_s^-}{k_s^+}\right) - J\left(\frac{k_s^-}{k_s^+}+1\right) = 0 \quad \text{as expected.}
\end{aligned}
$$

Using $\sum_{i=1}^{s}\chi_i = 1$, we can then produce an expression for J an hence the average crossing time

$$
\langle\tau\rangle = \sum_{i=1}^{s}\frac{1}{k_i^+}\left(1+\sum_{m=i+1}^{s}\prod_{l=i+1}^{m}\frac{k_l^-}{k_l^+}\right) . \tag{4.1.4}
$$

This general result applies to any one-dimensional barrier with known rates, k_i^+ and k_i^- although for large s this formula becomes expensive. However, in section 4.1.2, for smooth barriers, there is significant cancellation and we can transform this formula into a more useful expression in terms of $\exp(F(i))$ which is explained in section 4.1.2.2. There is also a similar solution to an analogous one-dimensional barrier crossing problem [77].

4.1.1.2 Rotation model specific fraction of success and average failure time

In our rotation model while a particle is on a particular pathway, its relative angle is fixed and hence the landscape is static until it revisits the base. To model this we modify the set-up from section 4.1.1.1, to a system where particles start in state 2 and nucleate once they go beyond some state s without falling back into state 1. The information we require is the fraction of particles that successfully nucleate without visiting state 1, which we denote by, σ_s, and the average failure time $\langle\tau_f\rangle$. The new set-up is similar to section 4.1.1.1 but here particles are injected into state 2 and this system has two exits. The particle nucleates if it reaches state s, but if it falls into state 1 then it is unable to return. Again we consider the flux of occupancies of each state, and write down a set of differential equations

$$\dot{\chi}_2 = J - (k_2^- + k_2^+)\chi_2 + k_3^-\chi_3 \ , \tag{4.1.5a}$$

$$\dot{\chi}_3 = k_2^+\chi_2 - (k_3^- + k_3^+)\chi_3 + k_4^-\chi_4 \ , \tag{4.1.5b}$$

$$\vdots$$

$$\dot{\chi}_{s-1} = k_{s-2}^+\chi_{s-2} - (k_{s-1}^- + k_{s-1}^+)\chi_{s-1} + k_s^-\chi_s \ , \tag{4.1.5c}$$

$$\dot{\chi}_s = k_{s-1}^+\chi_{s-1} - (k_s^- + k_s^+)\chi_s \ . \tag{4.1.5d}$$

Note that the these are similar to the set (4.1.1) but the term $k_1^+\chi_1$ is absent from $\dot{\chi}_2$. Following the previous calculation we investigate the steady state solution, $\dot{\chi}_i = 0$, and this produces a set of linear equations in the form $A_{i,j}\chi_j = b_i$, namely

$$\begin{pmatrix} -(k_2^- + k_2^+) & k_3^- & 0 & \cdots & & & 0 \\ k_2^+ & -(k_3^- + k_3^+) & k_4^- & 0 & \cdots & & 0 \\ 0 & \ddots & \ddots & \ddots & & & \vdots \\ \vdots & & & & k_{s-2}^+ & -(k_{s-1}^- + k_{s-1}^-) & k_s^- \\ 0 & \cdots & & & 0 & k_{s-1}^+ & -(k_s^- + k_s^+) \end{pmatrix}$$

$$\times \begin{pmatrix} \chi_2 \\ \chi_3 \\ \vdots \\ \chi_{s-1} \\ \chi_s \end{pmatrix} = \begin{pmatrix} -J \\ 0 \\ \vdots \\ \\ 0 \end{pmatrix} \ . \tag{4.1.6}$$

The rate at which particles are injected into the system can be obtained through normalising the occupancies, $\sum_{i=2}^{s}\chi_i = 1$. The matrix is tridiagonal and hence can easily be inverted numerically to find the occupancies of each state χ_i. However, as before, a highly ordered pattern emerges, and we systematically find a solution. We propose

$$\chi_i = \frac{J\Lambda(2, i-1)\Omega(i+1, s)}{\Omega(2, s)} \ , \tag{4.1.7}$$

$$\text{where } \ \Lambda(x, y) = \prod_{i=x}^{y} k_i^+ \ , \tag{4.1.8a}$$

$$\text{and } \ \Omega(x, y) = \sum_{j=x}^{y+1} \prod_{l=x}^{j-1} k_l^- \prod_{m=j}^{y} k_m^+ \ , \tag{4.1.8b}$$

$\Omega(x, y)$ possesses a useful recurrence relation

$$k_x^-\Omega(x+1, y) = \Omega(x, y) - \Lambda(x, y) \ .$$

We prove the occupancy result by directly substituting into equation (4.1.6), the first component of the resultant vector on the left hand side becomes

$$\begin{aligned} b_1 = A_{1,1}\chi_2 + A_{1,2}\chi_3 &= -\frac{(k_2^- + k_2^+)J\overbrace{\Lambda(2,1)}^{=1}\Omega(3,s)}{\Omega(2,s)} + \frac{k_3^- J\Lambda(2,2)\Omega(4,s)}{\Omega(2,s)} \ , \\ &= \frac{J}{\Omega(2,s)}\Big[- \Omega(2,s) + \Lambda(2,s) - k_2^+\Omega(3,s) + k_2^+\Omega(3,s) - k_2^+\Lambda(3,s)\Big] = -J \ , \end{aligned}$$

as expected. The components of b_i in the range $3 \leq i \leq s-1$ will be

$$\begin{aligned} b_i = A_{i,i-1}\chi_{i-1} + A_{i,i}\chi_i + A_{i,i+1}\chi_{i+1} &= \frac{k_{i-1}^+ J\Lambda(2,i-2)\Omega(i,s)}{\Omega(2,s)} \\ &- \frac{(k_i^- + k_i^+)J\Lambda(2,i-1)\Omega(i+1,s)}{\Omega(2,s)} + \frac{k_{i+1}^- J\Lambda(2,i)\Omega(i+2,s)}{\Omega(2,s)} \ , \\ &= \frac{J}{\Omega(2,s)}\Big[\Lambda(2,i-1)\Omega(i,s) - \Lambda(2,i-1)\Omega(i,s) + \Lambda(2,i-1)\Lambda(i,s) \\ &- \Lambda(2,i)\Omega(i+1,s) + \Lambda(2,i)\Omega(i+1,s) - \Lambda(2,i)\Omega(i+1,s)\Big] = 0 \ , \end{aligned}$$

as required, and for the last component, b_s, we have

$$\begin{aligned} b_s &= A_{s,s-1}\chi_{s-1} + A_{s,s}\chi_s \\ &= \frac{k_{s-1}^+ J\Lambda(2,s-2)\Omega(s,s)}{\Omega(2,s)} - \frac{(k_s^- + k_s^+)J\Lambda(2,s-1)\Omega(s+1,s)}{\Omega(2,s)} \ , \\ &= \frac{J}{\Omega(2,s)}\Big[\Lambda(2,s-1)\Omega(s,s) - \Lambda(2,s-1)\Omega(s,s) + \Lambda(2,s-1)\Lambda(s,s) \\ &- \Lambda(2,s)\underbrace{\Omega(s+1,s)}_{=1}\Big] = 0 \ , \end{aligned}$$

as predicted. Now we are able to calculate the fraction of particles that successfully nucleate

$$\sigma_s = \frac{k_s^+\chi_s}{J} = \frac{k_s^+\Lambda(2,s-1)\Omega(s+1,s)}{\Omega(2,s)} = \frac{\Lambda(2,s)}{\Omega(2,s)} \ , \qquad (4.1.9)$$

as well as the average time taken to leave the modified system, denoted by the subscript r

$$\langle\tau_r\rangle = \frac{1}{J} = \frac{1}{\Omega(2,s)}\sum_{i=2}^{s}\Lambda(2,i-1)\Omega(i+1,s) \ \text{using} \sum_{i=2}\chi_i = 1 \ .$$

Although this includes an occasional successful event, since we are interested in large nucleation barriers where successful events are rare, then $\langle\tau_r\rangle$ is an excellent approximate to the average failure time

$$\langle\tau_f\rangle \approx \langle\tau_r\rangle = \frac{1}{\Omega(2,s)}\sum_{i=2}^{s}\Lambda(2,i-1)\Omega(i+1,s) \ . \qquad (4.1.10)$$

To summarise the section, this steady state occupancy method for finding crossing times is a powerful technique. It is applicable to any one-dimensional discrete system, not even necessarily smooth landscapes, as long as the number of states is not too large. Three important results have been produced, in particular, we have an exact expression for the average crossing time displayed by equation (4.1.4). Also, with an adaptation to the general system, we have generated results that will be crucial in developing a rotational nucleation model. These are the fraction of successful nucleation attempts and the average failure time, given by equations (4.1.9) and (4.1.10) respectively. A crucial point to make about all the results from this method, is that for smooth energy landscapes there are considerable simplifications to be made, so this result becomes computationally inexpensive, with at most a double sum. Hence the scope of one-dimensional energy landscapes that can be practically solved is enormous.

4.1.2 Continuum approximations

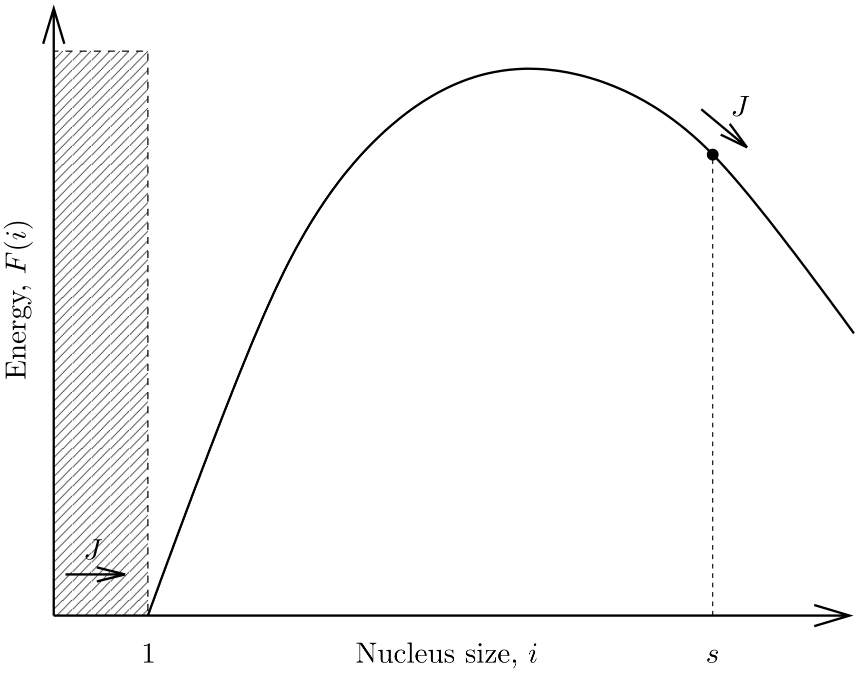

Figure 4.1: Continuous energy landscape with a constant stream of particles, J, entering the system at nucleus size, $i = 1$, and leaving the system at $i = s$.

Generating continuum approximations of discrete systems is always useful and can provide extra insight, as well as expanding the scope of such solutions through simplification. We begin by making several assumptions about the landscape, $F(i)$, which is measured in units of k_BT, that we intend to investigate and, in particular, find average crossing times. Without loss of generality we set $F(1) = 0$. Initially we require that the energy landscape is strictly increasing until a single maximum and then strictly decreasing from thereon, and that the barrier is both large in height as well as length, i.e. the critical nucleus, $n^* \gg 1$ and $F(n^*) \gg 1$. Additionally, it is also helpful, but not necessary, if the barrier is initially steep, or, in other words, the first few energy levels increase significantly, that is $F(1) = 0 \ll F(2) \ll F(3) \ll F(4)$. We have two strategies to find an approximation for barrier crossing times. The first, discussed in section 4.1.2.1, is to transform the discrete problem with distinct states into an analogous continuous system and then proceed in a similar manner to McLeish's chapter in [39] about particles escaping a potential well, which is a simplified version of a problem first studied by Kramers [76]. The second idea, which is discussed in section 4.1.2.2, is to analyse the exact expression for the average crossing time in equation (4.1.4), the aim being to simplify the sums with integral approximations. In section 4.1.2.3 we adapt the second approach to a set-up that would be useful in a crystallisation model that includes nucleus rotation.

4.1.2.1 Analogous continuous system

Figure 4.1 displays an analogous continuous energy landscape to our discrete problem, with particles entering the system at nucleus size, $i = 1$, and leaving the system, or as we consider it, nucleating, at $i = s$. We also have a continuous effective attachment area, $A(i)$, which acts in a similar way to a non-constant diffusion. However, the continuous $A(i)$ is marginally different to its discrete counterpart, because diffusion is the same forwards and backwards from a particular point which is not the case in the discrete set-up of equations 3.1.8. As in McLeish's method we let $n(i, t)$ represent the number of particles of size, i, at time t, and if the net flux through the system is J, then the average survival time is given by

$$\tau(s) = \frac{1}{J}\int_1^s n(i)\mathrm{d}i \ . \tag{4.1.11}$$

We employ the Smoluchowski diffusion equation, so that $n(i, t)$ satisfies

$$\frac{\partial n}{\partial t} = -\frac{\partial}{\partial i}\left(A(i)\biggl(-\frac{\partial n}{\partial i} - n\frac{\partial F}{\partial i}\biggr)\right) = 0 \ . \tag{4.1.12}$$

At steady state, we have a constant net supply of particles, J, arriving into state $i = 1$ and particles leaving at state $i = s$ do not return, giving us the boundary conditions

$$-A(i)\biggl(\frac{\partial n}{\partial i} + n(i)\frac{\partial F}{\partial i}\biggr)\bigg|_{i=1} = J \ \text{ and } \ n(s) = 0 \ .$$

Integrating once directly with aid of the boundary condition at $i = 1$, gives

$$\frac{\partial n}{\partial i} + n(i)\frac{\partial F}{\partial i} = \frac{-J}{A(i)} \ ,$$

and using an integrating factor, $\exp\left(F(i)\right)$, we perform a further integration between i and s with $n(s) = 0$ to obtain

$$n(i) = J \exp\left(-F(i)\right) \int_i^s \frac{\exp\left(F(i')\right)}{A(i')} \mathrm{d}i' \ .$$

Therefore the average survival time, after re-ordering the double integration is

$$\tau(s) = \int_1^s \frac{\exp\left(F(i')\right)}{A(i')} \int_1^{i'} \exp\left(-F(i)\right) \mathrm{d}i \, \mathrm{d}i' \ . \tag{4.1.13}$$

Expanding the inner integral around $i = 1$, so that

$$F(i) \approx F(1) + (i-1)F'(1) = (i-1)F'(1) \ ,$$

$$\text{therefore} \quad \int_1^{i'} \exp\left(-F(i)\right) \mathrm{d}i \approx \int_1^{\infty} \exp\big(-\left(i-1\right)F'(1)\big) \mathrm{d}i = \frac{1}{F'(1)} \approx \frac{1}{F(2)} \ ,$$

here $F'(1) \approx F(2) - F(1) = F(2)$. If we were to include the quadratic term in the expansion, our integral would be infinite as $F''(1) < 0$. To correct this, higher order terms would be required and the integral would become extremely difficult, thus in order to obtain a simple analytic expression we settle for linear accuracy

$$\tau(s) \approx \frac{1}{F(2)} \int_1^s \frac{\exp\left(F(i')\right)}{A(i')} \mathrm{d}i' \ . \tag{4.1.14}$$

For the outer integral, after dropping the dashes, we let $g(i) = F(i) - \ln A(i)$, and assume that the effective attachment area, $A(i)$, is of the form of a power law in equation (3.2.8) explained in section 3.2.3. The function $g(i)$ can then be transformed into a Gaussian by expanding $F(i)$ around n^*

$$g(i) \approx F\left(n^*\right) + \frac{1}{2}\left(i - n^*\right)^2 F''\left(n^*\right) - \ln \widetilde{A}\left(n^*\right) - \alpha \ln i + \alpha \ln n^* \ ,$$

$$\text{therefore} \quad g(i) \approx g\left(n^*\right) + \left(i - n^*\right) g'\left(n^*\right) + \frac{1}{2}\left(i - n^*\right) g''\left(n^*\right) \ ,$$

$$\text{with} \quad g\left(n^*\right) = F\left(n^*\right) - \ln \widetilde{A}\left(n^*\right) \ ,$$

$$g'\left(n^*\right) = -\frac{\alpha}{n^*} \quad \text{and} \quad g''\left(n^*\right) = F''\left(n^*\right) + \frac{\alpha}{\left(n^*\right)^2} \ .$$

Hence the average survival time can be approximated by

$$\begin{aligned} \tau = {} & \frac{1}{F(2)} \left(\sqrt{\frac{2\pi}{-g''\left(n^*\right)}} \right) \\ & \times \exp\left(g\left(n^*\right) - n^* g'\left(n^*\right) + \frac{\left(n^*\right)^2 g''\left(n^*\right)}{2} - \frac{\left(g'\left(n^*\right) + n^* g''\left(n^*\right)\right)^2}{2 g''\left(n^*\right)} \right) \ . \end{aligned} \tag{4.1.15}$$

Although the investigation of this analogous system was a good exercise, the various approximations and errors build up, which reduces the overall accuracy of this result, as we discuss in section 4.1.2.2.1.

4.1.2.2 Average crossing time simplification for smooth energy landscapes

In this section, we take the exact formula (4.1.4) for the average crossing time of a discrete system and, through several levels of approximation and simplification, we attempt to transform the result into a more useful form. We begin this approach by investigating the object, which we denote as

$$Y(i+1,m) = \prod_{l=i+1}^{m} \frac{k_l^-}{k_l^+} \ , \tag{4.1.16}$$

with rates k_l^-, k_l^+ defined by the couple of equations in set (3.1.8). Now $Y(i+1,m)$ simplifies in subtly different ways depending on whether the barrier is (i) increasing ($i+1 \leq m < n^*$), (ii) decreasing ($n^* < i+1 \leq m$) or, (iii) includes the peak ($i+1 \leq n^* \leq m$), resulting in

$$Y(i+1,m) = \frac{A(i)}{A(m)} \begin{cases} \exp\left(F(m+1) - F(i+1)\right) & \text{for } i+1 \leq m < n^* \ , \\ \exp\left(F(m) - F(i)\right) & \text{for } n^* < i+1 \leq m \ , \\ \exp\left(F(m) - F(i+1)\right) & \text{for } i+1 \leq n^* \leq m \ . \end{cases}$$

Also the definition of k_i^+ is dependent on the position i along the landscape in relation to n^*,

$$k_i^+ = \begin{cases} A(i)\exp\left(-\left(F(i+1) - F(i)\right)\right) & \text{for } i < n^* \ , \\ A(i) & \text{for } i \geq n^* \ . \end{cases}$$

Collecting these results together we write a modified expression for the average crossing time

$$\begin{aligned} \langle\tau\rangle = & \sum_{i=1}^{n^*-1} \frac{1}{A(i)} \exp\left(F(i+1) - F(i)\right) \\ & \times \left[1 + \sum_{m=i+1}^{n^*-1} \frac{A(i)}{A(m)} \exp\left(F(m+1) - F(i+1)\right) \right. \\ & \left. + \sum_{m=n^*}^{s} \frac{A(i)}{A(m)} \exp\left(F(m) - F(i+1)\right)\right] \\ & + \sum_{i=n^*}^{s} \frac{1}{A(i)} \left[1 + \sum_{m=i+1}^{s} \frac{A(i)}{A(m)} \exp\left(F(m) - F(i)\right)\right] \ , \end{aligned} \tag{4.1.17}$$

which can be rearranged and simplified into a more elegant form

$$\begin{aligned} \langle\tau\rangle = & \sum_{i=1}^{n^*-1} \frac{1}{A(i)} \exp\left(F(i+1) - F(i)\right) + \sum_{i=n^*}^{s} \frac{1}{A(i)} \\ & + \sum_{i=n^*}^{s} \exp\left(-F(i)\right) \sum_{m=i+1}^{s} \frac{\exp\left(F(m)\right)}{A(m)} \\ & + \sum_{i=1}^{n^*-1} \exp\left(-F(i)\right) \left[\sum_{m=i+1}^{n^*-1} \frac{\exp\left(F(m+1)\right)}{A(m)} + \sum_{m=n^*}^{s} \frac{\exp\left(F(m)\right)}{A(m)}\right] \ . \end{aligned} \tag{4.1.18}$$

Further investigation of this equation leads us to the conclusion that the final term is the only significant contribution to the crossing time for landscapes that concur with our assumptions. The first two terms are clearly small in comparison to the final term, their largest contributions are $\exp\left(F(2)\right)/A(1)$ and $1/A(1)$ which are minuscule in relation to terms of order $\exp\left(F(n^*)\right)/A(n^*)$. The double sums in the remaining three terms contribute when i is small and m is close to n^*, the third term begins with $i = n^*$ and thus can also be neglected. This allows us to approximate the average crossing time by

$$\langle\tau\rangle \approx \sum_{i=1}^{n^*-1} \exp\left(-F(i)\right)\left[\sum_{m=i+1}^{n^*-1} \frac{\exp\left(F(m+1)\right)}{A(m)} + \sum_{m=n^*}^{s} \frac{\exp\left(F(m)\right)}{A(m)}\right] . \tag{4.1.19}$$

If we assume that the effective attachment area is an increasing power law of the form of equation (3.2.8) which has been thoroughly explained in section 3.2.3, then the inner sum will be dominated by $\widetilde{n}^* \leq n^*$. Motivated by this, we estimate the inner sum by taking out the first term in the second part as well as slightly modifying $A(m)$ to $A(m-1)$ and this combines the two parts so that we can later approximate the complete sum as an integral over the whole domain

$$\langle\tau\rangle \approx \sum_{i=1}^{n^*-1} \exp\left(-F(i)\right)\left[\frac{\exp\left(F(n^*)\right)}{A(n^*)} + \sum_{m=i+1}^{s} \frac{\exp\left(F(m+1)\right)}{A(m)}\right] . \tag{4.1.20}$$

It is interesting to compare equation (4.1.20) which is our discrete average crossing time with equation (4.1.13) from the analogous continuous energy landscape method, particularly in the offset within the inner sum, $\exp\left(F(m+1)\right)/A(m)$. This offset in the discrete case can be traced back to the arbitrary choice for the kinetics in the move rates of equations (3.1.8). In order to approximate the inner sum in equation (4.1.20) as a Gaussian integral, we define

$$h(m) = F(m+1) - \ln A(m) , \tag{4.1.21}$$

and by modifying $F(m)$ from a discrete to a continuous function, we can expand $F(m+1)$ around its maximum, n^*, and substitute in $A(m)$ from equation (3.2.8), hence $h(m)$ becomes

$$h(m) \approx F(n^*) + \frac{1}{2}\left(m+1-n^*\right)^2 F''\left(n^*\right) - \ln \widetilde{A}\left(n^*\right) - \alpha \ln m + \alpha \ln n^* .$$

To proceed we have two options, simply expand this around n^* or attempt to find the maximum of $h(m)$, which we shall denote as , $\widetilde{n}^*$, and expand around that. For the first option $h(m)$ will be of the form

$$h(m) \approx h\left(n^*\right) + \left(m-n^*\right) h'\left(n^*\right) + \frac{1}{2}\left(m-n^*\right)^2 h''\left(n^*\right) , \tag{4.1.22}$$

$$\text{with } h\left(n^*\right) = F\left(n^*\right) + \frac{1}{2}F''\left(n^*\right) - \ln \widetilde{A}\left(n^*\right) ,$$

$$h'\left(n^*\right) = F''\left(n^*\right) - \frac{\alpha}{n^*} \text{ and } h''\left(n^*\right) = F''\left(n^*\right) + \frac{\alpha}{\left(n^*\right)^2} ,$$

and our inner sum can be transformed into an integral to become

$$\begin{aligned}\sum_{m=i+1}^{s}\exp\left(h(m)\right) &= \int_{-\infty}^{\infty}\exp\left(h(m)\right)\mathrm{d}m \\ &\approx \left(\sqrt{\frac{2\pi}{-h''\left(n^*\right)}}\right)\exp\left(h\left(n^*\right)-n^*h'\left(n^*\right)+\frac{\left(n^*\right)^2h''\left(n^*\right)}{2}\right. \\ &\quad\left.-\frac{\left(h'\left(n^*\right)+n^*h''\left(n^*\right)\right)^2}{2h''\left(n^*\right)}\right) .\end{aligned}$$

Alternatively, to find the maximum of $h(m)$, $\widetilde{n}^*$, we take the first derivative and set to zero to obtain

$$h'\left(\widetilde{n}^*\right)=\left(\widetilde{n}^*+1-n^*\right)F''\left(n^*\right)-\frac{\alpha}{\widetilde{n}^*}=0 .$$

Now if we assume $\widetilde{n}^*$ is a small perturbation of n^*, hence $\widetilde{n}^*=n^*-\delta$ with $\delta\ll n^*$ and this gives

$$\begin{aligned}&\delta\approx 1-\frac{\alpha}{n^*F''\left(n^*\right)} \quad\text{therefore}\quad \widetilde{n}^*\approx n^*-1+\frac{\alpha}{n^*F''\left(n^*\right)} , \\ &\text{and this implies}\quad \frac{1}{n^*}-\frac{\alpha}{(n^*)^2F''(n^*)}\ll 1 ,\end{aligned}$$

noting that $F''(n^*)$ will be negative. We can now approximate $h(m)$ by its expansion around $\widetilde{n}^*$,

$$h(m)\approx h\left(\widetilde{n}^*\right)+(1/2)\left(m-\widetilde{n}^*\right)^2h''\left(\widetilde{n}^*\right) , \tag{4.1.23}$$

$$\text{and hence our integral is}\quad \int_{-\infty}^{\infty}\exp\left(h(m)\right)\mathrm{d}m\approx\left(\sqrt{\frac{2\pi}{-h''\left(\widetilde{n}^*\right)}}\right)\exp\left(h\left(\widetilde{n}^*\right)\right) . \tag{4.1.24}$$

Here $h\left(\widetilde{n}^*\right)$ is found for accuracies $O(1)$ and $O((\delta/n^*))$, referred to as $h_0\left(\widetilde{n}^*\right)$ and $h_1\left(\widetilde{n}^*\right)$ respectively

$$\begin{aligned}h\left(\widetilde{n}^*\right)&\approx F\left(n^*\right)+\frac{1}{2}\left(\frac{\alpha}{n^*F''\left(n^*\right)}\right)^2F''\left(n^*\right)-\ln\widetilde{A}\left(n^*\right) \\ &\quad-\alpha\ln\left(n^*-1+\frac{\alpha}{n^*F''\left(n^*\right)}\right)+\alpha\ln n^* , \\ h_0\left(\widetilde{n}^*\right)&=F\left(n^*\right)-\ln\widetilde{A}\left(n^*\right) &&\text{(4.1.25a)} \\ h_1\left(\widetilde{n}^*\right)&=F\left(n^*\right)-\ln\widetilde{A}\left(n^*\right)-\frac{\alpha^2}{2\left(n^*\right)^2F''\left(n^*\right)}+\frac{\alpha}{n^*} . &&\text{(4.1.25b)}\end{aligned}$$

We find the second derivative at $\widetilde{n}^*$ to an accuracy of $O(1)$ because the curvature is of less importance than the peak value in the resulting integral,

$$\begin{aligned}h''\left(\widetilde{n}^*\right)&\approx F''\left(n^*\right)+\alpha\left(n^*-1+\frac{\alpha}{n^*F''\left(n^*\right)}\right)^{-2} , \\ h''\left(\widetilde{n}^*\right)&\approx F''\left(n^*\right)+\frac{\alpha}{\left(n^*\right)^2}=F''\left(n^*\right)\left(1+\frac{\alpha}{\left(n^*\right)^2F''\left(n^*\right)}\right) , \\ h_0''\left(\widetilde{n}^*\right)&=F''\left(n^*\right) . &&\text{(4.1.26)}\end{aligned}$$

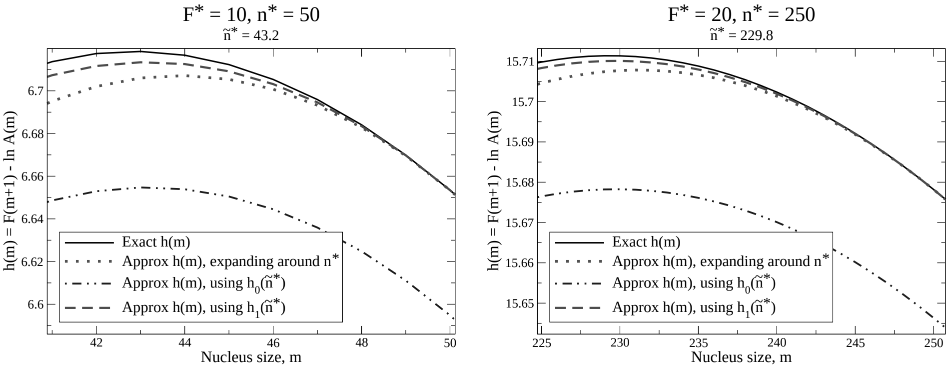

(a) (b)

Figure 4.2: Comparing modified energy landscapes of the exact $h(m)$ function with approximates (i) $h(m)$ through the expansion around n^* from equation (4.1.22), (ii) $h(m)$ formed by expanding around $\widetilde{n}^*$ from equation (4.1.23) with $h_0\left(\widetilde{n}^*\right)$ and $h_0''\left(\widetilde{n}^*\right)$ and (iii) $h(m)$ again through the expansion around $\widetilde{n}^*$ from equation (4.1.23) but with $h_1\left(\widetilde{n}^*\right)$ and $h_0''\left(\widetilde{n}^*\right)$ for original energy landscapes, with (a) $F^* = 10$, $n^* = 50$ and (b) $F^* = 20$, $n^* = 250$.

Figure 4.2 displays $h(m)$ against three approximate versions, focused on the peaks, for two energy landscapes with original values $F^* = 10$, $n^* = 50$ and $F^* = 20$, $n^* = 250$. The first observation, is the overall accuracy is good around the maximum value, obviously the accuracy of our expansions fall off away from the peaks, however since the tails provide only a small contribution to the integral the errors are negligible. The expansion around n^* is more accurate than our first attempt at expanding around $\widetilde{n}^*$ using $h_0\left(\widetilde{n}^*\right)$, because at $m = n^*$, $h(m)$ should coincide with equation (4.1.22), but the peak of the approximation is a little to the right. Our best approximation, is to expand around $\widetilde{n}^*$ with $h_1\left(\widetilde{n}^*\right)$, and we can execute the outer sum by just including the first few terms, the number of terms required is dependent on the steepness of the initial slope of the barrier. Collecting these expansions together gives us a continuous approximation to the crossing time of

$$\begin{aligned}\langle\tau\rangle \approx\ & \left(1 + \exp\left(-F(2)\right) + \exp\left(-F(3)\right) + \cdots\right) \\ & \times \left[\frac{\exp\left(F(n^*)\right)}{\widetilde{A}(n^*)}\left(1 + \sqrt{\frac{2\pi}{-F''\left(n^*\right)}}\exp\left(\frac{-\alpha^2}{2\left(n^*\right)^2 F''\left(n^*\right)} + \frac{\alpha}{n^*}\right)\right)\right]. \end{aligned} \tag{4.1.27}$$

This is a powerful result as it requires little information, only the initial slope as well as data connected to the peak, namely the critical nuclei, n^*, height of the barrier, $F(n^*)$, the kinetics at the peak, $\widetilde{A}(n^*)$, and the curvature $F''\left(n^*\right)$.

4.1.2.2.1 Average crossing time results

In this section we analyse the effectiveness of our approximate calculations, table 4.1 displays various aver-

	$n^* = 50$ $F^* = 10$	$n^* = 200$ $F^* = 10$	$n^* = 150$ $F^* = 40$	$n^* = 200$ $F^* = 50$
GO simulation	5.63×10^4	1.86×10^5	3.30×10^{17}	7.09×10^{21}
Exact discrete (4.1.18)	5.87×10^4	1.83×10^5	3.35×10^{17}	7.22×10^{21}
Continuous (4.1.15)	1.37×10^5	3.81×10^6	5.23×10^{17}	1.07×10^{22}
Approximation (4.1.27)	5.78×10^4	1.50×10^5	3.38×10^{17}	7.29×10^{21}
$\exp(F^*)$	2.20×10^4	2.20×10^4	2.35×10^{17}	5.19×10^{21}

Table 4.1: Various average crossing times for five differently shaped energy landscapes. We have compared the full polymer simulation with several one-dimensional representations, including the exact discrete equation (4.1.18), the analogous continuous system with equation (4.1.15) and the integral approximation to the discrete system in equation (4.1.27), as well as the basic Boltzmann approximation. The one-dimensional rate kinetics in use for the calculations through equation (3.2.8) with $\alpha = 0.8$, and formula (3.2.3) for $\widetilde{A}(n^*)$ with $\beta = 1.26$ and $\gamma = 0.643$.

age crossing times for five different energy landscapes. In the first row we have results for the full polymer simulation, it is interesting to compare these to the one dimensional calculations. Although this comparison is unfair as the rate kinetics are unknown for multi-dimensional systems, which was thoroughly discussed in chapter 3. Here rate kinetics are approximated from equation (3.2.8) with $\alpha = 0.8$ and the general growth fitting formula (3.2.3) for $\widetilde{A}(n^*)$ with $\beta = 1.26$ and $\gamma = 0.643$. These approximate rate kinetics is the reason for the slight decrepancy between full multi-dimensional GO simulation crossing times and one-dimensional discrete projected systems. The exact discrete results are a more appropriate measure of the success of our continuum approximations. As the table shows the analogous continuous system is a poor representation, this is due to compound errors in the calculation. At first the system has been transformed from a discrete energy landscape with distinct states into a continuous one, also the kinetics are different and there is a crude approximation at the base of the barrier for the inner integral. We would expect this set-up to perform reasonably well for high barriers ($F(n^*) \gg 1$), which to an extent it does, but it is still barely an improvement on the Boltzmann approximation. The integral approximation of the exact discrete equation is in general a superb result. We expect accuracy to suffer for low, flat barriers ($n^* \gg 1\ , F(n^*) \approx O(1)$), where diffusion across the peak plateau is more important. However for long, high barriers ($n^* \gg 1\ , F(n^*) \gg 1$) which are of more interest to us, this method is an excellent simplification.

Note that for the GO simulation results, we use the standard algorithm for small barriers ($F^* \leq 10$). For larger barriers this is impractical as visits to the barrier peak are too rare. In these cases we take advantage of the fast simulation algorithm which begins each attempt closer to the peak of the energy landscape, in fact we choose a state i that is at least $8K_BT$ below F^*, for details see section 1.6.3.4 and [46]. The error invloved in using this approximate technique is minimal for starting states far away from the energy peak. The publication discussed in detail the consistency of crossing times from simulation beginning further than $8K_BT$ below F^*. A high accuracy of simulation data is then available since we were able to record a huge number of crossing events using this fast technique. The overall simulation error for each of our cases was less than 1% of the average crossing time.

4.1.2.3 Fraction of success and average failure time calculations

In a similar manner to section 4.1.2.2 we can simplify results (4.1.9) and (4.1.10) by continuing to study barriers that conform to the assumptions made in the first paragraph of section 4.1.2. Let us start by looking at the objects $\Lambda(x,y)$ and $\Omega(x,y)$, which are dependent on the relative positions x and y on the landscape. For $\Lambda(x,y)$, we are only concerned with $x=2$, but its value is dependent on where y is situated

$$\Lambda(2,y) = A(2)\cdots A(y)\exp\left(F(2)\right)\begin{cases} \exp\left(-F(y+1)\right) & \text{for } \; y < n^*-1 \;, \\ \exp\left(-F(n^*)\right) & \text{for } \; y \geq n^*-1 \;. \end{cases}$$

On the other hand for $\Omega(x,y)$, the only relevant value $y=s$, but the position of x is important

$$\begin{aligned} \Omega(x,s) &= A(x-1)\cdots A(s) \\ &\times \begin{cases} \exp\left(-F(n^*)\right)\left[\sum\limits_{j=x}^{n^*}\frac{\exp\left(F(j)\right)}{A(j-1)} + \sum\limits_{j=n^*+1}^{s+1}\frac{\exp\left(F(j-1)\right)}{A(j-1)}\right] & \text{for } \; x \leq n^* \;, \\ \exp\left(-F(x-1)\right)\sum\limits_{j=x}^{s+1}\frac{\exp\left(F(j-1)\right)}{A(j-1)} & \text{for } \; x > n^* \;. \end{cases} \end{aligned}$$

Collecting these results together, we can write down equations for the fraction of successful nucleation events, σ_s, and the average failure time, $\langle\tau_f\rangle$

$$\sigma_s = \frac{\Lambda(2,s)}{\Omega(2,s)} = \frac{\exp\left(F(2)\right)}{A(1)}\left[\sum_{j=2}^{n^*}\frac{\exp\left(F(j)\right)}{A(j-1)} + \sum_{j=n^*+1}^{s+1}\frac{\exp\left(F(j-1)\right)}{A(j-1)}\right]^{-1} \;, \tag{4.1.28}$$

$$\begin{aligned} \langle\tau_f\rangle &\approx \langle\tau_r\rangle = \frac{1}{\Omega(2,s)}\sum_{i=2}^{s}\Lambda(2,i-1)\Omega(i+1,s) \;, \\ \langle\tau_f\rangle &\approx \sigma_s\left[\sum_{i=2}^{n^*-1}\exp\left(-F(i)\right)\left[\sum_{j=i+1}^{n^*}\frac{\exp\left(F(j)\right)}{A(j-1)} + \sum_{j=n^*+1}^{s+1}\frac{\exp\left(F(j-1)\right)}{A(j-1)}\right]\right. \\ &\qquad \left. + \sum_{i=n^*}^{s}\exp\left(-F(i)\right)\sum_{j=i+1}^{s+1}\frac{\exp\left(F(j-1)\right)}{A(j-1)}\right] \;. \end{aligned} \tag{4.1.29}$$

Further progress can be made with these two results by employing similar techniques to section 4.1.2.2. For the fraction of successful nucleation events, σ_s, if j is changed to $m+1$ then we have an expression extremely similar to the inner sum in equation (4.1.19). The most accurate way of approximating this sum as an integral was through the use of the $h(m)$ function in equation (4.1.23) with $h_1(\widetilde{n}^*)$ and $h_0''(\widetilde{n}^*)$, where $\widetilde{n}^*$ is the perturbed peak of the energy landscape. This enables us to obtain a simple expression

$$\sigma_s \approx \frac{\widetilde{A}(n^*)}{A(1)} \exp\left(F(2) - F(n^*)\right) \left(1 + \sqrt{\frac{2\pi}{-F''(n^*)}} \exp\left(\frac{-\alpha^2}{2(n^*)^2 F''(n^*)} + \frac{\alpha}{n^*}\right)\right)^{-1} . \tag{4.1.30}$$

As for the average failure time, $\langle \tau_f \rangle$, we can neglect the final term as the outer sum begins with $i = n^*$ which makes it small for reasons discussed in section 4.1.2.2. Again if j is changed to $m+1$ in the remaining inner sum, we have an expression similar to the inner sum in equation (4.1.19), which as long as $n^* \gg 1$ and $F(n^*) \gg 1$ this would cancel with part of the contribution from σ_s. Together with the assumption that the barrier is initially steep, this cancellation leaves us with a simple formulation

$$\langle \tau_f \rangle \approx \frac{\exp(F(2))}{A(1)} \Big(\exp(-F(2)) + \exp(-F(3)) + \exp(-F(4)) + \cdots \Big) , \tag{4.1.31}$$

which only contains information about the base of the barrier since the majority of particles fail quickly.

Table 4.2 displays the fraction of success σ_s and the average failure time $\langle \tau_f \rangle$ for a selection of one-dimensional energy barriers. The simulated fraction of success σ_s and the exact sum through equation (4.1.28) show excellent agreement. The error from the one-dimensional simulation is within the accuracy displayed, even for the case $n^* = 200$ and $F^* = 20$ which is an extremely high barrier but we collated enough crossing to produce good statistics. The approximation of σ_s (4.1.30) is also a good result obtaining reasonably precise values, with greater accuracy for high barriers with a steep initial slope. The simulated average failure time $\langle \tau_f \rangle$ and the detailed approximation (4.1.29) also show excellent agreement. However, since the approximation includes occasional successful crossing times, the values for the smaller barriers are affected, for $F^* = 10$ the times are marginally longer as expected. We also display average failure times from a much simpler expression (4.1.31) including terms upto $\exp(-F(5))$, which relies on a steep initial slope of the barrier. The agreement is generally within 10% of the simulated failure times apart from the case $n^* = 200$ and $F^* = 10$ which is a long flat barrier.

In this section, there were two distinct approaches to making continuum approximations for barrier crossing. From our analogous continuous system,

	$n^* = 50$ $F^* = 10$	$n^* = 100$ $F^* = 15$	$n^* = 200$ $F^* = 10$	$n^* = 200$ $F^* = 20$
Simulated σ_s	5.28×10^{-5}	3.54×10^{-7}	1.49×10^{-5}	1.94×10^{-9}
(4.1.28)	5.28×10^{-5}	3.53×10^{-7}	1.50×10^{-5}	1.96×10^{-9}
(4.1.30)	5.34×10^{-5}	3.80×10^{-7}	1.81×10^{-5}	2.21×10^{-9}
Simulated $\langle \tau_f \rangle$	0.920	0.856	1.57	0.867
(4.1.29)	0.923	0.856	1.58	0.867
(4.1.31)	0.830	0.798	1.08	0.808

Table 4.2: We present fraction of success values σ_s and average failure times $\langle \tau_f \rangle$ for a selection of one-dimensional energy barriers, using the basic set of rate kinetics $A(i) = 2i^{0.666}$. Comparing simulated results with the exact expression (4.1.28) and the approximation (4.1.30) for the fraction of success. As well as analysing simulated average failure times with a detailed approximation (4.1.29) and a simple initial approximation (4.1.31).

we derived an equation (4.1.15) to calculate the average crossing time. Alternatively, we made several assumptions on the energy landscape to adapt a result from the general discrete system to produce the superb estimates (4.1.19) and (4.1.20). We then developed this result further using integrals to generate an approximation of the average crossing time (4.1.27), which has few requirements about the initial slope and peak of the barrier. We also used our integral approximation techniques, to develop our calculation, specific to the rotation model, providing us with simple equations for the fraction of success (4.1.30) and average failure time (4.1.31).

4.1.3 Probability distribution of crossing times

The aim of this section is to analytically derive the full probability distributions of nucleation times, rather than concentrating solely on the average. We develop a powerful method using Laplace transforms. Section 4.1.3.1 studies a basic three-state system and this is built upon significantly in section 4.1.3.2 which investigates an n-state system. We then display a neat approach to finding the average and the variance of the distribution of crossing times from Laplace space in section 4.1.3.3.

4.1.3.1 Three-state system

We aim to analytically derive the distribution of crossing times over a simple fixed barrier with 3 states, see figure 4.3. A crossing event is a particle travelling from state 1 to state 3 via any route, and once it has reached state 3 it is blocked from returning. For a general one-dimensional system the rates between adjacent states k_i^+ and k_i^-, are known from equation (3.1.8). For

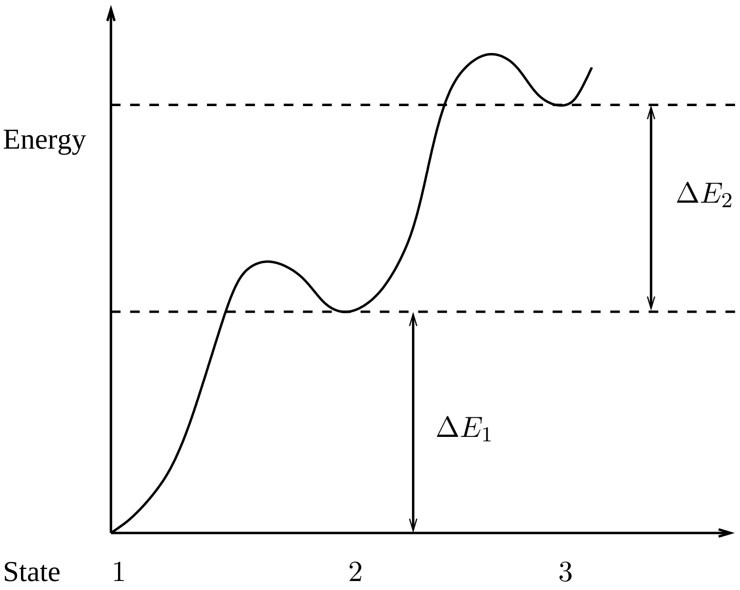

Figure 4.3: Simple system with three states and a static energy barrier.

convenience we initially assume the energy barrier is always increasing i.e. $\Delta E_i > 0$, simply to remove the minimum function, this is easily generalised in section 4.1.3.2. We begin the investigation of this system by defining $n_1(t)$ to be the fraction of particles which remain in state 1 after time, t. Consequently the instantaneous probability of a particle leaving state 1 at time, t, is

$$P_1^+(t) = -\frac{\mathrm{d}n_1(t)}{\mathrm{d}t} = k_1^+ n_1(t) = A(1)\exp\left(-\Delta E_1\right) n_1(t) \ , \tag{4.1.32}$$

with $\Delta E_1 = F(2) - F(1)$. Letting $f_1 = \exp\left(-\Delta E_1\right)$, therefore

$$n_1(t) = \exp\left(-A(1) f_1 t\right) \ ,$$

and hence the instantaneous probability is

$$P_1^+(t) = A(1) f_1 \exp\left(-A(1) f_1 t\right) \ .$$

If we then consider a particle in state 2, it has two options to escape with separate rate constants $k_1^- = A(1)$ and $k_2^+ = A(2)\exp\left(-\Delta E_2\right) = A(2) f_2$ respectively. Following a similar argument, the instantaneous probabilities of a particle leaving state 2 to either state 1 or state 3 at a time, t, are

$$\begin{aligned} P_2^-(t) &= A(1)\exp\left(-\left(A(1) + A(2) f_2\right) t\right) \ , \\ P_2^+(t) &= A(2) f_2 \exp\left(-\left(A(1) + A(2) f_2\right) t\right) \ . \end{aligned}$$

The crossing time distribution of interest is $P_{1,3}(t)$, which is the probability distribution of a particle travelling from state 1 to state 3 in any number of steps. Similarly $P_{2,3}(t)$ is defined to be the distribution of times from state 2 to state 3 with the particle potentially dropping back into state 1 in the intervening time. We have the inbuilt assumption that this system is memoryless, justified by the amount of time a particle spends in each state is long enough to neglect any small initial fluctuations in the energy landscape due to a recent move. Hence these probability distributions can be expressed in two coupled integral equations

$$P_{1,3}(t) = \int_0^t P_1^+(t')P_{2,3}(t-t')\mathrm{d}t' \ , \tag{4.1.33a}$$

$$P_{2,3}(t) = \int_0^t P_2^-(t')P_{1,3}(t-t')\mathrm{d}t' + P_2^+(t) \ . \tag{4.1.33b}$$

To make progress these equations can be Laplace transformed using the convolution theorem to obtain

$$\bar{P}_{1,3}(s) = \bar{P}_1^+(s)\bar{P}_{2,3}(s) \ , \tag{4.1.34a}$$

$$\bar{P}_{2,3}(s) = \bar{P}_2^-(s)\bar{P}_{1,3}(s) + \bar{P}_2^+(s) \ , \tag{4.1.34b}$$

which can be rearranged to find $\bar{P}_{1,3}(s)$ and $\bar{P}_{2,3}(s)$ in terms of known Laplace transforms

$$\bar{P}_{1,3}(s) = \frac{\bar{P}_1^+(s)\bar{P}_2^+(s)}{1-\bar{P}_1^+(s)\bar{P}_2^-(s)} \quad \text{and} \quad \bar{P}_{2,3}(s) = \frac{\bar{P}_2^+(s)}{1-\bar{P}_1^+(s)\bar{P}_2^-(s)} \ , \tag{4.1.35}$$

$$\text{with} \quad \bar{P}_1^+(s) = \frac{A(1)f_1}{s+A(1)f_1} \ , \quad \bar{P}_2^+(s) = \frac{A(2)f_2}{s+A(1)+A(2)f_2} \ ,$$

$$\text{and} \quad \bar{P}_2^-(s) = \frac{A(1)}{s+A(1)+A(2)f_2} \ . \tag{4.1.36}$$

Solving the system through substitution

$$\bar{P}_{1,3}(s) = \frac{A(1)A(2)f_1f_2}{(s+A(1)+A(2)f_2)(s+A(1)f_1)-A(1)^2f_1} \ , \tag{4.1.37a}$$

$$\bar{P}_{2,3}(s) = \frac{A(2)f_2(s+A(1)f_1)}{(s+A(1)+A(2)f_2)(s+A(1)f_1)-A(1)^2f_1} \ . \tag{4.1.37b}$$

The minor details of these results are of little importance, the main point is that the Laplace transform method is applicable to these convoluted systems. With this proof of concept, we investigate the more general n-state system in section 4.1.3.2.

4.1.3.2 The n-state system

In this section we present a method to analytically derive the probability distribution of a particle traversing an increasing multi-step energy barrier. We start by modifying the system in section 4.1.3.1 to four states; and we are solely interested in the probability distribution $P_{1,4}(t)$. Using the same argument that introduces the set of equations (4.1.33), we obtain an elaborate system of equations for the four state system in Laplace space

$$\bar{P}_{1,4}(s) = \bar{P}_1^+(s)\bar{P}_{2,4}(s) \ , \tag{4.1.38a}$$

$$\bar{P}_{2,4}(s) = \bar{P}_2^-(s)\bar{P}_{1,4}(s) + \bar{P}_2^+(s)\bar{P}_{3,4}(s) + \ , \tag{4.1.38b}$$

$$\bar{P}_{3,4}(s) = \bar{P}_3^-(s)\bar{P}_{2,4}(s) + \bar{P}_3^+(s) \ . \tag{4.1.38c}$$

These can be easily solved, by working from the bottom up, and we acquire an explicit solution for the Laplace transform of $P_{1,4}(t)$,

$$\begin{aligned}
\bar{P}_{1,4}(s) &= \frac{\bar{P}_1^+(s)\bar{P}_2^+(s)\bar{P}_3^+(s)}{1-\bar{P}_1^+(s)\bar{P}_2^-(s)-\bar{P}_2^+(s)\bar{P}_3^-(s)} \ , \qquad (4.1.39)\\
\text{with} \quad \bar{P}_i^+(s) &= \frac{A(i)f_i}{s+A(i-1)+A(i)f_i} \ ,\\
\bar{P}_i^-(s) &= \frac{A(i-1)}{s+A(i-1)+A(i)f_i} \quad \text{for} \quad i>1 \ ,
\end{aligned}$$

and $\bar{P}_1^+(s)$ is defined as in equation (4.1.36). We use the same approach for a higher number of states and below is a summary of the results

$$\text{defining} \quad R_i(s) = \bar{P}_i^+(s)\bar{P}_{(i+1)}^-(s) \quad \text{and} \quad Q_{i,j}(s) = \prod_{k=i}^{j} \bar{P}_k^+(s) \ ,$$

$$\bar{P}_{1,5}(s) = Q_{1,4}(s) / \left[1-R_1(s)-R_2(s)-R_3(s)+R_1(s)R_3(s)\right] \ ,$$

$$\bar{P}_{1,6}(s) = Q_{1,5}(s) \Bigg/ \left[1-\sum_{i=1}^{4}R_i(s)+R_1(s)R_3(s)+R_1(s)R_4(s)+R_2(s)R_4(s)\right] \ ,$$

$$\bar{P}_{1,7}(s) = Q_{1,6}(s) \Bigg/ \left[1-\sum_{i=1}^{5}R_i(s)+\sum_{i=1}^{3}\sum_{j=i+2}^{5}R_i(s)R_j(s)-R_1(s)R_3(s)R_5(s)\right] \ .$$

This pattern continues and enables us to write down an expression for an n-state system, which we prove by induction

$$\bar{P}_{1,n}(s) = Q_{1,(n-1)}(s)/U_{1,n}(s) \ , \qquad (4.1.40)$$

$$U_{i,n}(s) = 1+\sum_{m=1}^{\lfloor n/2 \rfloor}(-1)^m \sum_{k_1=i}^{n-2m}\ \sum_{k_2=k_1+2}^{n-2(m-1)}\ \sum_{k_3=k_2+2}^{n-2(m-2)} \cdots \sum_{k_m=k_{m-1}+2}^{n-2}\ \prod_{j=1}^{m} R_{k_j}(s) \ ,$$

for $i \leq n$. The aim is to find $\bar{P}_{1,n}(s)$ from the following set of equations

$$\begin{aligned}
\bar{P}_{1,n}(s) &= \bar{P}_1^+(s)\bar{P}_{2,n}(s) \ , && (4.1.41a)\\
\bar{P}_{2,n}(s) &= \bar{P}_2^-(s)\bar{P}_{1,n}(s)+\bar{P}_2^+(s)\bar{P}_{3,n}(s) \ , && (4.1.41b)\\
&\ \vdots\\
\bar{P}_{(n-2),n}(s) &= \bar{P}_{(n-2)}^-(s)\bar{P}_{(n-3),n}(s)+\bar{P}_{(n-2)}^+(s)\bar{P}_{(n-1),n}(s) \ , && (4.1.41c)\\
\bar{P}_{(n-1),n}(s) &= \bar{P}_{(n-1)}^-(s)\bar{P}_{(n-2),n}(s)+\bar{P}_{(n-1)}^+(s) \ . && (4.1.41d)
\end{aligned}$$

Our inductive hypothesis is

$$\bar{P}_{i,n}(s) = \frac{\bar{P}_i^-(s)\bar{P}_{(i-1),n}(s)U_{(i+1),n}(s)+Q_{i,(n-1)}(s)}{U_{i,n}(s)} \ , \qquad (4.1.42)$$

for $1 < i < n-1$ and following the example of the four state system (4.1.38) which are solved from the bottom up, we use induction on decreasing i and hence the base step is for $i = n-2$. Using equations (4.1.41c) and (4.1.41d), we find that

$$\bar{P}_{(n-2),n}(s) = \frac{\bar{P}^{-}_{(n-2)}(s)\bar{P}_{(n-3),n}(s) + Q_{(n-2),(n-1)}(s)}{1 - R_{n-2}(s)} ,$$

since $U_{(n-1),n}(s) = 1$ and $U_{(n-2),n}(s) = 1 - R_{n-2}(s)$, the base step holds. $U_{i,n}(s)$ has a useful recurrence relation

$$U_{(i-1),n}(s) = U_{i,n}(s) - R_{i-1}(s)U_{(i+1),n}(s), \text{ for } 2 \leq i \leq n , \tag{4.1.43}$$

and this allows us to complete the inductive step. Assuming

$$\bar{P}_{i,n}(s) = \frac{\bar{P}^{-}_{i}(s)\bar{P}_{(i-1),n}(s)U_{(i+1),n}(s) + Q_{i,(n-1)}(s)}{U_{i,n}(s)} ,$$

and from (4.1.41) we have

$$\bar{P}_{(i-1),n}(s) = \bar{P}^{-}_{(i-1)}(s)\bar{P}_{(i-2),n}(s) + \bar{P}^{+}_{(i-1)}(s)\bar{P}_{i,n}(s) ,$$

for $2 < i < n-1$ and manipulating, through the use of (4.1.43), we obtain

$$\bar{P}_{(i-1),n}(s) = \frac{\bar{P}^{-}_{(i-1)}(s)\bar{P}_{(i-2),n}(s)U_{i,n}(s) + Q_{(i-1),(n-1)}(s)}{U_{(i-1),n}(s)} .$$

The inductive step holds up to $\bar{P}_{2,n}(s)$ and this enables us to finish the calculation using equations (4.1.41b) and (4.1.41a), obtaining the result (4.1.40). This method has given us an expression for the distribution of crossing times in Laplace space, which can either be numerically inverted, as the following example will display, or be manipulated to find the average crossing time and variance, as shown in section 4.1.3.3.

4.1.3.2.1 Worked example of the four-state calculation To explain how the object $\bar{P}_{1,n}(s)$ in Laplace space is transformed into the probability distribution $P_{1,n}(t)$, it is useful to consider an example. For a given static energy barrier with the form $F(i) = 0.5(i-1)^{2/3}$ and, for simplicity, $A(i) = 1$, initially we shall concentrate on the four-state system, our goal is to find the probability distribution $P_{1,4}(t)$. Working to three significant figures, we substitute all of the relevant information into equation (4.1.39), obtaining

$$\begin{aligned}\bar{P}_{1,4}(s) &= \frac{\left(\frac{f_1}{s+f_1}\right)\left(\frac{f_2}{s+1+f_2}\right)\left(\frac{f_3}{s+1+f_3}\right)}{1 - \frac{f_1}{(s+f_1)(s+1+f_2)} - \frac{f_2}{(s+1+f_2)(s+1+f_3)}} \\ &= \frac{f_1 f_2 f_3}{(s+f_1)(s+1+f_2)(s+1+f_3) - f_1(s+1+f_3) - f_2(s+f_1)} ,\end{aligned}$$

with $f_1 = \exp(-\Delta E_1) = \exp(-0.5) = 0.607$, and similarly $f_2 = 0.746$ and $f_3 = 0.782$. In order to perform the inverse Laplace transform, we need to find the roots of the denominator, namely

$$\begin{aligned}&(s+f_1)(s+1+f_2)(s+1+f_3) - f_1(s+1+f_3) - f_2(s+f_1) \\ &= (s+0.101)(s+1.257)(s+2.775) ,\end{aligned}$$

and the method of partial fractions can be applied to obtain

$$\bar{P}_{1,4}(s) = 0.353\left(\frac{0.324}{s+0.101} - \frac{0.579}{s+1.257} + \frac{0.246}{s+2.775}\right) .$$

This Laplace transform is inverted by inspection

$$P_{1,4}(t) = 0.114\exp(-0.101t) - 0.204\exp(-1.257t) + 0.087\exp(-2.775t) , \tag{4.1.44}$$

notice that all three exponentials are decaying and when t is large $P_{1,4}(t)$ is dominated by the first term which decays the slowest. Figure 4.4 shows $P_{1,4}(t)$ compared to a simulated distribution, using a basic one-dimensional kinetic Monte Carlo simulation with the rates between states given by equation (3.1.8). The reason the probability distributions for these multi-step cases begin at $P(0) = 0$ is because the fastest route to success still requires multiple moves, each of which has an exponential distribution, so for early t the chance of success is small. The agreement for data is superb and even demonstrates the non-exponential early nature of these distributions. To confirm the extension of this method we also display $P_{1,21}(t)$ against the simulation, calculated by numerically determining the singularities of $\bar{P}_{1,21}(s)$ which is done by finding roots of high order polynomials and then applying partial fractions in order to invert and this also results in a series of exponentials with a single dominant timescale. Due to the nested sums within equation (4.1.40), the scope of this method is limited, by practicality, to a modest number of states.

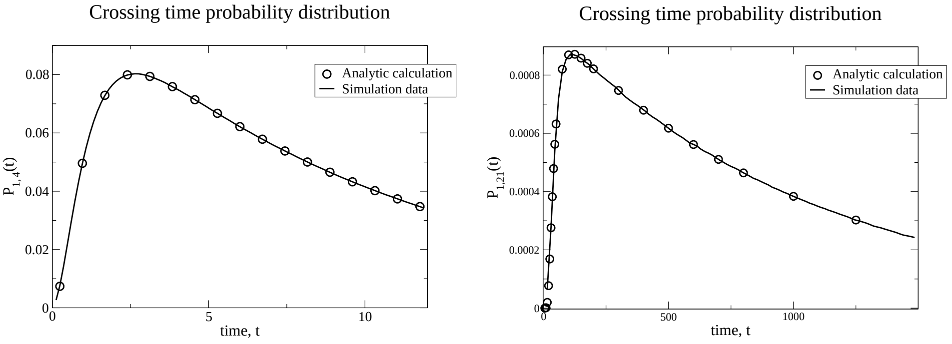

(a) (b)

Figure 4.4: (a) Probability distribution for the four state system, $P_{1,4}(t)$, comparing simulation data with the analytic calculation (4.1.44). (b) Similar probability distribution for a system with $n = 21$, showing $P_{1,21}(t)$ for both simulation data and the analytic calculation.

$F(i) = 0.5(i-1)^{2/3}$	Analytic calculation		Simulation data	
	Average $\langle\tau\rangle$	$\sigma/\langle\tau\rangle$	Average $\langle\tau\rangle$	$\sigma/\langle\tau\rangle$
$P_{1,2}(t)$	1.65	1.00	1.65	1.00
$P_{1,3}(t)$	5.20	0.915	5.20	0.915
$P_{1,4}(t)$	11.0	0.899	11.0	0.899
$P_{1,5}(t)$	19.5	0.897	19.5	0.897
$P_{1,6}(t)$	31.2	0.900	31.2	0.900
$P_{1,10}(t)$	120	0.919	120	0.919
$P_{1,15}(t)$	380	0.940	380	0.940
$P_{1,21}(t)$	1.10×10^3	0.959	1.10×10^3	0.959

Table 4.3: This table displays both calculated and simulated data for increasingly higher potentials of the form $F(i) = 0.5(i-1)^{2/3}$. The average crossing time, $\langle\tau\rangle$, is calculated using equation (4.1.46); we also show the ratio of the standard deviation and the average, $\sigma/\langle\tau\rangle$, using (4.1.47) to calculate the variance.

4.1.3.3 Average crossing time and variance from probability distribution in Laplace space

While the general shape of these probability distributions is of interest, an important piece of information is the average crossing time defined as

$$\langle\tau\rangle = \int_0^\infty tP(t)\mathrm{d}t \ . \tag{4.1.45}$$

However, there is an alternative method for determining $\langle\tau\rangle$ from the Laplace transform $\bar{P}(s)$, with the aid of the final value theorem [78]

$$\begin{aligned} \langle\tau\rangle = \lim_{t\to\infty} f(t) \ \text{ where } \ f(t) = t - \int_0^t P(t')(t-t')\mathrm{d}t' \ , \\ \text{hence } \ \langle\tau\rangle = \lim_{s\to 0}\left[s\bar{f}(s)\right] = \lim_{s\to 0}\left[\frac{1}{s}\left(1-\bar{P}(s)\right)\right] \ . \end{aligned} \tag{4.1.46}$$

This approach is far simpler than finding the full probability distribution from Laplace space. Another key measure of these distributions is the variance, defined as

$$\sigma^2 = \int_0^\infty t^2P(t)\mathrm{d}t - \langle\tau\rangle^2 \ .$$

We can again use the final value theorem to find σ^2 from $\bar{P}(s)$ in Laplace space, similarly to above

$$\begin{aligned} \sigma^2 &= \lim_{t\to\infty}\left[t^2 + 2\langle\tau\rangle t - \langle\tau\rangle^2 + \int_0^t P(t')(t-t')^2\mathrm{d}t'\right] \ , \\ \sigma^2 &= \lim_{s\to 0}\left[\frac{2}{s^2} + \frac{2\langle\tau\rangle}{s} - \langle\tau\rangle^2 + \frac{2\bar{P}(s)}{s^2}\right] \ . \end{aligned} \tag{4.1.47}$$

The great advantage of results (4.1.46) and (4.1.47), is that we are not required to do a potentially expensive numerical inverse Laplace transform. There is also a significant amount of information contained in the function $\bar{P}(s)$, setting $s = 0$ gives the total probability which for complete systems should be unity. If the Taylor expansion of this Laplace function is readily available, then the first and second moments are the mean and variance respectively. As we shown in section 4.1.3.2.1, the poles of $\bar{P}(s)$ are key to the inverse Laplace transform as they are linked to the exponential decay functions in the probability distributions. Consequently, the smallest pole in terms of magnitude will produce the dominant decay rate of the solution. Additionally, these techniques are widely applicable to any crossing time distribution in Laplace space which becomes useful for investigating dynamic barriers in section 4.2.

In table 4.3 we present a comparison between the average crossing time, $\langle\tau\rangle$, and the ratio of the standard deviation and the average, $\sigma/\langle\tau\rangle$, for barriers that have a progressively greater number of steps and are increasing in height. The first point to make is that the calculation produces excellent agreement with simulation's average and variance, although, as we have already shown we can find the full distribution of crossing times, so that was expected. The idea behind analysing the ratio $\sigma/\langle\tau\rangle$, is that for a perfectly exponential distribution this ratio is unity. For example in the case of $P_{1,2}(t)$ which just requires one step, is a truly memoryless process so must fit the exponential distribution. The ratio for small barriers with few steps is around 0.9, but with increasing barrier height it slowly tends towards one. As we are mainly interested in long ($n^* \gg 1$) and high ($F(n^*) \gg 1$) energy barriers, in which particles regularly revisit the base state, our systems become memoryless. We assume that crossing times fit the exponential distribution, this is important because a nucleation rate can be computed solely from the average crossing time. In the case of flat, low barriers the crossing times are certainly not exponential, due to the lack of a memoryless property in that they do not naturally return to the base of the barrier as often.

In this section, we have presented a method that successfully determines the probability distribution of energy barrier crossing times. The main result, (4.1.40), is for an n-state system and was proved by induction. The approach is involved due to the nested sums, which limits the practicality of this calculation. There is a possibility of coarse-graining the method by grouping states together but this would reduce the accuracy. However, this method does provide us with a solid foundation to build on in section 4.2 in which we investigate dynamic barriers.

4.2 Dynamic energy barriers

In this section we investigate dynamic energy barriers by building on our static barrier techniques and results from section 4.1. With a view to our overall goal of creating a polymer nucleation model including rotation we introduce two key features; the particle has different energy barriers to cross to replicate different orientations, and also has the ability to reset if it returns to small states. We start by looking at a simple system in section 4.2.1 that contains a continuous random height and crucially is able to reset. Section 4.2.2 expands this simple system into an n-state energy barrier now with a discrete random path selector. Appendix C introduces a model similar to the one in section 4.2.1 but contains a barrier that slowly decreases in height with time. The intention is to model the effect of convection; but as this effect was found to be minimal, and not physically relevant to the rotation problem, we decided not to proceed down that line of research, although initial results showed that the problem is solvable.

4.2.1 Three state system with a random barrier height and reset capability

In this section, we create a system that will eventually lead to a fixed-angle nucleation model. Here we present a simple set-up in which when a particle enters state 2, the height of the final nucleation state 3 is selected at random. Additionally if the particle fails and falls back to state 1, then crucially the system is reset. To this end, we set the rate k_2^+, with a dependence on a random variable u

$$k_2^+(u) = \begin{cases} \exp\left(u - \Delta E_2\right) = f_2 e^u & f_2 e^u \leq 1 \ , \\ 1 & f_2 e^u > 1 \ , \end{cases}$$

where $f_2 = \exp\left(-\Delta E_2\right)$ is as defined in section 4.1.3.1 and with u uniformly distributed on $[-G, G]$ and for simplicity, the kinetics, $A(i)$, are not included. $G \geq 0$ is a parameter of the model, namely the amount the barrier height can rise or fall from the mean. To ensure $f_2 e^u < 1$ we choose G such that $f_2 e^G < 1$ so that only the upper definition of $k_2^+(u)$ is used when integrating the system. Once again, we consider the fraction of particles which remain in state 2 after time t, $n_2(t)$,

$$\begin{aligned} \frac{\mathrm{d}n_2(u,t)}{\mathrm{d}t} &= -(k_2^- + k_2^+(u))n_2(u,t) = -(1 + f_2 e^u)n_2(u,t) \ , \\ \text{thus} \ \ n_2(u,t) &= \exp\left(-\left(1 + f_2 e^u\right) t\right) \ . \end{aligned}$$

Hence $P_2^-(u,t)$ and $P_2^+(u,t)$ are defined as

$$\begin{aligned} P_2^-(u,t) &= k_2^- n_1(u,t) \ , \\ P_2^+(u,t) &= k_2^+(u) n_2(u,t) \ . \end{aligned}$$

Concentrating on $P_2^+(u,t)$, we eliminate the conditional probability $P(u)$, then

$$P_2^+(t) = \int_{-G}^{G} P_2^+(u,t)P(u)\mathrm{d}u = \int_{-G}^{G} \frac{f_2 e^u}{2G} \exp\left(-\left(1 + f_2 e^u\right) t\right)\mathrm{d}u \ .$$

We apply the Laplace transform at this stage

$$\bar{P}_2^+(s) = \int_0^\infty e^{-st} P_2^+(t)\mathrm{d}t = \frac{f_1}{2G}\int_0^\infty e^{-(s+1)t}\int_{-G}^{G} e^u \exp\left(-f_2 e^u t\right)\mathrm{d}u\mathrm{d}t \ ,$$

and reverse the order of integration and using the substitution
$v(u) = s + 1 + f_2 e^u$, we obtain

$$\bar{P}_2^+(s) = \frac{1}{2G}\int_{v(-G)}^{v(G)} \frac{1}{v}\mathrm{d}v = \frac{1}{2G}\ln\left(\frac{s+1+f_2e^G}{s+1+f_2e^{-G}}\right) \ . \tag{4.2.1}$$

For $P_2^-(t)$, we use conditional probability and Laplace transform to obtain

$$\bar{P}_2^-(s) = \frac{1}{2G}\int_0^\infty e^{-(s+1)t}\int_{-G}^{G} \exp\left(-f_2 e^u t\right)\mathrm{d}u\mathrm{d}t \ .$$

As before we can reverse the order of integration and use the substitution $v(u) = s + 1 + f_2 e^u$ which, after a little manipulation, becomes

$$\bar{P}_2^-(s) = \frac{1}{2G(s+1)}\left[2G + \ln\left(s+1+f_2e^{-G}\right) - \ln\left(s+1+f_2e^{G}\right)\right] \ . \tag{4.2.2}$$

Our aim is to find $\bar{P}_{1,3}(s)$ in order to calculate average crossing times, which we can obtain from equation (4.1.35) with $\bar{P}_1^+(s)$ defined by (4.1.36),

$$\bar{P}_{1,3}(s) = \frac{f_1(s+1)\left[\ln\left(s+1+f_2e^G\right) - \ln\left(s+1+f_2e^{-G}\right)\right]}{2G(s+1)(s+f_1) - f_1\left[2G + \ln\left(s+1+f_2e^{-G}\right) - \ln\left(s+1+f_2e^{G}\right)\right]} \ . \tag{4.2.3}$$

Interestingly, if $G = 0$, i.e. the barrier is always set at the mean height, then applying L'Hôpital's rule, equation (4.2.3) indeed reverts back to equation (4.1.37) as in the case of the static barrier.

We obtain average crossing times by using (4.1.46) from section 4.1.3.3,

$$\langle\tau\rangle_{1,3} = \lim_{s\to 0}\left[\frac{1}{s}\left(1 - \bar{P}_{1,3}(s)\right)\right] \ .$$

Investigating the leading order terms in s from this expression we can acquire the exact average time

$$\langle\tau\rangle_{1,3} = \frac{2G(1+f_1) + f_1\left[\ln\left(1+f_2e^G\right) - \ln\left(1+f_2e^{-G}\right)\right]}{f_1\left[\ln\left(1+f_2e^G\right) - \ln\left(1+f_2e^{-G}\right)\right]} \ . \tag{4.2.4}$$

For small enough, f_2e^G, this expression can be approximated using

$$\ln\left(1+f_2e^G\right) - \ln\left(1+f_2e^{-G}\right) \approx 2f_2\sinh G \quad \text{for} \quad f_2e^G \ll 1 \ ,$$

giving us a simple estimate

$$\langle\tau\rangle_{1,3} \approx \frac{G(1+f_1) + f_1f_2\sinh G}{f_1f_2\sinh G} = 1 + \frac{G}{f_2}\left(1 + \frac{1}{f_1}\right)\operatorname{csch} G \ . \tag{4.2.5}$$

Figure 4.5 displays average crossing times for $G = 0, 1, 2, 3$, comparing simulated times with exact and approximate analytic data. As the graph shows,

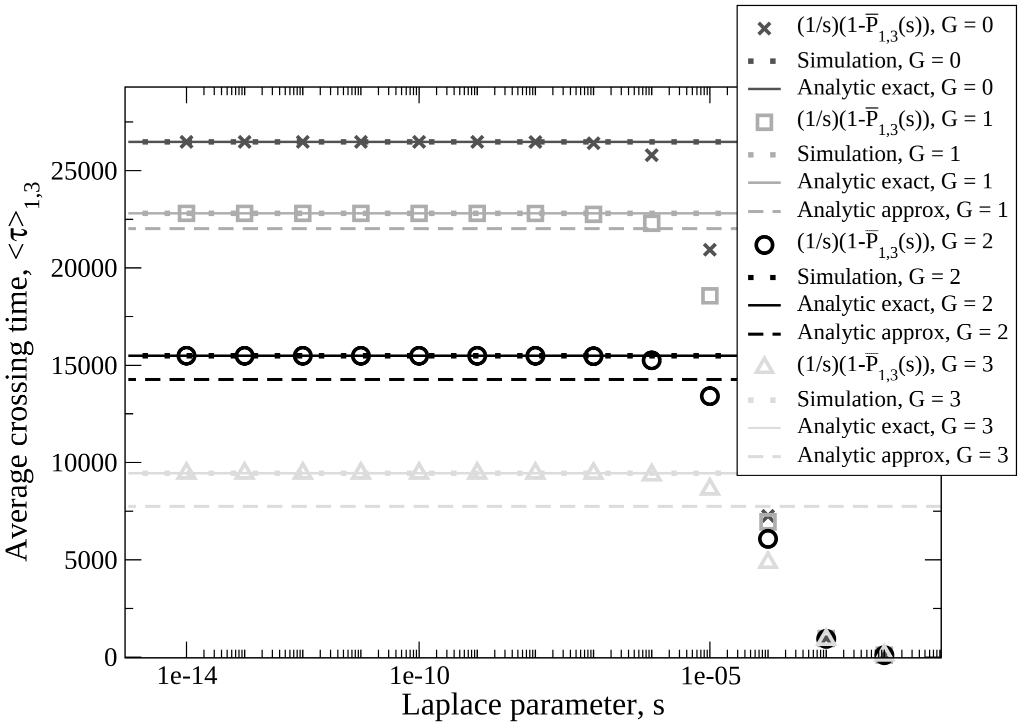

Figure 4.5: Comparison of average crossing times of simulations with the exact analytic expression (4.2.4) and the approximated version (4.2.5) for $G = 0, 1, 2, 3$.

for small enough s the expression $(1/s)(1 - \bar{P}_{1,3}(s))$, gives the average crossing times; the analytic calculation displaying complete agreement with simulations. The estimated data is fairly good, but accuracy falls away for larger values of G as expected. The most important conclusion to take from this section is that the method has successfully solved this problem, and we have found average crossing times for our system. The crucial new component is the ability to find $\bar{P}_2^-(s)$ and $\bar{P}_2^+(s)$ which include conditional probabilities. In section 4.2.2 we modify and expand this basic set-up to more appropriately replicate the effects of rotation on polymer nucleation.

4.2.2 $n + 1$ state energy barrier with a discrete random path selector

In this section, we further develop the ideas of barrier choice and the ability to reset the energy landscape from section 4.2.1. Instead of a continuous array of potential barriers, here we concentrate on distinct pathways each with an individual probability of selection, as well as expanding the system to n states. We make use of several results from section 4.1.3.2, and adapt the induction method for static energy barriers. Section 4.2.2.1 presents a model in which the pathway is selected at the smallest possible state and that still retains the ability to reset the energy landscape. Additionally, we investigate the

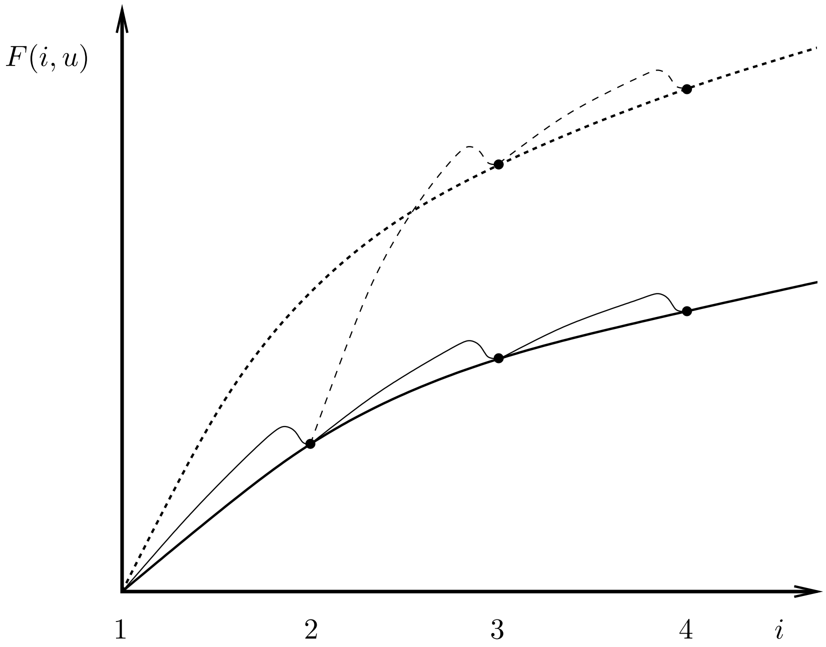

Figure 4.6: This diagram demonstrates a nucleation landscape with a choice of pathways to be selected at random upon arrival in a fixed state 2 from state 1, branching from state 3 onwards. The system is reset if and only if state 1 is revisited.

distribution of failure times using this approach, which is crucial to our rotation model. Section 4.2.2.2 adapts this system by delaying the selection point to a larger state.

4.2.2.1 Early pathway selection (state 1)

To model a nucleation process with alternative pathways, we begin with a model in which the energy landscape deviates as early as possible but is still able to be reset. Hence the path is randomly selected upon arrival in state 2 from state 1, and is only reset when the particle revisits state 1. Figure 4.6 displays the landscape. We modify the system from section 4.2.1 in two ways, first we discretise the continuous spread of random barrier heights, second we expand the system by altering the state of absorption from 3 to n. As before, the energy landscape is a balance between the reduction due to the bulk volume and the cost due to the surface area, which, when considering spheres, mapped to one dimension is

$$F(i) = -E_B(i-1) + E_S(i-1)^{2/3} \ . \tag{4.2.6}$$

To create separate pathways we modify this with a random variable u, which is able to take discrete values in the set $\{q\}$ with arbitrary probabilities $P(u=q)$. The energy landscape becomes

$$F(i,u) = -E_B(i-1) + (E_S+u)(i-1)^{2/3} \quad \text{for} \ \ i > 2 \ , \tag{4.2.7}$$

note that for $i = 2$ we still use equation (4.2.6) even if u is selected to be non-zero. Hence in a similar manner to section 4.1 we have

$$f_1 = \exp\left(-\left(F(2) - F(1)\right)\right) \ ,$$

and introducing the notation for the higher steps with the subscript in square brackets $[q]$ referring to the pathway chosen

$$f_{i,[q]} = \begin{cases} \exp\left(-\left(F(i+1,q) - F(i,0)\right)\right) \ , & \text{for} \ \ i = 2 \ , \\ \exp\left(-\left(F(i+1,q) - F(i,q)\right)\right) \ , & \text{for} \ \ i > 2 \ . \end{cases}$$

To clarify, particles start in state 1, upon arrival in a fixed state 2, a pathway to nucleation is then chosen at random. If the attempt is unsuccessful and the particle returns to state 1, the system is then reset. If we concentrate on strictly increasing barriers, we have the following definitions

$$\bar{P}_1^+(s) = \frac{A(1)f_1}{s + A(1)f_1} \ , \quad \bar{P}_{i,[q]}^+(s) = \frac{A(i)f_{i,[q]}}{s + A(i-1) + A(i)f_{i,[q]}} \ ,$$
$$\text{and} \ \ \bar{P}_{i,[q]}^-(s) = \frac{A(i-1)}{s + A(i-1) + A(i)f_{i,[q]}} \ .$$

To investigate decreasing barriers, it would be a simple exercise to switch around the positive and negative moves in the equations above.

The key objects we require to solve for in this system are the probability distributions of success and failure once the pathway has been selected. Defining $P_{2,n/1,[q]}(t)$ as the probability distribution of a particle in state 2 on pathway q, finishing in state n but not visiting state 1 en route, and $P_{2,1/n,[q]}(t)$ as the distribution of times of a particle starting in state 2 on pathway q, finishing in state 1 but not reaching state n at any point. Mathematically the Laplace transform of $P_{2,n/1,[q]}(t)$ can be found in a similar way to $\bar{P}_{1,n}(s)$ in equation (4.1.40) and can be proved using the same inductive method. This approach gives us the result

$$\bar{P}_{2,n/1,[q]}(s) = \frac{Q_{2,(n-1),[q]}(s)}{U_{2,n,[q]}(s)} \ , \tag{4.2.8}$$

with the objects $Q_{2,(n-1),[q]}(s)$ and $U_{2,n,[q]}(s)$ defined similarly to those in section 4.1.3.2. To find $\bar{P}_{2,1/n}(s)$ momentarily ignoring the particular pathway, we have the following set of equations

$$\bar{P}_{2,1/n}(s) = \bar{P}_2^-(s) + \bar{P}_2^+(s)\bar{P}_{3,1/n}(s) \ , \tag{4.2.9a}$$

$$\bar{P}_{3,1/n}(s) = \bar{P}_3^-(s)\bar{P}_{2,1/n}(s) + \bar{P}_3^+(s)\bar{P}_{4,1/n}(s) \ , \tag{4.2.9b}$$

$$\vdots$$

$$\bar{P}_{(n-2),1/n}(s) = \bar{P}_{(n-2)}^-(s)\bar{P}_{(n-3),1/n}(s) + \bar{P}_{(n-2)}^+(s)\bar{P}_{(n-1),1/n}(s) \ , \tag{4.2.9c}$$

$$\bar{P}_{(n-1),1/n}(s) = \bar{P}_{(n-1)}^-(s)\bar{P}_{(n-2),1/n}(s) \ . \tag{4.2.9d}$$

As in the proof in section 4.1 we use induction with i decreasing, effectively systematically solving equations (4.2.9) from the bottom up. Our inductive hypothesis for $3 \leq i \leq n-2$ is that

$$\bar{P}_{i,1/n}(s) = \frac{\bar{P}_i^-(s)U_{(i+1),n}(s)\bar{P}_{(i-1),1/n}(s)}{U_{i,n}(s)} \ . \tag{4.2.10}$$

The base of the induction is for $i = n-2$ and we show the base step holds by substituting $\bar{P}_{(n-1),1/n}(s)$ from equation (4.2.9d) into equation (4.2.9c) to obtain

$$\bar{P}_{(n-2),1/n}(s) = \frac{\bar{P}_{(n-2)}^-(s)U_{(n-1),n}(s)\bar{P}_{(n-3),1/n}(s)}{U_{(n-2),n}(s)} \ ,$$

taking advantage of the recurrence relation (4.1.43). To complete the inductive step we take one of the middle equations from (4.2.9) for $\bar{P}_{(i-1),1/n}(s)$ and substitute $\bar{P}_{i,1/n}(s)$ from our inductive hypothesis (4.2.10)

$$\begin{aligned} \bar{P}_{(i-1),1/n}(s) &= \bar{P}_{(i-1)}^-(s)\bar{P}_{(i-2),1/n}(s) + \bar{P}_{(i-1)}^+(s)\bar{P}_{i,1/n}(s) \ , \\ U_{i,n}(s)\bar{P}_{(i-1),1/n}(s) &= \bar{P}_{(i-1)}^-(s)U_{i,n}(s)\bar{P}_{(i-2),1/n}(s) \\ &\quad + R_{i-1}(s)U_{(i+1),n}(s)\bar{P}_{(i-1),1/n}(s) \ , \\ \text{therefore } \bar{P}_{(i-1),1/n}(s) &= \frac{\bar{P}_{(i-1)}^-(s)U_{i,n}(s)\bar{P}_{(i-2),1/n}(s)}{U_{(i-1),n}(s)} \ . \end{aligned}$$

This is justified until $i = 3$ in equation (4.2.10) and we can substitute this result into equation (4.2.9a) to obtain

$$\bar{P}_{2,1/n}(s) = \frac{\bar{P}_2^-(s)U_{3,n}(s)}{U_{3,n}(s) - R_2(s)U_{4,n}(s)} = \frac{\bar{P}_2^-(s)U_{3,n}(s)}{U_{2,n}(s)} \ . \tag{4.2.11}$$

To fully include all pathways, we use a similar idea to section 4.2.1 and sum up all the conditional probabilities

$$\bar{P}_{2,n/1}(s) = \sum_{\{q\}} P(u=q)\bar{P}_{2,n/1,[q]}(s) \ , \tag{4.2.12}$$

and similarly for $\bar{P}_{2,1/n}(s)$. To find the crossing time for the complete system, we need to evaluate $\bar{P}_{1,n}(s)$, which can be calculated explicitly using the following set of equations

$$\begin{aligned}
\bar{P}_{1,n}(s) &= \bar{P}_1^+(s)\bar{P}_{2,n}(s) \ , \\
\bar{P}_{2,n}(s) &= \bar{P}_{2,n/1}(s) + \bar{P}_{2,1/n}(s)\bar{P}_{1,n}(s) \ , \\
\text{therefore } \ \bar{P}_{1,n}(s) &= \frac{\bar{P}_1^+(s)\bar{P}_{2,n/1}(s)}{1-\bar{P}_1^+(s)\bar{P}_{2,1/n}(s)} \ .
\end{aligned} \tag{4.2.13}$$

From the explicit formula of $\bar{P}_{1,n}(s)$ we have two strategies to advance. First we can find the average crossing time using the method outlined in section 4.1.3.3. Alternatively we can numerically invert the Laplace transform to obtain the full probability distribution of crossing times.

To summarise, we have presented a system with multiple routes to nucleation. The distinct pathways that are selected on arrival into state 2 from state 1 each with an individual probability, and can only be reset if state 1 is revisited. This complex system is solved by being broken down into a series of static barriers, the two key results for each individual pathway were the success and failure distributions in Laplace space, equations (4.2.8) and (4.2.11) respectively. We then collected all potential pathways together using conditional probabilities in equation (4.2.12) for the overall distribution of successful crossing times, $\bar{P}_{2,n/1}(s)$, with a similar equation for the overall distribution of failure times, $\bar{P}_{2,1/n}(s)$. These results are then combined to find the full distribution in Laplace space for the whole system in equation (4.2.13). Since we have used the static n-state barrier results from section 4.1.3.2, the cost of evaluating $\bar{P}_{2,n/1}(s)$ and $\bar{P}_{2,1/n}(s)$ is still an issue due to the many nested sums, and so the scope of this method is limited. However the approach of breaking down our complex system in this way would still apply if $\bar{P}_{2,n/1}(s)$ and $\bar{P}_{2,1/n}(s)$ can be approximated for large n.

4.2.2.1.1 Probability distribution of failure times One of the important requirements for our rotation model is the ability to calculate the distribution of failure times given a known energy landscape and kinetics. In section 4.1.2.3, we produced a method for computing the average failure time. This does not, however, enable us to write down the distribution as an exponential, since the system is not inherently memoryless. It is sensible to assume that the distribution will be dominated by the majority of particles that either fail almost immediately or make a few positive steps but fall back to the base of the barrier quickly. Hence we intend to model the probability distribution of failure times using the inverse Laplace transform of equation (4.2.11). Figure 4.7 displays two such distributions and it is clear that the exponential distribution based on the average is a poor representation. The initial approximations on the other hand provide excellent accuracy and rapid convergence to the simulated data, especially as we have only shown the first three approximations. In the case of $P_{2,1/5}(t)$ which does not include particles that reach even state 5,

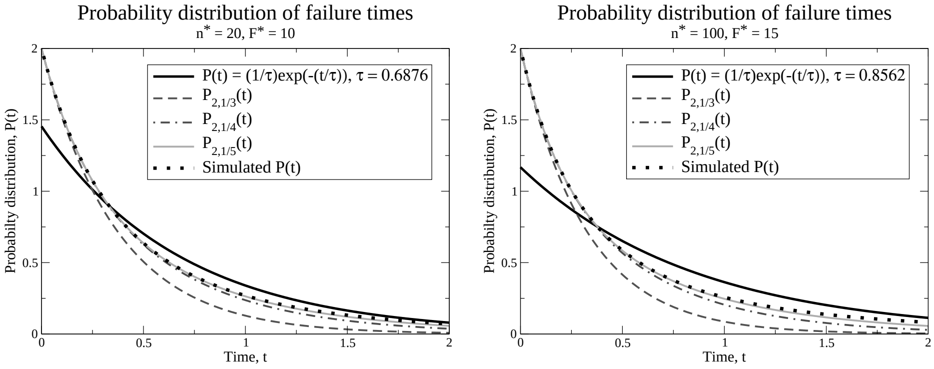

(a) (b)

Figure 4.7: Probability distributions of failure times for two energy barriers (a) $n^* = 20$, $F^* = 10$ and (b) $n^* = 100$, $F^* = 15$, both with an effective attachment area $A(i) = 2i^{2/3}$ displaying an exponential distribution based on the average time as well as the first three approximations against simulated data.

shows excellent agreement with the simulated failure distribution. This result allows us to model the distribution of failure times by considering just a small number of states at the base of the barrier, the number of states to include for suitable precision will depend on the initial steepness of the energy landscape. It provides an alternative to calculating the full distribution involving all states up to the point of nucleation which would be highly expensive due the nested sums in the object $U_{i,n}(s)$ in equation (4.1.40).

4.2.2.1.2 Example: Two potential pathways We test our method with a simple example, ensuring the energy landscape is strictly increasing by setting $E_B = 0$ and $E_S = 1$ in equations (4.2.6) and (4.2.7), to simplify the system we allow u to only take values $\{q\} = \{0, 0.5\}$ with equal probabilities, hence $P(u = 0) = P(u = 0.5) = 0.5$. Figure 4.8 displays both simulated and calculated probability distributions for $P_{1,3}(t)$, $P_{1,4}(t)$, $P_{1,7}(t)$, and $P_{1,11}(t)$ with excellent agreement.

4.2.2.2 Delayed pathway selection

In this section, we adapt the previous model, described in section 4.2.2.1 by allowing the location of the split point to be modified from state 2 to the state n_c+1. Hence the reset point is at state n_c. Taking inspiration from Jolley [46], we require that state n_c has a significantly lower energy level than n^*, as it is necessary that $F(n_c - 1) \ll F(n^*)$ to ensure state $n_c - 1$ is in the Boltzmann region. If we concentrate on a two stage system, as shown in figure 4.9, with this set-up a particle will spend the vast majority of its time occupying states below n_c. Once it arrives into state n_c, it then enters into our previous system

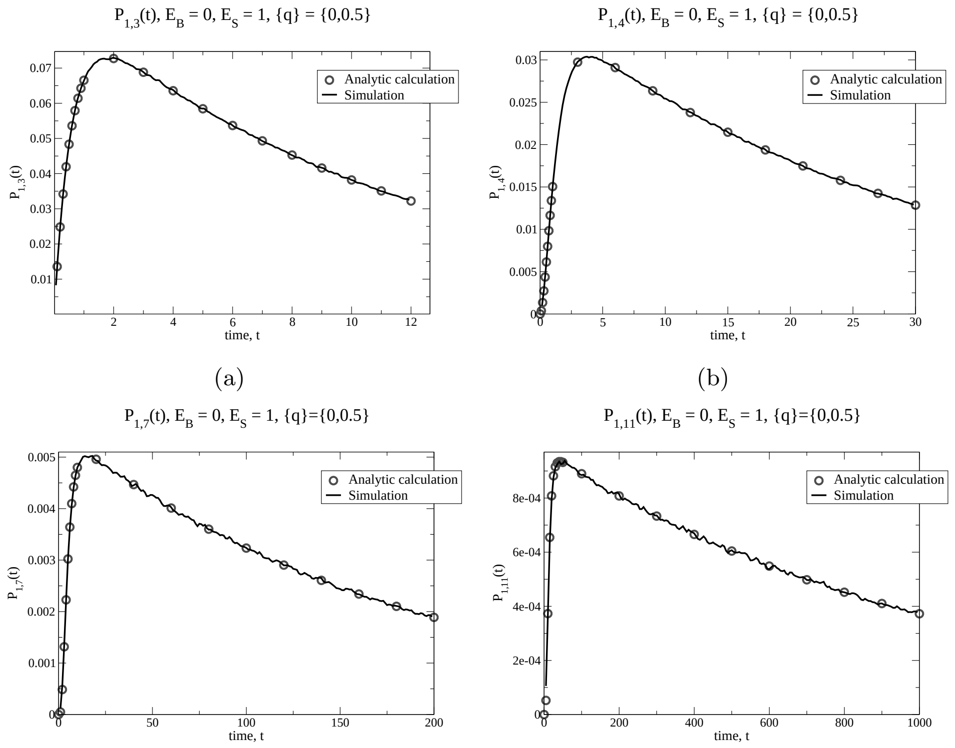

(a) (b) (c) (d)

Figure 4.8: Plots showing crossing time distributions for a system with two pathways to nucleation, deviating after state 1. We have compared simulation data with analytic calculation for (a) $P_{1,3}(t)$, (b) $P_{1,4}(t)$, (c) $P_{1,7}(t)$ and (d) $P_{1,11}(t)$.

described in section 4.2.2.1 with a random pathway selector. The object of interest is the fraction of particles that successfully nucleate by reaching state n_f, once entering state n_c, which we can find by working in Laplace space and translating equation (4.2.13), obtain

$$\begin{aligned} \bar{P}_{n_c,n_f/(n_c-1)}(s) &= \frac{\bar{P}_{n_c+}(s)\bar{P}_{(n_c+1),n_f/n_c}(s)}{1-\bar{P}_{n_c+}(s)\bar{P}_{(n_c+1),n_c/n_f}(s)}\ , \qquad (4.2.14)\\ \text{with}\ \ \bar{P}_{(n_c+1),n_f/n_c}(s) &= \frac{Q_{(n_c+1),(n_f-1)}(s)}{U_{(n_c+1),n_f}(s)}\ ,\\ \text{and}\ \ \bar{P}_{(n_c+1),n_c/n_f}(s) &= \frac{P_{(n_c+1)-}(s)U_{(n_c+2),n_f}(s)}{U_{(n_c+1),n_f}(s)}\ . \end{aligned}$$

To convert this from a quantity in Laplace space to a fraction of success, we use a similar method to section 4.1.3.3. Defining σ_c as the fraction that successfully nucleate from state n_c,

$$\sigma_c = \lim_{t\to\infty}\left[\int_0^t P_{n_c,n_f/(n_c-1)}(t')\mathrm{d}t'\right] = \lim_{t\to\infty} f(t)\ .$$

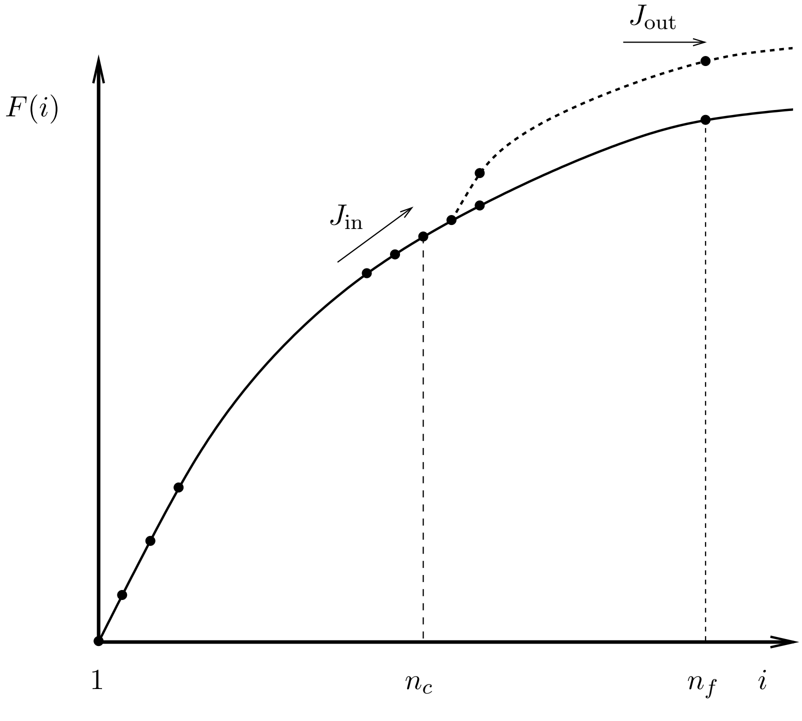

Figure 4.9: This diagram illustrates our system. From state 1 to state n_c it behaves as in the static case. Upon arrival into state $n_c + 1$ a pathway is selected at random for the particle to attempt to nucleate by reaching state n_f. J_{in} and J_{out} are the fluxes of particles entering state n_c from below and leaving the system by reaching state n_f per unit time respectively.

By writing the integral $f(t)$ as

$$f(t) = \int_0^t P_{n_c,n_f/(n_c-1)}(t')U(t-t')\mathrm{d}t' \text{ with } U(x) = 1 \ ,$$

we apply the convolution theorem together with the final value theorem to obtain

$$\sigma_c = \lim_{s\to 0}\left[s\bar{f}(s)\right] = \lim_{s\to 0}\left[\bar{P}_{n_c,n_f/(n_c-1)}(s)\right] \ . \tag{4.2.15}$$

The average time of a successful crossing from state n_c can be found in the same way as before but with a slight modification as the probability distribution must be normalised, the result is

$$\langle\tau\rangle_s = \lim_{s\to 0}\left[\frac{1}{s}\left(1 - \frac{\bar{P}_{n_c,n_f/(n_c-1)}(s)}{\sigma_c}\right)\right] \ , \tag{4.2.16}$$

although the overwhelmingly dominant contribution to the complete crossing time will be the amount of time the particle spends failing, so this quantity is unimportant.

By investigating the occupancy of state n_c-1, namely χ_{n_c-1}, with the fraction of success, σ_c, we aim to find the average crossing time for the complete system. If, a particle arrives at state n_f; we reflect it back down the barrier instead of it leaving the system, then an equilibrium can be reached. Furthermore, if a system is in equilibrium, we calculate the occupancy of each state, by finding the partition function $Z_p = \sum_i \exp(-F(i))$ which for steep barriers is dominated by the first few terms, hence $\chi_{n_c-1} = (1/Z_p)\exp(-F(n_c-1))$. Our system is not in equilibrium because particles leave at state n_f and new particles enter at state 1. However since these events are incredibly rare for high barriers, we say the system is effectively in equilibrium for states significantly below the maximum, n^*. Through this Boltzmann approximation we assert that $\chi_{n_c-1} \approx (1/Z_{\text{eff}})\exp(-F(n_c-1))$ where Z_{eff}, only includes the first few terms in the sum, being the effective partition function and this is valid for $F(n_c-1) \ll F(n^*)$. To progress, we focus on the section of landscape from state n_c to state n_f and look at the fluxes J_{in} and J_{out}, which are the number of particles entering this section into state n_c and the number of particles leaving the system at state n_f respectively per unit time. We know that $J_{\text{out}} = \sigma_c J_{\text{in}}$ and

$$J_{\text{in}} = \chi_{n_c-1}k^+_{n_c-1} \approx \frac{1}{\tau_0}\frac{\exp(-F(n_c-1))}{Z_{\text{eff}}}\exp\left(-(F(n_c)-F(n_c-1))\right) \ ,$$

$$J_{\text{in}} \approx \frac{1}{\tau_0 Z_{\text{eff}}}\exp(-F(n_c)) \text{ therefore } J_{\text{out}} \approx \frac{\sigma_c}{\tau_0 Z_{\text{eff}}}\exp(-F(n_c)) \ .$$

The average crossing time for the complete system is the inverse of the flux out of the system at state n_f, hence

$$\langle\tau\rangle_c \approx \frac{\tau_0 Z_{\text{eff}}}{\sigma_c}\exp(F(n_c)) \ . \tag{4.2.17}$$

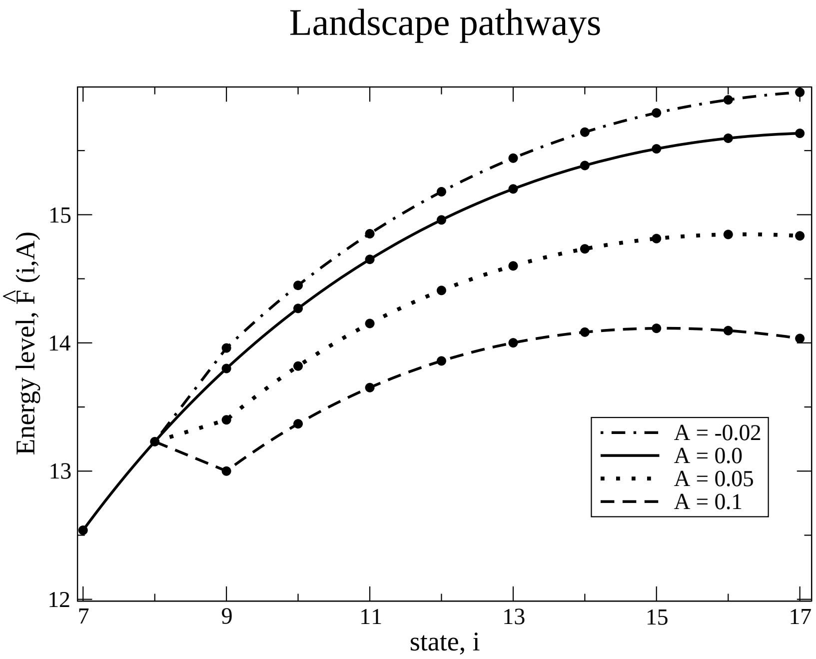

Figure 4.10: Separate energy landscapes for different values of A.

This calculation allows us to tune the point at which rotational effects become significant. It also improves the scope and would help enormously for narrow, high barriers, but we are still restricted for barriers with long, flat plateaus.

4.2.2.2.1 Example: delayed pathway selection In this example, we calculate the nucleation times over a barrier with $E_B = 1.9$ and $E_S = 7.25$, but on this occasion we create separate pathways slightly differently by modifying the bulk term

$$\Delta\widehat{F}(i,u) = -(E_B + u)(i-1) + E_S(i-1)^{2/3} \text{ for } i > n_c + 1 \ .$$

We select $n_c = 7$ and the nucleation point to be, $n_f = 17$ since for $u = 0$, the maximum is $n^* = 17$. Once a particle enters state $n_c + 1$ from state n_c a pathway is selected at random with probabilities $P(u = 0) = P(u = A) = 0.5$. Figure 4.10 shows the energy landscape for $A = -0.02, 0.0, 0.05, 0.1$, in the case of $A = 0.1$ the system is quite unphysical due to the energy barrier no longer being monotonically increasing to a single peak then decreasing as expected, but we are simply demonstrating that our calculation is correct no matter how strange the relative energy steps become. We calculate $\bar{P}_{7,17/6}(s)$ using equation (4.2.14) and to find the crossing times we numerically invert the Laplace transform to obtain $P_{7,17/6}(t)$. Figure 4.11 is a plot of simulated and analytic crossing times of a particle beginning in state $n_c = 7$ and nucleating at state $n_f = 17$ without dropping below state n_c for different values of A and the agreement is excellent. However, to obtain the key piece of information, the fraction of particles that successfully nucleate, σ_c, there is no need to

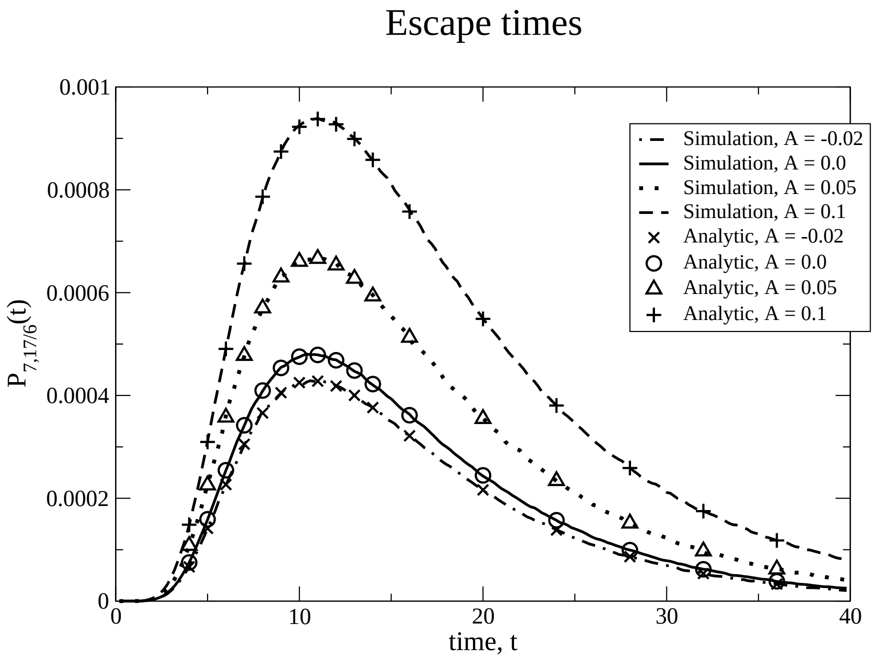

Figure 4.11: Distribution of crossing times for $P_{7,17/6}(t)$ for different values of A.

numerically invert the Laplace transform, instead we use equation (4.2.15). With σ_c known, we calculate the average crossing time for the complete system, $\langle\tau\rangle_c$, through equation (4.2.17), that is, beginning in state 1 and leaving at state n_f. Table 4.4 displays a summary of our results, and the agreement between analytic calculation and simulation is excellent for both the fraction of success from state n_c, σ_c, and the average crossing time for the complete system, $\langle\tau\rangle_c$.

A	Analytic		Simulation	
	σ_c	$\langle\tau\rangle_c$	σ_c	$\langle\tau\rangle_c$
–0.02	7.02×10^{-3}	3.99×10^{7}	7.01×10^{-3}	4.01×10^{7}
0.0	7.93×10^{-3}	3.54×10^{7}	7.92×10^{-3}	3.55×10^{7}
0.05	1.14×10^{-2}	2.46×10^{7}	1.14×10^{-2}	2.48×10^{7}
0.1	1.74×10^{-2}	1.61×10^{7}	1.74×10^{-2}	1.63×10^{7}

Table 4.4: The results of the fraction that successfully nucleate and the average total barrier crossing time for the complete system both for calculated and simulated data with different values of A.

4.3 Discussion

In this chapter we have thoroughly explored one-dimensional energy landscapes. Section 4.1 was focused completely on solving static barriers, particularly with finding average crossing times and probability distributions of crossing times. We presented a steady state occupancy method for finding average crossing times across discrete energy barriers, which produced several key results. In particular equation (4.1.4), which is an exact sum to determine the average crossing times over one-dimensional static barriers, and computationally inexpensive estimates (4.1.19) and (4.1.20). In addition, we calculated the fraction of particles that successfully nucleate (4.1.28) from a certain position on the landscape without falling back to the base, as well as the average failure time (4.1.29). Along with discrete results, we were able to make continuum approximations, which removed the need for large sums when $n^* \gg 1$. We also developed a method for obtaining the exact probability distribution of crossing times over a static one-dimensional barrier (4.1.40). Furthermore, we presented a crucial formula (4.1.46) for finding the average crossing times of these distributions in Laplace space without the need for an inversion. This probabilistic approach is extremely successful, but the scope is limited to modest n^* by practicality due to the nested sums in the main calculation.

In section 4.2, we built upon the static barrier techniques and results, and investigated dynamic barriers with a view to our overall objective of creating a polymer nucleation model that includes rotation. We began with a three state system that included a variable barrier height to reach the final state, which is selected at random upon arrival into the middle state and is reset if the particle re-visits the base state. The new component of this formulation was the introduction of conditional probabilities in the solution, which enabled us to break down the complex system into a series of static barriers. We further developed the method by discretising the potential pathways and expanding the nucleation state to n as well as having the option to adjust the selection point. This allows us to model the physical possibility of a crystal changing its angle relative to the flow by spending time in small configurations but not necessarily re-visiting the base of the barrier. The crucial element in the model is the ability to calculate the distribution of failure times once a pathway has been selected. Moreover, since these distributions are dominated by particles either falling back immediately or within their first few moves, it is not necessary to do a complete calculation of the rare long failure events. We can obtain an accurate approximate distribution by considering just a small number of states above the selection point, see figure 4.7. The discrete pathways are combined in Laplace space with equation (4.2.12), which then can be manipulated using equation (4.2.13) to obtain a crossing time distribution for the complete system.

Chapter 5

Rotation model of polymer nucleation

In this chapter, we present our show-piece model, of polymer nucleation including crystal rotation. We take advantage of a vital conclusion from the GO model [21, 22], which is the quasi-static result. This has been discussed in section 1.6.3 and is also relied upon throughout chapter 2. In fact, we have investigated the time taken for a nucleus to successfully grow directly from a single monomer to a stable nucleus, τ_s. That is not the expected time for nucleation to occur which is much longer and is dominated by failed crossing attempts. We found that $\tau_s \lesssim n_f \tau_0$, where n_f is the nucleation state and τ_0 is the base timescale of the model and related to single monomers movement. This result proved that within the GO model, this success timescale is significantly less than the smallest timescale in the GLaMM flow model, which is the Rouse time of an entanglement segment, hence $\tau_s \lesssim n_f \tau_0 \ll \tau_e$. It makes physical sense as particles are not likely to spend a large amount of time at the peak of an energy landscape without failing down either side. The quasi-static result permits us to study the system at fixed times and still witness transient behaviour with confidence. It is crucial to applying a rotational element because as we describe in this chapter, we assume that larger nuclei remain in the same orientation throughout a crossing attempt. Which enables us to develop an analytic model to study this multi-scale system.

To outline the chapter, we begin in section 5.1, and analyse the effects of the rotational elements within the successful Graham-Olmsted (GO) polymer simulation. In section 5.2, we explain a detailed calculation that replicates a physically relevant, simplified version of the GO simulation. We also produce a practical refinement of the calculation which enables us to increase the detail in the areas of most significance. Finally in section 5.3, we thoroughly test the model against nucleation times given by the fully resolved GO simulation in a crucial time period in the flow-induced crystallisation (FIC) of a polymer melt.

5.1 Analysis of rotation within GO simulation

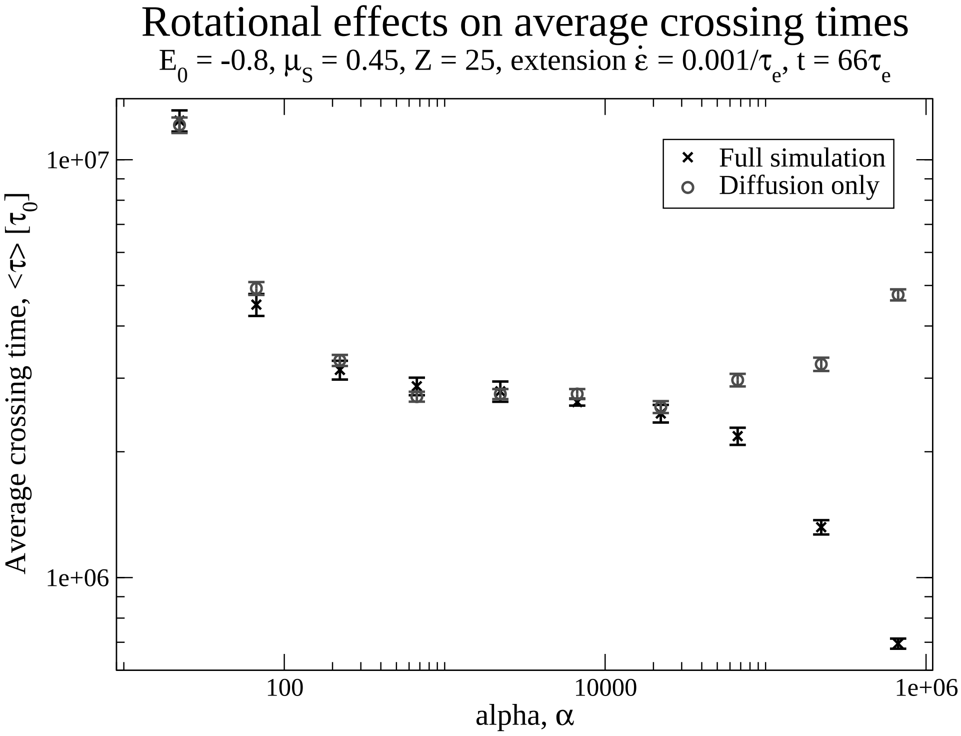

Figure 5.1: Plot of average crossing times for varying rotational diffusion using parameter α, displaying full simulation data as well as for simulations with the just the diffusion process in action.

We begin the analysis of the rotational effects within the GO polymer simulation with an investigation into the relative impacts of random diffusion and a convective drag force on average crossing times. All of the simulated crossing time results in this section are performed on a polymer melt with $E_0 = -0.8$, $\mu_S = 0.45$ containing purely long chains with $Z = 25$ entanglement segments, and at an extension rate $\dot{\epsilon} = 0.001/\tau_e$, quasi-statically fixed at time $t = 66\tau_e$ which is a stretch of $\lambda = 3.13$, see chapter 1.6.3 for thorough explanations. As chain stretch and a highly-aligned crystal has a huge impact on decreasing energy landscapes, these example parameters were chosen to produce appropriately practical nucleation times for the simulation. If no stretch were applied, the quiescent barrier height is greater than $300k_BT$ and would be an impossible challenge.

Rotational diffusion acts in a random direction with the relaxation time increasing as the size of the nucleus increases, as explained in section 1.6.3.3. The parameter α is used to tune the amount of diffusion that occurs. As we will discuss at length this is a crude linear description of a complex situation and later we also provide a physically relevant replacement. The convective drag force aligns the nucleus with the flow direction and is dependent on the flow rate and the aspect ratio ρ, but is independent of the nucleus size. In figure 5.1 we display average crossing times in units of τ_0 for a wide range of the diffusion parameter α. The rotational relaxation time is set through equation (1.6.29), with $\alpha = 1$ corresponding to $\tau_{\text{rot}} = O(\tau_0)$ for the base state ($N_T = 1$). We include results from the full simulation with both diffusion and convection processes in action and compare to a set with just the diffusion process. Here error bars refer to the standard error. The plot shows that for the wide region $200 \leq \alpha \leq 2 \times 10^4$ the crossing times are largely independent of α. For larger values of α the two data sets diverge. This separation is due to the rotational diffusion being so slow that the nucleus is unable to sufficiently reset in the base state, which gives the convection term time to align the nucleus with the flow direction without interference. This results in the average crossing times for the full simulation being significantly faster than for those with the just diffusion taking place for large values of α. However, these large values of α are not physical because the relaxation time in the base state which is only one monomer is much too long; it is expected to be of the same order as the attachment rate for self consistency. Thus from here on, we neglect the effect of the convective force by the flow on crystal rotation.

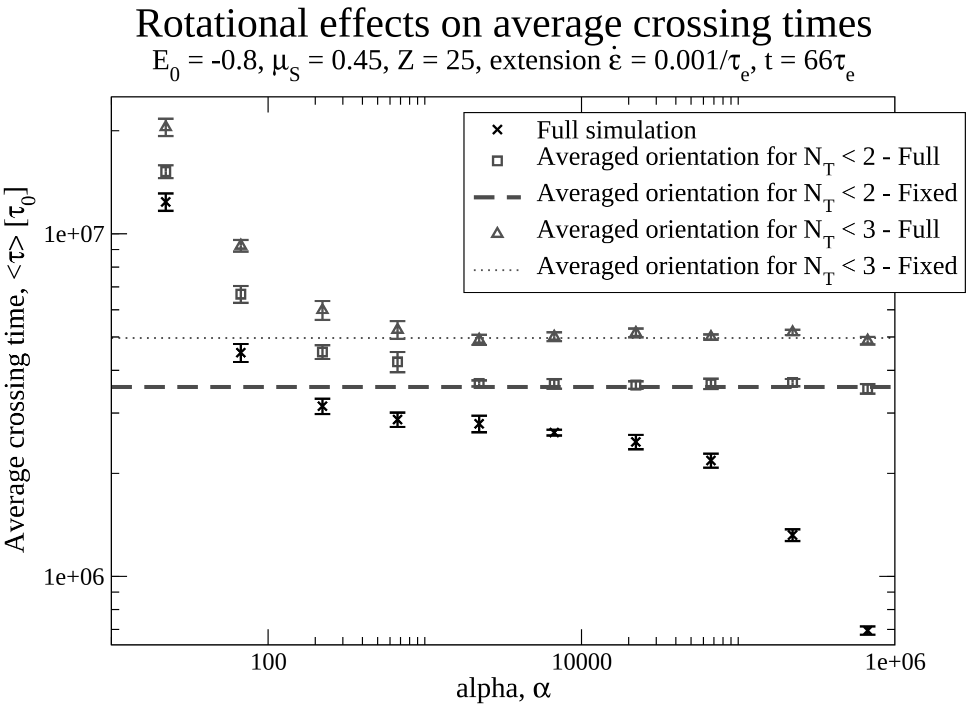

Figure 5.2: Along with the full simulation average crossing time results we display sets where the nucleus orientation has been averaged at the base for $N_T < 2$ and $N_T < 3$. For each of these we have a set where the rotation is fully resolved as in the full simulation for larger states (Full), as well as a simulation where the orientation is fixed for those larger nuclei (Fixed).

For the next stage in our analysis we consider the effect of allowing the orientation to completely reset at small nuclei sizes. This is achieved by having a threshold nucleus size, below which the initial energy landscape is averaged isotropically over all angles, and once the crystal grows to this threshold size the orientation with respect to the flow is picked at random. We can then either allow the rotation algorithm to operate as in the full simulation, or simply fix the orientation until the nucleus falls below this threshold size and the orientation is again averaged. Figure 5.2 displays average crossing times for a wide range of the diffusion parameter α. We compare the full simulation data set with averaged orientation for two threshold nucleus sizes, $N_T < 2$ and $N_T < 3$. For each of these sizes we have included a data set where the rotation algorithm is fully resolved at and beyond the threshold size which is dependent on α, and a single run where the orientation is fixed and hence independent of α since no diffusion is taking place. The first point to notice is that, as before, for the full simulation data set there is an extremely wide region ($200 \lesssim \alpha \lesssim 6 \times 10^4$) where the average crossing times almost plateau. Another observation is that the averaged orientation data sets show excellent agreement between the fully resolved rotation algorithm for $\alpha \gtrsim 2000$ and the fixed cases for both threshold sizes displayed. We conclude that for $\alpha \gtrsim 2000$ the diffusion is so weak that for nuclei larger than the threshold size, their orientation is effectively fixed during a crossing attempt.

The average crossing times for the threshold size of $N_T < 2$ in the averaged orientation case are of the same order as the full simulation's plateau but still noticeably slower. This is due to the averaging of the orientation at the base state which introduces two effects to the system. Note that a particle only has a realistic chance of a successful crossing if it is close to being fully aligned with the flow, seen as it will have a significantly lower energy barrier. The averaging of the orientation presents a higher first step than it should do in these aligned cases, hence particles have fewer opportunities at modest barriers than in the full simulation. Also for unaligned nuclei, the averaging of the orientation presents a lower first step allowing too many nuclei to grow, which whilst slowing rotational diffusion also wastes time attempting to cross an uncrossable barrier. Both of these factors result in slower crossing times for averaging the orientation at the base state. Moreover, the average crossing times are slower still for the $N_T < 3$ case, and they continue to get slower for averaging the orientation for nuclei $N_T < 4$ and $N_T < 5$.

We believe that the way to proceed in the development of an analytic model is to use the assumption that the orientation is effectively fixed during a crossing attempt. This is physically correct for polymer nucleation, since a growing nucleus within a polymer melt is extremely restricted, and any significant rotational movement is highly unlikely. The method by which the GO polymer simulation applies rotational diffusion is in need of refinement. Physically it is expected that the relaxation time of rotational diffusion in the base state

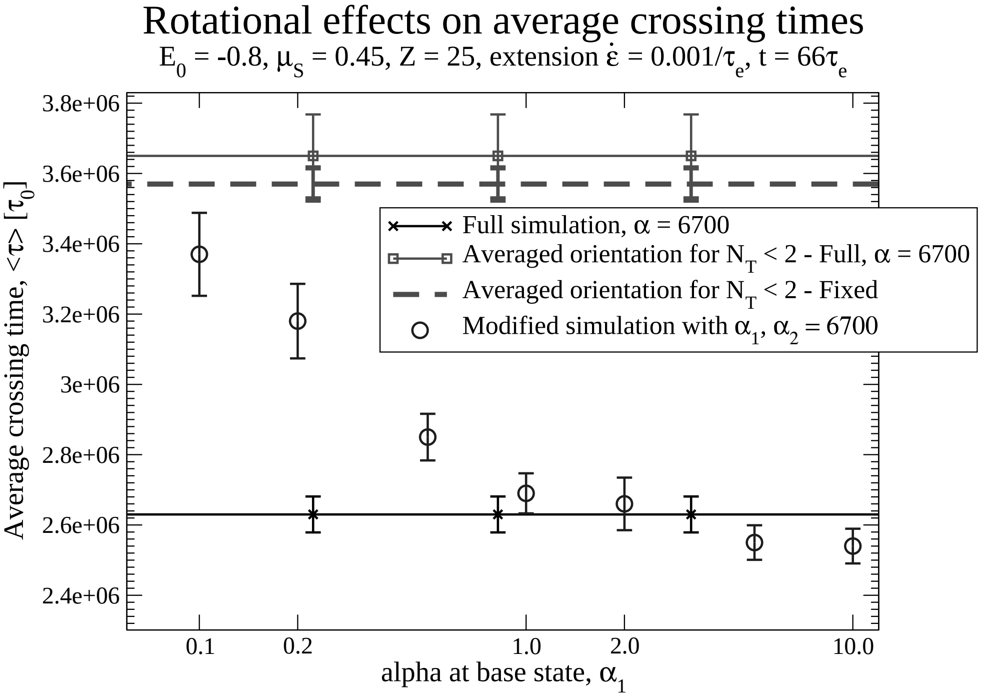

Figure 5.3: We display a series of average crossing time results for the modified simulation against base state parameter α_1, all with $\alpha_2 = 6700$, in comparison to results from the full simulation as well as both the fully resolved and fixed versions of the averaged orientation for $N_T < 2$ all with $\alpha = 6700$.

should be of the same order as the attachment time scale, τ_0, since both are describing the movement of one monomer. However due to the highly entangled and restrictive nature of polymer melts, once the size of the nucleus increases, it becomes increasingly connected to the surrounding chains, hence we would expect the rotational diffusion relaxation time to sharply rise, much faster than the prescribed linear growth. To improve the model using these physical ideas, we modify the parameter α in the simulation to have a special value at the base state, α_1, which will be small and have a much larger value, α_2, for nuclei of more than one monomer. The advantage of a stepped α is that the numerical value of α_2 for bigger nuclei is unimportant as long as it is large enough that the orientation is effectively fixed. In figure 5.3 we display several average crossing times employing this modified simulation with different values of α_1 for a particular value $\alpha_2 = 6700$. The plot shows as α_1 decreases towards zero and the rotational diffusion at the base state increases significantly, the average crossing times converge towards the averaged orientation for $N_T < 2$ results and away from the original simulation with an unmodified $\alpha = 6700$ throughout.

This investigation has provided us with ample justification to proceed in the development of an analytical model of polymer nucleation including crystal rotation. We aim to predict polymer nucleation through the simplifications of averaging the orientation at the base state (weighted by surface area of segments of an entire sphere) and fixing the orientation whilst a nucleus makes a crossing attempt, as this scenario is the physically relevant limit. This model would neglect plausible but extremely rare events of particles spending time hovering above the base state, particularly in smaller arrangements (states $N_T = 2$ and $N_T = 3$ for example) for long enough to rotationally diffuse significantly.

5.2 Model construction

In this section, we present our polymer nucleation model that includes crystal rotation. Beginning in section 5.2.1, we investigate the projected one-dimensional rate kinetics for highly-aligned nuclei applying simulation methods from chapter 3. An explanation of the selection process for the discrete set of relative angles between our nucleus and the principal flow direction of the polymer melt is given in section 5.2.2. The main calculation of nucleation times is detailed in section 5.2.3, including a reduced system that concentrates on highly-aligned orientations as well as a simple approximation technique.

5.2.1 Rate kinetics for nuclei highly-aligned with flow direction

In this section, we present an investigation similar to section 3.2.3.2, to find the effective rate kinetics of a one-dimensional projection of our multi-state system. In this case, we concentrate on highly-aligned nuclei whereas in chapter 3 rotational effects were averaged and hence not considered. We focus on highly-aligned nuclei because these are the most likely routes to nucleation. Following the method from chapter 3 but fixing the orientation of the nucleus relative to the flow direction to find the equibrium occupancies, Q_i, and nonequilibrium occupancies, χ_i, for each discrete state. To obtain a variety of energy landscapes we alter the parameters E_0, μ_S, and crucially the chain stretch, λ, which has a large effect on reducing the barrier height, see section 1.6.3.2. The effective rate kinetics or attachment area at each state is found through equation (3.1.11). We fit a power law around the critical nucleus, n^*, to reduce the statistical noise from our data, to find an accurate value of the effective attachment area at the critical nuclei, $A(n^*)$.

The orientation of the nucleus is described with a unit vector, $\mathbf{w}$. We choose the x direction to be the flow direction, hence a fully aligned nuclei has $\mathbf{w} = (1, 0, 0)$ or $\mathbf{w} = (-1, 0, 0)$ due to chain symmetry. In figure 5.4, we display our results, grouping the different cases by alignment, and for comparison we include the fitting curve (3.2.3) with $\beta = 1.26$ and $\gamma = 0.643$ from the investigation in chapter 3 where orientation was not included. We begin the analysis of these by looking at the various unaligned orientations. These follow

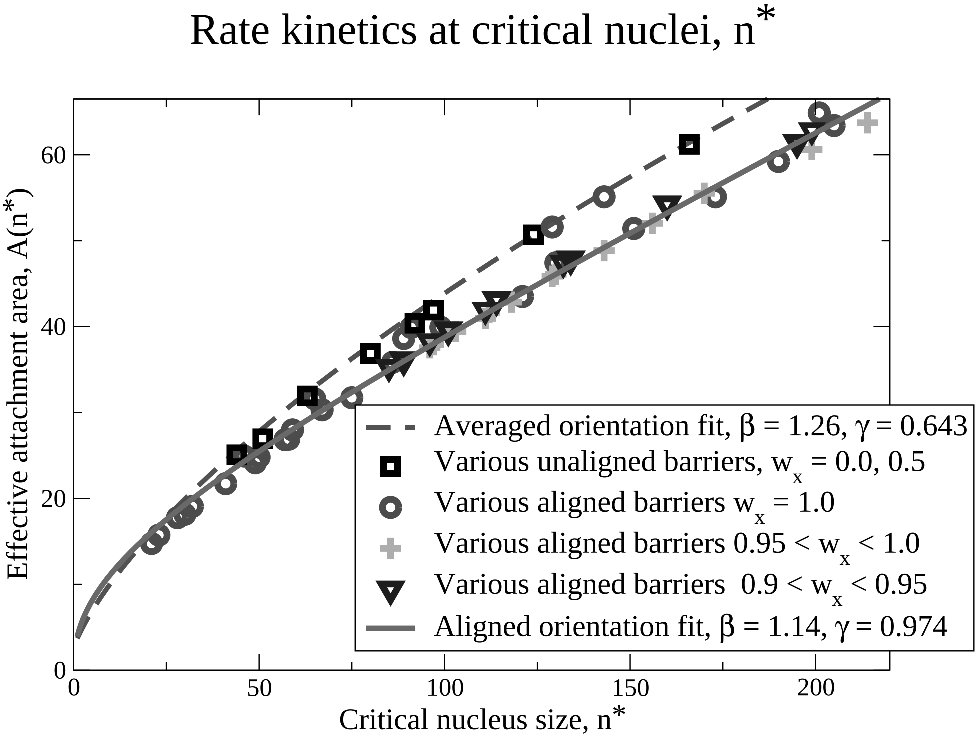

Figure 5.4: Comparison of the effective attachment area at the critical nucleus size, $A(n^*)$, for various energy landscapes where the alignment of the nucleus is fixed relative to the flow direction. Also displayed is a fitting curve from the investigation in chapter 3 where the nucleus orientation is averaged throughout, as well as a fit of our highly-aligned cases not including outliers, both with the power law expression (3.2.3).

close to the pattern found in chapter 3. On the other hand, the fully aligned cases are generally below this pattern. The few cases that follow close to the averaged orientation pattern are melts that have only been subjected to a small degree of stretch, and so the alignment effects on the energy barrier are minimal, hence the rate kinetics are unaffected. The highly-aligned groups with $0.95 < w_x < 1.0$ and $0.9 < w_x < 0.95$ also follow the majority of the fully aligned cases, and sit below our prescribed pattern. We apply the fitting formula (3.2.3) to our aligned data neglecting outliers to obtain a curve that has the potential to predict one-dimensional rate kinetics for fixed highly-aligned nuclei

$$A(n^*) = 2\beta n^{*\gamma} - 2\beta^2\gamma n^{*2\gamma-1} + 2\gamma\left(\pi\beta^3\right)^{1/2} n^{*3\gamma/2-1}\ , \quad \beta = 1.14\ , \quad \gamma = 0.974\ . \tag{5.2.1}$$

We expect the accuracy of this fitting curve to be reasonably good inside the range of the investigation. However, for larger nuclei, we suspect the accuracy could become poor, especially considering the high value of γ, which we would have assumed to be closer to 2/3 which is the exponent for spherical growth.

Also if the polymer melt is only subjected to a modest stretch, it is a possibility that the actual rate kinetics could lie in between our two fitting curves, which could be an explanation of the data points around $n^* = 100$.

5.2.2 Discrete angular selection

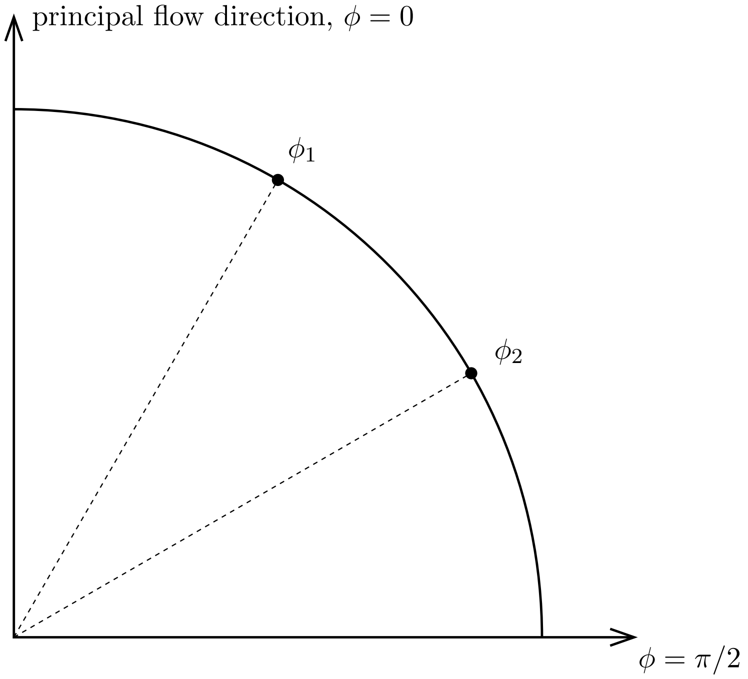

Figure 5.5: Basic diagram of the arc of relative angles with respect to the principal flow direction, after simplification by rotational and head-to-tail symmetries.

In this section, we detail the method for dividing the continuous area of potential orientations of our nucleus into a discrete set. We also calculate the probability of selection for each individual range of angles. We consider a unit sphere and use spherical coordinates, with $0 \leq \theta < 2\pi$ describing rotation around the principal direction of the flow, and $0 \leq \phi \leq \pi$ being the angle between the flow direction and main axis of the nucleus. As section 1.6.3.2 describes, ϕ has a huge impact on the energy landscape with highly-aligned nuclei having a much greater opportunity for nucleation. The GO model assumes there is rotational symmetry in θ around the principal flow direction which is not strictly true in the case of shear flows. To capture the GO model we apply the same assumption as well as head-to-tail symmetry. Hence we only need to consider an arc in ϕ between 0 and $\pi/2$ rather than the whole sphere, as shown in figure 5.5. We divide this arc into u equal sections and for each section, whilst considering its locus around the flow direction, we calculate the average angle as well as its contribution to the surface area. Concentrating on a single section containing angles in the range $\phi_1 < \phi < \phi_2$, we obtain the average angle through a simple centre of mass of the surface calculation, defining $\mathbf{c}$ to be the centre of mass

$$\mathbf{c} = \frac{\int_{\phi_1}^{\phi_2} \int_0^{2\pi} \mathbf{r} r^2 \sin\phi \;\, \mathrm{d}\theta \mathrm{d}\phi}{\int_{\phi_1}^{\phi_2} \int_0^{2\pi} r^2 \sin\phi \;\, \mathrm{d}\theta \mathrm{d}\phi} \quad \text{with } \mathbf{r} = (\cos\theta \sin\phi, \sin\theta \sin\phi, \cos\phi) \text{ and } r = 1 \; ,$$

and since the only direction of interest is the principal flow direction, we only require

$$c_3 = \frac{\int_{\phi_1}^{\phi_2} \int_0^{2\pi} \cos\phi \sin\phi \;\, \mathrm{d}\theta \mathrm{d}\phi}{\int_{\phi_1}^{\phi_2} \int_0^{2\pi} \sin\phi \;\, \mathrm{d}\theta \mathrm{d}\phi} = \frac{\frac{1}{2}\left(\sin^2\phi_2 - \sin^2\phi_1\right)}{\cos\phi_1 - \cos\phi_2} = \frac{1}{2}\left(\cos\phi_1 + \cos\phi_2\right) \; .$$

Hence our average angle for section j out of u is

$$\phi_{j,u} = \arccos\left[\frac{1}{2}\left(\cos\phi_1 + \cos\phi_2\right)\right] \; . \tag{5.2.2}$$

In order to determine the probability that each angle is selected, we must calculate the surface area, which is

$$\int_{\phi_1}^{\phi_2} \int_0^{2\pi} \sin\phi \;\, \mathrm{d}\theta \mathrm{d}\phi = 2\pi\left(\cos\phi_1 - \cos\phi_2\right) \; ,$$

and since the total surface area of the hemisphere is 2π, the selection probability of each section j is

$$P(j, u) = \cos\frac{(j-1)\pi}{2u} - \cos\frac{j\pi}{2u} \; . \tag{5.2.3}$$

Note that although the arc is divided equally, the three-dimensional sphere clearly produces a bias towards nuclei that are highly-aligned with the principal flow direction, which is corrected with the weighted probabilities. Although highly-aligned sections have less surface area on our unit sphere, and hence are less likely to be selected, they are also extremely important due to their smaller barrier heights.

5.2.3 Rotation model calculation

In this section, we present the main calculation of the rotational polymer nucleation model. The implementation of our model requires several key formulae from the one-dimensional systems in chapter 4. For each individual orientation, j, selected by the method in section 5.2.2 with equation (5.2.2), we require the associated energy landscape, $F_j(i)$, and rate kinetics, $A_j(i)$. We have the ability to calculate the energy landscapes using the method described in chapter 2, but it is more practical to employ the GO simulation (discussed in section 2.3). The rate kinetics can either be directly extracted from the simulation or we can use the estimation from our investigation in section 5.2.1. The vitally important fraction of success, $\sigma_{s,j}$, is calculated by equation (4.1.28)

$$\sigma_{s,j} = \frac{\exp\left(F(2)\right)}{A(1)} \left[\sum_{j'=2}^{n^*} \frac{\exp\left(F_j(j')\right)}{A_j(j'-1)} + \sum_{j'=n^*+1}^{n_f+1} \frac{\exp\left(F_j(j'-1)\right)}{A_j(j'-1)} \right]^{-1} . \tag{5.2.4}$$

We define the nucleation state to be, n_f, which is some state significantly larger than each of the individual critical nuclei considered ($n_f \gg n_j^*$ for each angle j with an associated energy landscape that is realistically crossable). To approximate the distribution of failure times, $P_{2,1/n_f,[j]}(t)$, which is dominated by nuclei that fail in their first few moves, we define a failure state nucleus size, n_a, and assume the majority of failure events occur without a visit to state n_a, then $P_{2,1/n_f,[j]}(t) \approx P_{2,1/n_a,[j]}(t)$. This approximation gives us a good shape of the distribution, as shown by figure 4.7. However since this approximation does not include all failure events, we must normalise our expression

$$P_{2,1/n_f,[j]}(t) \approx \frac{(1-\sigma_{s,j}) P_{2,1/n_a,[j]}(t)}{\int\limits_0^\infty P_{2,1/n_a,[j]}(t')\mathrm{d}t'} = \frac{(1-\sigma_{s,j}) P_{2,1/n_a,[j]}(t)}{\bar{P}_{2,1/n_a,[j]}(0)} ,$$

to ensure the total number of failure events is correct, which in Laplace space is

$$\bar{P}_{2,1/n_f,[j]}(s) \approx \frac{(1-\sigma_{s,j}) \bar{P}_{2,1/n_a,[j]}(s)}{\bar{P}_{2,1/n_a,[j]}(0)} . \tag{5.2.5}$$

We now consider the distribution of success times τ_s or in the model notation $P_{2,n_f/1,[j]}(t)$, and the situations we intend to represent involve nuclei failing to grow for the vast majority of their time. So the exact distribution of success times is unimportant, as it will only contribute a minuscule fraction of the total nucleation time. We expect the distribution of success times to be close to a Poissonian shape as in figure 4.11 with typical values less than $n_f \tau_0$. To produce a simple model, the average success time is presumed to be negligible, and not significantly add to the total crossing time. Specifically we use a crude delta function at the origin to represent the distribution of success times

$$P_{2,n_f/1,[j]}(t) \approx \sigma_{s,j} \delta(t) . \tag{5.2.6}$$

The probability that the relative angle j is selected upon arrival into state $N_T = 2$, $P(j,u)$, is determined by equation (5.2.3). We combine all of the separate failure and success distributions in Laplace space with equation (4.2.12), to give the overall distribution of failure times

$$\bar{P}_{2,1/n_f}(s) = \sum_{j=1}^{u} P(j,u) \bar{P}_{2,1/n_f,[j]}(s) , \tag{5.2.7}$$

and similarly for the overall distribution of success times $\bar{P}_{2,n_f/1}(s)$. These results are then manipulated using equation (4.2.13) to obtain the crossing time distribution for the complete system in Laplace space

$$\bar{P}_{1,n_f}(s) = \frac{\bar{P}_1^+(s)\bar{P}_{2,n_f/1}(s)}{1-\bar{P}_1^+(s)\bar{P}_{2,1/n_f}(s)} \ . \tag{5.2.8}$$

We determine $\bar{P}_1^+(s)$ by using orientationally averaged energy landscapes and rate kinetics for states $N_T = 1$ and $N_T = 2$. The result (5.2.8) can be either numerically inverted to give the crossing time distribution of the complete system or we can simply find the average crossing time through equation (4.1.46)

$$\langle \tau_{1,n_f} \rangle = \lim_{s \to 0} \left[\frac{1}{s} \left(1 - \bar{P}_{1,n_f}(s) \right) \right] \ . \tag{5.2.9}$$

This is a powerful technique that enables us to study a highly complicated system of convoluted escape probabilities. In section 5.2.3.1, we describe a sensible refinement of this complete system by reducing the number of orientations considered, and concentrate on highly-aligned nuclei. To further enhance the practicality, we present a major simplification in the failure distributions to our calculation in section 5.2.3.2, giving us a straightforward method to approximate average crossing times for these rotational systems.

5.2.3.1 Reduced angular considerations

It is clear that the vast majority of nucleation events will occur when our nucleus is highly-aligned with the flow direction, as these highly-aligned nuclei produce the lowest energy barriers to nucleation. In this section, we decide to focus our model on these highly-aligned nuclei by merging all of the unaligned angles with extremely high energy barriers into a single selection, and effectively ignore their chances of success. This will allow us to further refine the detail of the discretisation in the highly-aligned region. We reduce the number of angles considered in the model by selecting an angle with index, $u_c + 1$, which has an associated energy barrier significantly higher than the most aligned nuclei, $j = 1$. Hence for the neglected section, the probability of selection and associated fraction of success must satisfy

$$P(1,u)\sigma_{s,1} \gg P(u_c+1,u)\sigma_{s,u_c+1} \ , \tag{5.2.10}$$

and so we assume $\sigma_{s,j} = 0$ for $u_c + 1 \leq j \leq u$. This assumption allows us to rewrite our overall failure and success distributions, which in Laplace space are

$$\bar{P}_{2,1/n_f}(s) = \sum_{j=1}^{u_c} P(j,u)\bar{P}_{2,1/n_f,[j]}(s) + \left(1 - \sum_{j=1}^{u_c} P(j,u) \right) \bar{P}^c_{2,1/n_f}(s) \ , \tag{5.2.11}$$

$$\bar{P}_{2,n_f/1}(s) = \sum_{j=1}^{u_c} P(j,u)\bar{P}_{2,n_f/1,[j]}(s) \ , \tag{5.2.12}$$

where the notation c refers to our reduced or cut system. The average failure distribution $\bar{P}^{c}_{2,1/n_f}(s)$ for the unaligned angles is found through equation (5.2.5) by considering the set of merged angles $u_c + 1 \leq j \leq u$, for which the required energy landscape and rate kinetics can be approximated using the average values over the unaligned region

$$F_c(i) = \frac{F_a(i) - \sum_{j=1}^{u_c} P(j,u)F_j(i)}{1 - \sum_{j=1}^{u_c} P(j,u)} \;, \quad A_c(i) = \frac{A_a(i) - \sum_{j=1}^{u_c} P(j,u)A_j(i)}{1 - \sum_{j=1}^{u_c} P(j,u)} \;, \tag{5.2.13}$$

with $F_a(i)$ and $A_a(i)$ being the energy landscape and rate kinetics for the averaged orientation case. The huge advantage of this reduced model is that only a small number of highly-aligned angles $1 \leq i \leq u_c$ need to be considered to describe the whole system.

5.2.3.2 Approximation to the average crossing time for the rotational model

The aim of this section is to produce a simple approximation to the average crossing time for our rotational model. To achieve this, a major simplification is made to the failure event distributions by combining all angles to find a single failure rate, $1/\tau_f$, and we assume this distribution is exponential

$$P_{2,1/n_f}(t) \approx \left(1 - \sum_{j=1}^{u} P(j,u)\sigma_{s,j}\right) \frac{1}{\tau_f} \exp\left(-\frac{t}{\tau_f}\right) . \tag{5.2.14}$$

The prefactor ensures the combined total probability is correct, as we are still using the same distribution for successful events (equation (5.2.6)). Although figure 4.7 shows that this single exponential decay function is known to have the incorrect shape, to produce a simple output approximation we decide to use this convenient distribution with the correct average. This average failure time, τ_f, can be found by removing the rotational inputs to calculate an energy landscape and rate kinetics discussed in chapters 2 and 3 respectively, together with equation (4.1.10), or in practice the approximation (4.1.31), which is reasonably accurate when enough terms are included in the expansion. In Laplace space these probability distributions are transformed to

$$\bar{P}_{2,1/n_f}(s) = \left(1 - \sum_{j=1}^{u} P(j,u)\sigma_{s,j}\right) \frac{\tau_f^{-1}}{s + \tau_f^{-1}} \;, \tag{5.2.15a}$$

$$\bar{P}_{2,n_f/1}(s) = \left(\sum_{j=1}^{u} P(j,u)\sigma_{s,j}\right) \;, \tag{5.2.15b}$$

$$\text{with } \bar{P}_1^{+}(s) = \frac{\tau_0^{-1} A(1) \exp\left(-F(2)\right)}{s + \tau_0^{-1} A(1) \exp\left(-F(2)\right)} \;, \tag{5.2.15c}$$

hence we find an approximation to the average crossing time for this complete system by substituting these Laplace formulas into equations (5.2.8) and (5.2.9). Now we expect the average failure time to be of order τ_0 ($\tau_f \approx O(\tau_0)$). Our expression for the average crossing time can be simplified to

$$\left\langle \tau_{1,n_f} \right\rangle \approx \lim_{s\to 0} \left[\frac{\begin{gathered} \left(s + \tau_0^{-1} A(1) \exp\left(-F(2)\right)\right) \left(s + \tau_f^{-1}\right) \\ -\tau_f^{-1}\tau_0^{-1} A(1) \exp\left(-F(2)\right) \left(1 - \sum_{j=1}^{u} P(j,u)\sigma_{s,j}\right) \\ -\tau_0^{-1} A(1) \exp\left(-F(2)\right) \left(s + \tau_f^{-1}\right) \left(\sum_{j=1}^{u} P(j,u)\sigma_{s,j}\right) \end{gathered}}{\begin{gathered} s\left(s + \tau_0^{-1} A(1) \exp\left(-F(2)\right)\right) \left(s + \tau_f^{-1}\right) \\ -\tau_f^{-1}\tau_0^{-1} A(1) \exp\left(-F(2)\right) \left(1 - \sum_{j=1}^{u} P(j,u)\sigma_{s,j}\right) s \end{gathered}} \right],$$

by considering only the leading order terms in s, our approximation becomes

$$\left\langle \tau_{1,n_f} \right\rangle \approx \frac{\tau_0 + \tau_f A(1) \exp\left(-F(2)\right) \left(1 - \sum_{j=1}^{u} P(j,u)\sigma_{s,j}\right)}{A(1) \exp\left(-F(2)\right) \left(\sum_{j=1}^{u} P(j,u)\sigma_{s,j}\right)}.$$

This method is aimed at approximating extremely rare crossing time events, implying $\sigma_{s,j} \ll 1$, so our expression can be further simplified to

$$\left\langle \tau_{1,n_f} \right\rangle \approx \frac{\tau_0 + \tau_f A(1) \exp\left(-F(2)\right)}{A(1) \exp\left(-F(2)\right) \left(\sum_{j=1}^{u} P(j,u)\sigma_{s,j}\right)}. \tag{5.2.16}$$

This is an incredibly simple formula for approximating average crossing times of highly complicated systems. It is dominated by the sum of the individual fraction of successes which a detailed calculation is required for each orientation. The other quantities are connected to behaviour at the base of the barrier and are expected to be $O(1)$.

To summarise this section, we have presented a polymer nucleation model that includes crystal rotation. We first performed an extensive investigation into the rate kinetics at critical nuclei of one-dimensional projections of the energy landscape of nuclei that have a fixed orientation relative to the flow direction. Focusing on the cases where the nucleus is fully or highly-aligned, we have obtained a reasonably accurate estimation for $A(n^*)$ with equation (5.2.1), which can be inputted into our rotation model of section 5.2.3. The method began by splitting the continuous arc of possible orientations into a discrete set with equation (5.2.2) where each has an associated selection probability, equation (5.2.3). Our main calculation concludes with the formula (5.2.9) to find average crossing times. Finally, we produced a refinement to the model that concentrates on the highly-aligned orientations which have smaller barriers to nucleation, as well as a useful approximation (5.2.16) to the main calculation.

5.3 Results

In this section we present and analyse the results of our calculation and approximation which we also compare with the nucleation times from the GO simulation types described in section 5.1. We initially test various elements and parameters of our main calculation in section 5.3.1. Finally in section 5.3.2, we apply our calculations to a small range of time increments during an extensional flow and investigate the changing nucleation rate.

5.3.1 Test calculation

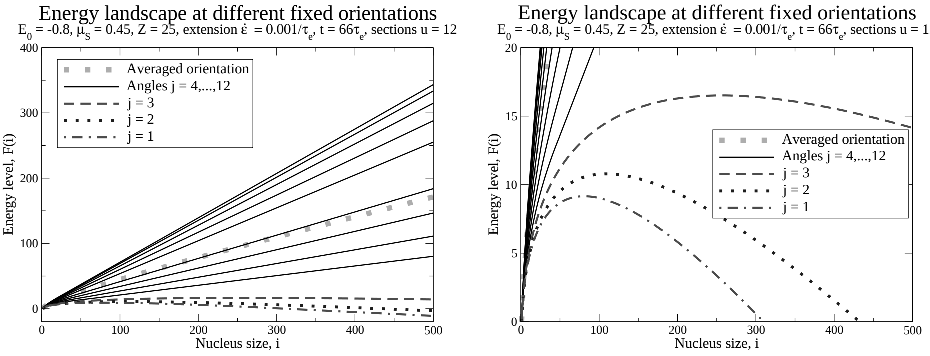

(a) (b)

Figure 5.6: Energy landscapes at different fixed nucleus alignments relative to the flow direction, for a polymer melt described by $Z = 25$, $E_0 = -0.8$, $\mu_S = 0.45$, with an extensional flow with rate $\dot{\epsilon} = 0.001/\tau_e$ and the system is quasi-statically fixed at time, $t = 66\tau_e$. Displaying the energy landscape where the nucleus orientation has been averaged, as well as energy landscapes where the nucleus is fixed at $u = 12$ distinct orientations. Ranging from the highly-aligned $j = 1$ to the very unaligned $j = 12$, (a) shows the complete picture, (b) focuses on the realistically crossable energy landscapes for aligned orientations $j = 1, 2, 3$ by zooming in on the region $0 < F(i) < 20$.

In this section, we throughly test our rotation model against the GO polymer simulation. In particular, we test the accuracy of our reduced system of section 5.2.3.1, as well as the effects of increasing the failure state, n_a in our calculation, and the level of discretisation required. We aim to find an accurate average crossing time for the same parameters used in section 5.1, that is a polymer melt described by $Z = 25$, $E_0 = -0.8$, $\mu_S = 0.45$, applying an extensional flow with rate $\dot{\epsilon} = 0.001/\tau_e$ and quasi-statically fixed at time $t = 66\tau_e$, which corresponds to a chain stretch $\lambda = 3.13$ (see section 1.6.3 for details on parameters). For a fair test of the model, we compare to the GO polymer simulation where the nucleus orientation is averaged at the base state ($N_T = 1$), and then fixed at a randomly selected angle for larger nuclei, which gives an average crossing time to form a nucleus of size $N_T = 500$ of $\langle\tau\rangle = 3.57 \times 10^6$.

Average crossing times, $[\tau_0]$	Full system	$u_c = 2$	$u_c = 3$
Full calculation (5.2.9)	3.39×10^6	3.39×10^6	3.39×10^6
Approximation (5.2.16)	3.41×10^6	3.42×10^6	3.41×10^6
1D toy simulation	3.45×10^6	3.44×10^6	3.44×10^6
(Standard error)	(1.26×10^4)	(1.25×10^4)	(9.67×10^3)

Table 5.1: Average crossing times for our test system in units of τ_0. We investigate the discrete system with $u = 12$ orientations, as well as the reduced system that focuses on highly-aligned nuclei for $u_c = 2$ and $u_c = 3$. We display the results of the full calculation with equation (5.2.9), the approximation with equation (5.2.16), as well as a one-dimensional toy simulation of the system.

We begin by dividing the continuous arc of possible orientations into $u = 12$ discrete selections, see section 5.2.2. In figure 5.6, we display the individual energy landscapes for each fixed orientation, as well as the averaged orientation case. Our chosen nucleation state $n_f = 500$, is significantly beyond the critical nuclei of the two most aligned orientations $j = 1$ and $j = 2$. The rate kinetics for the individual orientations are found through a combination of our Boltzmann technique from section 3.1.1.2.1 at the base of each barrier, in addition to our non-Boltzmann technique from section 3.1.1.2.2 at each critical nuclei. We assume that the Boltzmann technique is valid up to states with a total energy level $7k_BT$ lower than the peak $F(n^*)$. We use the non-Boltzmann rate kinetics extraction technique to find the value of the effective attachment area at each critical nuclei, $A_j(n_j^*)$, and obtain the rate kinetics for the remaining states by applying the formula (5.2.1) with $\alpha = 0.8$. Using these discrete one-dimensional energy landscapes $F_j(i)$ and rate kinetics $A_j(i)$ for each alignment j, we produce a simple one-dimensional toy simulation which applies the Monte Carlo algorithm and replicates system upon which the full calculation is based.

We calculate the fraction of successful attempts for each orientation through equation (4.1.28), the results for our test calculation with $u = 12$ are

$$\sigma_{s,1} = 4.19 \times 10^{-5} \ , \ \ \sigma_{s,2} = 8.07 \times 10^{-6} \ , \ \ \sigma_{s,3} = 2.40 \times 10^{-8} \ ,$$

and $\sigma_{s,j} = 0$ for $j = 4, \ldots, 12$ as the energy barriers are so large. In table 5.1, we display average crossing times for the full system considering all 12 discrete orientations, as well as the reduced systems with $u_c = 2$ and $u_c = 3$. For each set-up we use the full calculation with equation (5.2.9) with failure state $n_a = 10$, our approximation with equation (5.2.16), and also showing the toy simulation results. The main conclusion is that the overall accuracy of our simplifications are superb as all of our results are extremely close to one another, typical errors being less than 1% in all cases. For the full calculation, the reduced system with $u_c = 2$ that only considers the two most aligned orientations is still very accurate. The reduced system with $u_c = 3$ and the full system give the same value, which verifies the approach of merging of unaligned orientations. Our approximation also performs amazingly well considering the minimal amount of information required. This shows that the crucial elements of the calculation are obtaining an accurate fraction of successes for each orientation, and an overall average failure time, rather than finding individual failure distributions. The one-dimensional toy simulation produces slightly slower average crossing times for our three systems. This is due to these simulations having the ability to fully explore long failure events correctly which the calculation approximates with its failure time distribution (5.2.5). The simulation times are in fact so close that the three results overlap when considering the standard error. The toy simulation result of the full system tends to be marginally slower than the two reduced system results. This is explainable even though the calculation gives the same value for the full system and the reduced system with $u_c = 3$. The difference in the toy simulation is that it includes long failure events, which are slightly more likely to occur for orientations $j = 4$ and $j = 5$ and the reduced system merges these into an averaged combined unaligned energy landscape.

n_a	$\langle \tau_{1,n_f} \rangle$ $[\tau_0]$
6	3.27×10^6
7	3.32×10^6
8	3.36×10^6
9	3.38×10^6
10	3.39×10^6

Table 5.2: In this table, we display calculated average crossing times in units of τ_0, for the reduced system with $u = 12$ and $u_c = 2$ for different values of the failure state, n_a, in the failure time distribution (5.2.5).

In table 5.2, we present the results of an investigation into the effect of altering the failure state, n_a, in our full calculation. We use the reduced system with $u_c = 2$ and $u = 12$ total orientations, and change our failure state from $n_a = 6, \ldots, 10$. The general trend of the average crossing times is increasing, however, there is also a slow convergence in the general direction of the toy simulation result. The extent of our calculation is limited by practicality due to the inverse Laplace transform. Increasing n_a adds layers of detail in the formulation of the failure time distributions which are required to be resolved.

No. Angles		Simulated rate kinetics, $[\tau_0]$		
u	u_c	Full	Approximate	Toy Simulation (Error)
6	1	4.38×10^6	4.41×10^6	4.39×10^6 (1.91×10^4)
9	2	3.73×10^6	3.75×10^6	3.81×10^6 (1.42×10^4)
12	2	3.39×10^6	3.42×10^6	3.44×10^6 (1.25×10^4)
15	3	3.24×10^6	3.27×10^6	3.29×10^6 (1.16×10^4)
18	4	3.18×10^6	3.19×10^6	3.20×10^6 (1.16×10^4)
30	6	3.06×10^6	3.08×10^6	3.10×10^6 (1.10×10^4)

Table 5.3: Average crossing times in units of τ_0, for the reduced system with different levels of discretisations of the arc of orientations, with the number of angles considered $u = 6, 9, 12, 15, 18, 30$, and corresponding $u_c = 1, 2, 2, 3, 4, 6$. We use simulated rate kinetics from the extraction technique from chapter 3 to calculate average crossing times using the full calculation (5.2.9) and our approximation (5.2.16), we also display results from the toy simulation.

The success of our reduced system allows us to refine our calculation by including more orientations in the discrete selection process. In tables 5.3 and 5.4, and also figure 5.7, we display average crossing time results for an array of discretisation levels for $u = 6, 9, 12, 15, 18, 30$. For each of which, we show the full calculation (5.2.9) and our approximation (5.2.16) for the two cases of using simulated and estimated (with equation (5.2.1)) one-dimensional rate kinetics for each orientation. Using the simulated rate kinetics for this test calculation we have found that the critical values, $A(n^*)$ are marginally higher than the fitting curve (5.2.1). In fact, in comparison to figure 5.4, our simulated rate kinetics at the critical nuclei would sit roughly halfway in between the two fitting curves of averaged orientation cases and highly-aligned cases. These higher rate kinetics produce a larger fraction of successes for each orientation, which results in faster average crossing times for the simulated kinetics system. The agreement between the full calculation and our approximation is again superb. The effect of more detailed discretisation for both cases produces faster average crossing times, as the refinement close to the highly-aligned orientations is greater. The data sets are slowly converging with increasing detail of discretisation in our model, in fact they are roughly linearly convergent with $1/u$, as shown in figure 5.7. We can extrapolate to find crossing times for the limit $1/u \to 0$, or a full continuum of available angles. For the group of simulated kinetics results we estimate this limit to be approximately $2.9 \times 10^6 \tau_0$, and for estimated kinetics we predict crossing times around $3.1 \times 10^6 \tau_0$. Also on the plot, we display our one-dimensional toy simulation results for the various systems, proving the general accuracy of our calculations is superb. The toy simulations follow the same pattern as the $u = 12$ case as shown by table 5.1 and produce marginally slower average crossing times as they fully explore long failure events. In figure 5.7, we also include for comparison the average crossing time result of the GO simulation, where nucleus orientation is averaged at the base ($N_T = 1$) and fixed for larger nuclei.

No. Angles		Estimated rate kinetics, $[\tau_0]$		
u	u_c	Full	Approximate	Toy Simulation (Error)
6	1	4.77×10^6	4.80×10^6	4.81×10^6 (2.19×10^4)
9	2	3.99×10^6	4.02×10^6	4.05×10^6 (1.54×10^4)
12	2	3.67×10^6	3.69×10^6	3.72×10^6 (1.39×10^4)
15	3	3.50×10^6	3.53×10^6	3.60×10^6 (1.33×10^4)
18	4	3.44×10^6	3.45×10^6	3.50×10^6 (1.33×10^4)
30	6	3.31×10^6	3.33×10^6	3.38×10^6 (1.25×10^4)

Table 5.4: As table 5.3, but displaying results with estimated rate kinetics instead of simulated rate kinetics.

All of our calculations are close to the GO multi-dimensional simulation result (within 20%). The main error of our model calculation is the projection to one-dimension especially obtaining the mysterious true set of rate kinetics. We have confidence in our values at the base and peak of each energy landscape, however the values for the other states are estimates based on investigations in chapter 3. It is possible our mid-range rate kinetics approximations are too high or maybe the Boltzmann region is smaller than we assumed. Our calculations do not include accurate tails of long failure events in the distributions but this does not affect our toy simulations, which leaves the likely source of error to be the rate kinetics.

5.3.2 Calculation of polymer nucleation during a transient flow

In this section, we present and describe the main result of this thesis. It brings together the majority of the important results and ideas from throughout the project. We aim to accurately replicate the nucleation rates of the GO polymer simulation including rotational effects. The objective is to investigate the evolving nucleation rate for a polymer melt during a transient flow.

We present analytic calculation results from our rotation model. Comparing average crossing times for a polymer melt with $E_0 = -0.927$, $\mu_S = 0.33$ containing purely long chains with $Z = 50$ entanglement segments, subjected to an extensional flow at rate $\dot{\epsilon} = 0.001/\tau_e$. Parameters were chosen with great care, considering the full rotational simulation applicability. As well

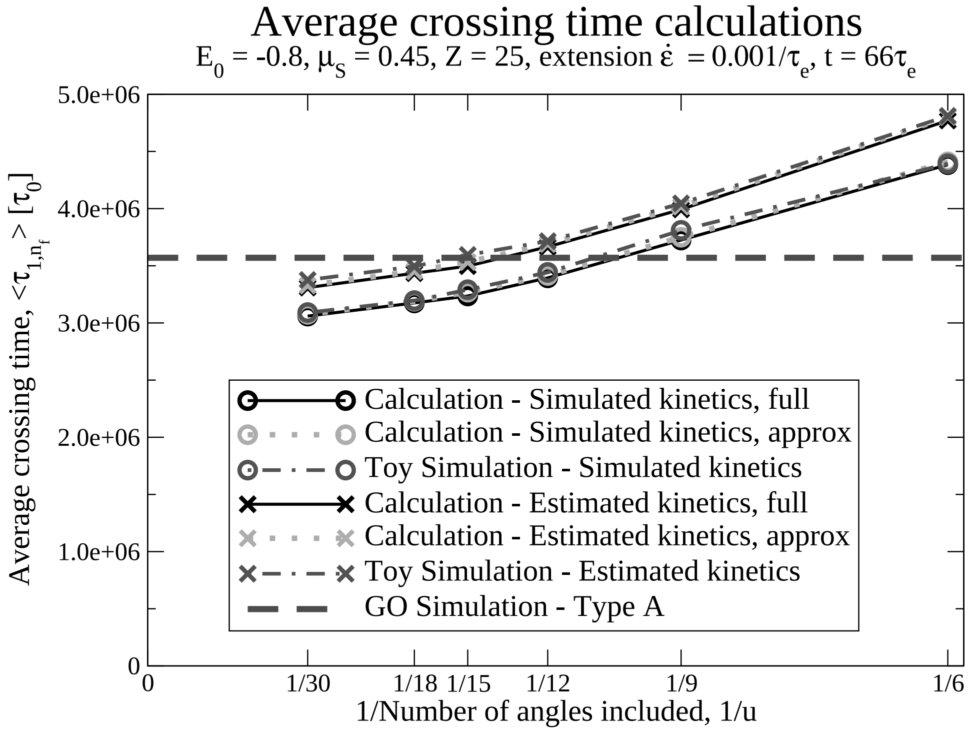

Figure 5.7: We display in graphical form the average crossing times against the level of discretisation in the arc of orientations with reciprocal of the number of angles considered being $u = 6, 9, 12, 15, 18, 30$. We use both simulated rate kinetics as well as estimated rate kinetics, produce average crossing times for each using the full calculation (5.2.9) and our approximation (5.2.16). We also include the results of our one-dimensional toy simulation. Finally, we compare our results to the GO polymer simulation labelled type A that uses an averaged orientation at the base state ($N_T = 1$) and fixed orientation for larger nuclei.

as the rate kinetics extraction technique which requires critical nuclei to be large, so that there are no discreteness effects. We concentrate on a brief time period $3360\tau_e \leq t \leq 3600\tau_e$, which corresponds to a chain stretch range of $3.0 < \lambda < 3.2$. Although this range appears to be small, for reasons to be discussed in detail later, primarily connected to rotational effects, the difference in nucleation rates is enormous. The average crossing times throughout this thesis are in relation to the rate of favourable moves in the GO model, τ_0, and $\tau_0 \ll \tau_e$, see section 1.6.3. Due to this separation in timescales, the quasi-static result from [21, 22] allows us to fix the polymer melt in time, and simulate or calculate nucleation times with confidence that the transient behaviour of the system is still observed. The quasi-static chain configurations are produced by the GLaMM model of polymer flow, see section 1.3.

In tables 5.5 and 5.6, we compare average crossing times to form a nucleus of size $n_f = 2000$, from two types of simulation and four different versions of our calculation at a series of fixed points in time. Simulation type A is where

Time	GO Simulation, $[\tau_0]$		Calculation, $[\tau_0]$	
$[\tau_e]$	Type A	Type B	Simulated kinetics	
	(Error)	(Error)	Full	Approximate
3400	4.83×10^8 (2.42×10^7)	-	3.97×10^8	4.04×10^8
3420	6.39×10^7 (2.80×10^6)	5.78×10^7 (2.86×10^6)	5.69×10^7	5.79×10^7
3440	1.49×10^7 (6.68×10^5)	1.24×10^7 (4.71×10^5)	1.32×10^7	1.35×10^7
3460	4.76×10^6 (1.50×10^5)	4.10×10^6 (2.05×10^5)	4.13×10^6	4.19×10^6
3480	1.76×10^6 (4.45×10^4)	1.41×10^6 (3.81×10^4)	1.73×10^6	1.76×10^6
3500	8.07×10^5 (2.01×10^4)	6.49×10^5 (1.22×10^4)	7.68×10^5	7.79×10^5
3520	3.97×10^5 (7.59×10^3)	3.19×10^5 (8.01×10^3)	3.84×10^5	3.89×10^5
3540	2.24×10^5 (7.01×10^3)	1.82×10^5 (3.65×10^3)	2.11×10^5	2.13×10^5
3560	1.25×10^5 (1.95×10^3)	1.02×10^5 (1.74×10^3)	1.25×10^5	1.35×10^5
3580	7.80×10^4 (1.02×10^3)	6.28×10^4 (9.25×10^2)	7.8×10^4	7.7×10^4
3600	5.23×10^4 (1.41×10^3)	4.19×10^4 (6.20×10^2)	5.1×10^4	5.0×10^4

Table 5.5: We display average crossing times in units of τ_0, for a polymer melt described by $Z = 50$, $E_0 = -0.927$, $\mu_S = 0.33$ subjected to an extensional flow at rate $\dot{\epsilon} = 0.001/\tau_e$, and quasi-statically fixed at times ranging from $t = 3400\tau_e$ to $t = 3600\tau_e$. We compare two different versions of the GO simulation, labelled type A and type B, both including the standard error. In simulation type A the orientation of the nucleus is averaged at the base state ($N_T = 1$), and then for larger nuclei, the orientation is fixed. Simulation type B is a modified simulation where the rotational algorithm is fully enabled however the key parameter α is split into two values, α_1 set so that $\tau_{\text{rot}} = \tau_0$ at the base state and $\alpha_2 = 10000$ elsewhere. We have also included calculated average crossing times for each time step using simulated rate kinetics, for the full calculation (5.2.9) and our approximation (5.2.16).

the orientation of the nucleus is averaged at the base state ($N_T = 1$), selected at random upon arrival into state $N_T = 2$ and fixed until it returns back to the

Time $[\tau_e]$	Stretch, λ	GO Simulation, $[\tau_0]$ Type A (Error)	Calculation, $[\tau_0]$ Estimated kinetics Full	 Approximate
3360	3.000	-	5×10^{11}	5.74×10^{11}
3380	3.017	-	5.9×10^{9}	5.99×10^{9}
3400	3.034	4.83×10^{8} (2.42×10^{7})	3.87×10^{8}	3.94×10^{8}
3420	3.050	6.39×10^{7} (2.80×10^{6})	5.81×10^{7}	5.90×10^{7}
3440	3.067	1.49×10^{7} (6.68×10^{5})	1.38×10^{7}	1.40×10^{7}
3460	3.083	4.76×10^{6} (1.50×10^{5})	4.37×10^{6}	4.44×10^{6}
3480	3.100	1.76×10^{6} (4.45×10^{4})	1.83×10^{6}	1.86×10^{6}
3500	3.117	8.07×10^{5} (2.01×10^{4})	8.18×10^{5}	8.30×10^{5}
3520	3.133	3.97×10^{5} (7.59×10^{3})	4.07×10^{5}	4.12×10^{5}
3540	3.150	2.24×10^{5} (7.01×10^{3})	2.22×10^{5}	2.24×10^{5}
3560	3.167	1.25×10^{5} (1.95×10^{3})	1.30×10^{5}	1.41×10^{5}
3580	3.183	7.80×10^{4} (1.02×10^{3})	8.1×10^{4}	8.1×10^{4}
3600	3.200	5.23×10^{4} (1.41×10^{3})	5.3×10^{4}	5.2×10^{4}

Table 5.6: This is an extension of table 5.5, here we have also included the chain stretch, λ, at each time increment. We compare the GO simulation type A to calculated average crossing time using estimated rate kinetics, for both the full calculation (5.2.9) and our approximation (5.2.16), in the range $t = 3360\tau_e$ to $t = 3600\tau_e$.

base state. Simulation type B is the modified simulation from section 5.1, where the rotation parameter α is split into two different values. Here α_1 is set such that $\tau_{\text{rot}} = \tau_0$ for $N_T = 1$ so rotational diffusion has the same relaxation time as favourable moves in the model, and $\alpha_2 = 10000$ for larger nuclei and therefore minimal rotation occurs. This modified simulation (type B) is considerably more computationally expensive than simulation type A as the orientation requires regular updating especially at the base state. This is the reason the type A data set begins at an earlier time step ($t = 3400\tau_e$) than the type B results. However, the GO simulation of type B is a more realistic model of nucleus rotation for polymer nucleation. The average crossing times from the significantly simplified simulation type A are generally accurate to within 25% in comparison to our most realistic set-up in the type B set. Moreover, the results from simualtion type A are consistently higher than type B, a pattern also found in figure 5.3 and discussed in section 5.1.

We present four sets of calculated results, using both simulated and estimated (from equation (5.2.1)) rate kinetics in our one-dimensional model, employing for each the full calculation (5.2.9) and our approximation (5.2.16). The calculations are based on the reduced system, described in section 5.2.3.1, with the total number of angles considered $u = 30$ for the range $3360\tau_e \leq t \leq 3460\tau_e$. For the remaining time steps $3480\tau_e \leq t \leq 3600\tau_e$, $u = 15$ is used since less refinement is required for smaller energy barriers. In theory, the reduced system should be selected by considering the fraction of success and the probabilities of each individual orientation to find a suitable u_c through the test (5.2.10). However, in practice, it is more convenient to compare the heights of the individual barriers to the most aligned orientation since the barrier height is the dominant factor in barrier crossing, with u_c chosen by the rule that $F_{u_c+1}(n^*_{u_c+1}) - F_1(n^*_1) > 7k_BT$ for each time increment. The calculations require the individual energy landscapes and rate kinetics for each orientation $1 \leq i \leq u_c$. For the Boltzmann region of each landscape, we use the technique from section 3.1.1.2.1 to find the rate kinetics. For the non-Boltzmann region of each landscape, we either use the technique from section 3.1.1.2.2 to extract the rate kinetics at each critical nuclei, $A_i(n^*_i)$, or use the estimate from fitting formula (5.2.1), and obtain the remaining states by applying the formula (3.2.8) with $\alpha = 0.8$. As discussed in chapter 3, simulating rate kinetics is difficult, especially for large critical nuclei on long, flat energy landscapes. This is the reason that there are no simulated kinetics calculations for $t = 3360\tau_e$ and $t = 3380\tau_e$, whereas our estimated kinetics calculations are for the full range, even though there is an increasing likelihood of inaccuracy for larger critical nuclei, as discussed in section 5.2.1.

We display calculations based on simulated rate kinetics in table 5.5, and estimated rate kinetics in table 5.6. Due to the approximation that the time taken during the successful crossing is negligible in our calculation (equation (5.2.6)), our average crossing times cannot be more predictive than order (10^3), since the nucleation state is defined as $n_f = 2000$ throughout. In general, the accuracy of the full calculation for both simulated and estimated rate kinetics data sets is excellent. In direct comparison to the GO simulation type A, the full calculation with simulated kinetics is within 15% of the standard error. The calculation systematically produces faster average crossing times, and there is a noted improvement for the range $3480\tau_e \leq t \leq 3600\tau_e$ where only $u = 15$ is employed. As in the test calculation of section 5.3.1, shown in figure 5.7, the accuracy of the calculation counterinuitively decreases with higher degrees of detail in the discretisation. The only explanation for this source of error is our projection to a one-dimensional system, particularly the rate kinetics, which must be marginally smaller than the sets we employ. In reality the superb accuracy in the $u = 15$ region is the fortunate result of errors cancelling, however, the calculation clearly demonstrates the ability to predict nucleation times precisely for a wide range of systems.

The calculation for the estimated rate kinetics displays similar behaviour to the simulation type A results. It shows excellent accuracy for the range $3480\tau_e \leq t \leq 3600\tau_e$ and predominantly produces slower average crossing times than the simulation results, with a noticeable shift in the comparison for the range $3400\tau_e \leq t \leq 3460\tau_e$. Since it is not necessary to employ difficult simulations to find rate kinetics at large critical nuclei, the calculation for the estimated rate kinetics is able to predict earlier time increments, and we here show results starting at $t = 3360\tau_e$. At these earlier times, the convergence of the limit in our full calculation using equation (5.2.9) is limited due to the enormous energy barriers involved, producing tiny values for the fraction of success even for fully aligned nuclei. For the majority of our data set the estimated rate kinetics calculation produces slower average crossing times than the simulated rate kinetics version. However, this is not the case for $t = 3400\tau_e$ because the critical nuclei for the individual barriers has become so large that it is beyond the region of the investigation from section 5.2.1. For these large critical nuclei, the accuracy of our fitting formula (5.2.1) that predicts rate kinetics is in question.

The performance of our approximation (5.2.16) is excellent for both simulated and estimated rate kinetics in comparison to the full calculation. This is a clear verification that our assumption that the failure distributions are of only minor importance, provided an accurate average failure time is known. Additionally, the approximation based on estimated rate kinetics is only restricted by the ability to simulate the individual energy landscapes, so it has good potential to explore large energy barriers with rotational elements. This method is particularly promising, if employed in collaboration with Jolley's method that obtains energy landscapes with a series of constrained simulations [46] (also see section 1.6.3.4).

In figure 5.8, we display the entire set of simulation and calculation results from tables 5.5 and 5.6 in a graphical format. We also convert average crossing times into instantaneous nucleation rates, using the relation $N_R = 1/\langle\tau\rangle$. This is valid because the distributions of nucleation times are very close to exponential. Even though the times produced are within the square of the length of the landscape (n_f), which would suggest a diffusional process, this is not the case. For consistency we use a standard nucleation state of

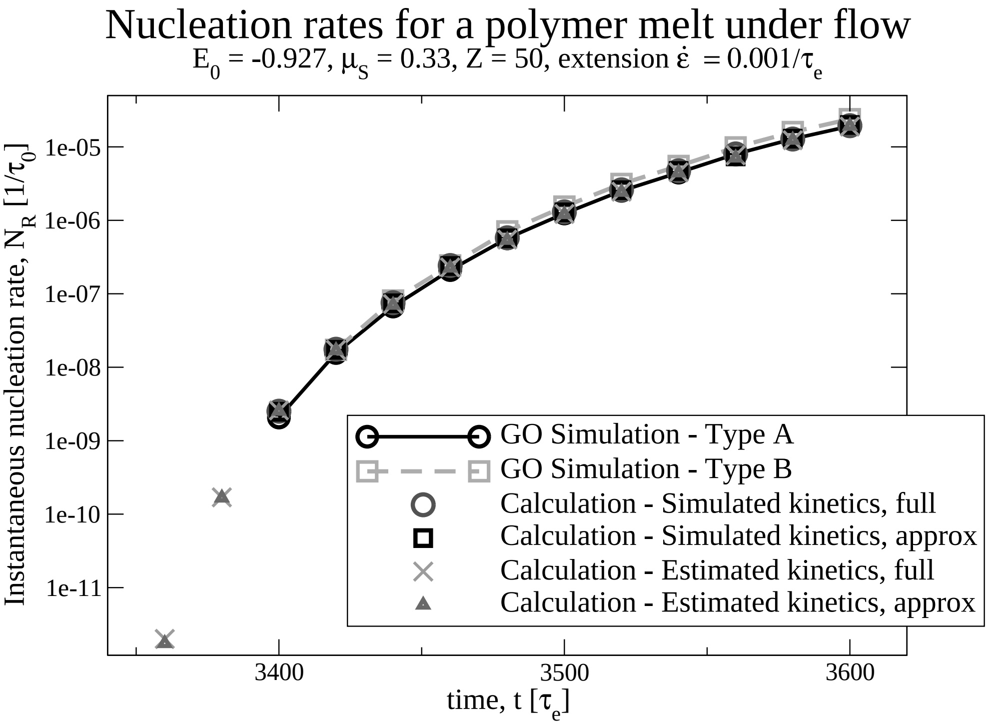

Figure 5.8: Plot of instantaneous nucleation rates at quasi-statically fixed points in time from $t = 3360\tau_e$ to $t = 3600\tau_e$ for a polymer melt described by $Z = 50$, $E_0 = -0.927$, $\mu_S = 0.33$ exerted by an extensional flow at rate $\dot{\epsilon} = 0.001/\tau_e$. We compare two versions of the GO simulation, namely type A and type B, see table 5.5, with four methods of calculation. We display instantaneous nucleation rates for one-dimensional projections with simulated and estimated rate kinetics; for each we use both the full calculation (5.2.9) and our approximation (5.2.16).

$n_f = 2000$ throughout, and for later times approaching $t = 3600\tau_e$, this nucleation point is unnecessarily beyond the critical nuclei of highly-aligned barriers. The simulations and calculation could have easily used a much smaller nucleation point, and it would have a negligible effect on crossing times. Hence in this period of time, the process is clearly not diffusional. The data sets are presented on a logarithmic axis meaning they are almost inseparable, but this plot allows us to focus on the general pattern. Note that from table 5.6 our linear time axis could equally represent a linear chain stretch, λ, in the small range $3.0 < \lambda < 3.2$. The first general observation is the vast expanse in nucleation rates produced for such a small increase in the chain stretch. It is clear that prior to the information on this plot, in the development of this polymer melt, the nucleation rate is increasing from an unimaginably small initial quiescent rate. Due to the enhancement of chain stretch and together with rotational effects, the nucleation rate enters a suitable range for simulation with an extremely steep gradient. From an experimental perspective, the effect could be seen as zero nucleation events for an initial time period, and then a sudden onset of growing nuclei. This waiting period has been referred to as an induction time [70]. As the chain stretch increases, the energy barriers for a highly-aligned nuclei reduce significantly and nucleation then begins to change from barrier crossing to a more diffusional process. The plot shows this effect beginning in the rapidly slowing gradient of our nucleation rates.

5.4 Discussion

In this section, we summarise and discuss the main ideas and results of the chapter. We began by analysing the rotational effects of the original GO polymer nucleation simulation. The model implemented nucleus rotation in two ways. First, through a convective drag force which is independent of nucleus size. In addition to a random rotational diffusion term, with a relaxation time linearly related to nucleus size. Figure 5.1 showed that the rotational convective drag force in the model has a negligible effect on nucleation times unless rotational diffusion is implemented so slowly that it would be clearly unphysical. We introduced a physically justified improvement to the model, referred to as the modified GO simulation, which contained a stepped rotational diffusion parameter. This simulation allows extremely fast rotational diffusion moves at the base state, but for larger nuclei, reflecting the highly restricted nature of polymer melts, rotational diffusion is extremely slow. To approximate this more physically relevant regime, we developed a model, where nuclei have an average orientation at the base state ($N_T = 1$) and a randomly selected fixed orientation for larger nuclei with a reset capability if it returns to the base state. For increasing rotational diffusion at the base state which is computationally expensive, figure 5.3 shows crossing times tend towards the simple cheaper regime of averaging the orientation.

We presented a rotational model calculation which aimed to replicate the simple GO simulation of averaging the nucleus orientation at the base state and fixing it in a randomly selected direction for larger nuclei. The calculations rely on our ability to project a complicated multi-dimensional system onto one-dimensional energy landscapes and rate kinetics. We completed a thorough investigation to find rate kinetics, focusing on highly-aligned, fixed nuclei, and produced the general fit curve (5.2.1). The full, extensive calculation contains multiple stages and culminates in the equation (5.2.8), with (5.2.9) used for finding average crossing times from Laplace space. We developed a practical refinement of the system to allow more detailed discretisation and to focus on highly-aligned nuclei by merging all unaligned nuclei with extremely high energy barriers together. We also presented an accurate approximation (5.2.16) of the full calculation by hugely simplifying the failure time distributions.

We completed an initial test of our rotation model, by comparing several different calculated nucleation times with the GO simulation as well as a one-dimensional toy simulation. The result of reducing the system by only resolving highly-aligned nuclei was highly successful as shown by table 5.1. We also explored variations in several calculated parameters, and the effect of the failure state, n_a, was displayed in table 5.2. The level of discretisation in the orientation selection process, also has an effect on crossing times as shown by figure 5.7. In general, the accuracy of our full calculation is superb, and even the approximation is good, especially since it requires such a small amount of information. In fact our formulation has the ability to solve rotational systems with much higher barriers than any stochastic simulation could even partially explore. We also completed an in-depth comparison of various calculations and simulations for a series of time increments in a transient polymer melt under flow using chain configuration data from the GLaMM model. This work modelled FIC and particularly the effects of enhanced nucleation due to the inclusion of nucleus rotation, summarised by figure 5.8. The nucleation rates produced are accurate in comparison to the GO simulation for a wide range of these dynamical systems.

Chapter 6

Discussion and future work

6.1 Summary

The overall aim of this thesis was to develop analytic models of polymer nucleation, particularly flow-induced crystallisation (FIC). We reviewed background material on polymer and classical nucleation theory in chapter 1. As well as detailing the Graham-Olmsted (GO) polymer nucleation simulation, which we intensely explored and significantly enhanced with analytic treatment. We achieved a complete combinatorial formulation to obtain energy landscapes from the basic rules of the GO model in chapter 2. A common method to obtain nucleation times from energy barriers is to apply the Boltzmann approximation; we improved on this crude barrier height assumption by investigating the kinetic prefactor. At first in chapter 3, we presented a novel technique to extract rate kinetics from certain non-equilibrium simulatons, that enabled us to create equivalent one-dimensional problems of these multi-dimensional systems. Additionally in chapter 4, we provided an exact discrete barrier crossing calculation to accurately predict nucleation times. Finally in chapter 5 we applied several results of the thesis to develop a nucleation model that includes the impact of nucleus rotation. This feature as shown by the GO model is crucially important to polymer nucleation under flow.

In greater detail chapter 2 presented an analytic calculation that accurately predicts nucleation energy landscapes from the successful GO polymer simulation. We used a combinatorial technique to systematically count the number of arrangements of energetically similar nuclei. This method was specifically useful for high energy barriers, too difficult for simulation. This calculation supported the universal master curve obtained from the GO simulation (see figure 2.3), that the rate of nucleation is directly linked to the degree of chain stretch in the polymer melt. We also suggested an empirical function (2.2.2), as a simple model for FIC. This implied the rate of nucleation is independent of other factors such as the molecular weight of the individual chains and the flow geometry. In addition, we investigated the nucleation of bimodal blends, which are mixtures of long and short linear chains in polymer melts, by including a concentration term for attaching new chains to the nucleus. In the analysis of these bimodal systems we discovered a complimentary empirical description (2.2.3) generalising the pure melt cases. This formulation contains an extra parameter, β, that has a clear power law dependence on the volume fraction of the long chains. Significantly this expression for the nucleation rate, and specifically the separate components of the formula, have the potential be tested experimentally. However, due to the multiple nested sums in our combinatorial calculation, there is a practical limitation to small critical nuclei. The main use of our analytic calculation was to validate GO simulation results. It has proven to be extremely helpful to ensure the algorithm is correct, particularly when executing alterations.

In chapter 3 we presented a method to project multi-dimensional barrier crossing problems onto one-dimensional systems. This included a novel technique to extract effective rate kinetics with expression (3.1.11) from non-equilibrium simulations. These rate kinetics along with the equilibrium energy barrier produce an equivalent one-dimensional system. We expect our projection to be applicable to a broad range of barrier crossing problems. Although we note several underlying assumptions have been employed, so our extraction technique may not be suitable to certain models. In section 3.1.2 we discussed clear guidelines as to which types of general barrier crossing problems our method is potentially able to provide useful analysis. We performed an extensive investigation of the GO simulation using this technique. Our findings were of great interest, first we discovered the height of an energy barrier has a negligible affect on the rate kinetics at critical nuclei. Also the rate kinetics for quiescent and modestly stretched, pure melts noticeably deviated from an expected spherical growth pattern but remained independent of barrier height. For bimodal blends, this deviation was further enhanced, implying these melts take significantly different routes over the energy landscape to nucleation producing more elongated nuclei.

Chapter 4 developed crucially important mathematical models of one-dimensional barrier crossing. At first we concentrated on basic static barriers, obtaining an exact formula (4.1.4) and an excellent approximation (4.1.19) for the average crossing time. We also discovered using the same technique, formula for the fraction of successful nuclei from an initial size of two monomers (4.1.28) as well as the average failure time (4.1.29) to return to the base state. We used a probabilistic approach to barrier crossing, and solved the resulting convoluted systems in Laplace space to obtain complete distributions of crossing times (4.1.40). The result (4.1.46) was essential to the second part of chapter 4 which investigated dynamic barriers, it gave us the ability to find average crossing times from the probability distributions in Laplace space without the need for a potentially impractical inverse transform. We developed several toy nucleation models with dynamic energy barriers. These included features such as a randomly chosen, variable continuous barrier height, models with multiple discrete paths with a reset capability, and the option to alter the selection state. The crucial results were collecting together the success and failure distributions of separate paths, using conditional probabilities (4.2.12), and solving the complete system in Laplace space (4.2.13).

In chapter 5, we presented our foremost model of polymer nucleation that includes crystal rotation. The relative alignment of a nucleus with respect to the flow direction has a massive impact on the likelihood of a successful nucleation event as more monomers in the melt are correctly oriented for attachment. At first we analysed the rotational elements of the GO simulation and concluded from the crossing time results in figure 5.1 that the convective drag force within the model is negligible. We implemented the other element, rotational diffusion, with a greater physical relevance to polymer melts than the original GO simulation with a key modification. This was achieved by introducing a stepped rotational diffusion parameter, that allowed small nuclei to rotate easily, but movement for larger nuclei was highly restricted. To represent this regime by an analytic model, we averaged the orientational effects at the base state and ensured that larger nuclei remained fixed in a randomly selected direction. The analytic calculation was based on the one-dimensional model from chapter 4, and hence we obtained average nucleation times for the convoluted system through results (5.2.8) and (5.2.9). We tested our model with a calculation of FIC using a series of quasi-static time increments for a polymer melt under an extensional flow, applying chain configuration data from the GLaMM model. Figure 5.8 displayed the evolution of the nucleation rate from our calculations and showed that they accurately compare to two types of GO simulation.

6.2 Conclusions

This thesis has progressed the understanding of polymer nucleation in several areas. The ideas and results presented can be used as vital components of a model to describe FIC in polymer processing. The complex flows of industrial polymer production require finite element solvers to apply crystallisation models through processes of nucleation and growth. We calculate energy barriers to nucleation from a basic description of nuclei on the molecular level. Since the nucleation rate must be known for each fluid element as a function of time, simple deterministic inputs are required, hence analytic tools must be deployed in the final model. These analytic calculations ought to be fueled by highly detailed molecular simulations, which will have a large role in the investigation. We developed techniques to project these multi-dimensional systems onto one-dimensional representations by grouping together states with the same volume. Moreover, we introduced an extraction technique to find effective rate kinetics from a non-equilibrium simulation. This enabled us to produce a barrier crossing model for polymer nucleation which included crystal rotation, concentrating on highly-aligned nuclei. These calculations are still too expensive for finite element schemes, so further levels of simplification are required. However our approximation (5.2.16), focused on highly-aligned nuclei with a generalised failure rate, is a major advancement. Eventually the progress in this area of research could allow the plastics industry to finely tune the internal morphology of semi-crystalline polymers. This impacts greatly on many physical characteristics of the resultant material.

6.3 Comparison with experiments

In section 1.6.3.6 we reviewed an initial comparison between the GO polymer nucleation simulation and experimental data [6]. Here we update the examination by describing recent work by Jolley [79], which provides further results to compare with new data by Pantani [80]. The fast algorithm [46] (reviewed in section 1.6.3.4) for simulating crossing times over extremely high barriers enabled Jolley to map a large previously untouchable region of the parameter space with included experimentally relevant regimes. They were also able to create a semi-analytic model to predict nucleation rates for purely long chain melts. Key to this development were the one-dimensional projection and rate kinetics extraction technique from chapter 3 along with the barrier crossing calculation from chapter 4. A rescaling method was then employed to estimate nucleation rates for bimodal blends of long and short chains. Note that this work does not include a nucleus rotation component, a similar detailed analysis of the model presented in chapter 5 over a broad region of the parameter space is required to assess rotational effects.

The nucleation rate comparison was made on the same industrial polydisperse isotactic polypropylene melt at three different temperatures (originally $140°C$ [6] with new data from $138°C$ and $144°C$ [80]). The results are displayed in figure 12 of [79], there is excellent agreement with most data points except for large shear rates. It has been postulated that this error is due to a local exhaustion of favourable monomers from long chains at high shear rates. This possible kinetic occurrence is not a feature of the GO model, and could be a reason for the overprediction of nucleation rates.

Jolley was also able to produce a speculative prediction of the polymer melting point. This was achieved by calculating the asymptotic limit in the bulk parameter E_0 which produces an infinite energy barrier in conjunction with the other fitted parameters. The three values from the different temperature measurements then provide a base for the linear extrapolation shown in figure 13 of [79]. The predicted melting point of $224°C$ was not too far away from the actual experimental value of 194°C, and is a reasonable estimate considering the small amount of data.

6.4 Immediate future work

In this section, we consider some immediate potential research ideas. Beginning in section 6.4.1, concentrating on the area of polymers, and we describe more general applications in section 6.4.2.

6.4.1 Polymers

This section focuses on presenting ideas for further work in the area of polymers, particularly the nucleation of polymers. Describing the behaviour of entangled polymer chains has been a great scientific challenge for many years, both in terms of experimental and theoretical work. Moreover, it is likely to remain an important element of research as many phenomena and problems are far from being fully understood. In this thesis we used the GLaMM model of entangled polymer flow [31], detailed in section 1.3. The model has been extensively tested against experimental data on amorphous polymers [31, 32, 33, 35, 36], and accurately predicts the behaviour of polymers under strong flow. It does, however, have several weaknesses that are mentioned in section 1.3, in particular, the model is incapable of describing an industrial polydisperse melt containing molecules with a wide distribution of molecular weights. Especially pertinent to polymer nucleation, the GLaMM model uses an averaged ensemble to describe chain configurations. Thus rare occurrences of highly stretched chains, which could have a large impact on nucleation, are neglected. All nucleation techniques and models in this thesis could readily incorporate chain configuration data from a new entangled polymer flow description.

We now focus on advising the next research steps directly following the ideas and results on polymer nucleation from this thesis. In chapter 2, we produced an analytic calculation of energy landscapes to nucleation, and although it predicted the GO simulation exactly, it was computationally expensive due to the involvement of multiple nested sums. To enhance the scope and investigate the energy landscapes surrounding large critical nuclei, we could attempt an expansive integral approximation of the combinatorial calculations. If successful, this approach, together with predicted rate kinetics and our one-dimensional barrier crossing work, would give us a completely analytic model of polymer nucleation for a wide range of potential energy barrier shapes. In addition, a combined analytic and simulation investigation into the effect of bimodal blends of long and short chain molecules and melts with greater polydispersity on FIC would be huge step for the research field. In particular, the interplay of multiple stretched species on the nucleation barrier. This approach could also be employed to explore the formation of shish-kebab shaped crystals.

Our foremost model of polymer nucleation including crystal rotation, was explained in chapter 5, and has yet to be fully utilized. We applied the method to a purely long chain polymer melt subjected to an extensional flow to predict the GO simulation. The calculation could also be performed on a shear flow geometry. In addition, the model could investigate FIC in bimodal blends with chain configuration data from the GLaMM model, which are more closely related to industrial products. This technique has large potential to investigate the nucleation of polymer melts in regimes of undercooling significantly lower than the GO simulation can achieve solely. By grouping the convoluted system together, the only restriction is the ability to obtain energy barriers for individual highly-aligned nuclei via simulation or calculation. Our rotation model of polymer nucleation could also incorporate a different molecular description, perhaps a more detailed MD simulation provided that a projected one-dimensional barrier is available for each relevant orientation. As discussed in section 6.2, this analytic model is still too expensive for deployment in finite element calculations, that are needed to study polymer nucleation in an industrial context. However, the patterns discovered with this approach, together with further simplifications, could be important steps in the understanding of FIC in polymers.

6.4.2 General applications to barrier crossing

In this section, we propose further applications outside of the field of polymers, for the barrier crossing techniques and models employed throughout this thesis. Although the calculation in chapter 2 for the number of arrangements of similar nuclei, was specifically designed for the molecular description in the GO model, the counting techniques could be applied to other areas of statistical physics. Particularly for simplifying complicated systems, as in the split calculation we used to separate the different species.

A method that has the potential to be widely applicable to numerous multi-dimensional energy barrier crossing problems is the one-dimensional projection from chapter 3. In particular, our technique for extracting rate kinetics could be used to examine various simulation types. The scenarios we expect our method to be potentially useful are situations where barrier crossings are rare, and the dominant mechanism is through a series of unlikely incremental steps. The technique is also reliant on the equilibrium energy barrier being relevant to non-equilibrium system, but is not appropriate when strong kinetic contributions dominate the process, and enable crossings over highly unfavouable energetic pathways. We also derived a complementary technique to simulate the same quantity far below the barrier peak where the non-equilibrium distribution is close to the Boltzmann case. This is provided these systems can be simplified onto a single reaction coordinate; in nucleation, this coordinate could be the volume or radius of growing nuclei; or, in terms of general energy wells, it could be the distance from a minimum. The rate kinetics could be vital in providing insight into specific problems, particularly if they are independent of barrier characteristics, which could enable the formulation of a deterministic model. Furthermore, for systems where a one-dimensional projection may not sufficiently describe the physics of a problem. We could generalise this technique to higher dimensional barrier crossing, for example to find kinetic information across a saddle-shaped landscape, this would require an extension of our net flux between adjacent states set-up (3.1.1) into a higher dimensional form.

In chapter 4, we developed several one-dimensional energy barrier crossing models with dynamic features. These included uncertainty in the energy level of the next state, as well as a time dependent decreasing barrier height, and our models had the ability to reset the landscape. We solved these configurations of convoluted probabilities with a Laplace transform approach to find complete distributions of crossing times. There is a wide range of potential applications for these models, for example, in the area of genetics, they could be used to study the popularity and spread of advantageous mutations over many generations with a changing environment or climate. Alternatively, in the field of economics, they could be useful in developing a simple business growth model, that assesses the success and failure of different sizes of companies with fluctuating market conditions. The dynamic tools in our one-dimensional barrier crossing approach could become very powerful for these and many other possible applications.

6.5 Long term future work

In this section, we take a long term view of the potential insight this thesis could add to the area of polymer nucleation. Future models may contain a more detailed description of molecular dynamics, and resolve monomer interactions in both solid and amorphous phases. These may use a Lennard-Jones style, hard sphere potential within a polymer framework. Our technique for extracting rate kinetics from a one-dimensional projection could be of great use in these simulation regimes. In particular, patterns in the rate kinetics, will help assess the shape of stable crystals produced by these models.

The fundamental nature of nucleation is that it is the study of rare events, hence highly coarse-grained simplistic models, such as the GO model are required to ease computational expense. To advance the understanding of polymer nucleation, we aim to combine models describing behaviour at different scales to learn from each other. For example the GO model would benefit from a detailed investigation focused on the attachment of monomers from new chains, which it implements through a side area function, and contributes to the rate kinetics. More detailed simulations may suggest a better functional form for the side area functions. They could also question and improve the choice of coarse graining used to produce the GO model, particularly the simple description of the nucleus, as well as the assumption in making stem lengthening moves and the effect of concentration of competing species. The analytic tools of this thesis, namely the calculation of energy landscapes, nucleation kinetics and the rotation model, can provide an efficient method for executing alterations. Even if the highly detailed models suggest a new molecular description of the nucleus is required, the combinatorial calculation could be adapted to obtain new degeneracies for similar nuclei, and also provides a framework to interpret deviations. The overall aim for the advancement of the research field is to produce an accurate but sufficiently simplified model for polymer nucleation to be implemented in a finite element scheme for FIC. This could be compared with experimental data [81], and used to improve the processing of plastic materials.

Bibliography

[1] P E Rouse. A theory of the linear viscoelastic properties of dilute solutions of coiling polymers. *Journal of Chemical Physics*, 21:1272, 1953.

[2] M Doi and S F Edwards. *The Theory of Polymer Dynamics*. Oxford University Press, Oxford, 1986.

[3] S F Edwards. The statistical mechanics of polymerized material. *Proceedings of the Physical Society*, 92:9–16, 1967.

[4] P G de Gennes. Reptation of a polymer chain in the presence of fixed obstacles. *Journal of Chemical Physics*, 55:572–579, 1971.

[5] E L Heeley, C M Fernyhough, R S Graham, P D Olmsted, N J Inkson, J Embery, D J Groves, T C B McLeish, A C Morgovan, F Meneau, W Bras, and A J Ryan. Shear-induced crystallization in model blends of linear and long-chain branched hydrogenated polybutadienes. *Macromolecules*, 39:5058–5071, 2006.

[6] I Coccorullo, R Pantani, and G Titomanlio. Spherulitic nucleation and growth rates in an iPP under continuous shear flow. *Macromolecules*, 41:9214–9223, 2008.

[7] A Keller and H W Kolnaar. Flow induced orientation and structure formation. In *Processing of Polymers*, volume 18, page 189. Wiley-VCH, Weinheim, 1997. H E H Meijer (editor).

[8] F L Binsbergen. Orientation-induced nucleation in polymer crystallization. *Nature*, 211:516–517, 1966.

[9] R S Graham. Molecular modelling of flow-induced crystallisation in polymers. *Journal of Engineering Mathematics*, 71:237–251, 2010.

[10] B S Hsiao, L Yang, R H Somani, C A Avila-Orta, and L Zhu. Unexpected shish-kebab structure in a sheared polyethylene melt. *Phys Rev Lett*, 94:117802, 2005.

[11] M Seki, D W Thurman, J P Oberhauser, and J A Kornfield. Shear-mediated crystallization of isotactic polypropylene: The role of long chain-long chain overlap. *Macromolecules*, 35:2583–2594, 2002.

[12] L Balzano, N Kukalyekar, S Rastogi, G W M Peters, and J C Chadwick. Crystallization and dissolution of flow-induced precursors. *Phys Rev Lett*, 100:048302, 2008.

[13] O O Mykhaylyk, P Chambon, R S Graham, J P A Fairclough, P D Olmsted, and A J Ryan. The specific work of flow as a criterion for orientation in polymer crystallization. *Macromolecules*, 41:1901–1904, 2008.

[14] S Kimata, T Sakurai, Y Nozue, T Kasahara, N Yamaguchi, T Karino, M Shibayama, and J A Kornfield. Molecular basis of the shish-kebab morphology in polymer crystallization. *Science*, 316:1014–1017, 2007.

[15] D Turnbull and J C Fisher. Rate of nucleation in condensed systems. *Journal of Chemical Physics*, 17:71–73, 1949.

[16] M J Ko, N Waheed, M S Lavine, and G C Rutledge. Characterization of polyethylene crystallization from an oriented melt by molecular dynamics simulation. *Journal of Chemical Physics*, 121:2823, 2004.

[17] N Waheed, M J Ko, and G C Rutledge. Molecular simulation of crystal growth in long alkanes. *Polymer*, 46:8689–8702, 2005.

[18] W Hu, D Frenkel, and V Mathot. Simulation of shish-kebab crystallite induced by a single prealigned macromolecule. *Macromolecules*, 35:7172–7174, 2002.

[19] W Hu and D Frenkel. Polymer crystallization driven by anisotropic interactions. In *Advances in Polymer Science*, pages 1–35. Springer, 2005.

[20] J Zhang and M Muthukumar. Monte Carlo simulations of single crystals from polymer solutions. *Journal of Chemical Physics*, 126:234904, 2007.

[21] R S Graham and P D Olmsted. Kinetic Monte Carlo simulations of flow-induced nucleation in polymer melts. *Faraday Discuss*, 144:71–92, 2010.

[22] R S Graham and P D Olmsted. Coarse-grained simulations of flow-induced nucleation in semicrystalline polymers. *Phys Rev Lett*, 103:115702, 2009.

[23] G Eder and H Janeschitz-Kriegl. Crystallization. In *Processing of Polymers*, volume 18, page 189. Wiley-VCH, Weinheim, 1997. H E H Meijer (editor).

[24] H Zuidema, G W M Peters, and H E H Meijer. Development and validation of a recoverable strain-based model for flow-induced crystallization of polymers. *Macromolecules Theory Simulations*, 10:447–460, 2001.

[25] R J A Steenbakkers. *Precursors and nuclei, the early stages of flow-induced crystallization.* PhD thesis, Eindhoven University, 2009.

[26] S Coppola, N Grizzuti, and P L Maffettone. Microrheological modelling of flow-induced crystallization. *Macromolecules*, 34:5030–5036, 2001.

[27] W Schneider, A Köppl, and J Berger. Non-isothermal crystallization. *International Polymer Processing*, 3:151–154, 1988.

[28] H Janeschitz-Kriegl. Polymer solidification by crystallization under heat transfer and flow conditions. In *Progress in Colloid and Polymer Science*, page 116. Springer, 1992.

[29] A E Likhtman and T C B McLeish. Quantitative theory for linear dynamics of linear entangled polymers. *Macromolecules*, 35:6332–6343, 2002.

[30] R S Graham. *Molecular modelling of entangled polymer fluids under flow.* PhD thesis, University of Leeds, 2002.

[31] R S Graham, A E Likhtman, T C B McLeish, and S T Milner. Microscopic theory of linear, entangled polymer chains under rapid deformation including chain stretch and convective constraint release. *Journal of Rheology*, 47:1171–1200, 2003.

[32] M W Collis, A K Lele, M R Mackley, R S Graham, D J Groves, A E Likhtman, T M Nicholson, O G Harlen, T C B McLeish, L R Hutchings, C M Fernyhough, and R N Young. Constriction flows of monodisperse linear entangled polymers: Multiscale modeling and flow visualization. *Journal of Rheology*, 49:501–522, 2005.

[33] D Auhl, J Ramirez, A E Likhtman, P Chambon, and C Fernyhough. Linear and nonlinear shear flow behavior of monodisperse polyisoprene melts with a large range of molecular weights. *Journal of Rheology*, 52:801, 2008.

[34] J Bent, L R Hutchings, R W Richards, T Gough, R Spares, P D Coates, I Grillo, O G Harlen, D J Read, R S Graham, A E Likhtman, D J

Groves, T M Nicholson, and T C B McLeish. Neutron-mapping polymer flow: Scattering, flow-visualisation and molecular theory. *Science*, 301:1691–1695, 2003.

[35] R S Graham, J Bent, L R Hutchings, R W Richards, D J Groves, J Embery, T M Nicholson, T C B McLeish, A E Likhtman, O G Harlen, D J Read, T Gough, R Spares, P D Coates, and I Grillo. Measuring and predicting the dynamics of linear monodisperse entangled polymers in rapid flow through an abrupt contraction. a small angle neutron scattering study. *Macromolecules*, 39:2700–2709, 2006.

[36] A Blanchard, R S Graham, M Heinrich, W Pyckhout-Hintzen, D Richter, A E Likhtman, T C B McLeish, D J Read, E Straube, and J Kohlbrecher. SANS observation of chain retraction after a large step deformation. *Phys Rev Lett*, 95:166001, 2005.

[37] S Auer and D Frenkel. Numerical simulation of crystal nucleation in colloids. *Adv. Polym. Sci.*, 173:149–207, 2005.

[38] J B Zeldovich. On the theory of new phase formation; cavitation. *Acta Physico Chimica*, 18:1–22, 1943.

[39] M E Cates and M R Evans. *Soft and Fragile Matter.* The Scottish Universities Summer School in Physics, 2000.

[40] P G De Gennes. Reptation of stars. *J. Phys. France*, 36(12):1199–1203, 1975.

[41] M Doi and N Y Kuzuu. Rheology of star polymers in concentrated solutions and melts. *Journal of Polymer Science: Polymer Letters Edition*, 18(12):775–780, 1980.

[42] M Rubinstein and E Helfand. Statistics of the entanglement of polymers: Concentration effects. *The Journal of chemical physics*, 82(5):2477, 1985.

[43] R C Ball and T C B McLeish. Dynamic dilution and the viscosity of star polymer melts. *Macromolecules*, 22:1911–1913, 1989.

[44] S T Milner and T C B McLeish. Parameter-free theory for stress relaxation in star polymer melts. *Macromolecules*, 30:2159–2166, 1997.

[45] A F Voter. Introduction to the kinetic Monte Carlo method. In *Radiation Effects in Solids*, NATO Science Series. Springer, Dordrecht, The Netherlands, 2007. K. E. Sickafus and E. A. Kotomin (editors).

[46] K Jolley and R S Graham. A fast algorithm for simulating flow-induced nucleation in polymers. *Journal of Chemical Physics*, 134:164901, 2011.

[47] D Frenkel and B Smit. *Understanding Molecular Simulations. From Algorithms to Applications. second edition.* Academic Press, San Diego, 2001.

[48] M P Allen and D J Tildesley. *Computer Simulation of Liquids.* Oxford University Press, New York, 1987.

[49] D T Gillespie. Exact stochastic simulation of coupled chemical-reactions. *Journal of Chemical Physics*, 81:2340–2361, 1977.

[50] K B Petersen and M S Pedersen. The matrix cookbook. http://www2.imm.dtu.dk/pubdb/views/edoc_download.php/3274/pdf/imm3274.pdf. last visited 25 June 2010.

[51] L Jarecki. Kinetic theory of crystal nucleation under transient molecular orientation. In *Progress in Understanding of Polymer Crystallization*, volume 714, pages 65–86. Springer, Berlin, 2007. G Reiter and G R Strobl (editors).

[52] A Cohen. A Padé approximant to the inverse Langevin function. *Rheologica Acta*, 30:270–273, 1991.

[53] L G Leal and E J Hinch. The rheology of a suspension of nearly spherical particles subject to Brownian rotations. *Journal of Fluid Mechanics*, 55:745–765, 1972.

[54] G B Jeffery. The motion of ellipsoidal particles immersed in a viscous fluid. *Proc. Royal Society London A*, 102:161–179, 1922.

[55] L G Leal and E J Hinch. The effect of weak Brownian rotations on particles in shear flow. *Journal of Fluid Mechanics*, 46:685–703, 1970.

[56] P G Bolhuis, D Chandler, C Dellago, and P L Geissler. Transition path sampling: Throwing ropes over rough mountain passes, in the dark. *Annu. Rev. Phys. Chem.*, 53(1):291–318, 2002.

[57] A K Faradjian and R Elber. Computing time scales from reaction coordinates by milestoning. *J Chem Phys*, 120:10880–10889, 2004.

[58] A C Pan and B Roux. Building markov state models along pathways to determine free energies and rates of transitions. *J Chem Phys*, 129(6):064–107, 2008.

[59] R Allen, P Warren, and P R ten Wolde. Sampling rare switching events in biochemical networks. *Phys Rev Lett*, 94(1):018–104, 2005.

[60] R J Allen, C Valeriani, and P R ten Wolde. Forward flux sampling for rare event simulations. *J Phys-Condens Mat*, 21(46):463102, 2009.

[61] L Mandelkern. *Crystallization of Polymers*. McGraw-Hill, New York, 1964.

[62] M Avrami. Kinetics of phase change i. *Journal of Chemical Physics*, 7:1103–1112, 1939.

[63] M Avrami. Kinetics of phase change ii. *Journal of Chemical Physics*, 8:212–224, 1940.

[64] M Avrami. Kinetics of phase change iii. *Journal of Chemical Physics*, 9:177–183, 1941.

[65] M C Tobin. Theory of phase transition kinetics with growth site impingement i. *Journal of Polymer Science*, 12:399–406, 1974.

[66] M C Tobin. Theory of phase transition kinetics with growth site impingement ii. *Journal of Polymer Science*, 14:2253–2257, 1976.

[67] M J Hamer, J A D Wattis, and R S Graham. Analytic calculation of nucleation rates from a kinetic Monte Carlo simulation of flow induced crystallization in polymers. *Journal of Non-Newtonian Fluid Mechanics*, 165:1294–1301, 2010.

[68] R J A Steenbakkers, G W M Peters, and H E H Meijer. Rheological modeling of flow-induced crystallization in polymer melts and limitations on classification of experiments. In *The XV International Congress On Rheology: The Society of Rheology 80th Annual Meeting*, volume 1027 of *AIP Conference Proceedings*, pages 493–495, 2008.

[69] R S Graham, J Bent, N Clarke, L R Hutchings, R W Richards, T Gough, D M Hoyle, O G Harlen, I Grillo, D Auhl, and T C B McLeish. The long-chain dynamics in a model homopolymer blend under strong flow: small-angle neutron scattering and theory. *Soft Matter*, 5:2383–2389, 2009.

[70] Y Masubuchi, K Watanabe, W Nagatake, J I Takimoto, and K Koyama. Thermal analysis of shear induced crystallization by the shear flow thermal rheometer: isothermal crystallization of polypropylene. *Polymer*, 42:5023 – 5027, 2001.

[71] S T Milner and T C B McLeish. Arm-length dependence of stress relaxation in star polymer melts. *Macromolecules*, 31:7479–7482, 1998.

[72] C D Snow, E J Sorin, Y M Rhee, and V S Pande. How well can simulation predict protein folding kinetics and thermodynamics? *Annual Review of Biophysics and Biomolecular Structure*, 34(1):43–69, 2005.

[73] E Vanden-Eijnden and M Venturoli. Exact rate calculations by trajectory parallelization and tilting. *Journal of Chemical Physics*, 131(4):044120, 2009.

[74] S Auer and D Frenkel. Prediction of absolute crystal nucleation rate in hard-sphere colloids. *Nature*, 409:1020–1023, 2001.

[75] M J Hamer, J A D Wattis, and R S Graham. A method to project the rate kinetics of high dimensional barrier crossing problems onto a tractable 1d system. *Soft Matter*, 8:11396–11408, 2012.

[76] H A Kramers. Brownian motion in a field of force and the diffusion model of chemical reactions. *Physica*, 7:284–304, 1940.

[77] M Einax, M Körner, P Maass, and A Nitzan. Nonlinear hopping transport in ring systems and open channels. *Phys. Chem. Chem. Phys.*, 12(3):645, 2010.

[78] W R Le Page. *Complex Variables and the Laplace Transform for Engineers.* Courier Dover Publications, 1980.

[79] K Jolley and R S Graham. Flow-induced nucleation in polymer melts: a study of the go model for pure and bimodal blends, under shear and extensional flow. *Rheologica Acta*, 35-4511, 2012.

[80] R Pantani, I Coccorullo, V Volpe, and G Titomanlio. Shear-induced nucleation and growth in isotactic polypropylene. *Macromolecules*, 43(21):9030–9038, 2010.

[81] L Scelsi, M R Mackley, H Klein, P D Olmsted, R S Graham, O G Harlen, and T C B McLeish. Experimental observations and matching viscoelastic specific work predictions of flow-induced crystallization for molten polyethylene within two flow geometries. *Journal of Rheology*, 53, 2009.

[82] M Abramowitz and I A Stegun. *Handbook of Mathematical Functions with formulas, graphs, and mathematical tables.* Dover Publications, New York, 1972.

Appendix A

Concentration of attaching stems free energy argument

We need to investigate the affect of the concentration of each of our different species in the polymer melt, on the free energy $\mathcal{F}$ of a particular arrangement. The impact of concentration is only felt when an additional stem is added to the nucleus. If we lengthen an existing stem, we can think of the concentration to be 100%, as we are effectively zipping-up the chain connected to the segment already attached to the crystal. The rate of moving from one state to another is defined from the simulation to be $k = \phi(1/\tau_0)\ \min(1, e^{-\Delta E})$, where ϕ is the concentration of attaching monomer and only applies if we are adding a new stem and ΔE is the difference in energy between states. Note if the move is a removal of a particular monomer then concentration is not required. Even favourable moves must overcome a small barrier, hence the inclusion of the minimum function with the base rate $(1/\tau_0)$ and at this point we will take $\tau_0 = 1$.

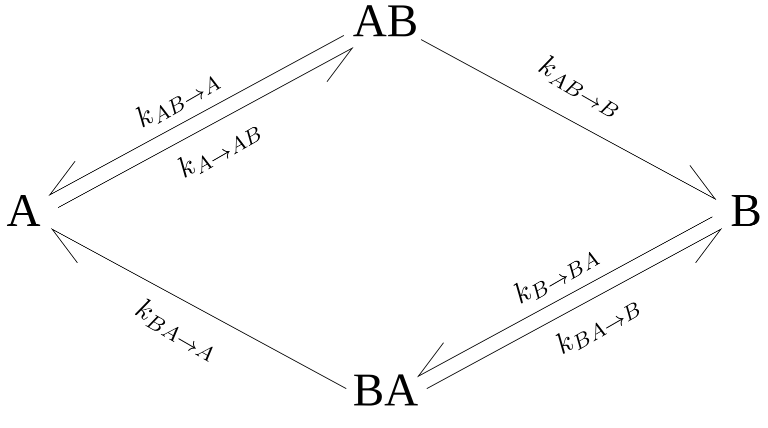

Figure A.1: Simple rate system between states $\{A\}$, $\{B\}$, $\{BA\}$ and $\{AB\}$, showing valid moves and the corresponding rates.

To do this, we analyse the simple system shown in figure A.1. Note that the states $\{AB\}$ and $\{BA\}$ are assumed to be equivalent, and the simulation [21] does not allow a move from $\{A\}$ to $\{BA\}$ because new stems must be added on the right. This does not conflict with detailed balance as it is possible to move from $\{A\}$ to $\{AB\}$ which is equivalent to $\{BA\}$.

At this point we assume $\mu_{\mathrm{S}} = 0$, since we know the surface area cost is unaffected by concentration. We also let $E_B > 0$ so that a move from state $\{A\}$ to state $\{AB\}$ is favourable and a move from state $\{BA\}$ to state $\{A\}$ is unfavourable. Now, let species A and B have different concentrations ϕ_A and ϕ_B. The rate from state $\{A\}$ to $\{AB\}$ is $k_{A\to AB} = \phi_B \min(1, e^{E_B}) = \phi_B$. The rate from $\{AB\}$ or $\{BA\}$ to $\{A\}$ is
$k_{AB\to A} = k_{BA\to A} = \min(1, e^{-E_B}) = e^{-E_B}$, no concentration is included because we are removing a stem. We merge the two states $\{AB\}$ and $\{BA\}$ each carrying equal weight into one new state, and call it $\{\overline{AB}\}$, this assumption has been confirmed using the simulation [21]. Therefore the combined rate from $\{\overline{AB}\}$ to $\{A\}$ will be

$$k_{\overline{AB}\to A} = \frac{1}{2}e^{-E_B} + \frac{1}{2}e^{-E_B} = e^{-E_B} \ .$$

The simulation simply records the amount of time spent in each state, which corresponds to the relative energy of the states. Define $P(A)$ and $P(\overline{AB})$ to be the proportion of time spent in those particular states, by detailed balance at equilibrium we have

$$P(A)k_{A\to\overline{AB}} = P(\overline{AB})k_{\overline{AB}\to A} \ \text{ therefore } \ P(A)\phi_B = P(\overline{AB})e^{-E_B} \ .$$

We can then say that $P(A) = (1/Z_p)e^{-F_A}$ and $P(\overline{AB}) = (1/Z_p)e^{-F_{\overline{AB}}}$, where Z_p is the total energy of all the states, and F_A and $F_{\overline{AB}}$ are the energy of the states $\{A\}$ and $\{\overline{AB}\}$ respectively, therefore

$$\begin{aligned} -F_A + \ln\phi_B &= -F_{\overline{AB}} - E_B \\ \text{hence } \ F_{\overline{AB}} - F_A &= -E_B - \ln\phi_B \ , && \text{(A.0.1a)} \\ \text{and similarly } \ F_{\overline{AB}} - F_B &= -E_A - \ln\phi_A \ . && \text{(A.0.1b)} \end{aligned}$$

Considering we are only interested in the differences between energy levels not the actual values, we define the baseline at our convenience as

$$F_A = -E_A - \ln\phi_A \ \text{ which means that}$$
$$F_{\overline{AB}} = -E_A - E_B - \ln\phi_A - \ln\phi_B \ \text{ and therefore } \ F_B = -E_B - \ln\phi_B \ .$$

A similar argument can be made for $E_B < 0$ which gives the same result. Thus we can see the cost due to concentration of adding a stem of concentration ϕ_i is $-\ln\phi_i$.

Appendix B

Further investigations into full landscape rate kinetics

In this appendix we have performed similar investigations to those of section 3.2.3.1, but with different critical nuclei, $n^* = 150$ and 20 respectively. In figure B.1 we have shown the effective attachment area extracted from the simulation, for fixed critical nuclei, $n^* = 150$, and at different barrier heights of $F^* = 10$, 15, 25, and 50 respectively. Similarly in figure B.2, we have displayed the effective attachment area for $n^* = 20$ and $F^* = 2$, 5, 10, and 25 respectively. In our final plots of figure B.3, we have presented the power law fittings of the effective attachment area data to compare. The four sets in figure B.3(a) are certainly close at $n^* = 150$. For the $n^* = 20$ data sets even though there are discreteness issues with the small critical nucleus size, they also are close at $n^* = 20$ in figure B.3(b). These two investigations reaffirm our conclusion that the effective attachment area only has a weak dependence on barrier height.

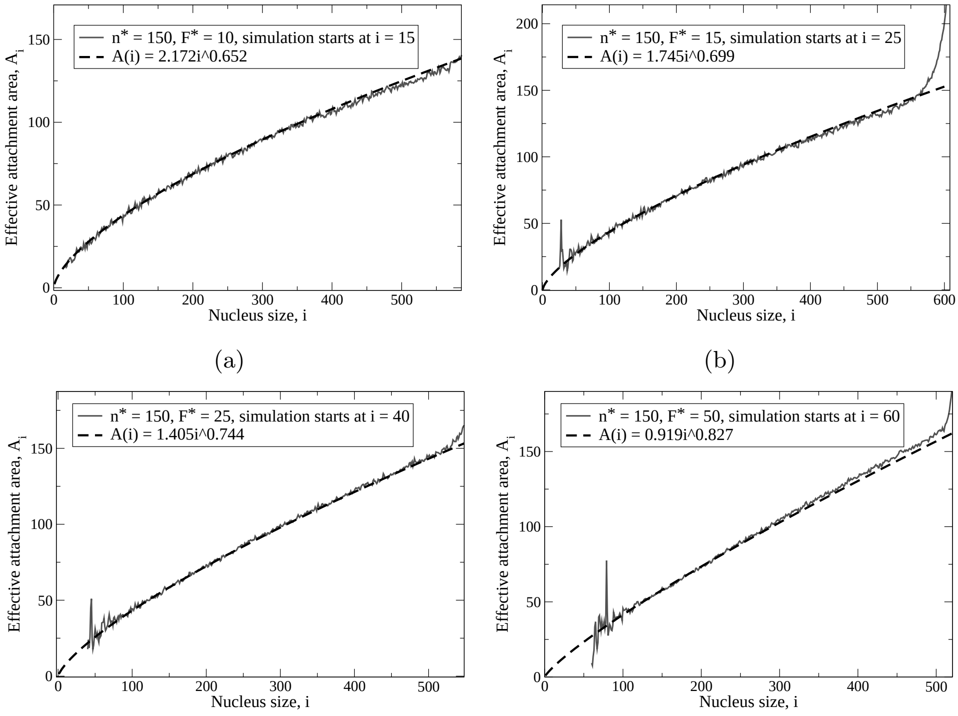

(a) (b)

(c) (d)

Figure B.1: Simulation data for energy landscapes with a fixed n^* and a wide range of varying barrier heights (a) $F^* = 10$, (b) $F^* = 15$, (c) $F^* = 25$, (d) $F^* = 50$.

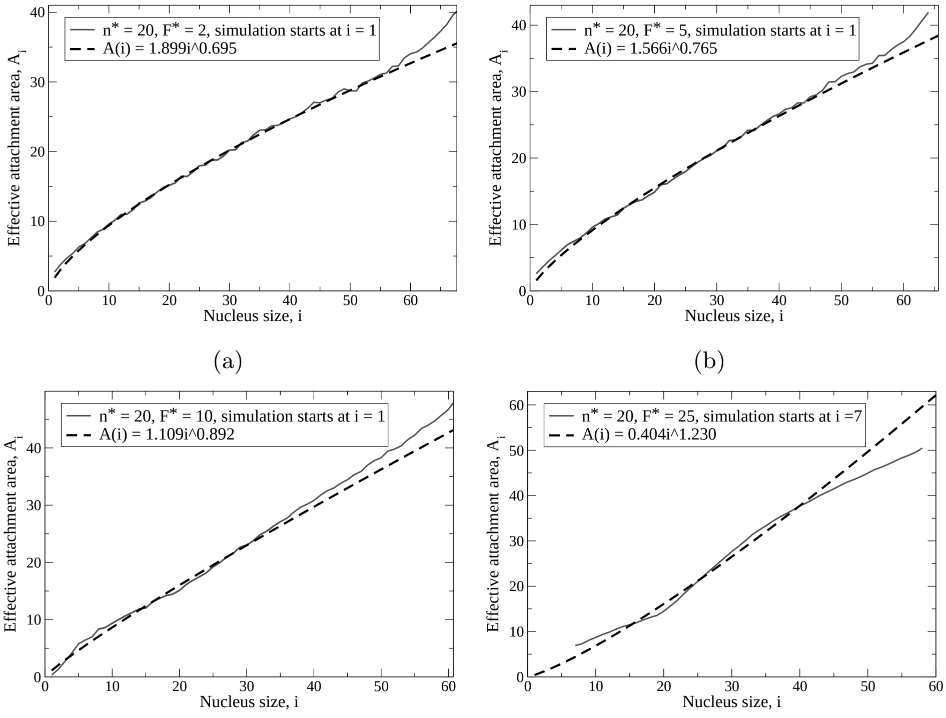

(a) (b)

(c) (d)

Figure B.2: Simulation data for energy landscapes with a fixed n^* and a wide range of varying barrier heights (a) $F^* = 2$, (b) $F^* = 5$, (c) $F^* = 10$, (d) $F^* = 25$.

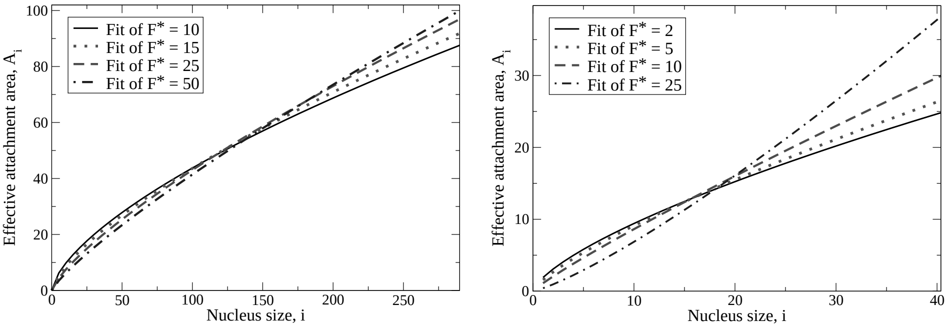

(a) (b)

Figure B.3: Comparison between power law fitting formula for fixed (a) $n^* = 150$ and (b) $n^* = 20$.

Appendix C

Three state system with decreasing barrier and reset capability

During the extensive investigation into the effects of crystal rotation on polymer nucleation, a variety of systems were developed. One such system was created to replicate the effect of a convective drag force, in which the flow acts to slowly align the crystal with the melt to lower the entropic penalty of a monomer attaching. The analysis of the GO simulation [21, 22] described in chapter 5 finds that this effect is not so physically relevant to polymer nucleation. However the one-dimensional models to describe such effects are detailed here.

To model the effect by which convection accelerates polymer nucleation, we construct the simplest system which contains a falling barrier which is reset if a particle reverts back to its initial state. This is a three state system, in which the height of the barrier between state 2 and state 3 gradually decreases while a particle occupies state 2. However if the particle returns to state 1, the barrier is reset to its original height.

To achieve this time dependent barrier, we change the rate, k_2^+, which was a constant in the static case, to be increasing with time in the form

$$k_2^+(t) = \begin{cases} (\phi_0 + Ct)f_2, & t < \frac{1}{C}\left(\frac{1}{f_2} - \phi_0\right) = t_C \ , \\ 1, & t \geq t_C \ . \end{cases}$$

The rate back to state 1 remains constant, $k_2^- = 1$, and we calculate the fraction of particles that remain in state 2 after time t, $n_2(t)$.

$$\begin{aligned}\frac{\mathrm{d}n_2}{\mathrm{d}t} &= -(k_2^- + k_2^+(t))n_2(t) \ , \\ \frac{\mathrm{d}n_2}{\mathrm{d}t} &= -(1 + (\phi_0 + Ct)f_2)n_2(t) \ , \\ n_2(t) &= \exp\left(-\left(1 + \left(\phi_0 + \frac{C}{2}t\right)f_2\right)t\right) \ ,\end{aligned}$$

here $f_2 = \exp(-\Delta E_2)$ and we have assumed that $C \ll 1$, therefore $t_C \gg 1$, thus we neglect the extremely unlikely events where particles remain in state 2 for a greater time than t_C. $P_1^+(t)$ remains the same as in section 4.1.3.1 and from $n_2(t)$ we define $P_2^-(t)$ and $P_2^+(t)$ to be

$$P_2^-(t) = k_2^- n_2(t) = \exp\left(-\left(1 + \left(\phi_0 + \frac{C}{2}t\right)f_2\right)t\right) \ , \tag{C.0.1}$$

$$P_2^+(t) = k_2^+(t)n_2(t) = (\phi_0 + Ct)\,f_2 \exp\left(-\left(1 + \left(\phi_0 + \frac{C}{2}t\right)f_2\right)t\right) \ . \tag{C.0.2}$$

As in section 4.1.3.1, to proceed, these probabilities need to be Laplace transformed; first we concentrate on $P_2^-(t)$

$$\bar{P}_2^-(s) = \int_0^\infty \exp\left[-(s + 1 + \phi_0 f_2)\,t - \frac{Cf_2}{2}t^2\right]\mathrm{d}t \ ,$$

which can be manipulated into the form

$$\bar{P}_2^-(s) = \exp\left[\frac{(s + 1 + \phi_0 f_2)^2}{2Cf_2}\right]\int_0^\infty \exp\left[-\frac{Cf_2}{2}\left(t + \frac{s + 1 + \phi_0 f_2}{Cf_2}\right)^2\right]\mathrm{d}t \ ,$$

using the substitution $t' = \sqrt{\frac{Cf_2}{2}}\left(t + \frac{s + 1 + \phi_0 f_2}{Cf_2}\right)$ we obtain

$$\begin{aligned}\bar{P}_2^-(s) &= \sqrt{\frac{2}{Cf_2}}\exp\left[\frac{(s + 1 + \phi_0 f_2)^2}{2Cf_2}\right]\int_{\sqrt{\frac{1}{2Cf_2}}(s+1+\phi_0 f_2)}^\infty \exp\left[-t'^2\right]\mathrm{d}t' \ , \\ &= \sqrt{\frac{\pi}{2Cf_2}}\exp\left[\frac{(s + 1 + \phi_0 f_2)^2}{2Cf_2}\right]\mathrm{erfc}\left(\frac{s + 1 + \phi_0 f_2}{\sqrt{2Cf_2}}\right) \ .\end{aligned}$$

If we assume $s > -1 - \phi_0 f_2$, the expansion of the complementary error function [82] can be used for large x

$$\mathrm{erfc}(x) = \frac{e^{-x^2}}{x\sqrt{\pi}}\sum_{n=0}^\infty (-1)^n \frac{(2n)!}{n!\,(2x)^{2n}} \ .$$

We calculate $\bar{P}_2^+(s)$ using a similar method

$$\bar{P}_2^+(s) = \int_0^\infty (\phi_0 + Ct)\,f_2 \exp\left[-(s + 1 + \phi_0 f_2)\,t - \frac{Cf_2}{2}t^2\right]\mathrm{d}t \ , \tag{C.0.3}$$

and if we let $u = (s + 1 + \phi_0 f_2)\,t + \frac{Cf_2}{2}t^2$

$$\bar{P}_2^+(s) = \int_0^\infty \exp[-u]\mathrm{d}u - (s+1)\int_0^\infty \exp\left[-(s + 1 + \phi_0 f_2)\,t - \frac{Cf_2}{2}t^2\right]\mathrm{d}t \ ,$$

$$\bar{P}_2^+(s) = 1 - (s+1)\bar{P}_2^-(s) \ . \tag{C.0.4}$$

Interestingly, if we approximate the complimentary error function to leading order, $\bar{P}_2^-(s)$ and $\bar{P}_2^+(s)$ revert back to the equations in (4.1.36) from the static barrier case. If we take two terms in the expansion, which is justified by C and f_2 being small and $s > 0$, the argument of the erfc function is large, then we obtain

$$\bar{P}_2^-(s) = \frac{1}{s+1+\phi_0 f_2}\left(1 - \frac{C f_2}{(s+1+\phi_0 f_2)^2}\right) , \tag{C.0.5a}$$

$$\bar{P}_2^+(s) = \frac{f_2}{s+1+\phi_0 f_2}\left(\phi_0 + \frac{C(s+1)}{(s+1+\phi_0 f_2)^2}\right) . \tag{C.0.5b}$$

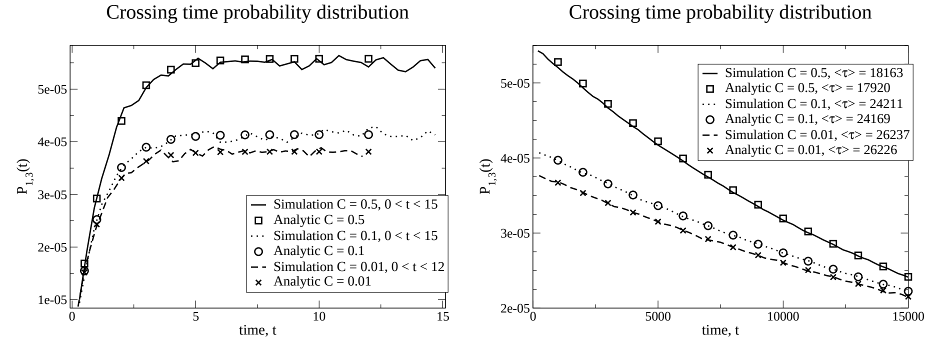

(a) (b)

Figure C.1: (a) Probability distribution, $P_{1,3}(t)$, for various values of C, early time behaviour. (b) Probability distribution, $P_{1,3}(t)$, over a longer time period, average nucleation times for simulation and analytic calculation are also displayed.

With these results, there are two strategies to advance. We could proceed in a similar manner to the example in section 4.1.3.2.1 and find $P_{1,3}(t)$ numerically, or take advantage of equation (4.1.46) to calculate the average crossing time $\langle\tau\rangle_{1,3}$. Using the first approach, with the initially using an infinite potential $F(i) = 6.4(i-1)^{2/3}$, chosen because $f_2 = \exp(-\Delta E_2) = \exp(-3.76) = 0.023$ is small and also so that the overall height at nucleation state 3 is not too large, hence the simulation is not too expensive. For various values of C, we have displayed both the early and the late time behaviour of $P_{1,3}(t)$ in figure C.1. The data sets showing early time behaviour presented in figure C.1(a), were simulated by discarding any nucleation events that take any longer than the interval $0 < t < 20$ in order to rapidly obtain good statistics for the early crossing behaviour. The plot clearly shows good agreement and the non-exponential feature of these probability distributions is more noticeable. When t becomes large, $P_{1,3}(t)$ is dominated by the slowest decaying term and so produces a more familiar exponential shape as in figure C.1(b). For the larger values of C the barrier height decreases quicker while the particle is in state 2, thus the average nucleation times are shorter. Also for relatively large C the accuracy of the analytic calculation decreases since the likelihood of a particle occupying state 1 for longer than $t_C = (1/C)\left((1/f_2) - \phi_0\right)$ becomes more significant. This effect explains the slight deviation between the simulation and analytic calculation for $C = 0.5$. Using the simpler average crossing time approach, we substitute $\bar{P}_{1,3}(s)$ from equation (4.1.35) into definition (4.1.46)

$$\langle\tau\rangle_{1,3} = \lim_{s\to 0}\left[\frac{1}{s}\left(1 - \frac{\bar{P}_1^+(s)\bar{P}_2^+(s)}{1 - \bar{P}_1^+(s)\bar{P}_2^-(s)}\right)\right] ,$$

and we proceed by applying the calculated expression for $\bar{P}_2^-(s)$ and $\bar{P}_2^+(s)$ as well as the basic result for $\bar{P}_1^+(s)$

$$\langle\tau\rangle_{1,3} = \lim_{s\to 0}\left[\frac{\left\{\begin{array}{c} (s+f_1)(s+1+\phi_0 f_2)^3 - f_1(s+1+\phi_0 f_2)^2 - Cf_1f_2 \\ -\phi_0 f_1 f_2(s+1+\phi_0 f_2)^2 + Cf_1f_2(s+1) \end{array}\right\}}{s(s+f_1)(s+1+\phi_0 f_2)^3 - f_1 s(s+1+\phi_0 f_2)^2 + Cf_1f_2 s}\right] .$$

Up to leading order in s, this becomes

$$\langle\tau\rangle_{1,3} = \frac{(1+\phi_0 f_2)^3 + f_1(1+\phi_0 f_2)^2 - Cf_1f_2}{f_1(1+\phi_0 f_2)^3 - f_1(1+\phi_0 f_2)^2 + Cf_1f_2} , \qquad \text{(C.0.6)}$$

and if we assume $f_1, f_2 \ll 1$, $\langle\tau\rangle_{1,3}$ can be approximated by

$$\langle\tau\rangle_{1,3} = \frac{1}{f_1 f_2}\left(\frac{1}{\phi_0 + C}\right) . \qquad \text{(C.0.7)}$$

Figure C.2 exhibits the limit as $s \to 0$ of $\langle\tau\rangle_{1,3}$ for various values of C, and compares these to the average crossing times of the simulation, exact analytic calculation (C.0.6) and the approximate analytic calculation (C.0.7). The first point to note is that the limit as $s \to 0$ of $\langle\tau\rangle_{1,3}$ and the exact analytic calculation show perfect agreement as expected. The simulated average crossing times also display excellent agreement with both those sets of data, especially for $C = 0.01$ and 0.1; in the case of $C = 0.5$ the small discrepancy is due to our assumption that t_C is large is not quite as secure. The approximate calculation is also in reasonable agreement with the other methods of calculating average crossing times.

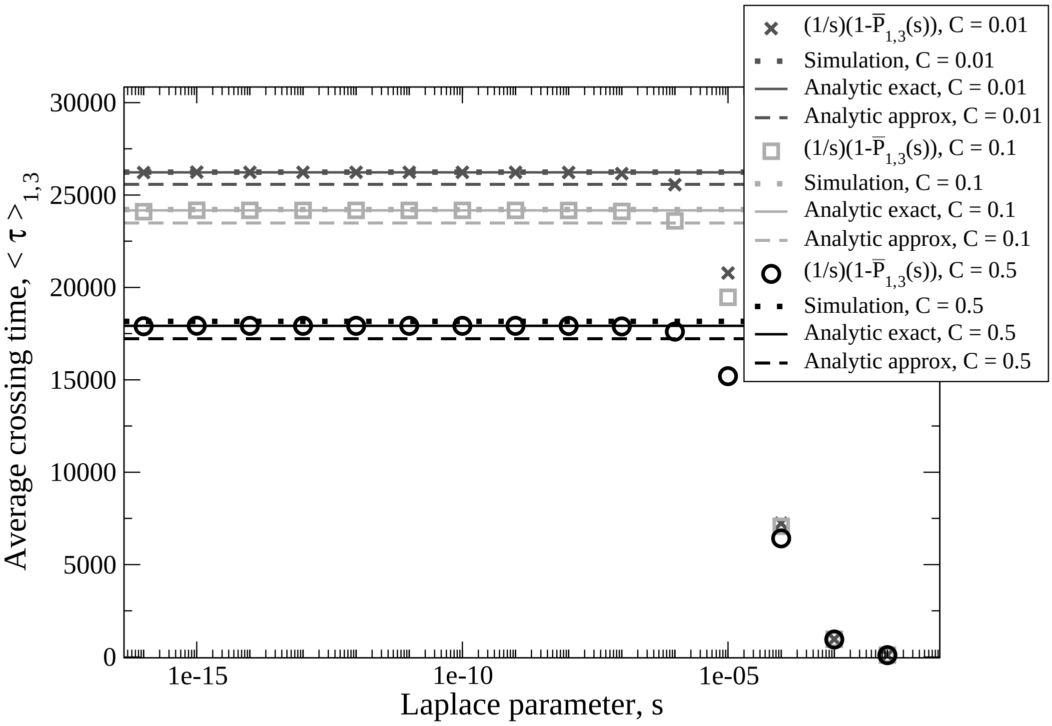

Figure C.2: Average crossing time, $\langle\tau\rangle_{1,3}$, for each $C = 0.01, 0.1, 0.5$ we have displayed the limit as $s \to 0$ and compared that to the averages for the simulation, the exact analytic calculation (C.0.6) and the approximate analytic calculation (C.0.7).